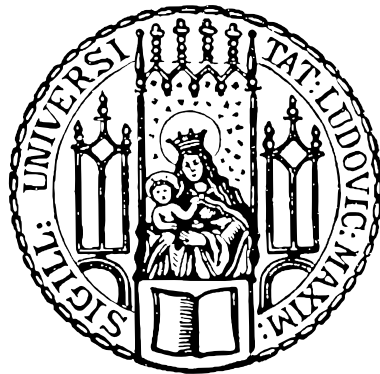
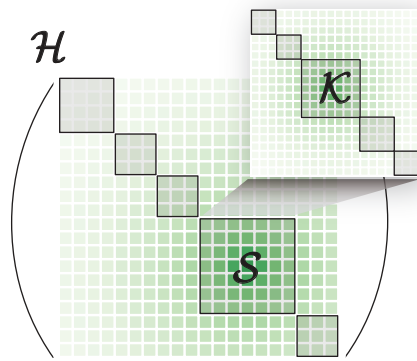

**Probing nonequilibrium dynamics in
Fermi-Hubbard chains - from
extensively-many to few conserved
quantities**

Sebastian Michael Scherg



München 2020

Probing nonequilibrium dynamics in Fermi-Hubbard chains - from extensively-many to few conserved quantities



Dissertation an der Fakultät für Physik
Ludwig-Maximilians-Universität München

vorgelegt von
Sebastian Michael Scherg
aus München

München, den 17. Dezember 2020

Tag der mündlichen Prüfung: 28.01.2021

Erstgutachter: Prof. Immanuel Bloch

Zweitgutachter: Prof. Frank Pollmann

Weitere Prüfungskommissionsmitglieder: Prof. Alexander Högele, Prof. Jan Lipfert

Zusammenfassung

Nichtgleichgewichtsdynamik in abgeschlossenen Quanten-Vielteilchensystemen ist typischerweise ergodisch und erreicht einen stationären Zustand, der durch die Hypothese der Eigenzustandsthermalisierung bestimmt ist. Zwei bekannte Ausnahmen stellen vielteilchenlokalisierte und integrable Systeme dar, in denen aufgrund einer extensiven Anzahl von Erhaltungsgrößen nicht-ergodische Dynamik auftritt. Vor Kurzem wurde eine weitere Ausnahme in Systemen mit fragmentierten Hilberträumen gefunden, die trotz nur weniger Erhaltungsgrößen nicht-ergodisches Verhalten aufweisen.

Diese Arbeit behandelt Experimente mit einer zwei-komponentigen fermionischen Mischung ultrakalter ^{40}K Atome in optischen Gittern. Es werden Messungen der Nichtgleichgewichtsdynamik gezeigt, sowohl im homogenen eindimensionalen (1D) Fermi-Hubbard Modell, als auch im gekippten 1D Fermi-Hubbard Modell, welches sowohl Vielteilchenlokalisierung also auch Hilbertraum-Fragmentierung aufweisen kann.

In Messungen zu dem homogenen 1D Fermi-Hubbard Modell wird die Expansion der Fermionen in das homogene eindimensionale optische Gitter durch einen Quench der Gittertiefe initialisiert. Anfangszustände mit einer merklichen Anzahl doppelt besetzter Gitterplätze weisen eine dynamische Phasenseparation zwischen schnell expandierenden Atomen auf einfach besetzten und langsamer expandierenden Atomen auf doppelt besetzten Gitterplätzen auf, welche im Zentrum verbleiben. Dadurch wird der entscheidende Aspekt von fermionischer Quantendestillation im starkwechselwirkenden Grenzfall realisiert. Für Anfangszustände ohne doppelt besetzte Gitterplätze wird die asymptotischen Expansionsgeschwindigkeit untersucht. Diese weist eine im Vergleich zu Bosonen geringere Wechselwirkungsabhängigkeit auf, was sich durch die Wechselwirkungsenergie erklären lässt, die durch den Quench produziert wird. Die Integrabilität des Fermi-Hubbard Modells im Vergleich zum nicht-integrablen Bose-Hubbard Modell scheint für diese Erklärung keine große Rolle zu spielen.

Bei Messungen im gekippten 1D Fermi-Hubbard Modell wird untersucht, ob nicht-ergodische Dynamik auftritt, indem die Zeitentwicklung einer Ladungsdichtemodulation innerhalb eines großen Parameterbereichs beobachtet wird. Auf kurzen Zeitskalen finden wir eine von Blochoszillationen im Ortsraum geprägte kohärente Dynamik, die wir zur

Kalibrierung aller wichtigen Parameter unseres Systems benutzen. Die Langzeitdynamik weist eine bemerkenswerte Robustheit der Ladungsdichtemodulation auf, welche ausgezeichnet von numerischen Simulationen reproduziert wird, in denen Unreinheiten vernachlässigt werden. Dies lässt die Schlussfolgerung zu, dass das beobachtete nicht-ergodische Verhalten der Ladungsdichtemodulation von emergenten kinetischen Einschränkungen hervorgerufen wird, welche mit der Fragmentierung des Hilbertraums in Verbindung stehen. Dies steht im Gegensatz zum Phänomen der Vielteilchenlokalisierung in einem gekippten Gitter mit schwacher Unordnung.

Summary

Non-equilibrium dynamics in closed quantum many-body systems are generically ergodic and reach a thermal steady-state, predicted by the eigenstate thermalization hypothesis. Many-body localized and integrable systems constitute two well known exceptions, which exhibit non-ergodic dynamics due to an extensive set of conservation laws. Recently, Hilbert-space fragmentation was predicted to showcase non-ergodic behavior even for systems with only few conservation laws. This thesis reports on experiments with a two-component fermionic mixture of ultra-cold ^{40}K atoms in optical lattices, probing out-of-equilibrium dynamics in the integrable one-dimensional (1D) Fermi-Hubbard model and the tilted 1D Fermi-Hubbard model, which lies at the interface of many-body localization and Hilbert-space fragmentation.

We probe the dynamics of the 1D Fermi-Hubbard model by quenching the lattice depth, thereby initializing the expansion of a tightly confined cloud of fermions into a homogeneous one-dimensional optical lattice. At large interaction strengths initial states with an appreciable amount of doubly-occupied sites (doublons) exhibit a dynamical phase separation between rapidly expanding singly-occupied sites and slow doublons. This realizes the key aspect of fermionic quantum distillation in the strongly interacting limit. For initial states without doublons, we study the asymptotic expansion speed and find a reduced interaction dependence compared to bosons. This observation is explained with the interaction energy produced in the quench and does not rely on the integrability of the 1D Fermi-Hubbard model as opposed to the non-integrable 1D Bose-Hubbard model.

In a second set of experiments, we investigate the tilted 1D Fermi-Hubbard model by monitoring the evolution of an initial charge-density wave over a wide range of interaction strengths and tilts. We find that the coherent short-time dynamics are characterized by real-space Bloch oscillations, which we utilize to precisely characterize our system. On longer time scales, we observe a remarkably long-lived initial-state memory. Our observations are well reproduced by numerical simulations of a clean system without imperfections, suggesting that the non-ergodic behavior appears as a result of emergent kinetic constraints and is connected to the phenomenon of Hilbert-space fragmentation. This interpretation is in contrast non-ergodic dynamics due to many-body localization, which occurs in the 1D tilted Fermi-Hubbard model with weak disorder.

Publications

This thesis reports on the work described in the following publications:

- **Sebastian Scherg**, Thomas Kohlert, Pablo Sala, Frank Pollmann, Bharath Hebbe Madhusudhana, Immanuel Bloch, Monika Aidelsburger. "Observing non-ergodicity due to kinetic constraints in tilted Fermi-Hubbard chains". *arXiv* 2010.12965 (2020)
- **Sebastian Scherg**, Thomas Kohlert, Jacek Herbrych, Jan Stolpp, Pranjal Bordia, Ulrich Schneider, Fabian Heidrich-Meisner, Immanuel Bloch, Monika Aidelsburger. "Nonequilibrium Mass Transport in the 1D Fermi-Hubbard Model". *Phys. Rev. Lett.* 121 (2018), p. 130402

The following additional publications are not covered in this thesis:

- Thomas Kohlert, **Sebastian Scherg**, Pablo Sala, Frank Pollmann, Bharath Hebbe Madhusudhana, Immanuel Bloch, Monika Aidelsburger. "Experimental evidence for Hilbert-space fragmentation in tilted Fermi-Hubbard chains". *In preparation.*
- Bharath Hebbe Madhusudhana, **Sebastian Scherg**, Thomas Kohlert, Immanuel Bloch, Monika Aidelsburger. "Benchmarking an approximate theory for localized 1D Fermi-Hubbard system on a quantum simulator". *In preparation.*
- Thomas Kohlert, **Sebastian Scherg**, Xiao Li, Henrik P. Lüschen, Sankar Das Sarma, Immanuel Bloch, Monika Aidelsburger. "Observation of Many-Body Localization in a One-Dimensional System with a Single-Particle Mobility Edge". *Phys. Rev. Lett.* 122 (2019), p. 170403
- Henrik P. Lüschen, **Sebastian Scherg**, Thomas Kohlert, Michael Schreiber, Pranjal Bordia, Xiao Li, Sankar Das Sarma, Immanuel Bloch. "Single-Particle Mobility Edge in a One-dimensional Quasiperiodic Optical Lattice". *Phys. Rev. Lett.* 120 (2018), p. 160404
- Henrik P. Lüschen, Pranjal Bordia, **Sebastian Scherg**, Fabien Alet, Ehud Altman, Ulrich Schneider, Immanuel Bloch. "Observation of Slow Dynamics near the Many-Body Localization Transition in One-Dimensional Quasiperiodic Systems". *Phys. Rev. Lett.* 119 (2017), p. 260401

Summary

- Pranjal Bordia, Henrik Lüschen, **Sebastian Scherg**, Sarang Gopalakrishnan, Michael Knap, Ulrich Schneider, Immanuel Bloch. "Probing Slow Relaxation and Many-Body Localization in Two-Dimensional Quasiperiodic Systems". *Phys. Rev. X* 7 (2017), p. 041047

Contents

Introduction	1
I. Nonequilibrium mass transport in Fermi-Hubbard chains	7
1. Theoretical background	9
1.1. Expansion dynamics of a single particle	9
1.1.1. Toymodel: A single particle in a lattice	9
1.1.2. Expansion of a single particle in a harmonic trap	12
1.1.3. Dynamics of incoherent initial density distributions	15
1.1.4. Random walks and the quantum speed-up	17
1.2. Many-body dynamics: the role of interactions	19
1.2.1. Sudden expansion in Fermi-Hubbard chains	19
1.2.2. Integrability of the one-dimensional Fermi-Hubbard model	21
1.2.3. Symmetries of the one-dimensional Fermi-Hubbard model	23
1.3. Numerical results of different fillings	26
1.3.1. Quantum distillation for initial states with doublons	26
1.3.2. Initial state dependence of strong quantum distillation	27
1.3.3. Asymptotic expansion velocity of initial states without doublons	30
2. Setup and methods	33
2.1. Initial state preparation	33
2.1.1. Experimental sequence	33
2.1.2. Characterization	35
2.2. Calibration methods	35
2.2.1. Doublon fraction	35
2.2.2. Doublon blast duration	36
2.3. Creating a flat potential landscape	38
3. Results	39
3.1. Quantum distillation	39
3.1.1. Bimodal expansion dynamics	39
3.1.2. Weak quantum distillation	41

3.1.3.	Evidence for strong quantum distillation	42
3.1.4.	Role of different initial states	44
3.1.5.	Generating low entropy states with quantum distillation	47
3.2.	Asymptotic expansion velocity	47
3.2.1.	Second moment of the density distribution	47
3.2.2.	Interaction dependence of radial velocities	49
3.3.	Conclusion and outlook	51
II.	Nonergodicity due to kinetic constraints in tilted Fermi-Hubbard chains	53
4.	Theoretical background	55
4.1.	Dynamics of a single particle in a tilted lattice	55
4.1.1.	Bloch oscillations in real-space: Breathing dynamics	55
4.1.2.	Imbalance: A local probe of real-space Bloch oscillations	58
4.1.3.	Collapse and revival of Bloch oscillations in a harmonic trap	60
4.1.4.	Wannier-Stark localization: Imbalance of a Wannier-Stark state	61
4.1.5.	Role of the gauge: tilted lattice versus driven homogeneous lattice	64
4.2.	Many-body dynamics in tilted Fermi-Hubbard chains	66
4.2.1.	The tilted one-dimensional Fermi-Hubbard model	66
4.2.2.	Analytic limits: The Schrieffer-Wolff transformation	70
4.2.3.	Nonergodicity due to Hilbert-space fragmentation	73
4.2.4.	Symmetries in the tilted Fermi-Hubbard model	75
4.3.	Numerical results for different parameter regimes	77
4.3.1.	Limitations of fragmentation in the dipole conserving regime	77
4.3.2.	Limitations of fragmentation in the resonant regime $ U \simeq 2\Delta$	79
5.	Setup and methods	83
5.1.	Experimental sequence and observable	83
5.2.	Initial state preparation & spin-resolved imbalance readout	85
5.3.	Creating a linear potential	87
5.4.	Gradient-induced interaction averaging	88
5.5.	Calibration methods	90
5.5.1.	Spin-dependent tilt Δ_σ	90
5.5.2.	Tunneling rate J	92
5.5.3.	Onsite interaction U	93
5.5.4.	Superlattice phase	94
5.5.5.	Imbalance	95

6. Experimental results	97
6.1. Single-particle dynamics	97
6.1.1. Observation of real-space Bloch oscillations	97
6.1.2. Collapse time of real-space Bloch oscillations in a harmonic trap	99
6.1.3. Steady-state imbalance: probing incoherent dynamics	101
6.1.4. Observation of Wannier-Stark localization	102
6.2. Many-body dynamics in the presence of interactions	104
6.2.1. Interacting-induced dephasing of Bloch oscillations	104
6.2.2. Non-ergodic dynamics over a wide range of parameters	108
6.2.3. Long-time dynamics in the limit of weak tilt	112
6.2.4. Long-time dynamics at the tilt resonance	114
6.2.5. Interpretation: Constrained dynamics in the presence of a tilt	115
6.3. Conclusion and outlook	118
III. Appendix	121
A. Fermi-Hubbard interaction in the Wannier-Stark basis	123
A.1. Identities of Bessel functions	124
A.2. Onsite interactions in the Wannier-Stark basis	124
B. Numerical analysis of the dynamically relevant states	129
B.1. Construction of the numerical fragment	129
B.2. Numerical fragment \mathcal{N}_ϵ versus fragment \mathcal{K}^{res}	130
Bibliography	131

List of Figures

1.1. Particle in a lattice.	10
1.2. Particle in a lattice with harmonic confinement.	13
1.3. Expansion of a cloud of non-interacting particles.	16
1.4. Strong quantum distillation.	27
1.5. Initial state dependence of the doublon cloud radius.	29
1.6. Radial velocity as a function of the interaction energy.	31
2.1. Control of the doublon fraction.	36
2.2. Atom number decay in the presence of a near-resonant laser pulse.	37
3.1. Dynamical phase separation of singlons and doublons.	40
3.2. Weak quantum distillation.	41
3.3. Time traces of R_d with linear fits.	44
3.4. tDMRG results for the relative doublon cloud size.	45
3.5. Extraction of the cloud size r	49
3.6. Radial expansion velocities v_r	51
4.1. Breathing dynamics of real space Bloch oscillations.	57
4.2. Real-space Bloch oscillations probed in a parity-projected manner.	59
4.3. Bloch oscillations in the presence of harmonic confinement.	61
4.4. Steady-state imbalance versus tilt.	64
4.5. Hilbert-space fragmentation.	74
4.6. Role of higher-order diagonal and off-diagonal terms.	78
4.7. Numerical study of the resonant regime $ U \simeq 2\Delta$	80
4.8. Finite-size scaling analysis of imbalance and entanglement entropy.	82
5.1. Timing protocol of the experimental sequence.	84
5.2. Initial state preparation and imbalance readout in the superlattice.	86
5.3. Energy and magnetic moment for different hyperfine states of ^{40}K	88
5.4. Impact of interaction averaging.	90
5.5. Spin-resolved real-space Bloch oscillations.	92
5.6. Calibration of the zero-crossing of the Feshbach resonance.	93
5.7. Calibration of the superlattice phase.	94

6.1. Real-space Bloch oscillations.	99
6.2. Calibration of harmonic confinement.	100
6.3. Long-time dynamics of a spin-polarized Fermi gas in a tilted lattice. . .	102
6.4. Spin-resolved steady-state imbalance as a function of the tilt.	103
6.5. Real-space Bloch oscillations for interacting particles.	106
6.6. Interaction scan of the peak power spectral density.	107
6.7. Steady-state imbalance in the presence of interactions.	108
6.8. Finite steady-state imbalance over a large range of parameters.	110
6.9. Steady-state imbalance in the limit of weak tilt.	113
6.10. Renormalized onsite interaction in the resonant regime.	115
6.11. Illustration of the structure of the Hilbert space.	116
6.12. Theoretical analysis of the relevant many-body states for $\omega_h = 0$, $\Delta_\uparrow =$ $\Delta_\downarrow \equiv \Delta$ and a Néel-ordered initial state.	118
B.1. Numerical fragment \mathcal{N}_e	130

Introduction

The eigenstate thermalization hypothesis (ETH), first formulated by Deutsch and Srednicki, constitutes a cornerstone of our current understanding of thermalization in closed quantum many-body systems [1, 2]. The thermal steady-state of any observable is reached through the loss of coherence and described by a diagonal ensemble of eigenstates. Thus, thermalization in these systems happens on the level of individual eigenstates. The diagonal ensemble is equivalent to the micro-canonical ensemble of statistical mechanics in closed systems, where the mean energy of the system corresponds to the energy of the initial quantum many-body state. Therefore each eigenstate itself behaves locally like a thermal ensemble [3].

The ETH is conjectured to hold for ergodic systems and offers an elegant explanation for thermalization in quantum-many body systems, where the time evolution is linear [4] and chaotic dynamics, which drive thermalization in classical systems [5], are absent. Despite its generality, the ETH does not apply to integrable systems [6], which exhibit non-ergodic dynamics. In these systems, extensively many conserved quantities impede thermalization. First studies on integrable quantum systems date back to Bethe, who investigated spin chains [7]. In succeeding works, the celebrated Bethe ansatz has been extended to many other integrable models [8], such as the one-dimensional Fermi-Hubbard model [9] or the Lieb-Liniger model [10]. However, integrable systems are particularly vulnerable to small perturbations. A more robust form of integrability can be realized in disordered quantum systems, where Anderson localization occurs in the non-interacting limit [11]. If this localization persists in the presence of interactions, many-body localization (MBL) occurs and showcases an emergent integrability, which appears robust to local perturbations [12–15]. Moreover, MBL constitutes a useful candidate for quantum memories [16, 17]. Similar to integrable models, MBL impedes thermalization due to extensively many emergent quasi-local integrals of motion [18–20]. This results in a characteristic logarithmic growth of the entanglement entropy in these systems [21].

Studying thermalization in isolated quantum-systems poses three main challenges to experiments. First, it requires a setup, which is well-isolated from the environment to ensure that bath effects are not dominating the thermalization [22]. Second, relaxation dynamics need to be triggered by preparing a nonequilibrium state, as opposed to initializing the

system in the ground state. This can be accomplished with a quantum quench, i.e., a sudden change of the system's parameters [23]. By probing the subsequent evolution of the system on long timescales, experiments can infer whether a steady state emerges and if it is thermal or not [24]. Third, one-dimensional systems need to be accessible to study non-thermal dynamics in models, where the ETH does not apply, since both MBL and integrable systems have so far been rigorously established in one dimension only [8, 12, 25]. Ultracold gases are a versatile platform for such experiments [26], because they constitute well-isolated quantum systems, where coherent out-of-equilibrium dynamics after quantum quenches can be studied on long timescales [27]. Furthermore, the trapping potential can be made strong enough to restrict the motion of atoms to lower dimensions [26, 27]. Outside of the field of ultracold atoms, nonequilibrium quantum dynamics have also been observed with other experimental platforms, such as trapped ions [28], superconducting circuits [29], and Rydberg atoms in optical tweezer arrays [30].

While today many of these platforms are able to experimentally implement one-dimensional systems, the first out-of-equilibrium experiments were performed with ultracold atoms, realizing a one-dimensional Bose gas [31, 32]. In these experiments non-thermal behavior was found and attributed to the integrability [33] of the underlying Lieb-Liniger model [10]. Other experiments realized a Tonks-Girardeau gas [34, 35] and found evidence for the fermionization of this bosonic system in the momentum distribution, which is expected in one dimension [36]. Furthermore, prethermalization [37] to a state described by a generalized Gibbs ensemble [38] was observed [39] and recently non-thermal fixed points [40] were studied [41, 42]. While the previous experiments were all performed in one-dimensional Bose gases in the continuum, the integrability of the underlying model can also affect its properties in the lattice, for example when studying transport properties [43–46]. Many transport experiments have been carried out with ultracold atoms in optical lattices both in one and higher dimensions, probing far-from-equilibrium dynamics [47–52], as well as close-to-equilibrium dynamics in the linear-response regime [53–55]. Complementary results were obtained for spin systems [56–58] and mesoscopic systems [59–61]. Overall, nonequilibrium dynamics have been intensively studied with ultracold gases, probing both ergodic and non-ergodic dynamics and contributing to a better understanding of thermalization and its absence in closed quantum systems.

MBL constitutes an example for strictly non-ergodic dynamics. While original theoretical studies of MBL were motivated by transport properties of weakly interacting electrons in disordered conductors, the presence of phonons in metals is expected to initiate delocalization due to bath effects [62]. This highlights the quest to investigate MBL in platforms, where bath effects are strongly suppressed and closed system dynamics can be studied. The first evidence was brought forward in an out-of-equilibrium experiment [63], where the relaxation dynamics was monitored after preparing a charge-density wave initial state.

Persisting memory of this initial state, even in the presence of interactions, was attributed to non-ergodic dynamics emerging from MBL. Succeeding works studied MBL in the presence of system-bath coupling [64–66], in higher dimensions [64, 67], in the presence of a single-particle mobility edge [68] and in the regime of the dynamical phase transition between non-ergodic and thermal dynamics [69–71]. Furthermore, MBL experiments were also carried out in different platforms, such as trapped ions [72], superconducting circuits [73–75] and nuclear spins [76]. Experiments on MBL started about a decade later compared to the first experiments on integrable system. These experiments demonstrate that a rich variety of other platforms can access nonequilibrium dynamics and contribute complementary observables to study non-ergodic dynamics.

In general, the relaxation dynamics of quantum systems, which obey the ETH are not expected to show a strong dependence on the initial state. In fact, the ETH predicts that any eigenstate in the spectrum, which is sufficiently close to the energy of the initial state, correctly describes the thermal state. This conjecture was challenged in a recent experiment with Rydberg atoms in optical tweezers, where a strong initial state dependence of the relaxation dynamics was observed [77]. This was attributed to a weak form of ergodicity breaking [78, 79], where a small set of non-thermal eigenstates is embedded in an otherwise thermal spectrum. Even though the fraction of these non-thermal states, dubbed many-body scar states, vanishes in the thermodynamic limit, these states can affect the dynamics of certain initial product states [78, 80–84]. In line with the suggested weak form of ergodicity breaking, a new class of models has been put forward recently, which exhibit a fragmented Hilbert space [85–88]. Such models have only few conserved quantities, which define symmetry sectors within the global Hilbert space according to these conservation laws. Remarkably, each of these symmetry sectors consist of many disconnected parts, so-called fragments, which occupy only a small fraction of the symmetry sector. This fraction vanishes in the thermodynamic limit. Such fragmentation of the symmetry sectors is called Hilbert-space fragmentation (HSF) and gives rise to non-ergodic dynamics, since the initial product state remains within in its fragment.

Important examples for HSF are fractonic models [89, 90], where charge and dipole-moment conservation constrain the mobility of excitations [85, 86, 88, 91]. Similar dynamics are found in kinetically constrained models, which impose dynamical constraints explicitly in the Hamiltonian [92, 93]. Furthermore charge- and dipole-moment conservation also arises naturally in Hamiltonians related to the quantum Hall effect [94–97] and in systems with a strong electric field [98, 99], which have been realized with ultracold atoms in tilted optical lattices [100–103]. Recent theoretical work suggested that the tilted one-dimensional Fermi-Hubbard model is at the interface between MBL and HSF and in that way can exhibit non-ergodic dynamics without requiring disorder [85, 86, 88, 98, 99, 104]. While in both MBL and HSF such non-ergodic dynamics emerge due to localization,

HSF does not show the characteristic logarithmic growth of the entanglement entropy [85], expected for MBL. Since disorder is absent in systems which exhibit HSF, this phenomenon might shed light on the question, whether localization occurs in translationally-invariant many-body systems without disorder [105–110], which was recently investigated experimentally with a two-component gas with different mobilities [111].

This thesis reports on nonequilibrium dynamics with ultracold atoms in optical lattices, which allows to answer some of the theoretical questions discussed above. We probe mass transport in the homogeneous 1D Fermi-Hubbard model and monitor the relaxation dynamics of a charge-density wave in the tilted 1D Fermi-Hubbard model. Ultracold atoms in optical lattices are well suited to study Hubbard-type Hamiltonians and in this way emulate condensed matter physics [112]. After the Bose-Hubbard model was realized [113, 114], many experiments have been performed within the Fermi-Hubbard model as well [115–120]. Due to the Fermi-Dirac statistics, this model is naturally closely related to the dynamics of electrons in solids. With single-site resolved imaging of both charge and spin at hand [121, 122], the Fermi-Hubbard model has received a lot of interest in recent experiments with quantum gas microscopes [123–127], both in one dimension [128–130] and two dimensions [131–136].

Optical lattices are an ideal tool for realizing a defect-free system, where all important parameters are tunable [137]. While onsite interactions can be controlled with Feshbach resonances [138, 139], the tunneling rate between neighboring lattice sites is adjustable with the lattice depth, which can be utilized to effectively freeze the dynamics along an arbitrary lattice axis, thereby also controlling the dimensionality of the system at will. Furthermore, large and homogeneous systems can be realized by combining confining and anti-confining potentials, which is particularly crucial for transport experiments, relying on a flat potential landscape during the expansion of an atom cloud in the lattice [50, 55, 120]. While transport experiments usually probe global observables, relaxation dynamics can be accessed locally as well by using a charge-density wave (CDW), where even lattice sites are occupied with atoms and odd sites are empty. The relaxation dynamics of a CDW towards a homogeneous density distribution happens locally and is usually faster than relaxation dynamics of global observables in transport experiments. A CDW was first created with a bichromatic optical superlattice [140, 141] and utilized to demonstrate the feasibility of ultracold atoms as quantum simulator [142] along the lines of Feynman [143]. Since then, the CDW has been used successfully in many other experiments to probe relaxation dynamics and their absence due to MBL [63, 66, 68, 70, 144, 145]. Recently, an experiment with a quantum gas microscope studied a CDW with variable periodicity [146] and generalized versions of the CDW are also used in other platforms [72, 74, 75], illustrating that the CDW has remained a powerful tool to probe relaxation dynamics and investigate the presence of localized states in the many-body spectrum.

Contents of this thesis

This thesis is divided into two parts. Part I focuses on nonequilibrium mass transport in the homogeneous 1D Fermi-Hubbard model. Part II reports on non-ergodic dynamics in the tilted 1D Fermi-Hubbard model. In part I, **chapter 1**, we introduce important theoretical concepts, which are relevant for understanding the experimental results. We start with the single-particle dynamics in a homogeneous lattice and successively add experimentally relevant modifications. Next, we generalize the results of the single-particle dynamics towards an interacting many-body system and comment on the integrability of the 1D Fermi-Hubbard model and its symmetries. Finally, we present numerical results on strong quantum distillation in the 1D Fermi-Hubbard model and discuss the feasibility to use quantum distillation for entropy reduction. Furthermore, we numerically study the interaction energy dependence on the asymptotic expansion velocities to understand differences between the Fermi-Hubbard and the Bose-Hubbard model. In **chapter 2**, we explain the experimental sequence and the initial state preparation. We describe how to create a homogeneous potential landscape. Moreover, we explain how to extract the occupation number resolved in-situ density from absorption images, which is an important tool for our experiments on quantum distillation. In **chapter 3**, we present experimental results on quantum distillation. Starting from initial states with singly-occupied sites (singlons) and doubly-occupied sites (doublons), we observe quantum distillation in the weak regime and discuss limitations for observing strong quantum distillation. Starting from an initial state with singlons, we show results for the asymptotic expansion velocity as a function of the interaction strength and discuss differences to the one-dimensional Bose-Hubbard model.

Part II discusses non-ergodic dynamics in the tilted 1D Fermi-Hubbard model. In part II **chapter 4**, we establish important theoretical concepts to understand the experimental results. We begin with non-interacting dynamics in a tilted lattice and study real-space Bloch oscillations and Wannier-Stark localization. Next, we add interactions and understand the corresponding dynamics in terms of correlated two-particle hoppings. We discuss implications for the persistence of Wannier-Stark localization in the presence of interactions. To this end, we introduce the concept of Hilbert-space fragmentation with effective Hamiltonians. Finally, we present numerical result for the limitations of the effective Hamiltonians in experimentally realizable parameter regimes. In **chapter 5**, we introduce the experimental sequence, the charge-density wave initial state (CDW) and our observable, the imbalance, which is a measure for the amplitude of the CDW. Furthermore, we describe the generation and calibration of the tilt in the presence of both a magnetic field gradient and a homogeneous Feshbach field. In **chapter 6**, we begin with experimental results on the single-particle dynamics, which show Bloch oscillations during the coherent short-time dynamics and Wannier-Stark localization at late times. We discuss

effects of the residual harmonic confinement on both the short and the long-time dynamics, with important implications for the interacting dynamics. In the presence of interactions, we find interaction-induced damping at short times and a robust imbalance for a large range of tilts and interaction strengths at long times, signalling a non-ergodic behavior of our system. By numerically identifying the dynamically relevant set of states, we can connect our experimental results with the strongly fragmented effective Hamiltonians in two different limits. This enables us to interpret the finite steady-state imbalance in terms of constrained dynamics.

Part I.

Nonequilibrium mass transport in Fermi-Hubbard chains

One-dimensional (1D) systems are fundamentally different from their higher-dimensional counterparts. For instance, in two and three dimensional systems, Fermi liquid theory [147] captures the dynamics of interacting electrons in terms of fermionic quasiparticles, which inherit many properties from non-interacting electrons. Yet, in one dimension, Fermi-Liquid theory breaks down, because the Fermi surface becomes unstable and the dynamics are described in terms of collective excitations, such as bosonic density waves and spin waves [148]. Another peculiarity of 1D many-body systems are integrable models such as the Lieb-Liniger model [36], the Heisenberg chain [149], or the 1D Fermi-Hubbard model [9]. This integrability arises from an extensive set of conservation laws, which prevents the system from thermalizing [38, 150] and can affect the transport properties of the system [43–46, 151]. In this part, we investigate mass transport in the 1D Fermi-Hubbard model in far from-equilibrium expansion experiments [49–51], where an initially trapped gas is suddenly released into a homogeneous potential landscape. We study both asymptotic expansion velocities and fermionic quantum distillation.

1. Theoretical background

1.1. Expansion dynamics of a single particle

1.1.1. Toy model: A single particle in a lattice

Let's assume a particle in a one-dimensional periodic potential, which is deep enough such that we can apply the tight-binding limit to restrict the system to the lowest band and describe the dynamics with the following Hamiltonian \hat{H}_{kin}

$$\hat{H}_{\text{kin}} = -J \sum_{i=1}^L (\hat{c}_i^\dagger \hat{c}_{i+1} + \hat{c}_{i+1}^\dagger \hat{c}_i). \quad (1.1)$$

Here, \hat{c}_i^\dagger (\hat{c}_i) is the creation (annihilation) operator of a spinless fermion on site i , J is the tunneling rate between neighboring sites and L is the number of sites. We now transform this Hamiltonian to quasi-momentum space, i.e. we change the basis states from Wannier states to Bloch waves, using the definition $\hat{c}_j^\dagger = 1/\sqrt{L} \sum_{k \in \text{1.Bz}} e^{-ijkd} \hat{c}_k^\dagger$. Here, we sum over all quasi-momenta $k \in [-\pi/d, \pi/d]$ in the first Brillouin zone, \hat{c}_k^\dagger (\hat{c}_k) creates (annihilates) a spinless fermion with quasi-momentum k and d is the lattice constant. The resulting Hamiltonian in quasi-momentum space is diagonal

$$\hat{H}_{\text{kin}} = \sum_{k \in \text{1.BZ}} \epsilon(k) \hat{c}_k^\dagger \hat{c}_k, \quad (1.2)$$

with the dispersion relation $\epsilon(k) = -2J \cos(kd)$. This result illustrates that an initial state, which is localized in quasimomentum space at quasimomentum k , will perform trivial dynamics under time evolution, since it is an eigenstate of the Hamiltonian. In contrast, an initial state, localized in real space on lattice site j , is equivalent to a superposition of Bloch waves. Therefore, non-trivial dynamics is expected, when time evolving such state in a system described by the Hamiltonian \hat{H}_{kin} of Eq. (1.1). The dynamics in real-space can be calculated analytically, and the probability $n_{j,i}$ of finding a particle in the final Wannier-State $|i\rangle$ after time-evolving the initial Wannier-State $|j\rangle$ is equal to

1. Theoretical background

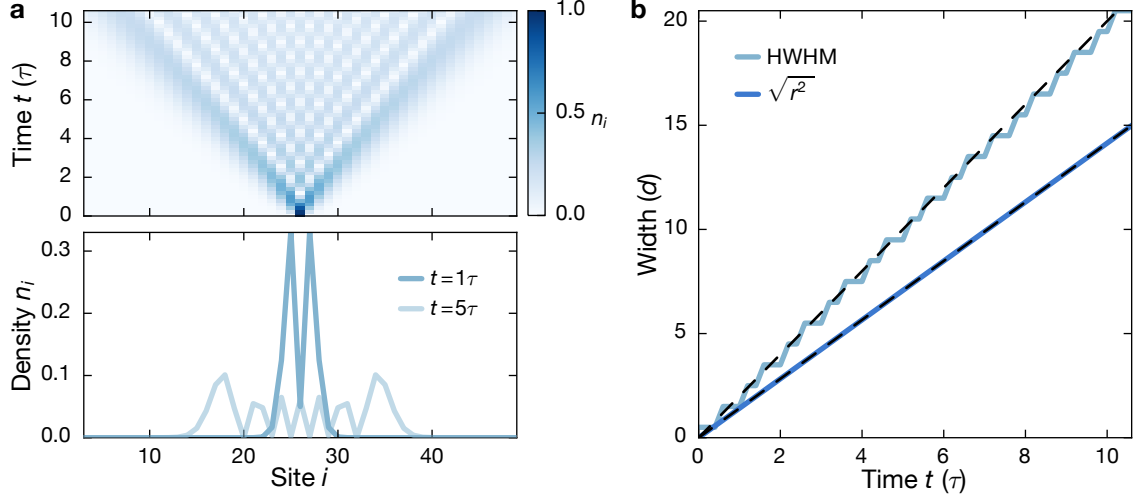


Figure 1.1.: Particle in a lattice. **a** Upper panel: Probability $n_i \equiv n_{i,L/2}$ of finding a particle on lattice site i after time evolution of an initial Wannier-State from the center of the lattice at site $i = L/2$. The time is scaled in units of the tunneling time $\tau = \hbar/J$. Lower panel: n_i at two different times $t = 1\tau$ and $t = 5\tau$. **b** Width of the probability distribution n_i in units of the lattice constant d versus time. We compare two different definitions of the width of the density distribution, the half-width-at-half-maximum (HWHM) and the square root of the second moment $\sqrt{r^2}$. The black dashed lines correspond to the analytic prediction for the slopes of the two time traces. For the HWHM, we expect v_{\max} and for $\sqrt{r^2}$ we anticipate v_r .

$$n_{i,j} = |\langle i | \exp(-i\hat{H}t/\hbar) | j \rangle|^2 = \mathcal{J}_{i-j}^2(2Jt/\hbar) \equiv \mathcal{J}_{i-j}^2(2t/\tau). \quad (1.3)$$

Here, $\mathcal{J}_i(x)$ is the i^{th} -order Bessel function of first kind and $\tau = \hbar/J$ is the tunneling time, the characteristic time scale of the dynamics. The result for the single-particle density distribution according to Eq. (1.3) is plotted in the upper panel of Fig. 1.1a, showing that the particle spreads symmetrically from its origin outwards in a "fan-like" pattern. Additionally, the coherent dynamics manifest itself in a substructure made of many different strands, resembling an interference pattern. This becomes most obvious in the lower part of Fig. 1.1a. A cut through the density distribution at $t = 5\tau$ reveals many local minima and maxima in between the two outer global maxima, which define the extent of the fan-like pattern and contain the largest weight of the density distribution. Clearly, the emergence of strands indicates that the width of the probability distribution increases linearly in time, which is dubbed ballistic dynamics.

Performing a quantitative analysis of the velocity for ballistically spreading particles within a lattice requires a proper definition for the width of the density distribution. Different definitions for the widths are possible as shown in Fig. 1.1b. First, the width

can be defined as the half-width at half maximum (HWHM) of the density distribution. Starting from the outer edges of the profiles, we move inwards in both directions to find the positions, where the density distribution first reaches $n_{\max}/2$. If the density distribution exhibits a double peak structure (see for example the lower panel of Fig. 1.1a at $t = 5\tau$), the HWHM measures half the distance between the outer edges. This definition mainly captures the most prominent strand in Fig. 1.1a and corresponds to the fastest possible expansion velocity (large slope in Fig. 1.1b). Second, the width can be characterized with the square root of the second moment of the density distribution

$$\sqrt{r^2} = \sqrt{\sum_{i=1}^L n_{i-j} (i-j)^2}. \quad (1.4)$$

Here, n_{i-j} corresponds to the probability of finding a particle at a distance of $i-j$ sites from site j , where it was initialized. Note, that $\sqrt{r^2}$ can be understood as average width, taking into account the whole density distribution. Strands in the center of the density distribution have a smaller velocity and this results in a smaller slope of $\sqrt{r^2}$ in Fig. 1.1b, compared to the HWHM. The slopes of both the $\sqrt{r^2}$ and the HWHM can be related to the group velocity $v_g(k)$, which is defined in quasi-momentum space according to

$$v_g(k) = \frac{1}{\hbar} \frac{\partial \epsilon(k)}{\partial k} = \frac{2Jd}{\hbar} \sin(kd) = \frac{2d}{\tau} \sin(kd). \quad (1.5)$$

The group velocity is bounded, $|v_g| \leq v_{\max} = 2d/\tau$ [Eq. (1.5)] and the velocity at which the HWHM increases, fits very well to the fastest possible velocity v_{\max} (see dashed line in Fig. 1.1b), confirming our expectation that the HWHM captures the fastest possible dynamics of the spreading density distribution. The velocity at which the square root of the second moment increases is called radial velocity $v_r = \frac{d}{dt} \sqrt{r^2}$. For a non-interacting system, one can show that the radial velocity v_r is equal to the average group velocity v_{av} , which is defined in momentum space according to

$$v_{av} = \sqrt{\sum_k n_k \left(\frac{2d}{\tau} \sin(kd) \right)^2} = \frac{\sqrt{2}d}{\tau}. \quad (1.6)$$

In the last step of Eq. (1.6), we used that the initial state, a Wannier state, has a flat distribution of quasi-momenta $n_k = 1/L$. This quasi-momentum distribution is conserved, since it commutes with the Hamiltonian, as can be inferred from Eq. (1.2). Therefore, the radial velocity v_r is a good quantitative measure for the expansion velocity. The prediction for the radial velocity is in excellent agreement with the numerical simulations,

as indicated by the dashed line Fig. 1.1b. This confirms, that the definition of $\sqrt{r^2}$ as an average width of the density distribution results in smaller expansion velocity compared to the HWHM.

1.1.2. Expansion of a single particle in a harmonic trap

Any experiment which probes the dynamics of an expanding particle will obviously take place in a finite system. This modifies the dynamics on large enough time scales due to finite size effects, after the particle explored the limited system size. Many experiments with ultracold atoms take place in a harmonic trap, which is characterized by a trapping frequency ω . We can model the harmonic trap by adding a potential energy term \hat{H}_{pot} to the Hamiltonian \hat{H}_{kin} , defined in Eq. (1.1) to obtain

$$\hat{H} = \hat{H}_{\text{kin}} + \hat{H}_{\text{pot}} = -J \sum_{i=1}^L (\hat{c}_i^\dagger \hat{c}_{i+1} + \hat{c}_{i+1}^\dagger \hat{c}_i) + \alpha \sum_{i=1}^L \left(i - \frac{L}{2}\right)^2 \hat{c}_i^\dagger \hat{c}_i, \quad (1.7)$$

where $\alpha = m\omega^2 d^2/2$ and m is the mass of the atoms. Note, that we define the potential energy such that a particle initialized in a Wannier state $|L/2\rangle$ in the center of the lattice with L sites has zero potential energy $\langle L/2 | \hat{H}_{\text{pot}} | L/2 \rangle = 0$ and therefore also zero total energy, since the kinetic energy of a Wannier state is zero. The Hamiltonian \hat{H} is not diagonal in quasi momentum space, since the potential energy term \hat{H}_{pot} leads to a coupling of states with different quasi momenta and breaks the discrete translational invariance of the clean system. Therefore, quasi-momentum is not a conserved quantity anymore and Bloch waves no longer represent the eigenstates of the system. To analyze the dynamics, we need to use numerical simulations. We define the probability to find a particle in Wannier state $|i\rangle$, after initializing it in Wannier state $|L/2\rangle$ in the center of the lattice as $n_i = \langle i | e^{-i\hat{H}t/\hbar} | L/2 \rangle$. Additionally, we analyze the distribution of quasi-momenta n_k , which we define as $n_k = \langle k | e^{-i\hat{H}t/\hbar} | L/2 \rangle$, where $|k\rangle$ is a quasi-momentum mode, corresponding to a Bloch-wave with in the limit of zero harmonic confinement.

In the left panel of Fig. 1.2a we show numerical simulations for a harmonic confinement with curvature $\alpha = 0.01J$. At short times $t \leq 6\tau$, the density distribution in real space shows a symmetric and ballistic expansion, which resembles the clean system very closely. The expansion speed of the two dominant strands, which exhibit the fastest spreading within the fan-like pattern, agrees well with the analytic prediction for the fastest expansion velocity $v_{\text{max}} = 2d/\tau$ in the clean system, as indicated by the dashed lines. This is confirmed in Fig. 1.2b, where a time trace of the HWHM of the real-space density distribution increases linearly according to the analytic prediction of the clean system at

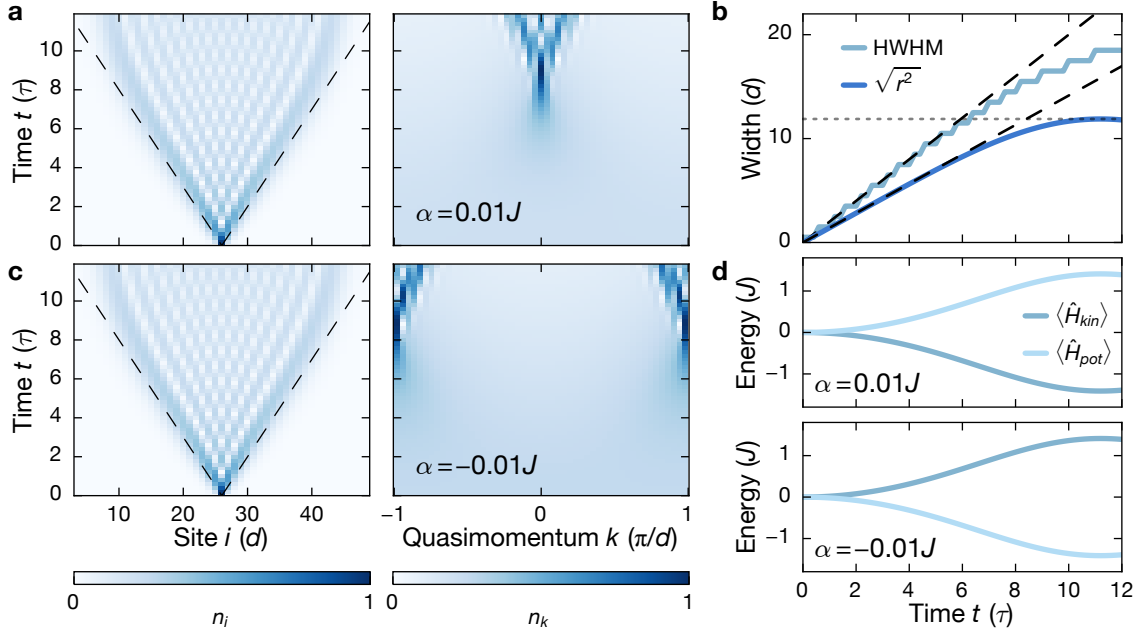


Figure 1.2.: Particle in a lattice with harmonic confinement. **a** Time evolution of the density distribution in real space (left panel) and in quasimomentum space (right panel) for $\alpha = 0.01J$. **b** Width of the density distribution in the left panel of (a), measured with the HWHM and $\sqrt{r^2}$. The black dashed lines indicated the respective prediction for a free system without harmonic confinement. The horizontal grey dotted line indicates the maximum possible width $\sqrt{r_{max}^2}$ due to energy conservation. **c** Same plots as in (a) but for an anti-confining potential with $\alpha = -0.01J$. **d** Expectation value of the kinetic energy $\langle \hat{H}_{kin} \rangle$ and the potential energy $\langle \hat{H}_{pot} \rangle$ for $\alpha = 0.01J$ (upper panel) and $\alpha = -0.01J$ (lower panel) in units of the tunneling constant J . The dashed lines in (a), (c) indicate an expansion with velocity of $2d/\tau$.

short times. This suggests that the confining potential can be neglected on short times. Only at later times the expansion slows down and completely ceases at $t \approx 11\tau$.

A better intuition for the dynamics in the presence of a harmonic confinement is revealed by analyzing the density distribution in quasi-momentum space in the right panel of Fig. 1.2a. Starting from a homogeneous distribution at $t = 0$, which is characteristic for a Wannier state, the distribution evolves towards a sharp peak in the center of the first Brillouin zone around $k = 0$ at later times $t > 6\tau$, when the expansion of the density distribution in real-space starts to slow down. This is in contrast to an anti-confining potential ($\alpha = -0.01J$), as displayed in Fig. 1.2c, where the density distribution in quasi-momentum space accumulates around $k = \pm\pi/d$. In real-space, the dynamics of the density distribution is indistinguishable for both potentials due to a dynamical symmetry between a confining and an anti-confining potential [50].

1. Theoretical background

We can understand the dynamics by analyzing the time evolution of the potential energy and the kinetic energy in Fig. 1.2d, keeping in mind that the sum of both energies needs to be conserved. In the case of a confining potential, the spreading density distribution causes the potential energy to rise at the cost of a decreasing kinetic energy. In the limit of zero harmonic confinement, the kinetic energy can be inferred from the dispersion relation $\epsilon(k)$ and the lowest possible kinetic energy is $\epsilon_{\min} = -2J$ at $k = 0$. Therefore, the kinetic energy can be reduced by changing the density distribution in quasi momentum space from a homogeneous distribution at $t = 0$ towards a distribution, peaked around the $k = 0$. In the case of an anti-confining potential the behavior of the kinetic and the potential energy is exactly opposite (lower panel of Fig. 1.2d). Here, the expanding density distribution in real space reduces the potential energy, hence the kinetic energy needs to increase. This is achieved by a redistribution of quasi-momentum around $k = \pm\pi/d$, where the kinetic energy is highest $\epsilon_{\max} = 2J$.

For finite but weak harmonic confinement, the kinetic energy cannot be inferred from the dispersion relation of the free system and we expect small quantitative corrections to the preceding discussion. Indeed, the absolutes of kinetic and potential energies in Fig. 1.2d are always smaller than $2J$, but the symmetry between minimal and maximal kinetic energy ($|\epsilon_{\max}| = |\epsilon_{\min}|$) survives. This explains why the real-space expansion cannot distinguish between a confining and an anti-confining potential. The initial state has zero energy and therefore the absolute energy difference with respect to the smallest and largest possible kinetic energy is the same. This difference ultimately limits the maximal possible potential energy difference $\langle \hat{H}_{\text{pot}}^{\max} \rangle$ and the maximum achievable expansion of the cloud $\sqrt{r_{\text{max}}^2}$. The potential energy can be written in terms of the second moment of the density distribution $\langle \hat{H}_{\text{pot}} \rangle = \alpha r^2$ and we find $\sqrt{r_{\text{max}}^2} = \sqrt{\langle \hat{H}_{\text{pot}}^{\max} \rangle / \alpha}$, which is in excellent agreement with the maximum achievable square root of the second moment (horizontal grey dotted line in Fig. 1.2b).

We conclude with two important points. First, even in the presence of a harmonic confinement, the dynamics of the expanding probability distribution in real space can be approximated by the free system without confinement as long as the potential energy difference between final and initial state is small compared to J . Second, the real space expansion exhibits a dynamical symmetry with respect to confining and anti-confining potential. This symmetry can be used to minimize the residual harmonic confinement in the experimental setup, as explained in section Sec. 2.3.

1.1.3. Dynamics of incoherent initial density distributions

So far, we investigated the dynamics of a single particle in a lattice, when starting from a perfectly localized initial state. In contrast, in the experiment we start from initial states with plenty of particles, distributed around the center of the lattice. In the non-interacting limit, each particle evolves independently in time. An experimental average over the whole distribution of particles is therefore equivalent to a weighted average of successive experiments with a single particle, each time starting from different initial lattice sites. In order to describe the dynamics originating from such initial states, it is useful to work with the density matrix formalism. We model the initial state with the density matrix $\hat{\rho}_0$ of an incoherent mixture (all off-diagonal elements of $\hat{\rho}_0$ are zero) with suitable probability distribution over the lattice (for example a Gaussian distribution or a box distribution) and use the von-Neumann equation to calculate the time evolution under the Hamiltonian defined in Eq. (1.7)

$$\hat{\rho}(t) = \exp(-i\hat{H}t/\hbar)\hat{\rho}_0 \exp(i\hat{H}t/\hbar), \quad n_i = \text{tr}\{\hat{\rho}(t) |i\rangle \langle i|\}. \quad (1.8)$$

The probability of finding a particle on lattice site i is equal to the trace over the time-evolved density matrix $\hat{\rho}(t)$ times the projector onto Wannier state $|i\rangle$. We construct the diagonal elements of the initial density matrix $\hat{\rho}_{ii}$ using two different kinds of distributions:

$$\hat{\rho}_{ii}^{\text{box}} = \begin{cases} C & \text{if } |i - L/2| \leq \sigma_\rho \\ 0 & \text{otherwise} \end{cases} \quad (1.9)$$

$$\hat{\rho}_{ii}^{\text{Gauss}} = \frac{1}{N} \sum_{i=1}^L \exp\left(\frac{-(i - L/2)^2}{2\sigma_\rho^2}\right) \quad (1.10)$$

where the factors N and C are chosen such that $\text{tr}\{\hat{\rho}^{\text{box}}\} = \text{tr}\{\hat{\rho}^{\text{Gauss}}\} = 1$ and σ_ρ sets the width of both distributions. The results for the expansion of both initial states are shown in Fig. 1.3. The density n_i depicts very different dynamics for both initial distributions compared to a single initial Wannier state (Fig. 1.3a). As expected, the initial density distribution across many lattice sites averages out the interference-pattern-like substructure, which was found for the dynamics initiated with a single Wannier state. Additionally, the dynamics exhibit different regimes, when starting from a density distribution. Initially, the expansion seems to halt, before it accelerates after $t \approx 10\tau$ to finally reach the familiar linear spreading with time. This is most obvious for the Gaussian distribution. In order to quantitatively characterize the dynamics, we analyze the HWHM (Fig. 1.3b) and $\sqrt{r^2}$

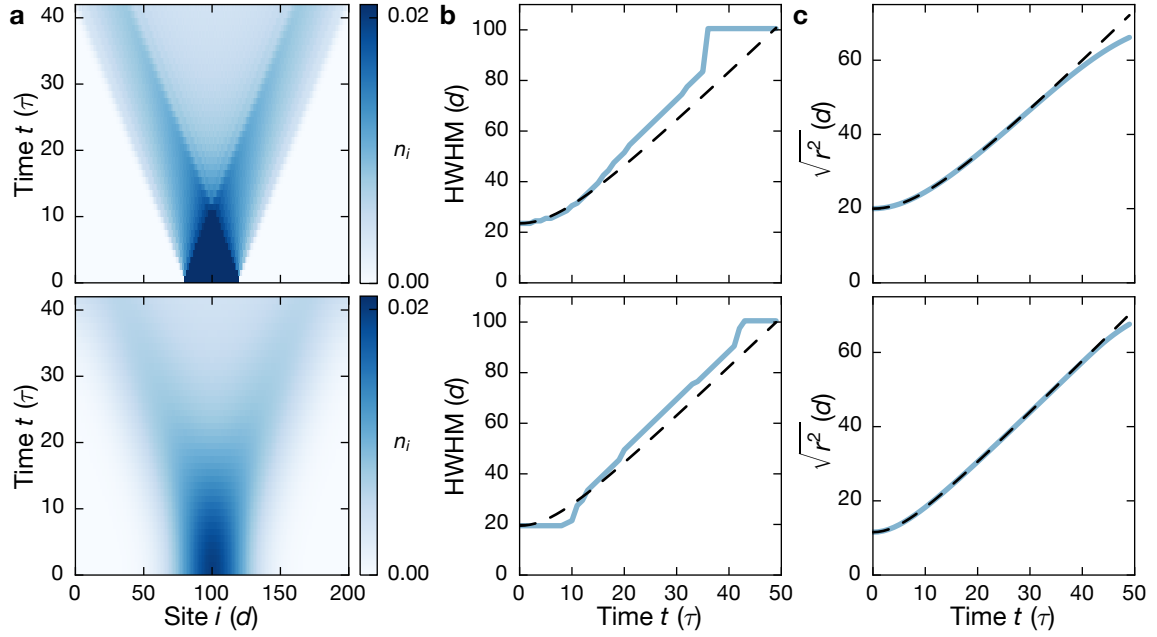


Figure 1.3.: Expansion of a cloud of non-interacting particles. Upper panels correspond to the initial box distribution and lower panels correspond to the initial Gaussian distribution. We use $\sigma_\rho = 20d$ and $\alpha = 10^{-4}J$. **a** Time evolution of the density distribution. **b** Time evolution of the HWHM. The dashed line shows the analytic result according to Eq. (1.11). **c** Time evolution of the cloud radius $\sqrt{r^2}$. The dashed line shows the analytic prediction according to Eq. (1.12).

(Fig. 1.3c), which we will from now on call the radius of the cloud for obvious reasons. Both observables confirm a time-dependent expansion speed for both initial density distributions, which is approximately constant for times $15\tau \leq t \leq 30\tau$. At late times $t \geq 40\tau$, the harmonic confinement causes the expansion to cease, similar to a Wannier initial state discussed in Sec.1.1.2. For the cloud radius $\sqrt{r^2}$, the time dependence can be calculated analytically in the absence of harmonic confinement [152]:

$$\sqrt{r^2} = \sqrt{r_0^2 + v_{av}^2 t^2}. \quad (1.11)$$

This result shows that the time-dependent expansion speed is an artifact of the finite initial cloud radius, which is convoluted with the spreading density distribution. Eq. (1.11) can also be understood from the potential energy $\langle \hat{H}_{\text{pot}} \rangle = \alpha r^2$, as we found in Sec. 2.3. Due to the finite cloud radius the initial potential energy is non-zero, in contrast to an initial Wannier-state in the center of the lattice. The total potential energy is the sum of the initial potential energy and the potential energy of the expanding cloud, in agreement with Eq. (1.11). Once the cloud radius is large compared to the initial cloud size, the

total potential energy is dominated by the contribution of the expanding cloud and the expansion occurs at constant speed reproducing the ballistic dynamics obtained for an initial Wannier state. The analytic prediction is in excellent agreement with the numerical result for r^2 , until the expansion slows down at late times (dashed line in Fig. 1.3c). Similarly to r^2 , the dynamics of the HWHM can be analytically approximated by:

$$\text{HWHM}(t) = \sqrt{\text{HWHM}^2(t=0) + v_{\max}^2 t^2}. \quad (1.12)$$

Note, the different expansion velocity v_{\max} for the HWHM. The agreement of Eq. (1.12) with the numerical result for the HWHM (dashed line in Fig. 1.3b) is only approximate due to finite size effects, but it reproduces the expansion velocity at large enough times correctly, especially for the case of a Gaussian initial density distribution.

1.1.4. Random walks and the quantum speed-up

It is instructive to compare the dynamics derived with a quantum mechanical description to the classical counterpart. We model the classical system with a random walk [153]. To this end, we assume that a particle starts out in the center of the lattice and hops with equal probability $p = 1/2$ either one site to the left or one site to the right after time τ (symmetric random walk). We want to know the probability to find the particle on site m after it completed n hops. This is the same process used to describe dynamics on a Galton board [154]. The resulting distribution after n hops is a binomial distribution, which for large enough n converges to a Gaussian distribution with mean $n/2$ and variance $n/4$. This shows that the width of this Gaussian distribution, which is proportional to the standard deviation $\sigma = \sqrt{n/4}$, spreads diffusively, i.e. $\sigma \propto \sqrt{t}$. Here, we define the time t according to the time step τ times the number of hops n , $t = n\tau$. Diffusive dynamics are characteristic for Brownian motion and one can show that Brownian motion indeed emerges in the continuum limit in both time and space of the classical random walk [153]. Thus the dynamics of the classical random walk are fundamentally different from the ballistic quantum mechanical counterpart, also called the quantum walk [155–157], which we studied in Sec. 1.1.1.

Why is the expansion of a classical particle, driven by diffusion, slower than the ballistic dynamics of its quantum mechanical counterpart? The reason is wave coherence. It is also called coherent transport in the quantum and incoherent transport in the classical dynamics [158]. This is best understood, when comparing the dynamics of a free one-dimensional Gaussian wave packet $\psi(x, t)$, described by the Schrödinger equation with Hamiltonian $\hat{H}_{\text{free}} = -\frac{\hbar^2}{2m} \frac{d^2}{dx^2}$ [Eq. (1.13)] to the dynamics of a one-dimensional Gaussian density distribution $\rho(x, t)$, captured by the diffusion equation [Eq. (1.14)]. We use a

1. Theoretical background

Gaussian wave packet, initially centered at the origin with zero wave vector, obeying the initial condition $\psi(x, 0) = (1/\pi\sigma_0^2)^{1/4}e^{-x^2/(2\sigma_0^2)}$. This corresponds to a wave packet with zero momentum ($\langle \hat{p} \rangle = 0$), centered at the origin ($\langle \hat{x} \rangle = 0$). For the density distribution, we use a similar initial condition $\rho(x, 0) = (1/2\pi\sigma_0^2)^{1/2}e^{-x^2/(2\sigma_0^2)}$.

Quantum	Classical
$i\hbar \frac{d}{dt} \psi(x, t) = -\frac{\hbar^2}{2m} \frac{d^2}{dx^2} \psi(x, t) \quad (1.13)$	$\frac{d}{dt} \rho(x, t) = D \frac{d^2}{dx^2} \rho(x, t) \quad (1.14)$

$ \psi(x, t) ^2 = \frac{e^{\frac{-x^2}{\sigma_0^2 \left(1 + \frac{\hbar^2 t^2}{m^2 \sigma_0^4}\right)}}}{\sigma_0 \sqrt{\pi} \sqrt{1 + \frac{\hbar^2 t^2}{m^2 \sigma_0^4}}} \quad (1.15)$	$\rho(x, t) = \frac{e^{\frac{-x^2}{2\sigma_0^2 \left(1 + \frac{2Dt}{\sigma_0^2}\right)}}}{\sigma_0 \sqrt{2\pi} \sqrt{1 + \frac{2Dt}{\sigma_0^2}}} \quad (1.16)$
---	---

$\sigma(\psi(x, t) ^2) = \frac{\sqrt{2}\sigma_0}{2} \sqrt{1 + \frac{\hbar^2 t^2}{m^2 \sigma_0^4}} \quad (1.17)$ <p style="text-align: center;">$\xrightarrow{t \rightarrow \infty} t$</p>	$\sigma(\rho(x, t)) = \sigma_0 \sqrt{1 + \frac{2Dt}{\sigma_0^2}} \quad (1.18)$ <p style="text-align: center;">$\xrightarrow{t \rightarrow \infty} \sqrt{t}$</p>
---	--

Notice the similarity of the differential equations, describing the quantum mechanical and the classical dynamics. In both cases, the initial Gaussian distribution remains Gaussian during the time evolution but the width increases [Eq. (1.15), Eq. (1.16)]. The crucial difference is, however, that quantum mechanical probability amplitude of the Gaussian wave packet $\psi(x, t)$ is not observable. Instead, the observable probability density $|\psi(x, t)|^2$ needs to be calculated, reflecting the coherent nature of the dynamics in quantum mechanics. This leads to a ballistic increase of the standard deviation at large enough times [Eq. (1.17)] in the quantum mechanical description as opposed to a diffusive scaling [Eq. (1.18)] in the classical counterpart. $|\psi(x, t)|^2$ captures the coherence of the time-evolving wave function, as illustrated in the interference pattern-like substructure in Fig. 1.1a. This wave coherence leads to a speed-up of the expansion of a quantum mechanical Gaussian wave packet. A possible application of this quantum speed up constitutes quantum computation, where interference effects can result in faster algorithms compared to classical computers [155, 159–161]. This illustrates the practical and interdisciplinary relevance of the toy model of a single particle in a lattice, which started this chapter.

1.2. Many-body dynamics: the role of interactions

1.2.1. Sudden expansion in Fermi-Hubbard chains

The one-dimensional Fermi-Hubbard model can be understood as a generalization of the tight-binding Hamiltonian introduced in Eq. (1.1) towards interacting two-component fermions. It is described by the following Hamiltonian

$$\hat{H}_{\text{FHM}} = -J \sum_{i,\sigma=\uparrow,\downarrow} (\hat{c}_{i,\sigma}^\dagger \hat{c}_{i+1,\sigma} + \hat{c}_{i+1,\sigma}^\dagger \hat{c}_{i,\sigma}) + U \sum_i \hat{n}_{i\uparrow} \hat{n}_{i\downarrow}, \quad (1.19)$$

where $\hat{c}_{i\sigma}^\dagger$ ($\hat{c}_{i\sigma}$) is the fermionic creation (annihilation) operator, σ encodes the spin of the fermions $\sigma \in \{\uparrow, \downarrow\}$, $\hat{n}_{i\sigma} = \hat{c}_{i\sigma}^\dagger \hat{c}_{i\sigma}$ is the number operator and i is the lattice-site index. The on-site interaction strength is set by U . Adding interactions to the tight-binding Hamiltonian in Eq. (1.2) tremendously complicates exact calculations of the dynamics, since the many-body wave function no-longer factorizes into a product of single-particle states. The Hilbert space grows exponentially in the system size, such that exact calculations are elusive on the scale of our experiment (a typical one dimensional system contains about 100 particles and expands up to a full-width at half maximum of 200 sites.) Therefore, we rely on the concepts, previously established for the non-interacting system, and appropriately extend these concepts to the many-body system in the next sections.

A sudden expansion experiment with an interacting cloud of atoms probes the far-from-equilibrium dynamics. In our experiments, we start from product states as opposed to ground states and the sudden expansion begins with a quench of two distinct parameters, i.e. a fast and non-adiabatic change of these parameters. We remove the confinement to initiate the expansion of the cloud and we additionally quench the interaction strength from the hard-core limit to the desired value during the expansion (see Sec. 2.1.1 for experimental details). This generates a highly excited state. Furthermore, the interaction energy generated with the quench is an important physical observable to understand the relaxation dynamics towards thermal equilibrium (for details see Sec. 1.3.3).

Naively, one might expect diffusive relaxation dynamics, when tracking the expanding cloud, because of scattering events between the particles in the presence of interactions, as opposed to ballistic dynamics, which we observe for non-interacting particles in the absence of scattering [162]. However, during the sudden expansion of initially confined particles, the density of the cloud of interacting particles decreases steadily and after a long enough time in the dilute limit, we expect the particles to become effectively non-interacting and expand ballistically [162]. Furthermore, such a time-dependent density

complicates the distinction between diffusive and ballistic dynamics, as it results in a density-dependent diffusion constant and a non-linear diffusion equation, which was shown to allow for ballistic solutions in the limit of a dilute cloud [49, 163]. At intermediate times, when the density is still relatively large, a finite diffusion constant might still be hidden in experiments. If the diffusion constant is large enough to result in a mean free path of the cloud size, one may still observe ballistic dynamics [162].

Using the second moment of the density distribution to define the radius r of the cloud (Eq. (1.4)), we define the following criteria for ballistic dynamics in sudden expansion experiments [162]:

1. $r(t) \propto t$ when excluding short transient times.
2. Density profiles and expansion velocities are identical to a non-interacting system.

The first point is motivated by the ballistic dynamics of a cloud of non-interacting particles, as explained in Sec. 1.1.3. A finite width of the initial density distribution results in an initial accelerated expansion, albeit the expansion is ballistic. For this reason, we need to exclude short transient times. The second point is motivated by mappings of many-body systems in certain limiting cases to non-interacting systems, as explained in Sec. 1.2.3. For example, hard-core bosons exhibit ballistic dynamics, because they can be mapped onto non-interacting spin-less fermions. A similar mapping can be done for hard-core fermions. We define indications for the absence of strictly ballistic dynamics as [162]:

1. significant deviations from $r(t) \propto t$.
2. slower expansion velocity compared to the non-interacting prediction $v_r = \sqrt{2d}/\tau$.
3. the formation of a slowly expanding high-density core.

The second point is crucial for our experiments on the behavior of the asymptotic expansion velocity in the presence of interactions (Sec. 3.2.2). We characterize the dynamics of the cloud radius with the same fit function as in the non-interacting case (Eq. 1.11) but find smaller expansion velocities, similarly to experiments with bosons [50]. The third point is motivated by experimental findings in the two dimensional Fermi-Hubbard model [49] and also by the dynamics of initial states with doublons, where a doublon core is formed as discussed in Sec. 3.1.2.

1.2.2. Integrability of the one-dimensional Fermi-Hubbard model

While the nature of the transport dynamics is particularly relevant on intermediate time scales, studying late times in sudden expansion experiments can reveal information about the thermalization of the initial far-from-equilibrium state. The one-dimensional Fermi-Hubbard model offers the possibility to investigate these relaxation dynamics in an integrable model, i.e. there are exact solutions for all interaction strengths U , which can be found with the Bethe ansatz. The Bethe ansatz was first developed to find exact solutions for the Heisenberg spin chain [7] and successively extended to other models such as the one-dimensional Fermi-Hubbard model [9]. Meanwhile, the overall progress in understanding intergrable models is very clearly outlined in the book "Beautiful Models" by Bill Sutherland [8], on which this section is based to convey the basic ideas of the Bethe ansatz.

The Bethe ansatz only holds for one-dimensional systems that "support scattering", i.e. systems that will expand unless confined. This is similar to a system in the gas phase and exactly what we observe in the sudden expansion experiments of a cloud of atoms, after releasing the cloud. Let's assume, the interaction in such system is described by a pair potential v , falling off sufficiently fast and let's further assume, that we work in the continuum limit for now. The Hamiltonian of this system with N particles is

$$\hat{H} = \sum_{j=1}^N \frac{\hat{p}_j^2}{2m} + \sum_{j,k=1, j < k}^N v(\hat{x}_k - \hat{x}_j), \quad (1.20)$$

where the total energy E and the total momentum P are conserved asymptotically, when the particles are far apart from each other and effectively free. If we consider only a single particle, the eigenfunctions are plane waves $\psi(x) = e^{ikx/\hbar}$ and the dispersion is quadratic $\epsilon(k) = \hbar^2 k^2 / (2m)$.

Next, we consider two particles. If the two particles are far apart from each other, they can be understood as free particles, because the pair potential is short ranged. Thus, the wave function of this two-particle system is a product of plane waves with total momentum $P = \hbar \sum_{j=1}^2 k_j$ and total energy $E = \sum_{j=1}^2 \epsilon(k_j)$. Here, $\hbar k_1$ and $\hbar k_2$ are the asymptotic momenta. When the particles come close to each other, the pair potential v results in scattering between the two particles. However, in a one-dimensional system, two-body scattering is very ineffective. If the two incoming momenta are $\hbar k_1$ and $\hbar k_2$, the only possibility for the two outgoing momenta is $\hbar k'_1 = \hbar k_2$ and $\hbar k'_2 = \hbar k_1$ due to the conservation of total energy and total momentum. This means, that the particles simply pass through each other and results in an asymptotic wave function

1. Theoretical background

$$\Psi(x_1, x_2) \rightarrow e^{i(k_1 x_1 + k_2 x_2)/\hbar} - e^{-i\theta(k_1 - k_2)/\hbar + i(x_1 k_2 + x_2 k_1)/\hbar}. \quad (1.21)$$

Here, we consider the sector $x_1 \ll x_2$ and $\hbar k_1 > \hbar k_2$ are the incoming momenta. We see that the scattering amplitude can only contain a phase factor $\theta(k_1 - k_2)$ due to the conservation of probabilities. The wave function for the other sector $x_1 \gg x_2$ needs to be determined by the statistics of the particles.

We now consider three particles, such that the total energy and the total momentum are given by $P = \hbar \sum_{j=1}^3 k_j$ and $E = \sum_{j=1}^3 \epsilon(k_j)$, with the asymptotic incoming momenta $\hbar k_1 > \hbar k_2 > \hbar k_3$. We have $3! = 6$ ways to rearrange the particles and therefore get for the asymptotic wave function

$$\begin{aligned} \Psi(x_1, x_2, x_3) \rightarrow \sum_P \Psi(P) e^{i(k_{P1} x_1 + k_{P2} x_2 + k_{P3} x_3)/\hbar} \\ + \iiint_{\substack{k'_1 < k'_2 < k'_3 \\ P, E \text{ fixed}}} dk'_1 dk'_2 dk'_3 S[k'_1, k'_2, k'_3] e^{i(k'_1 x_1 + k'_2 x_2 + k'_3 x_3)/\hbar}. \end{aligned} \quad (1.22)$$

Here, a shorter notation is used in terms of the six permutations $P = (P1, P2, P3)$ of the incoming asymptotic momenta k_j . And the argument distinguishes the wave function $\Psi(x_1, x_2, x_3)$ from the scattering amplitude $\Psi(P)$. With this notation, the two-particle wave function is

$$\Psi(x_1, x_2) \rightarrow \sum_P \Psi(P) e^{i(k_{P1} x_1 + k_{P2} x_2 + k_{P3} x_3)/\hbar} = \Psi(12) e^{i(k_1 x_1 + k_2 x_2)/\hbar} + \Psi(21) e^{i(x_1 k_2 + x_2 k_1)/\hbar}, \quad (1.23)$$

with $\Psi(21)/\Psi(12) = -e^{-i\theta(k_1 - k_2)/\hbar}$. The first six terms in Eq. (1.22) constitute all possible combinations of the two-body scattering for the three particles. These terms must be there, as one can always imagine a collision between two particles, moving off into the asymptotic region before one of them collides with the third particle. The phase shifts for three particles can be inferred from the two body collisions according to $\Psi(213)/\Psi(123) = -e^{-i\theta(k_1 - k_2)/\hbar}$. The phase shifts of all successive collisions between pairs of particles can be determined similarly. Thus, the first six terms of the sum in Eq. 1.22, where the 3-body scattering factorizes into successive 2-body scattering events. Note, that this equation only holds in one sector of the $3!$ sectors $x_1 \ll x_2 \ll x_3$ and the wave function in the other sectors is determined by the particle statistics.

The last term in Eq. (1.22) is the only true 3-body scattering, since it does not factorize into successive 2-body scattering events. This term causes the wave function to depart from the

plane wave structure in the vicinity of $x_1 \approx x_2 \approx x_3$ and renders the scattering diffractive. It enables the thermalization of the asymptotic momenta and can only be present, if a third conservation law $L = \sum_{j=1}^3 \lambda(k_j)$ is absent. Systems with diffractive scattering are non-integrable and the Bethe ansatz does not work here. In contrast, if we were to find three conservation laws E, P, L for the 3-body scattering, then the outgoing asymptotic momenta would be only rearrangements of the incoming asymptotic momenta and if this also holds for 4-body scattering due to another conservation law and so on, the pair potential would be nondiffractive. Thus, non-diffraction could be ensured by a complete set of local conservation laws. If the pair potential is non-diffractive, the asymptotic Bethe ansatz can be used to find the wave function:

$$\Psi(x_1, \dots, x_N) \rightarrow \sum_P \Psi(P) e^{i \sum_{j=1}^N k_{Pj} x_j / \hbar}, \quad (1.24)$$

where we have $N!$ scattering amplitudes $\Psi(P)$, which are related by 2-body scattering according to $\Psi(P)/\Psi(P') = -e^{-i\theta(k-k')/\hbar}$ with permutations P, P' the same, except $Pj = P'(j+1), P(j+1) = P'j$ and $k = k_{Pj} = k_{P'(j+1)}, k' = k_{P'j} = k_{P(j+1)}$. The Bethe ansatz was used for the one-dimensional Fermi-Hubbard model to predict the momentum distribution at late times when initiating the sudden expansion from ground states [164, 165].

1.2.3. Symmetries of the one-dimensional Fermi-Hubbard model

The one-dimensional Fermi-Hubbard model exhibits many symmetries, which simplify an analysis of the sudden expansion dynamics. These symmetries rely on exact mappings between different parameter regimes and are in many cases unique to one-dimensional systems. Furthermore, the Fermi-Hubbard and the Bose-Hubbard model are related in one-dimensional systems as well for certain parameter regimes, which is important when comparing both models theoretically in Sec. 1.3.3 and experimentally in Sec. 3.2.2. In particular, we aim to address the following symmetries in this part and give a brief overview of their derivation.

- Mapping from hard-core fermions to spinless fermions
- Mapping from spinless fermions to the XX spin-chain
- Mapping from hard-core bosons to the XX spin-chain
- Dynamical symmetry between repulsive and attractive interactions

Mapping from hard-core fermions to spinless fermions. This mapping only holds for initial states without doublons. Furthermore, we consider the Fermi-Hubbard model in the limit $U/J \rightarrow \infty$, where doublons cannot be dynamically generated due to energy conservation, such that the Hilbert space without doublons is closed under time evolution. We can describe the dynamics with a modified version of the Hamiltonian in Eq. (1.19), where the subspace with doublons is projected out with the operator \hat{P}_G [63]:

$$\hat{H}_{hc} = -J \sum_{i,\sigma=\uparrow,\downarrow} \left(\hat{P}_G \hat{c}_{i\sigma}^\dagger \hat{c}_{i+1\sigma} \hat{P}_G + \text{h.c.} \right). \quad (1.25)$$

Furthermore, the spin-configuration of the initial state $\{\sigma\} = \{\sigma_1, \sigma_2, \dots, \sigma_N\}$, where N is the total number of fermions, becomes an invariant of the dynamics. Spin-exchange in a one-dimensional system corresponds to a second-order hopping process with a rate J_{ex} , scaling as $J_{ex} \propto J^2/U$ at large interaction strength and vanishes in the limit $U/J \rightarrow \infty$. Thus, the spin-configuration enters the Hamiltonian as a parameter $\hat{H}_{hc}\{\sigma\}$ and its Hilbert space can be represented by the Fock space of spinless fermions $|n_1, \dots, n_L\rangle_{\{\sigma\}}$, because the fermion position uniquely determines their spin according to the configuration $\{\sigma\}$. Hence, we recover the Hamiltonian of spinless fermions, equivalent to Eq. (1.1)

$$\hat{H}_{hc}(\{\sigma\}) = -J \sum_i \left(\hat{c}_i^\dagger \hat{c}_{i+1} + \hat{c}_{i+1}^\dagger \hat{c}_i \right), \quad (1.26)$$

where projecting out doublons is directly taken into account by the spinless fermion representation.

Mapping from spinless fermions to the XX spin-chain. This mapping relies on a Jordan-Wigner transformation [166], which enables a representation of spinless fermions in terms of spin-1/2 operators. We use the set of Pauli matrices $\{\hat{\sigma}_i^x, \hat{\sigma}_i^y, \hat{\sigma}_i^z\}$, where i is the site index and $\hat{\sigma}_i^\pm = \hat{\sigma}_i^x \pm i\hat{\sigma}_i^y$. The Hamiltonian of the XX spin-chain model is defined as

$$\hat{H}_{XX} = -2J \sum_{j=1}^L (\hat{\sigma}_j^x \hat{\sigma}_{j+1}^x + \hat{\sigma}_j^y \hat{\sigma}_{j+1}^y). \quad (1.27)$$

This Hamiltonian becomes equivalent to the Hamiltonian of spinless fermions, using the Jordan-Wigner transformation, defined according to:

$$\hat{\sigma}_j^+ = \hat{c}_j^\dagger e^{-i\pi \sum_{m<j} \hat{c}_m^\dagger \hat{c}_m}, \quad \hat{\sigma}_j^- = e^{i\pi \sum_{m<j} \hat{c}_m^\dagger \hat{c}_m} \hat{c}_j, \quad \hat{\sigma}_j^z = \hat{c}_j^\dagger \hat{c}_j - 1/2 \quad (1.28)$$

Mapping from hard-core bosons to the XX spin-chain. Equivalently to hard-core fermions, this mapping applies for the Bose-Hubbard Hamiltonian in the limit $U/J \rightarrow \infty$ for initial states without doublons and higher occupations. For convenience, we define the Bose-Hubbard model

$$\hat{H}_{\text{BHM}} = -J \sum_i \left(\hat{b}_i^\dagger \hat{b}_{i+1} + \text{h.c.} \right) + U \sum_i \hat{n}_i (\hat{n}_i - 1) \quad (1.29)$$

where \hat{b}_i^\dagger (\hat{b}_i) is the bosonic creation (annihilation) operator, $\hat{n}_i = \hat{b}_i^\dagger \hat{b}_i$ is the number operator and i is the lattice-site index. The on-site interaction strength is set by U . In limit of hard-core bosons ($U/J \rightarrow \infty$), the Hamiltonian reduces to the kinetic energy

$$\hat{H}_{\text{LTG}} = -J \sum_i \left(\hat{b}_i^\dagger \hat{b}_{i+1} + \text{h.c.} \right) \quad (1.30)$$

in addition to the constraint that $(\hat{b}_i^\dagger)^2 |\Psi_{\text{phys}}\rangle = 0$ and $(\hat{b}_i)^2 |\Psi_{\text{phys}}\rangle = 0$ on all physical states $|\Psi_{\text{phys}}\rangle$. This Hamiltonian can be mapped onto an XX spin-chain model, when expressing the bosonic creation and annihilation operators in terms of spin-operators according to a Holstein-Primakoff transformation [166]:

$$\hat{\sigma}_j^+ = \hat{b}_j^\dagger \sqrt{1 - \hat{n}_j}, \quad \hat{\sigma}_j^- = \sqrt{1 - \hat{n}_j} \hat{b}_j, \quad \hat{\sigma}_j^z = \hat{n}_j - 1/2. \quad (1.31)$$

The XX spin-chain model is equivalent to spinless fermions, which establishes a mapping from hard-core bosons to spinless fermions.

Dynamical symmetry between repulsive and attractive interactions. In contrast to the previous mappings, this symmetry is neither restricted to one-dimensional systems nor does it hold for fermions only. It was already experimentally observed in the one- and two-dimensional Bose-Hubbard model [50] and in the two dimensional Fermi-Hubbard model [49]. This dynamical symmetry can be characterized according to the following theorem [49, 167]:

If an observable \hat{O} is invariant under both time-reversal and π -boost and the initial state $|\Psi_0\rangle$ is time-reversal invariant, acquiring only a global phase factor under the π -boost transformation, then the observed time evolutions $\langle \hat{O}(t) \rangle_{\pm} = \langle \Psi_0 | e^{i\hat{H}_{\pm}t} \hat{O} e^{-i\hat{H}_{\pm}t} | \Psi_0 \rangle$ are identical: $\langle \hat{O}(t) \rangle_{+} = \langle \hat{O}(t) \rangle_{-}$.

Here, \hat{H}_{\pm} refers to repulsive or attractive interactions $\pm|U|$ in the Fermi-Hubbard model defined in Eq. 1.19 and the π -boost $\hat{B}_{\pi/d}$ is a self-adjoint operator ($\hat{B}_{\pi/d}^2 = 1$), defined

according to his effect on the creation operator of a Bloch wave \hat{c}_k^\dagger with quasi-momentum k , adds half a reciprocal lattice vector to k ($\hat{B}_{\pi/d}\hat{c}_k^\dagger\hat{B}_{\pi/d} = \hat{c}_{k+\pi/d}^\dagger$). Sudden expansion experiments are in accordance with the requirements of the theorem: First, one can show that the onsite density operator \hat{n}_i is invariant under π -boost and time reversal. Second, the initial product states of site localized particles, obey both time reversal invariance and only acquire an overall global phase under the π -boost transformation.

1.3. Numerical results of different fillings

1.3.1. Quantum distillation for initial states with doublons

Here we analyze initial states with an average filling larger than one, which can be understood from an effective two-component picture consisting of singlons and doublons once the interaction strength U is larger than the bandwidth $W = 4J$. In this limit doublons become stable compound particles, since energy conservation forbids the decay of a doublon in two singlons as soon as the interaction energy is larger than the kinetic energy of the singlons, determined by the bandwidth W . Thus, energy conservation in this regime results in the lifetime of doublons increasing exponentially with U/J [168]. The dynamics of this effective two-component mixture is characterized by the vastly different tunneling rates of singlons and doublons. Singlons can be understood as the light and fast component, expanding according to their tunneling rate J . In contrast, doublons form the slow and heavy component during the expansion dynamics due to their effective tunneling rate $J_{\text{eff}} = 2J^2/U \ll J$, which is much smaller than the singlon tunneling rate in the limit of large interaction strength U . The different tunneling rates of both components cause a dynamical demixing of singlons and doublons during the expansion dynamics and result in a bimodal density distribution of the cloud, dominated by a slowly expanding core of doublons in the center and fast singlons in the wings of the cloud. At long enough expansion times when all singlons left the doublon core in the center of the cloud, a dynamical phase separation of the two components is realized, which is termed as weak quantum distillation.

For specific initial states this dynamical phase separation can be accompanied by a shrinking of the doublon core, mediated by expanding singlons and called strong quantum distillation (Fig. 1.4). The mechanism, causing the contraction of the doublon core, is depicted in Fig. 1.4a for an initial product state, where every lattice site is randomly occupied by either a singlon or a doublon. Outwards moving singlons encounter frozen doublons and in the one-dimensional system pass the doublons by exchanging their respective position. This exchange of positions effectively results in doublons moving towards the

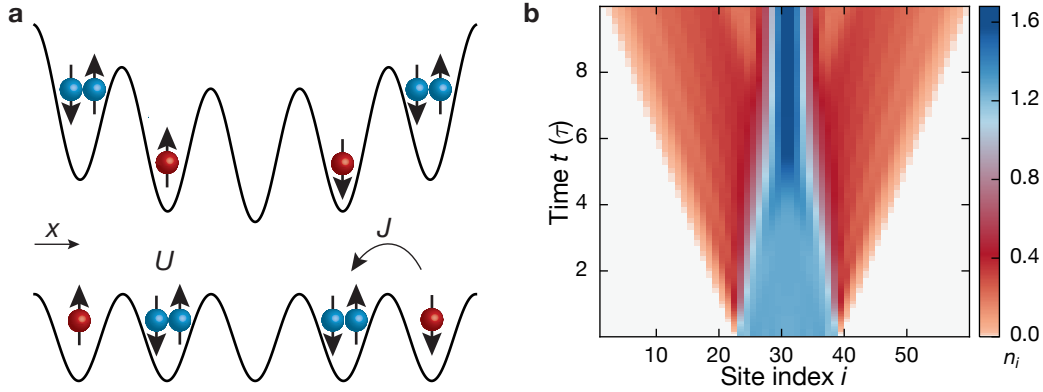


Figure 1.4.: Strong quantum distillation. **a** Initial state of the harmonically trapped two-component Fermi gas with singlons (red) and doublons (blue). After quenching to lower lattice depths and removing the harmonic trap fermions expand in a homogeneous 1D lattice. The expansion dynamics is dominated by first-order processes: resonant exchange of singlon and doublon positions leads to strong quantum distillation. **b** Time-dependent density matrix renormalization group simulations of the atomic density for $U = 20J$ as a function of time t in units of the tunneling time τ . Numerical simulations are done by Jacek Herbrych and Jan Stolpp [169].

center of the cloud, while singlons move further outwards. Furthermore, these mediated doublons dynamics happen with a tunneling rate J , as they are caused by singlons and are thus fast compared to the doublon tunneling rate J_{eff} . The contraction of the doublon core is a transient phenomenon (Fig. 1.4b). It is completed after all singlons expanded out of the doublon core and at large times $t \gg \hbar/J_{\text{eff}}$ the doublon core itself starts to slowly expand with the effective second order tunneling rate J_{eff} , at late times negating the contraction achieved at early times. Singlons can mediate the doublon dynamics only for specific initial states, highlighting the importance of the initial conditions for observing strong quantum distillation. While a remarkable contracting of the doublon cloud can be observed for an initial state, which consist of a random mixture of singlons and doublons (Fig. 1.4b), no contraction at all would be observable for an initial state with doublons already in the center of the cloud and singlons at the edges, since the phase separation of both components is already completed.

1.3.2. Initial state dependence of strong quantum distillation

In this part, we investigate in detail how different distributions of singlons and doublons in the initial state affect the contraction of the doublon cloud in the regime of strong quantum distillation. This is particularly relevant for understanding the efficiency of strong quantum distillation in experiments, where a random distribution of singlons

1. Theoretical background

and doublons, as studied in Fig. 1.4, is not easy to realize in the initial state. Rather, an inhomogeneous distribution of singlons and doublons is often realized in experiments with ultracold atoms due to the harmonic trap, which preferentially hosts doublons in the center and singlons in the wings of the cloud, resulting in a spatially varying average filling. Furthermore, the initial state usually contains empty sites in between singlons and doublons owing to non-adiabatic loading processes during the initial state preparation and experimental imperfections (2.1.2). Clearly, both the spatially inhomogeneous filling and additional empty sites are important modifications to the ideal initial state, studied in Fig. 1.4, potentially affecting the dynamics of the doublon cloud.

In order to benchmark the contraction of the doublon cloud, we characterize the doublon cloud radius with the second moment r_d of the doublon density distribution

$$r_d = \sqrt{(1/N_d(t)) \sum_{i=1}^L n_i^d(t) (i - i_0)^2}. \quad (1.32)$$

Here, we use the center of mass $i_0 = L/2 + 0.5$ of the doublon cloud and we define $n_i^d = \langle \hat{n}_{i\uparrow} \hat{n}_{i\downarrow} \rangle$ as average over all random configurations. $N_d(t)$ denotes the number of particles on doubly occupied sites. With this definition for the doublon cloud radius, we can quantify the contraction of the doublon cloud as relative change of the doublon cloud radius $\Delta r_d = r_d(t)/r_d(0) - 1$. An expanding cloud result in $\Delta r_d > 0$, whereas a contracting cloud is indicated by $\Delta r_d < 0$.

We analyze four different initial states, as depicted in Fig. 1.5a. **A**: the ideal scenario with twelve singlons and four doublons in a box trap, resulting in an average filling $n = 1.25$. **B** and **C**: twelve singlons and four doublons in a box trap with different numbers of empty sites, such that the average filling is reduced and the width of the initial density distribution is increased. **D**: equivalent to case **A**, but including singlon wings at the outer parts of the cloud, which are modeled by two singlons on the left and on the right side, respectively. This case is supposed to resemble the spatially inhomogeneous density distribution, characteristic for initial states in experiments with a harmonic trap.

The dynamics of the relative change in doublon cloud radius are depicted in Fig. 1.5b for the different initial states. As expected, case **A** shows the fastest and most pronounced shrinking of the doublon cloud radius, saturating at about half of its initial size. Decreasing the filling of the initial state in case **B** and case **C** results in both a weaker and slower contraction of the cloud. The weaker contraction of the doublon cloud, is caused by holes remaining trapped in between doublons on the time scale of the quantum distillation dynamics, which are first order in the tunneling J in contrast to an exchange of a hole and a doublon, which is second order in the tunneling J . The slower dynamics are a result of

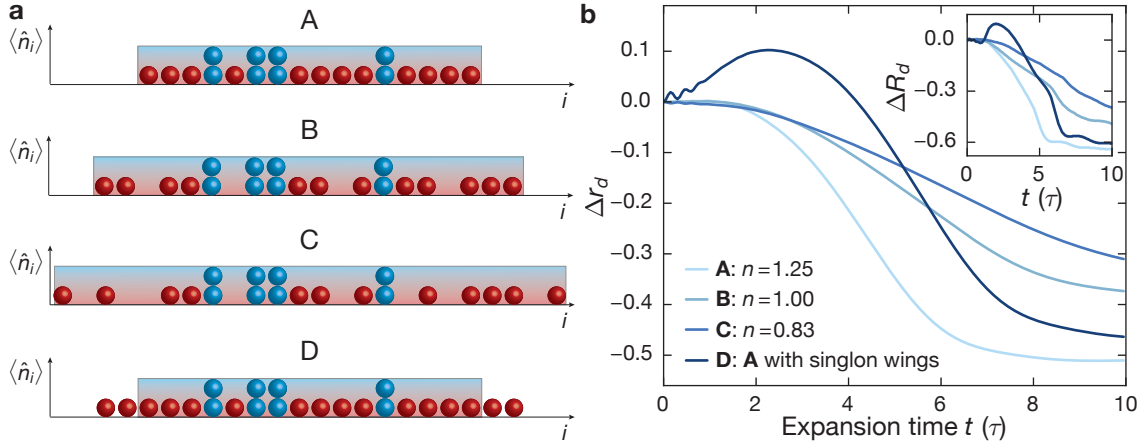


Figure 1.5.: Initial state dependence of the doublon cloud radius. **a** Different initial states of singlons and doublons. i represents the lattice site: **A**: Box trap with singlons and doublons, **B** and **C**: Box trap containing doublons, singlons and holons, **D**: singlons and doublons as in case **A**, but surrounded by singlon wings. The shaded area depicts the region in which we randomly distribute doublons, singlons or holons keeping $N_d/2 = 4$ and $N_s = 12$ fixed. Outside those regions, we only allow for singlons (case **D**) or no atoms. **b** Time evolution of the relative change in doublon cloud radius Δr_d for $U = 20J$ and various initial configurations as explained in (a). Inset: Time traces of the relative change in the HWHM of the doublon cloud ΔR_d . Numerical simulations are done by Jacek Herbrych and Jan Stolpp [169].

the larger initial radius of the cloud in the presence of empty sites. The singlons need to expand across a larger number of lattice sites and therefore take more time in order for the dynamics of strong quantum distillation to halt after singlons and doublons have spatially separated. The presence of additional singlons at the edges of the cloud in case **D** shows a small expansion of the doublon cloud, before a contraction is visible in analogy to case **A**. This can be understood by singlon wings, allowing doublons to move outwards on the singlon wings in the early stage of the expansion. Hence, the presence of singlon wings delays the contraction of the doublons cloud. We experimentally study strong quantum distillation in Sec. 3.1.3, where we use the half-width-at-half-maximum (HWHM) of the doublon cloud instead of the doublon cloud radius to quantify the contraction. A comparison in the inset of Fig. 1.5b shows that the relative change in doublon cloud radius behaves qualitatively similar to the relative change in the HWHM of the doublon cloud. To summarize, the dynamics of strong quantum distillation can be significantly altered in the presence of experimentally relevant modifications to the ideal initial state conditions. The findings are consistent with other studies, which identified the most important parameters affecting the reduction of the doublon cloud size: the number of singlons initially confined in the doublon cloud, the initial density and the cloud size [170, 171].

1.3.3. Asymptotic expansion velocity of initial states without doublons

Here, we investigate the expansion dynamics when starting from initial product states with one particle per site and compare the dynamics of the one dimensional Fermi-Hubbard model to the dynamics of the one dimensional Bose-Hubbard model. It was found that the expansion from the ground state of both models is ballistic with $v_r = \sqrt{2}$, if the ground state is a Mott insulator [162, 163]. In contrast, the expansion dynamics are expected to show a pronounced dependence on the interaction strength, when starting from experimentally realizable product states, which we study in Sec. 3.2.2. For small to intermediate interaction strength, diffusive dynamics with a velocity smaller than $v_r = \sqrt{2}$ takes place in both models, but the reduction of the expansion velocity is larger in the case of the Bose-Hubbard model.

We numerically study the reduced expansion velocity in terms of the interaction energy, which is generated when initiating the expansion from a product state. This effectively imitates the quench protocol used in the experiment and results in highly-excited states, where doublons are dynamically formed and where in the case of the Bose-Hubbard model also higher occupancies than doublons are present. For the Fermi-Hubbard model, we define the interaction energy $E_{\text{int}}^{\text{FM}}$ as:

$$E_{\text{int}}^{\text{FM}} = U \sum_{i=1}^L \langle \hat{n}_{i\uparrow} \hat{n}_{i\downarrow} \rangle. \quad (1.33)$$

The interaction energy is expected to depend on the spin-configuration of the initial state, as adjacent fermions with the same spin cannot form a doublon due to Pauli blocking. In contrast the formation of doublons is enhanced for adjacent fermions of opposite spin. Thus, we distinguish different initial states by the number of domain walls, i.e. the number of adjacent fermions with opposite spin. For $N = 10$ particles in the initial state, considered in the simulations, the number of domain walls ranges from one to nine and the expansion velocities are calculated for each number of domain walls separately, keeping the total magnetization equal to zero. The Bose-Hubbard model has a unique product state with one boson per site, because the spin degree of freedom is absent. We define the interaction energy $E_{\text{int}}^{\text{BH}}$ in this model:

$$E_{\text{int}}^{\text{BH}} = \frac{U}{2} \sum_{i=1}^L \langle \hat{n}_i (\hat{n}_i - 1) \rangle. \quad (1.34)$$

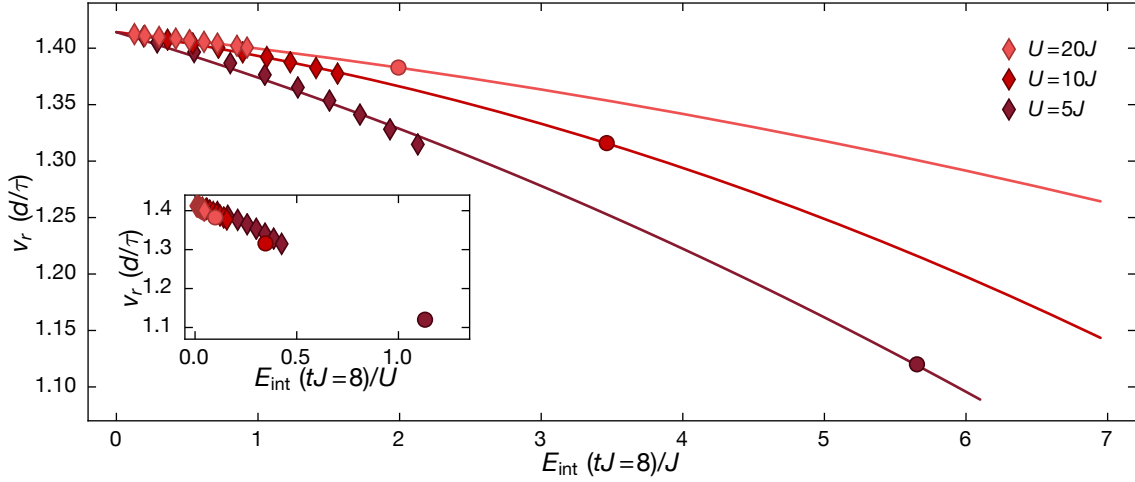


Figure 1.6.: Radial velocity as a function of the interaction energy. The three colors correspond to interaction strengths $U/J = 5, 10, 20$. Diamonds indicate fermions, circles show bosons. Diamonds of the same color depict different numbers of domain walls in the initial state (only one domain wall to nine domain walls from left to right). Solid lines are quadratic fits to the data. The inset shows the same data but versus E_{int}/U . We use initial states without doublons and without empty sites on a lattice of $L = 100$ sites with $N = 10$ particles placed in the center of the system. The velocities v_r are extracted from fits to numerical simulations of the cloud radius according to the second moment of the density distribution. Numerical simulations are done by Jacek Herbrych and Jan Stolpp [169].

In Fig. 1.6, we plot the velocities for different numbers of domain walls versus the interaction energy at time $tJ = 8$ as diamonds (one to nine domain walls in the initial state from left to right) [162]. The data for the Bose-Hubbard model is shown as circles in Fig. 1.6 and lie well outside the accessible range of interaction energies for fermions because of higher site occupations. Using a quadratic extrapolation, however, the bosonic interaction energies can be related to their fermionic counterparts. The interaction quench from $U/J = \infty$ to $U/J < \infty$ causes the dynamical formation of doublons (there were none in the initial state) and the trap opening induces a decrease of E_{int} towards the asymptotic value. We do not reach the asymptotic regime in our simulations, but we choose a time large enough to capture most of the decay of E_{int} . The results in Fig. 1.6 suggest that for large U/J , the asymptotic radial velocity is indeed primarily a function of the interaction energy that is generated due to the interaction quantum quench over the first tunneling times [172, 173]. The inset of Fig. 1.6 depicts an additional U -dependence, because doublons are only well-conserved objects for $U \gg W$ and they expand with a non-zero velocity for finite $U \sim W$. In contrast Ref. [174], which explains the expansion velocities at large U/J , assumes immobile doublons (and higher site occupancies) on the relevant time scales, which is only correct for $U \gg W$.

1. Theoretical background

The interaction energy is only a proxy for the actual heavy objects involved in the dynamics, in particular, since E_{int} still undergoes a slow decrease beyond the times reached in the simulations. A more rigorous argument is to relate v_r to the overlap of the initial state with bound states (see [175] for the two-body case) in the integrable one-dimensional Fermi-Hubbard model, in extension of the approach taken in [164]. Hence, the integrability of the one-dimensional Fermi-Hubbard model does not seem to be the dominant reason for the differences to the bosonic case. An interesting extension would be the calculation of expansion velocities by exploiting the integrability along the lines of [164, 165].

2. Setup and methods

2.1. Initial state preparation

2.1.1. Experimental sequence

We start with a degenerate Fermi gas of $30(1) \times 10^3$ ^{40}K atoms in a crossed beam dipole trap at the initial temperature $T/T_F = 0.15(1)$, where T_F is the Fermi temperature. Details on how to prepare a degenerate Fermi gas can be found elsewhere [176]. The Fermi gas consists of an equal mixture of two spin components corresponding to the hyperfine states $|\uparrow\rangle = |m_F = -7/2\rangle$ and $|\downarrow\rangle = |m_F = -9/2\rangle$ in the $F = 9/2$ hyperfine ground-state manifold of the ^{40}K atoms.

This mixture is loaded into a blue-detuned three-dimensional optical lattice with wavelength $\lambda_x = 532$ nm and lattice constant $d = \lambda_x/2$ along the x direction and $\lambda_\perp = 738$ nm along the transverse directions. The depth of the lattices is increased slowly, using a sequence of different linear ramps. First, within 7 ms, the lattice along the x direction and the transversal lattices are ramped to a depth of $1 E_{rx}$ and $1 E_{r\perp}$, respectively. Then, after waiting for 100 ms to adjust the dipole trap confinement, the depth of all three lattices is further increased to $8 E_{rx}$ and $8 E_{r\perp}$, respectively, during 75 ms. Finally, the lattice along the x direction is ramped up to $20 E_{rx}$ and the transversal lattices reach their final depth of $33 E_{r\perp}$ within 15 ms, freezing the populations of singly-occupied lattice sites (singlons) and doubly-occupied lattice sites (doublons). Here, $E_{rj} = \hbar^2 k_j^2 / (2m)$ are the respective recoil energies with $j \in \{x, \perp\}$, $k_j = 2\pi/\lambda_j$ denotes the corresponding wave vector and m is the mass of ^{40}K . The transverse lattices remain at their final depth during the whole sequence to realize individual 1D systems. Furthermore, an additional superlattice along the x direction is added at a depth of $20 E_s$, where $E_s = \hbar^2 / (2m\lambda_s^2)$ is the recoil energy of the superlattice with wavelength $\lambda_s = 1064$ nm. The phase of the superlattice is set such that tilted double wells along the x direction are created to suppress residual dynamics and remaining correlations between neighboring sites (Sec. 5.5.4).

The resulting initial state can be approximated as an incoherent mixture with density matrix $\hat{\rho} = \frac{1}{\mathcal{N}} \sum_{\{\sigma\} | \sum_i \sigma_i = 0} |\psi_0(\{\sigma\})\rangle \langle \psi_0(\{\sigma\})|$, where the sum includes all \mathcal{N} possible permutations of spin configurations $\{\sigma\}$, since the spins are randomly distributed among

2. Setup and methods

the sites. We define each product state $|\psi_0(\{\sigma\})\rangle = \prod_{i \in \text{trap}} (\hat{c}_{i\uparrow}^\dagger)^{n_{i\uparrow}} (\hat{c}_{i\downarrow}^\dagger)^{n_{i\downarrow}} |0\rangle$, where $\hat{c}_{i\sigma}^\dagger$ is the fermionic creation operator, $n_{i\sigma} \in \{0, 1\}$, $\sigma \in \{\uparrow, \downarrow\}$ and i is the lattice-site index. The fraction of atoms on doubly-occupied sites $n_d = N_d / (N_s + N_d)$ in the initial state can be tuned via the interaction strength during the loading process employing a Feshbach resonance at 202.1 G (see Sec. 2.2.1). Here, N_s (N_d) denotes the number of particles on singly (doubly)-occupied sites. Holding the atoms in the deep 3D optical lattice for 25 ms, both the dipole trap strength and the magnetic field strength are adjusted to their target values during the expansion of the cloud. We ramp the magnetic field within 15 ms to change the scattering length from $a_s = -20 a_0$ (attractive loading to generate initial states with doublons) or $a_s = 140 a_0$ (repulsive loading to realize initial states without doublons) to the scattering length, which sets the desired interaction strength during the expansion of the cloud in the lattice. Moreover, the dipole traps along the x and the y direction (trap frequency of $\omega_x = \omega_y = \omega = 2\pi \times 54(1)$ Hz, measured in the $(8E_{rx}, 8E_{r\perp}, 8E_{r\perp})$ deep lattice) are switched off within 22 ms, whereas the dipole trap along the z direction (trap frequency of $\omega_z = 2\pi \times 184(2)$ Hz, measured in the $(8E_{rx}, 8E_{r\perp}, 8E_{r\perp})$ deep lattice) is ramped within the same time, such that the lattice potential is flat during the expansion (see Sec. 2.3). The preparation sequence ends with removing the superlattice and quenching the lattice along the x direction within 10 μ s from $20 E_{rx}$ to $8 E_{rx}$ to initiate the expansion of the cloud.

Ramping down the lattice along the x direction together with the previous adjustment of the dipole trap depths realizes a quench of both the confinement and the interaction strength, which is rapidly changed from the hard-core limit in the deep lattice to the desired interacting strength during the expansion of the cloud. Even for small scattering length, necessary to realize weak interaction strengths $U \approx J$, the interaction strength in the deep lattice before the quench is $U \approx 20J$. While quenching the confinement initiates the expansion of the cloud, quenching the interaction strength generates a highly excited out-of-equilibrium state.

After a variable expansion time t the on-site population is frozen by suddenly increasing the lattice depth to $20 E_{rx}$. Subsequently, we use occupation number resolved in-situ absorption imaging to probe singlons and doublons separately. Hereby, we successively iterate between images with both singlons and doublons and images with singlons only, where all doublons are removed after time evolution by using a short near-resonant light pulse, dubbed doublon blast pulse, to trigger light-assisted collisions (Sec. 2.2.2). The in-situ density of the doublons can be inferred by subtracting the in-situ density of the singlons from the in-situ density of both singlons and doublons. The in-situ absorption imaging needs to be performed with Feshbach field, because ramping this magnetic field to zero before imaging would require crossing the Feshbach resonance at 202.1 G, converting doublons to Feshbach molecules [138], which are invisible to imaging light.

2.1.2. Characterization

Loading a Fermi gas into the lowest band of a three-dimensional optical lattice can result in a variety of different phases in the lattice. Possible scenarios are for example a finite temperature band-insulator with metallic wings or a Mott insulator with only one atom per site. We characterize the initial state by estimating the dimensionless compression $E_t/(12J)$ and the renormalized cloud size $R_{sc} = R/(\gamma_y\gamma_z N_\sigma)^{1/3}$ during loading, where we use $E_t = V_t[3\gamma_y\gamma_z N_\sigma/(4\pi)]^{2/3}$ and $V_t = m\omega^2 d^2/2$. Here, $\gamma_y = 738/532$ takes into account the different lattice constants between the x direction and the transversal y and z directions, $\gamma_z = \omega_z/\omega = 184/54$ takes into account the different harmonic confinement along the z direction compared to x and y directions, $N_\sigma = 15(1) \times 10^3$ is the number of atoms per spin state σ , m is the mass of ^{40}K and d is the lattice constant along the x direction. With the parameters R_{sc} and E_t it is possible to distinguish between the Mott-insulating and the metallic regime of the Fermi-Hubbard model for repulsively interacting fermions [115]. The renormalized cloud size can be understood as a rough estimate for the distance between two particles in the same spin state and only depends on the dimensionless compression, the interaction strength and the entropy set by the temperature in the pure harmonic trap. The dimensionless compression is the ratio between the characteristic trap energy E_t , equivalent to the Fermi energy of a non-interacting gas in the atomic limit at zero-tunneling, and the bandwidth $12J$ in a 3D optical lattice. We estimate $R_{sc} = 0.9(1)d$ and $E_t/(12J) = 0.1(1)$ in the $(8E_{rx}, 8E_{r\perp}, 8E_{r\perp})$ deep lattice. This means that we work in the metallic regime with a mean density in the center of the cloud of $\langle n_i \rangle < 1$.

2.2. Calibration methods

2.2.1. Doublon fraction

While large repulsive interactions ($a_s > 0$) result in initial states with a negligible doublon fraction, attractive interactions ($a_s < 0$) favor initial states with a large doublon fraction n_d , as illustrated in Fig. 2.1a. Creating initial states with a large doublon fraction, however, also increases the number of holes, since a pair of neighboring singlons is converted into a doublon and a hole. In order to generate a high doublon fraction with as few holes as possible, we scan the scattering length a_s and measure the cloud size and the doublon fraction (Fig. 2.1). We find an appreciable fraction of atoms on doubly-occupied sites [$n_d = 0.40(2)$], when preparing the initial state with $a_s = -20 a_0$. As shown in Fig. 2.1b, the cloud radius is the same as the one, where the scattering length was set to $25 a_0$ during loading with $U/(12J) = 0.12$ in the $(8E_{rx}, 8E_{r\perp}, 8E_{r\perp})$ deep lattice. The measured cloud

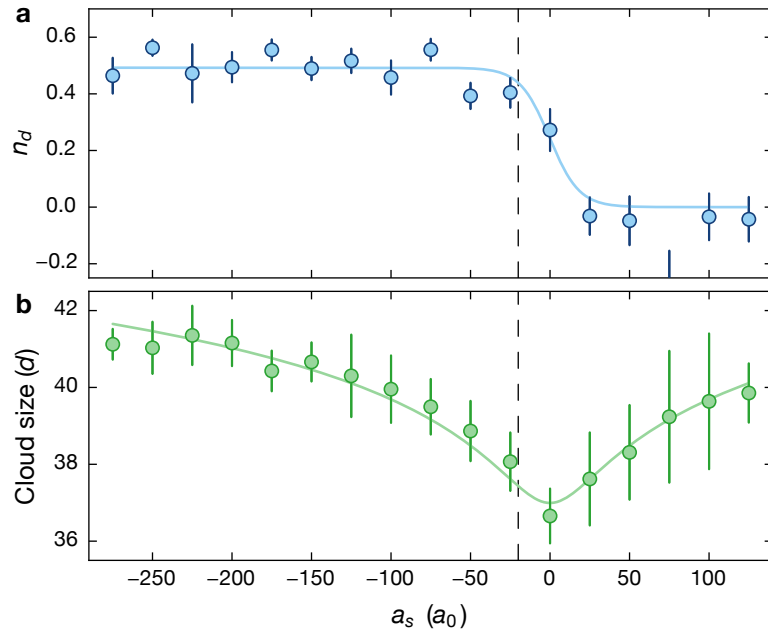


Figure 2.1.: Control of the doublon fraction. **a** Fraction of atoms on doubly-occupied sites n_d depending on the loading scattering length in units of the Bohr radius a_0 and **b** the resulting cloud size in units of the lattice constant d . We characterize the cloud size with the half-width-at-half-maximum of the in-situ density distribution. To prepare initial states with a large number of doublons, we use a loading scattering length of $a_s = -20 a_0$ (dashed vertical line), which yields a significant fraction of atoms on doubly-occupied sites $n_d = 0.40(2)$ and a minimal cloud size. Each data point is averaged three times and error bars denote the standard error of the mean.

radius (Fig. 2.1b) at $25 a_0$ is in agreement with the values obtained in Ref. [115], where, for our parameters, the central density of the cloud was shown to be $\langle \hat{n}_i \rangle \lesssim 0.9$.

For initial states without doublons ($n_d < 0.05$), we use a loading scattering length of $a_s = 140 a_0$. The cloud size in this regime suggests that more holes are present in the initial state than compared to the initial state in the regime at $a_s = -25 a_0$. However, the dynamics we probe with initial states without doublons (Sec. 3.2.2), is rather affected by residual doublons than by residual holes, motivating a large scattering length $a_s = 140 a_0$.

2.2.2. Doublon blast duration

A direct access to the in-situ density of both singlons and doublons is important to quantify the expansion dynamics of each of the two components separately. Here, we rely on the successive iteration of images with both singlons and doublons and images with singlons only, where all doublons are removed with a doublon blast pulse. This short light pulse

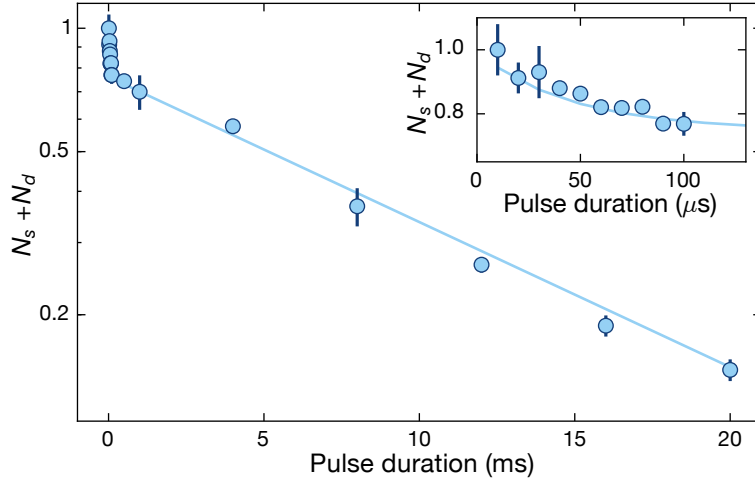


Figure 2.2.: Atom number decay in the presence of a near-resonant laser pulse. Total atom number $N_s + N_d$ normalized to the initial value as a function of the pulse duration. The data was taken for $U = 20J$ after an expansion time in the lattice of $t = 40\tau$ at a detuning of the pulse of $\Delta = 364$ MHz. Each data point is averaged twice and error bars denote the standard error. Solid lines show the fit using the sum of two exponentials. Inset: Same data as in the main plot, but with a shorter time scale to show the fast initial doublon decay due to light-assisted collisions.

is created with an additional blue-detuned laser, with detuning Δ from the imaging transition of ^{40}K ($|F = 9/2, m_F = -9/2\rangle \rightarrow |F' = 11/2, m_{F'} = -11/2\rangle$). As a result, atoms on doubly-occupied sites are lost due to light-assisted collisions. The mechanism underlying light-assisted collisions can be briefly described as follows [167, 177]. An atom is excited by absorbing a photon and collides with another atom. This results in a strong long-range dipole-dipole interaction between the ground state and the excited state atom, which is repulsive for our blue-detuned light pulse. Moving away from each other, both atoms pick up a fraction of the detuning as kinetic energy, until the excited state atom returns to its ground state by spontaneously emitting a photon. The increase in kinetic energy is usually enough for both atoms to leave the trap. In Fig. 2.2, we show a calibration measurement for the optimal pulse length to extinguish doublons. As indicated by the semi-log-plot, the total atom number shows a bimodal decay with well-separated time scales, which we characterize by fitting a sum of two exponential functions to the atom number $N_s(t) + N_d(t) = N_s(0)e^{-t/\tau_s} + N_d(0)e^{-t/\tau_d}$. N_s refers to the number of singlons and N_d indicates the number of particles bound in doublons. We extract a fast decay with a lifetime of $\tau_d = 40(10) \mu\text{s}$, which is attributed to the loss of atoms on doubly-occupied sites due to light-assisted collisions and an additional slow decay with a lifetime of $\tau_s = 12(1) \text{ms}$, which results from the loss of atoms on singly-occupied sites due to off-resonant photon scattering. For all experiments, the duration of the light pulse was set

to $150\ \mu\text{s}$, so as to reliably remove all doublons while leaving the singlons unaffected. The detuning Δ of the pulse with respect to resonant imaging light depends on the magnetic field used to set the final interaction strength with the Feshbach resonance and varies between $\Delta(U=5J) = 296\ \text{MHz}$ and $\Delta(U=20J) = 364\ \text{MHz}$. We found that the different detunings have only a negligible effect on the doublon lifetimes.

2.3. Creating a flat potential landscape

A crucial step in realizing a successful expansion experiment is the generation of a flat potential such that any residual effects of the harmonic trap remain as small as possible along the expansion direction. As we found in Sec. 1.1.2, the residual harmonic confinement can well be neglected as long as the potential energy difference, picked up by the particles with respect to the initial state of the expanding cloud is smaller than the tunneling rate J . In our setup the atomic cloud is confined by three dipole traps: one along each of the horizontal directions, x and y (x is the longitudinal direction of the tubes), and one along the vertical z direction. The vertical dipole trap has a Gaussian beam waist of $150\ \mu\text{m}$. The horizontal dipole traps are elliptical with waists of $30\ \mu\text{m}$ in the vertical and waists of $300\ \mu\text{m}$ in the horizontal direction. The optical lattices along all spatial axes have beam waists of $150\ \mu\text{m}$ (as the vertical dipole trap) and are blue detuned, providing an anti-confining potential. A flat potential along the x direction during the expansion of the cloud can be generated by choosing the strength of the vertical dipole trap such that it compensates the anti-confinement of the optical lattices. As the horizontal dipole traps have different beam geometries, they cannot be used to compensate the anti-confinement and therefore, they are switched off during the time evolution of the expanding cloud. Creating a flat potential requires optimizing both the z dipole beam alignment and its strength to maximize the in-situ cloud size after a long evolution time (see also Ref. [50]). Note, that this optimization technique works, because the expansion dynamics are symmetric with respect to a confining and an anti-confining potential, such that the largest possible expansion necessarily corresponds to the smallest achievable residual confinement (Sec. 1.1.2). This method works well for canceling the harmonic part of the confining potential. Note, however, that at large enough distance from the center, higher-order contributions to the confining potential become important and ultimately limit the system size, which can be used for the expansion experiments.

3. Results

3.1. Quantum distillation

3.1.1. Bimodal expansion dynamics

We begin the discussion of our experimental results with sudden expansion measurements using initial product states of atoms localized on individual lattice sites. First, we start with a mixture of singlons and doublons at a fixed doublon fraction $n_d = 0.40(2)$. We monitor the dynamics of the singlon and doublon clouds separately as a function of the expansion time using occupation number resolved in-situ imaging, as outlined in Sec. 2.2.2. In particular, we investigate the effect of interactions on the expansion dynamics and focus on the regime of large interactions, where isolated doublons are expected to become stable objects [168].

We study the dynamics of the width of the singlon and the doublon cloud by monitoring their respective cloud sizes $R_{s,d}(t)$ at half-width-at-half maximum (HWHM) in Fig. 3.1. The HWHM is most sensitive on the fastest particles, which determine the width of the cloud for sufficiently long expansion times. Due to the first-order hopping of singlons, we expect a fast increase of the singlon cloud size R_s , which should at late times, and in the case of non-interacting singlons increase according to the singlon expansion velocity $v_s = 2d/\tau$ (see Sec. 1.1.1). Doublons, in contrast, can only expand via a second-order hopping process, which scales as $J_{\text{eff}} = 2J^2/U$ and in the limit of large U is much smaller than J . Therefore, a fictitious cloud of non-interacting doublons would expand at a velocity $v_d = 2d/\tau_{\text{eff}}$, with $\tau_{\text{eff}} = \hbar/J_{\text{eff}}$, resulting in a drastically reduced doublon expansion velocity compared to the singlon expansion velocity in the limit of large U . As illustrated in Fig. 3.1 we observe a rapidly-expanding singlon cloud, which has approximately doubled in size at $t = 40\tau$ for both $U = 5J$ and $U = 20J$. In contrast, the doublon cloud size grows much slower for $U = 5J$ and we even observe a weak shrinking of the cloud for $U = 20J$. Such a behavior is not expected for a fictitious cloud of non-interacting doublons expanding according to J_{eff} [178], as indicated by the dashed lines in Fig. 3.1. This shows, that while we do witness the expected bimodal dynamics of the singlon and the doublon cloud, the

3. Results

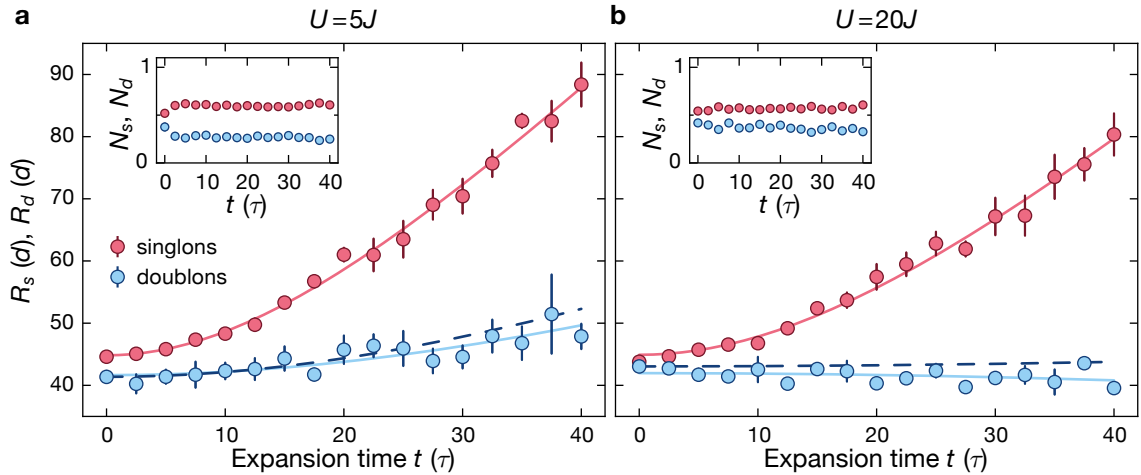


Figure 3.1: Dynamical phase separation of singlons and doublons. Half-width-at-half-maximum (HWHM) size $R_{s,d}$ of singlon (s, red) and doublon (d, blue) clouds as a function of time for **a** $U = 5J$ and **b** $U = 20J$. The dashed lines illustrate the hypothetical expansion of a non-interacting doublon cloud with effective tunneling $J_{\text{eff}} = 2J^2/U$. τ is the tunneling time $\tau = \hbar/J$. Every data point is averaged over four measurements and error bars represent the standard-error-of-the-mean. Solid lines are guides to the eye. Insets: Number of atoms on singly- and doubly-occupied sites, N_s and N_d , as a function of time.

dynamics affecting the doublon cloud size is more complicated and cannot simply be explained by two independently expanding components.

Furthermore, we probe the atom number on singly-occupied sites (doubly-occupied sites) N_s (N_d) in the insets of Fig. 3.1. For $U = 5J$ we witness a fast doublon decay of about 25% in the early stages of the expansion $t \lesssim 5\tau$, which is accompanied by a compatible increase of the singlon number. In contrast, both numbers remain approximately constant for $U = 20J$. The doublon decay at $U = 5J$ can be explained in the following way: At a finite interaction strength, a doublon can be understood as excited state with energy U . The decay of a doublon into two singlons requires a conversion of its interaction energy into kinetic energy of the singlons due to energy conservation. However, the maximum kinetic energy each singlon can acquire in the lowest band of the lattice is bounded by the bandwidth $W = 4J$. Note, that this is fundamentally different from the continuum limit, where the quadratic dispersion does not bound the maximum kinetic energy, that a particle can acquire. Therefore, in the lattice, the decay of a doublon into two singlons is energetically forbidden once the interaction energy becomes much larger than the bandwidth $U \gg W$ [179], since in this case the interaction energy released in the doublon decay cannot be transferred into kinetic energy of singlons in low-order processes [179, 180]. This is in agreement with our observation that the doublon decay is mainly visible at $U = 5J$ and that this decay is accompanied by an increasing number of singlons. At

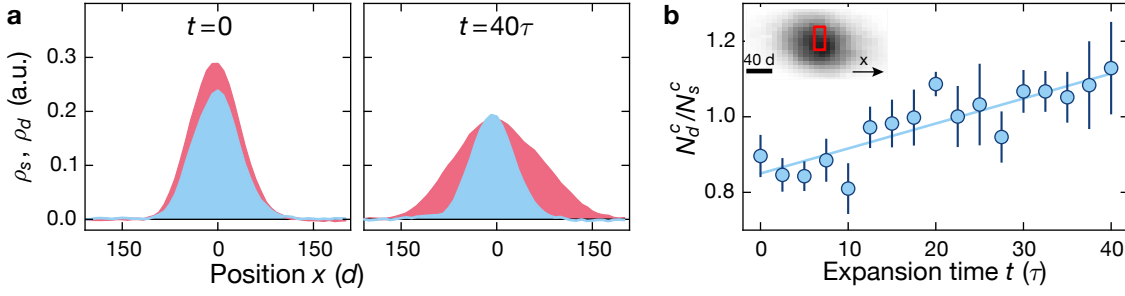


Figure 3.2.: Weak quantum distillation. **a** Experimental snapshots of the integrated line densities for singlon and doublon clouds, $\rho_s(x)$ and $\rho_d(x)$, at $t = 0$ (left) and $t = 40\tau$ (right) for $U = 20J$. **b** Ratio N_d^c/N_s^c of atom numbers on doubly- and singly-occupied sites in the central region of the cloud (red rectangle in the inset) as a function of time for $U = 20J$. Every data point is averaged over four measurements and error bars represent the standard-error-of-the-mean. Solid lines are guides to the eye.

$U = 20J$ we do expect the doublons to be stable particles with long lifetimes. Therefore, we attribute the small residual decay at $U = 20J$ to light-assisted losses of doublons [181].

We conclude that we are able to probe the bimodal expansion dynamics of singlons and doublons at approximately constant doublon numbers, when the interaction strength is large enough. Note, that this regime is vastly different compared to earlier experiments with bosons [51], which were carried out at intermediate interaction strengths, such that doublons can decay to singlons on experimentally relevant time scales.

3.1.2. Weak quantum distillation

We further characterize the bimodal dynamics described in the previous chapter by comparing the integrated line densities of singlons and doublons at $t = 0$ and $t = 40\tau$ for our strongest interactions $U = 20J$ in Fig. 3.2a. Clearly, the singlons expand significantly, while the doublons essentially remain in the center of the cloud. As a consequence, we observed that the ratio of atom numbers on doubly- and singly-occupied sites N_d^c/N_s^c in the center of the cloud increases as a function of time, indicated in Fig. 3.2b. Thus, we can understand the bimodal dynamics as a dynamical phase separation between fast singlons, which populate the outer parts of the cloud at large enough expansion times and slow doublons, which remain in the center of the cloud. This is emphasized by an increase of N_d^c/N_s^c at late times by about 40%. This phase separation has been investigated theoretically and is termed "weak quantum distillation" [170, 171, 182]. Intuitively, we would expect the phase separation dynamics to be a transient effect, which stops once the singlon and doublon clouds do not overlap anymore. The timescale would be set by

the initial size of the doublon cloud and the expansion velocity of the singlons, which determines the time until all singlons left the doublon cloud.

Note, that the increase of N_d^c/N_s^c in Fig. 3.2b could in principle be caused by 1D systems that contain mostly singlons and only a small amount of doublons. As our absorption imaging intrinsically integrates along the z -direction, it averages over many individual realizations of 1D systems with different density distributions. In these systems, the expansion would decrease the singlon number in the center N_s^c , without mediating a phase separation between singlons and doublons. In order to estimate the contribution of 1D systems with negligible doublon fraction to the ratio N_d^c/N_s^c , we can approximate the initial shape of the cloud in the lattice with an ellipsoid, where the ratio of the principal axes is set by the trap frequencies. Using an Abel transformation [183], the full 3D density distribution of singlons and doublons can be reconstructed. The width of the singlon and doublon distribution along the x direction thereby translates into a width along the z direction by implying the symmetry of the ellipsoid. As a result, the extent of the cloud along the z direction amounts to about 30 individual planes, where only the four outermost planes are primarily occupied with singlons. Assuming that the dynamics and therefore the change in the ratio N_d^c/N_s^c is solely governed by singlons expanding in these outermost 1D systems we obtain a conservative upper bound of $N_d^c/N_s^c \lesssim 10\%$. The observed effect reported in Fig. 3.2b is much larger than this bound, which clearly indicates a dynamical phase separation and thus weak quantum distillation in 1D systems with singlons and doublons.

3.1.3. Evidence for strong quantum distillation

The dynamical phase separation between singlons and doublons can result in more involved dynamics, which cannot be understood in terms of these two independent components. In Fig. 3.1b, for instance, our observations indicate a possible shrinking of the doublon cloud, which contradicts the prediction of a fictitious cloud of non-interacting doublons (dashed line), but rather exhibits a slight shrinking.

In order to study this effect in more detail, we quantify the change of the doublon cloud size $R_d(t)$ with a linear fit $f(t) = at + b$. The fits to the data are shown in Fig. 3.3a for $U = 5J$, $U = 7.5J$, $U = 10J$ and $U = 15J$ and additionally in Fig. 3.3b for the strongest interaction of $U = 20J$. While the fits indicate an increase of R_d for weak interactions of $U = 5J$, intermediate interactions of $U = 10J$ already result in a slower spreading of the doublon cloud and for $U = 20J$, the fit indicates a contraction of the doublon cloud as shown in the left panel of Fig. 3.3b. In order to test the goodness of the linear fit to the doublon cloud size for strong interactions of $U = 20J$, we compare it to fitting a constant

function to the doublon cloud size in the right panel of Fig. 3.3b. A common quantitative estimate for the goodness of a fit is χ_{red}^2 , which is defined as

$$\chi_{\text{red}}^2 = \nu^{-1} \sum_{i=1}^N \left(\frac{R_d(t_i) - g(t_i)}{\sigma_i} \right)^2, \quad (3.1)$$

where $R_d(t_i)$ is the doublon cloud size at time t_i , calculated from the mean of four data points, σ_i is the corresponding standard deviation for each $R_d(t_i)$, $g(t_i)$ is the value of the fit function at time t_i and ν is the difference between the total number N of discrete points t_i ($N = 17$ for all time traces of the doublon cloud size) and the number of fitting parameters. For the linear fit, we obtain $\chi_{\text{red}}^2 = 0.61$, whereas the fit with the constant function yields a slightly larger $\chi_{\text{red}}^2 = 0.84$. This χ_{red}^2 analysis indicates that the decreasing linear function describes the data better than a constant function, even after accounting for the increased number of fit parameters.

While a linear fit is well suited to characterize whether the doublon cloud contracts or expands, we additionally want to quantify the relative change in doublon cloud size $\Delta R_d(t)$. We define $\Delta R_d(t) = R_d(t)/R_d(0) - 1$, which we evaluate at the maximum expansion time $t = 40\tau$ to $\Delta R_d = a/b \cdot 40\tau$, using the fit parameters of the linear fit for all interactions. The error of the linear fit parameters indicates the one sigma confidence interval and the error bars of the relative doublon cloud size are calculated by using Gaussian error propagation. A positive (negative) relative change of the cloud size corresponds to an expansion (contraction) of the doublon cloud. We find that ΔR_d decreases with increasing interaction strength from $\Delta R_d = 0.16(7)$ at $U = 5J$ to $\Delta R_d = -0.05(2)$ at $U = 20J$.

A contraction of the doublon cloud on top of the dynamical phase separation is a hallmark of so-called "strong quantum distillation" [170, 171, 182]. This process explains, why assuming singlons and doublons as two independent components during the expansion is too simplistic (Sec. 1.3.1) and can be understood in the following way: Rapidly expanding singlons encounter slow doublons during the expansion dynamics, which necessarily leads to an exchange of their positions in a one-dimensional system (Fig. 1.4). This exchange happens with the singlon tunneling rate J and not with the effective tunneling rate J_{eff} of the doublons. Therefore, fast doublon dynamics occur towards the center of the cloud, which are mediated by outwards moving singlons. While this process explains the contraction of the doublon cloud, a quantitative understanding of the contraction relies on many properties of the initial state and is discussed for our experiments in Sec. 3.1.4.

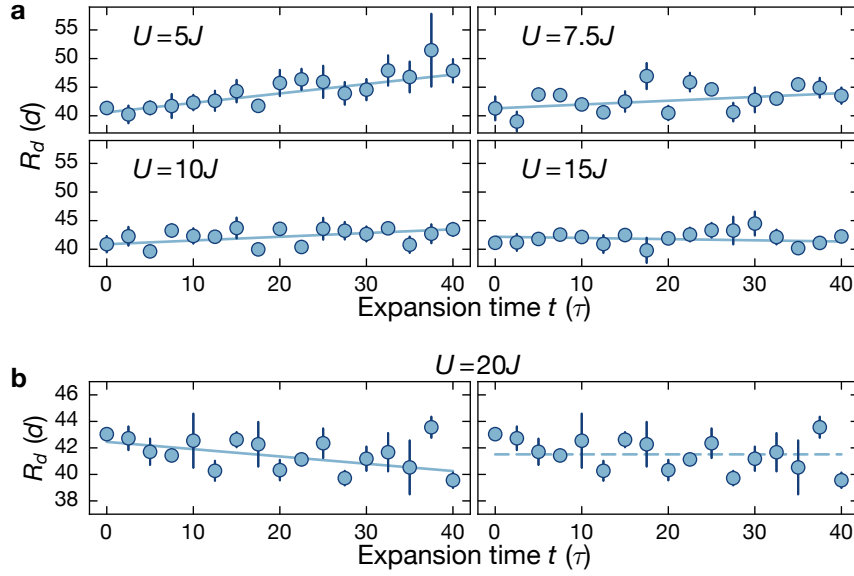


Figure 3.3.: Time traces of R_d with linear fits. **a** Time traces of the HWHM of the doublon cloud R_d for different interactions. Solid lines indicate a linear fit to the data. **b** Time trace of R_d for $U = 20J$ with a linear fit (solid line) resulting in $\chi_{\text{red}}^2 = 0.61$ (left) and a fit of a constant function (dashed line) resulting in $\chi_{\text{red}}^2 = 0.84$ (right). Every data point in (a) and (b) is averaged over four measurements and error bars represent the standard-error-of-the-mean.

3.1.4. Role of different initial states

In Sec. 1.3.2 we numerically investigate the achievable decrease of the relative change in doublon cloud radius Δr_d for the regime of strong quantum distillation and observe a maximum possible contraction with $\Delta r_d \approx -0.5$. This contraction is a lot more pronounced than what we experimentally witness for the maximum relative change of the doublon cloud size in Sec. 3.1.3: $\Delta R_d = -0.05(2)$ at $U = 20J$.

In this section, we want to shed light on what causes this deviation between numerical and experimental results by numerically studying different initial conditions. Studying ΔR_d numerically, we focus on the role of different average initial densities $n = (N_s + N_d)/L_{\text{init}}$, which has the largest influence on the contraction of the doublon cloud (see Sec. 1.3.2). We use an ideal box trap of length L_{init} for constant doublon fraction $n_d = 0.4$ (twelve singlons and four doublons) and compare three initial states with a different number of holons (empty sites), as depicted in Fig. 3.4a. Note, that studying the role of holons is also important from the experimental perspective, since we expect a significant number of holons in our initial state, when generating doublons and clearly cannot realize an ideal initial state without holons (see Sec. 2.2.1). In Fig. 3.4b, we show tDMRG simulations of

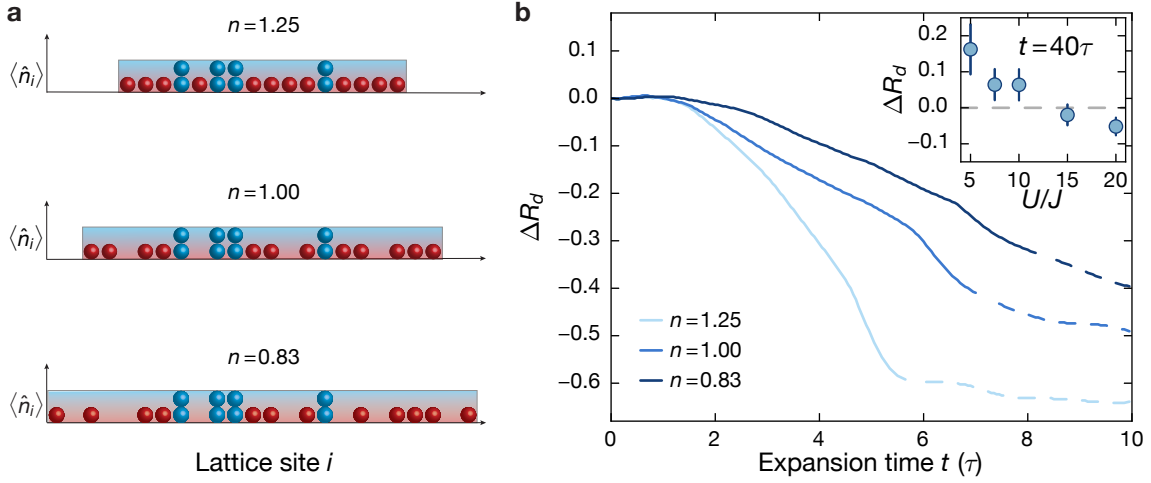


Figure 3.4.: tDMRG results for the relative doublon cloud size. **a** Initial states of singlons and doublons in a box trap with a different number of holons, resulting in a different average filling n . The displayed absolute number of singlons, doublons and holes is chosen according to the numerical simulations, display in (b). The initial state consists of 12 singlons, 4 doublons and $\{0, 4, 8\}$ holons, respectively. **b** Relative change in doublon cloud size $\Delta R_d(t)$ for three different initial uniform densities n as indicated in (a) at $U/J = 20$. The solid lines end at time t_{\max} , when the width of the singlon cloud increased to $\Delta R_s = 0.8$. This value corresponds to the experimental one at $t = 40\tau$. Inset: Experimental data for ΔR_d as a function of the interaction strength at $t = 40\tau$, which was evaluated using linear fits to the time traces $R_d(t)$ as shown in Fig. 3.1. Numerical simulations are done by Jacek Herbrych and Jan Stolpp [169].

the relative change of the doublon cloud size $\Delta R_d(t)$ as a function of time for the different average initial densities n . Negative values of ΔR_d indicate a shrinking of the doublon cloud, while $\Delta R_d > 0$ corresponds to an expanding doublon cloud. For the initial state with the largest density $n = 1.25$, we observe a large decrease of $\Delta R_d(t)$.

This effect is substantially reduced for smaller densities (Fig. 3.4b) due to the presence of holons, which remain trapped between doublons on the time scales of the quantum distillation process [171]. The reason is that exchanging the position of a doublon and a holon can only happen via a second order tunneling process, scaling with $2J^2/U$, as opposed to the quantum distillation mechanism, which is first order in J . Additionally, the dynamics becomes slower, both due to holons and due to the larger cloud sizes used for simulations with smaller average densities [171]. The time scale to complete the phase separation between singlons and doublons can be estimated by the width of the cloud and the expansion velocity of the singlons. The larger the cloud, the more time is necessary in order for the expanding singlons to move from the center through the whole doublon cloud and to complete the quantum distillation process. Therefore, we expect that increasing the cloud size results in a larger transient time scale at which the doublon cloud

contraction occurs. Despite these quantitative differences to the ideal scenario without holons, we find that the fundamental aspect of quantum distillation, i.e., the dynamical phase separation of singlons and doublons, is generally robust.

As reference for the numerically observed contraction, the inset in Fig. 3.4b shows the experimentally measured relative changes ΔR_d as a function of interaction strength, which are obtained in Sec. 3.1.3 from linear fits to the time traces of the doublon HWHM to calculate ΔR_d at the maximum expansion time $t = 40\tau$. We observe that $\Delta R_d(40\tau)$ approaches zero with increasing interaction strength and becomes slightly negative at $U/J = 20$. However, even the numerical traces with the lowest average initial density shows a larger contraction than experimentally observed at $U = 20J$.

In order to better understand this remaining difference between theory and experiment, we reconcile that the contraction of the doublon cloud is a transient effect, which can only occur during the phase separation between singlons and doublons. Once both clouds are spatially separated, doublon dynamics towards the center of the cloud cannot be mediated. The time scale of this separation depends on both the extend of the doublon cloud and the singlon velocity and is therefore system size dependent. The system sizes and particle numbers in the numerical simulations are very different from the experimental setup. While the initial state, realized in the experiment, has a width of approximately 90 lattice sites (this is the FWHM, see Fig. 3.1), numerically simulated initial states have at most width of 22 lattice sites for the largest fraction of holons (Fig. 3.4). Thus, we expect differences between experiment and numerics for the time scale at which quantum distillation is completed. In order to facilitate a comparison between experiment and numerics, we define a time t_{\max} for the simulation at which the relative singlon cloud size ΔR_s has reached the same value as in the experiment according to Fig. 3.4. The numerical results indicate that the contraction is not completed at this time for all fillings considered in Fig. 3.4. Furthermore, in the experiment, we expect an average filling of $n \leq 0.9$ (Sec. 2.2.1), which is best reproduced by the numerical trace for filling $n = 0.83$, which indicates a pronounced shrinking for $t > t_{\max}$. In the experiment, however, this time is limited by the degree of flatness of the homogeneous potential. Extending the experiment to larger expansion times would result in back reflections of the expanding singlons from the potential walls and therefore complicate the analysis. The remaining difference between the numerical and experimental results is most likely due to other initial-state properties, such as inhomogeneous density distributions and the averaging over several 1D systems with different initial-state properties (Sec. 3.1.2).

3.1.5. Generating low entropy states with quantum distillation

Quantum distillation in the strong regime can in the ideal case lead to a remarkable decrease of the entropy per particle in the center of the cloud, where the doublon core accumulates [170]. The entropy is proportional to the logarithm of the number of microstates [184], which is equivalent to the number of possible configurations of atoms in the atomic limit [167], where quantum distillation typically occurs. A pure doublon core without singlons and without holes, i.e. a pure bandinsulating state, has only one possible configuration resulting in zero entropy. Indeed the entanglement entropy was numerically found to asymptote towards zero for suitable initial states, which generate ideal doublon cores [170]. The total entropy of the initial state is of course conserved and clearly non-zero for initial product states consisting of a mixture of singlons and doublons. The entropy is carried away, by the expanding singlons and their spin-degree of freedom, thus quantum distillation appears to be a feasible mechanism to locally engineer very low entropy states. Yet, including experimental imperfections such as empty sites in the initial state, compromises the achievable purity of the band-insulator since these holes remain trapped between doublons and lower the density of the doublon core (Sec. 1.3.2). This results in more available microstates and a less efficient entropy reduction. We conclude that strong quantum distillation offers a feasible possibility to create low entropy states, but it requires very fine-tuned and clean initial states which are experimentally not easy to realize. Besides quantum distillation, many other methods have been proposed to reach colder temperatures in the Fermi-Hubbard model [185–187]. Additionally, generating low entropy states has been an ongoing effort in experiments with ultra-cold atoms [188] to reach out closer to the ground state of the Fermi-Hubbard model and realize long-range antiferromagnetic spin-correlations [188]. Thus, it will be an important task for future experiments to benchmark the feasibility of the different methods to probe new physics at lower temperatures.

3.2. Asymptotic expansion velocity

3.2.1. Second moment of the density distribution

In this second part we focus on experimental results with sudden expansion measurements using initial product states, which consist of a negligible doublon fraction ($n_d < 0.05$), as opposed to the previous chapter on quantum distillation. We analyse the effect of different interaction strengths on the expansion dynamics of the cloud and characterize the width of the cloud by extracting the cloud radius r from the second moment r^2 of the density distribution

$$r^2 = \sum_l \rho_l (l - l_c)^2 \cdot 8.3^2 d^2. \quad (3.2)$$

Here, ρ_l is the normalized optical density at pixel l with distance $|l - l_c|$ from the central pixel l_c of the 1D integrated line densities and the factor 8.3 converts pixels to lattice sites in units of the lattice spacing d . The sum runs over the whole cloud and convergence is ensured once the distance from the center is large enough (Fig. 3.5a). The second moment has a couple of advantages compared to characterizing the density distribution with the HWHM, used for R_d and R_s in Sec. 3.1. First, it simplifies a quantitative comparison between experimental data and theory, where it is routinely computed in numerical simulations [162–164]. Second, it is less affected by details of the density distribution than R_d and R_s , since it takes into account the density of the whole cloud and not only the height of the cloud at a chosen width. This, however, leaves it more susceptible to noise, which is amplified with the squared distance from the center and which could potentially compromise the convergence of the sum in Eq. 3.2. For this reason we refrain from an analysis in terms of the second moment, when studying doublon clouds, which intrinsically are more susceptible to noise due to the occupation number resolved imaging (see Sec. 2.2.2).

We extract the second moment r^2 from the density distribution by subtracting the background from the raw integrated line densities before summing over the integrated line densities of the cloud from the center outwards, until r^2 saturates. Finally, the cloud size r is defined as $r = \sqrt{r^2}$. In Fig. 3.5a we demonstrate this analysis for the cloud size of the initial state at $t = 0$ and for a final state after an expansion time $t = 40\tau$ at interaction strength $U = 5J$. The truncated cloud size r_i increases as long as the summation takes place within a region with finite optical density, as indicated by the shaded red area. Once the optical density drops to zero far enough away from the center of the cloud, r_i converges to the cloud size r . The stability of the cloud size far away from the center of the cloud highlights, that the analysis is not compromised by noise and ensures a reliable extraction of r .

Exemplary time traces of the cloud size are shown in Fig. 3.5b for both $U = 5J$ and $U = 20J$. We find a monotonously increasing cloud size, which approximately doubles in size after an expansion time $t = 40\tau$ for both interaction strengths. Additionally, the cloud size seems to indicate an accelerated expansion initially, while at late times, the slope becomes constant. Note, however, that in our case the cloud initially has a Gaussian density distribution and this results in a convolution of the expansion dynamics with the initial cloud size (Sec. 1.1.3). Since even in the interacting case we expect qualitatively similar dynamics as in the non-interacting gas for large enough expansion times (Sec. 1.2.1), we

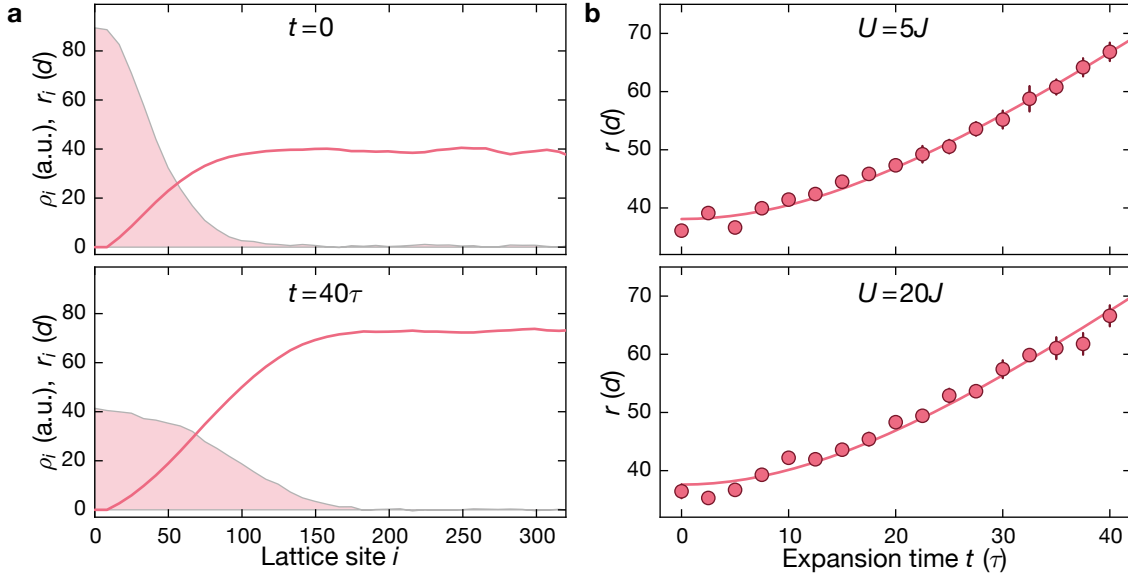


Figure 3.5.: Extraction of the cloud size r . (a) Density distribution ρ_i (red shaded area) and truncated cloud size r_i (solid line) as a function of the lattice site i measured at $U = 5J$ and $t = 0$ (upper panel) and $t = 40\tau$ (lower panel). The truncated cloud size r_i is defined as $r_i = \sqrt{\sum_{j=0}^i \rho_j^2 d^2}$, such that the sum is truncated at lattice site i . Note, that the lattice sites are binned in groups, since we use a factor of 8.3 to convert pixels to lattice sites. The cloud size r is extracted as average of r_i over five points equally spaced between lattice site 200 and 330 at large distance from the cloud center, where r_i saturates, such that r_i^2 is equivalent to the second moment of the density distribution. (b) Exemplary time traces of the cloud size r for $U = 5J$ (upper panel) and for $U = 20J$ (lower panel). Solid lines are fits to the time traces to extract the radial velocities. The cloud size at every time step is averaged over five measurements and error bars denote the standard-error-of-the-mean.

fit the cloud size with a similar expression as we obtain for the non-interacting dynamics (Sec. 1.1.3), i.e. we use $r = \sqrt{r_0^2 + v_r^2 t^2}$, where r_0 is the initial cloud size.

3.2.2. Interaction dependence of radial velocities

In the previous section, we extracted the radial velocity v_r with a fit to time traces of the cloud size r in Fig. 3.5. Next, we study how the radial velocity v_r is modified in the presence of interactions. In Fig. 3.6 we find $v_r = 1.40(6) d/\tau$ for $U = 0$ and $U = 20J$, whereas for intermediate interactions $U \sim 3J$, the radial velocity decreases weakly. Note, that for $U \gg W$, the mass transport in the one-dimensional Fermi-Hubbard model in the absence of doublons in the initial state becomes identical to a non-interacting gas of spinless fermions (Sec.1.2.3), which is known to expand ballistically with velocity $v_r = \sqrt{2} d/\tau$ (Sec.1.1.1). The experimental data agrees well with these theoretical predictions in the

limiting cases of free fermions expanding from our initial state. A comparison to the one-dimensional Bose-Hubbard model, studied separately [50], reveals that in these limits the radial velocities are the same for both models, in agreement with the theoretical prediction that the mass transport of hardcore bosons in 1D can be mapped onto spinless fermions and is therefore equivalent to the non-interacting limit with $v_r = \sqrt{2}d/\tau$. Remarkably, compared to the Bose-Hubbard model, the reduction of v_r at intermediate interaction strengths is much weaker in the Fermi-Hubbard model (Fig. 3.6).

Starting from the limit of very strong interactions, the interaction dependence of v_r can be understood in a two-component picture of independent singlon and doublon gases [174, 189]. Note, that even though the initial state is free of doublons, these will be created in the quench, which initializes the expansion experiment. In our experiments (Sec. 2.1.1), the expansion begins with rapidly lowering the lattice depth of the short lattice, which correspond to a quench from very large U/J to the set U/J during the expansion. Additionally, the flat potential is optimized for the lattice laser power corresponding to the lattice depth during expansion and this results in an additional quench of the confinement when decreasing the lattice depth. The excess energy of these two quenches results in a highly excited far-from-equilibrium state which consists of dynamically generated doublons. These doublons can undergo a quantum distillation mechanism and are then inert on the time scales of the experiment. Thus, the more doublons are generated, the less kinetic energy is available for the rapidly expanding singlons.

Focusing on the quantitative difference between the $v_r(U)$ curves for bosons and fermions two aspects are important. First, in the case of fermions, doublons can only be generated between sites with fermions of different spin orientation [162]. The initial state that has the most of such $\uparrow\downarrow$ neighbors is the Néel state, and this initial state leads to the most pronounced minimum of v_r (Fig. 3.6, [162]). In order to compare theory and experiment for realistic conditions, we need to average over many 1D systems with random spin orientations for a balanced spin mixture (dark red diamonds in Fig. 3.6). This averaging leads to a weaker minimum in v_r than for the Néel state and is in agreement with our experimental data. The second reason for the stronger minimum in v_r for bosons is the fact that the interaction energy can become much larger, since larger local occupancies are possible [50] because of the bosonic statistics. The effect of the interaction energy bound in doublons on the radial expansion velocity is studied theoretically in Sec.1.3.3. It indeed shows that an increasing interaction energy is correlated with a decreasing expansion velocity. Moreover, the interaction energies for bosons lie well outside the accessible range of interaction energies for fermions because of higher site occupations, but fall onto an extrapolation of the fermionic data.

The reduced expansion velocity at intermediate interaction strengths with respect to the non-interacting case is an indication for diffusive transport in both the Bose-Hubbard and

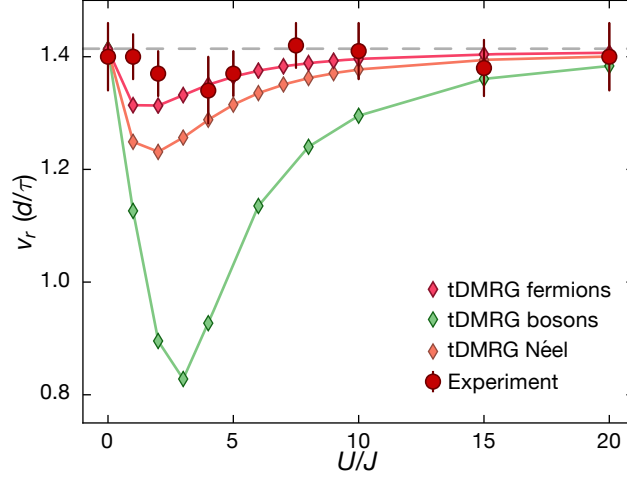


Figure 3.6.: Radial expansion velocities v_r . Experiment (circles) and tDMRG simulations for fermions (red dark-shaded diamonds) and bosons (green light-shaded diamonds, from [50]) as a function of U/J . Solid lines are guides to the eye. The grey dashed line indicates $v_r = \sqrt{2} d/\tau$ in the limiting cases $U/J = 0$ and $U/J \rightarrow \infty$. All initial states in the numerical simulations have a uniform average density of $n = 1$ in a box with initial size $L_{\text{init}} = 10$. Numerical simulations are done by Jacek Herbrych and Jan Stolpp [169].

the Fermi-Hubbard model according to the classification in Sec. 1.2.1. The emergence of diffusive mass transport in this regime seems to be well explained by the interaction energy generated in the quench. Hence, the integrability of the one-dimensional Fermi-Hubbard model, which might hint towards ballistic dynamics for all interactions in the Fermi-Hubbard model, does not seem to be the dominant reason for the differences to the non-integrable bosonic counterpart. Rather, the statistics of the particles seem to be crucial to understand the dynamics in terms of the interaction energy and the spin-configuration in the case of fermions. The Fermi statistics forbid more than two particles on the same site in the Fermi-Hubbard model and in this way cause its integrability as opposed to the non-intergrable Bose-Hubbard model with unbounded site occupation (Sec. 1.2.2).

3.3. Conclusion and outlook

We investigated the sudden expansion of an interacting cloud of fermions for different kinds of initial product states. Starting with an appreciable doublon fraction, we observed a dynamical phase separation between singlons and doublons, theoretically known as fermionic quantum distillation in the weak regime. The strong regime of fermionic quantum distillation results in a shrinking of the doublon core due to effective doublon

dynamics directed to the center of the cloud, which are mediated by the expanding singlons. While we found evidence for a shrinking doublon cloud at our largest interaction strength, the contraction was small. A careful analysis revealed the importance of the initial state conditions for a discernible contraction of the doublon cloud, which is in our experiment compromised by the presence of empty sites in the initial state, hindering pronounced doublon dynamics towards the center of the cloud.

Additionally, we analyzed the radial velocities of the expanding cloud for different interaction strengths using initial states consisting purely of singlons. We found a decrease of the radial velocities at weak to intermediate interactions and attributed this effect to dynamically generated doublons. The weak decrease of radial velocities for expanding fermions compared to bosons is attributed to the Pauli principle leading to a crucial dependence of the radial velocities on the initial spin configuration. In contrast, the integrability of the one-dimensional Fermi-Hubbard model does not seem to be the dominant reason for the differences to the bosonic case. An interesting extension would be the calculation of expansion velocities by exploiting the integrability similarly as was already done in Ref. [164, 165] for initial ground states, which we leave for future work.

Future experiments could use the singlon and doublon resolved scheme to detect signatures of FFLO states [165, 190, 191] in the expansion velocity of the unpaired spin component. Moreover, observing strong quantum distillation unambiguously might be at reach, if the initial state properties are improved towards fewer empty sites. This could pave the way to study the resulting dynamical formation of low-entropy regions [170]. Furthermore, improving imaging techniques, such as microwave dressing to isolate central 1D systems, might be advantageous as this would enable studying the dynamics, where the conditions for strong quantum distillation are best.

Part II.

Nonergodicity due to kinetic constraints in tilted Fermi-Hubbard chains

Non-ergodic dynamics occurs in integrable [6] and many-body localized systems (MBL) [18–20], where extensively many conservation laws impede the system from thermalizing. Recently, this paradigm was challenged by systems, where non-ergodic dynamics emerges due to Hilbert-space fragmentation (HSF) in the presence of few conservation laws [85–88]. In such systems, the Hilbert space consists of disconnected parts, dubbed fragments, which trap the initial state in an exponentially small part of the total Hilbert space. The tilted 1D Fermi-Hubbard model was predicted at the interface between MBL and HSF. In the presence of harmonic confinement, theoretical studies have found characteristic MBL phenomenology such as a logarithmic growth of the entanglement entropy and a finite steady-state imbalance [98, 99, 104, 192, 193]. In contrast, in the dipole conserving limit of the clean model, HSF is expected to occur [85, 86, 88, 98, 104], showcasing a finite steady-state imbalance and fast entanglement entropy growth towards a plateau related to the fragment [85]. In this part, we study non-ergodic behavior in the tilted 1D Fermi-Hubbard model. Performing an out-of-equilibrium experiment, we track the relaxation dynamics of a charge-density wave, gaining direct information about potential thermalization in the system.

4. Theoretical background

4.1. Dynamics of a single particle in a tilted lattice

4.1.1. Bloch oscillations in real-space: Breathing dynamics

As we found in Sec. 1.1.1, the discrete translational invariance of a lattice has profound consequences for the dynamics of a particle in such a system. The periodicity of the lattice in real space carries over to quasi-momentum space, where it causes a periodic dispersion relation $\epsilon(k)$ in the first Brillouin zone, to which all other momenta can be restricted. In contrast to the unbounded parabolic dispersion of a free particle in the continuum limit, the dynamics in a sufficiently deep lattice are restricted to the ground band and the dispersion relation is bounded from below and above. This limits the kinetic energy ϵ_{kin} of a particle to the bandwidth $\min[\epsilon(k)] \leq \epsilon_{\text{kin}} \leq \max[\epsilon(k)]$ of the dispersion relation. A system which illustrates the consequences of such a bounded kinetic energy in a very striking way is the so-called "tilted lattice", i.e. a superposition of a lattice potential and a linear potential. What dynamics can we expect for a particle, initialized on one site of such a tilted lattice? Naively, one might anticipate the particle to simply "hop down" the lattice, similar to a classical particle rolling down an inclined plane and in principle converting an unbounded amount of potential energy into kinetic energy during its descent. In quantum mechanics a particle in a tilted lattice, however, can only pick up a bounded amount of kinetic energy and in such a system the dynamics are oscillatory. The so-called Bloch oscillations have been observed both in real space and momentum space, within many different systems [102, 103, 194–199]. Here, we focus on the real space dynamics and consider the limit of a large band gap, such that even in the presence of an additional energy scale, set by the tilt, the ground band is well separated from higher bands, which can therefore be neglected. We assume a single particle in a periodic potential similar to Sec. 1.1.1 and superimpose a linear potential to the Hamiltonian

$$\hat{H}_{WS} = -J \sum_{i=-L/2}^{L/2} \left(\hat{c}_i^\dagger \hat{c}_{i+1} + \hat{c}_{i+1}^\dagger \hat{c}_i \right) + \Delta \sum_{i=-L/2}^{L/2} i \hat{n}_i. \quad (4.1)$$

4. Theoretical background

Here, \hat{c}_i^\dagger (\hat{c}_i) is the creation (annihilation) operator of a spinless fermion on site i , $\hat{n}_i = \hat{c}_i^\dagger \hat{c}_i$ is the number operator, J is the tunneling rate between neighboring sites, Δ sets the energy difference between neighboring sites due to the tilt and L is the number of sites. When studying the Wannier-Stark Hamiltonian, it is convenient to transform the operator \hat{c}_i^\dagger from the Wannier basis into an operator $\hat{\beta}_j^\dagger$ in the Wannier-Stark basis, which is defined according to the relation

$$\hat{\beta}_j^\dagger = \sum_{i=-L/2}^{L/2} \mathcal{J}_{i-j} \left(\frac{2J}{\Delta} \right) \hat{c}_i^\dagger. \quad (4.2)$$

Here, we introduce $\mathcal{J}_l(x)$, corresponding to the l^{th} -order Bessel function of the first kind. Each Wannier-Stark operator $\hat{\beta}_j^\dagger$ shares its center-of-mass with the Wannier operator $\hat{c}_{i=j}^\dagger$ and has a super-exponentially decreasing overlap with Wannier operators $\hat{c}_{|i-j|}^\dagger$ at distance $|i-j|$. This rapid decrease can be inferred from an asymptotic expansion of the higher order Bessel functions of the first kind according to $\mathcal{J}_l(x) \approx \frac{(x/2)^l}{l!}$, in the limit $0 < x \ll \sqrt{l+1}$ for $l \in \mathbb{N}$. This expansion also applies to negative orders of the Bessel function, when using the identity $\mathcal{J}_{-l}(x) = (-1)^l \mathcal{J}_l(x)$. This shows, that a Wannier-Stark state is localized within a certain number of lattice sites, determined by the ratio J/Δ and emphasizes the locality in real-space of the basis transformation in Eq. (4.2). Therefore, for any argument x , there exists an l_x such that $\mathcal{J}_l(x) \approx 0$ for $l > l_x$. Usually, $l_x \approx \pm 2J/\Delta$ is a good approximation, i.e. the index of the Bessel function needs to be smaller than its argument [200]. This motivates the definition of the width A of a Wannier-Stark state according to $A = 2l_x d = 4Jd/\Delta$ (A is benchmarked with Wannier-Stark states in Sec. 4.1.4). Here, d is the lattice constant and A is equivalent to the Bloch oscillation amplitude, as will be explained in Fig. 4.1a. Thus, a Wannier-Stark operator can be understood as a dressed Wannier operator for large Δ/J and the two basis sets become equivalent in the limit $\Delta/J \rightarrow \infty$. The Wannier-Stark Hamiltonian is diagonal in the Wannier-Stark basis

$$\hat{H}'_{\text{WS}} = \Delta \sum_{j=-L/2}^{L/2} j \hat{\beta}_j^\dagger \hat{\beta}_j \quad (4.3)$$

The spectrum of the Wannier-Stark Hamiltonian consists of integer multiples of the tilt Δ , forming the so-called Wannier-Stark ladder. The locality of the Wannier-Stark operators hints towards the dynamics we anticipate for the time evolution of a wave packet in real space, initialized in a Wannier state. Such a state has a finite overlap with only the Wannier-Stark states within the localization length, because of the super-exponential decrease of the overlap at large enough distance from the center of mass. Thus, we expect localized dynamics of the wave packet, which time-evolves according to a superposition of few Wannier-Stark states and their respective dynamical phases, encoding the discrete

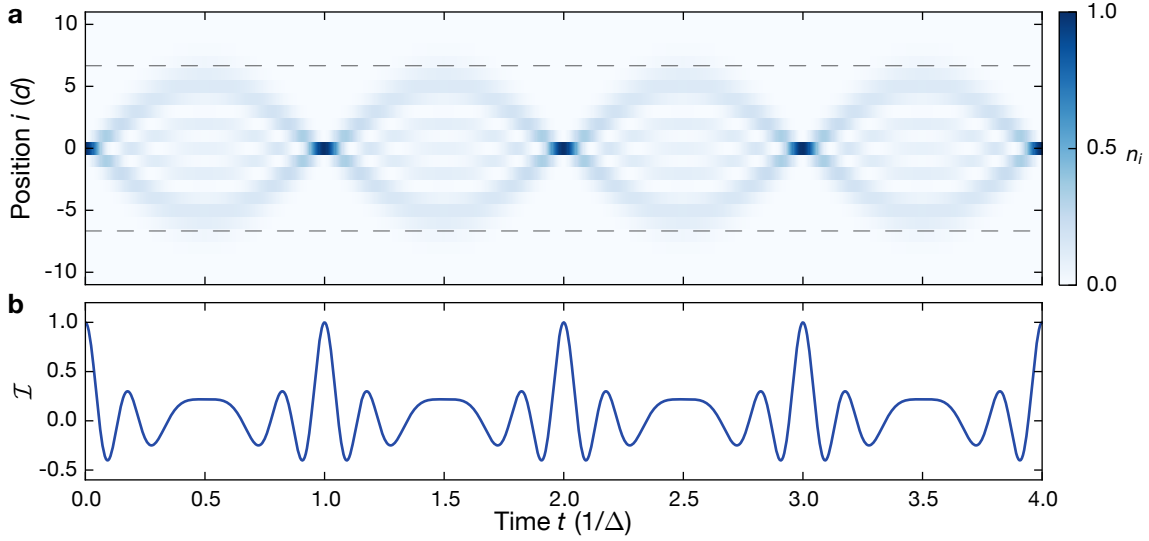


Figure 4.1.: Breathing dynamics of real space Bloch oscillations. **a** Dynamics of the on-site probability density n_i of a particle initialized in the center of the lattice on site $i = 0$ according to Eq. (4.4). The particle exhibits a breathing mode with amplitude $A = 4Jd/\Delta$, which is indicated by the dashed horizontal lines. We use $\Delta/J = 0.6$ and d is the lattice constant. **b** Imbalance time trace resulting from the breathing dynamics for the same parameters as in (a).

set of equally spaced energies. The probability density n_i of finding a wave packet after time t on site i , when initializing it in a Wannier state $|i = 0\rangle$ in the center of the lattice, can be calculated analytically and we obtain

$$n_i(t) = \mathcal{J}_i^2 \left(\frac{4J}{\Delta} \sin \left(\frac{\pi \Delta t}{h} \right) \right), \quad (4.4)$$

where h is Planck's constant. The corresponding dynamics are referred to as real space Bloch oscillations and exhibit a periodic breathing motion, characterized by a mean displacement $\langle \hat{x} \rangle = 0$ and an oscillatory variance $\Delta \hat{x}^2 = \langle \hat{x}^2 \rangle - \langle \hat{x} \rangle^2 \neq 0$ as illustrated in Fig. 4.1a. The time scale of the periodic dynamics is set by the tilt Δ and their breathing amplitude [200] can be determined approximately by the Bloch oscillation amplitude $A = 4Jd/\Delta$ (see dashed lines in Fig. 4.1a), which we already used to define the width of a Wannier-Stark state. In general, Bloch oscillations exhibit a rich variety of dynamics, which depends on the initial occupation in momentum space. If the dynamics are initialized in a Wannier state, delocalized in momentum space, we find Bloch oscillations with a breathing mode. In contrast, starting from an initial state, localized in momentum space, i.e. a Bloch wave, the dynamics exhibit an oscillatory mode with zero variance $\Delta \hat{x}^2 = 0$ and oscillating mean displacement $\langle \hat{x} \rangle \neq 0$.

4.1.2. Imbalance: A local probe of real-space Bloch oscillations

The on-site probability density n_i is an observable, well-suited for illustrating the periodic breathing dynamics determined by the tilt Δ . Yet, we also expect higher harmonics of Δ to be relevant for the dynamics due to the spectrum of the Wannier-Stark Hamiltonian in Eq. (4.3). Arguably, these higher harmonics are not obvious in the probability density n_i . Hence, we define the parity-projected on-site occupation of the wave packet as additional observable, which can be understood as the imbalance \mathcal{I} between the probability densities on even and odd sites

$$\mathcal{I}(t) = \sum_{i=-L/2}^{L/2} (-1)^i n_i(t) = \mathcal{J}_0 \left(\frac{8J}{\Delta} \sin \left(\frac{\pi \Delta t}{h} \right) \right). \quad (4.5)$$

In order to study the effect of the breathing dynamics on the imbalance, we compare a time trace of the imbalance \mathcal{I} with the on-site density n_i in Fig. 4.1. The dynamics observed in the imbalance show the same periodicity as the breathing dynamics of the probability density and the breathing amplitude A manifests itself in additional oscillations within one Bloch cycle of the imbalance (Fig. 4.1b).

These additional oscillations, resulting from probing the real space dynamics in a parity-projected manner, are studied in detail in Fig. 4.2a for different ratios Δ/J . Indeed, the oscillations within one Bloch cycle depend on the Bloch oscillation amplitude $A = 4Jd/\Delta$ and hence on the extent of the real space breathing dynamics. For a small $A \approx d$ at a tilt $\Delta/J = 5$, we observe a clean sinusoidal oscillation. Increasing the Bloch oscillation amplitude up to $A = 6.7d$ by decreasing the tilt to $\Delta/J = 0.6$ clearly results in rich additional oscillations (left and center panel of Fig. 4.2a). Furthermore, we clearly witness that the time-averaged mean imbalance $\bar{\mathcal{I}} = \Delta \int_0^{1/\Delta} \mathcal{I} dt$ within one Bloch cycle seems to depend on the tilt (dashed horizontal lines in Fig. 4.2a). For $\Delta/J = 0.6$, it is approximately zero, whereas for large tilt $\Delta/J = 5$ the mean imbalance of the sinusoidal oscillation is clearly non-zero, hinting towards the strongly localized dynamics, which we expect in the limit of large tilt (Sec. 4.1.4).

To better understand the oscillatory dynamics, we perform a Fourier transform \mathcal{F} of the imbalance time traces and define $\tilde{\mathcal{I}}(\nu) = \mathcal{F}[\mathcal{I}(t)]$. In Fig. 4.2b the power spectral density of the imbalance $|\tilde{\mathcal{I}}(\nu)|^2$, normalized to the dominant frequency component, is displayed for three different Bloch oscillation amplitudes. The frequency components in all spectra are always integer multiples of the tilt Δ , which is a direct consequence of the spectrum of the Hamiltonian, exhibiting eigenenergies according to the Wannier-Stark ladder. The number of frequency components is directly related to the Bloch oscillation amplitude $A = 4Jd/\Delta$. While for small tilt $\Delta/J = 0.6$ and large Bloch oscillation amplitude

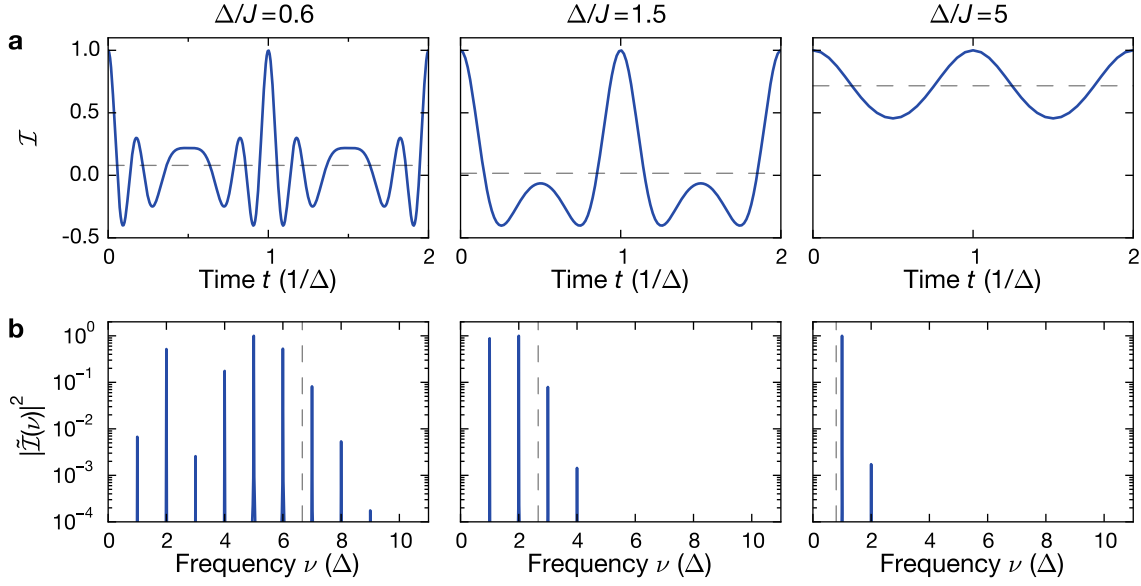


Figure 4.2.: Real-space Bloch oscillations probed in a parity-projected manner. Coherent dynamics of the imbalance for three different tilts Δ in units of the tunneling rate J : $\Delta/J = 0.6$ (left column), $\Delta/J = 1.5$ (center column), $\Delta/J = 5$ (right column). **a** Imbalance time traces $\mathcal{I}(t)$ for the corresponding parameters according to Eq. (4.5). The time-averaged mean imbalance $\bar{\mathcal{I}} = \Delta \int_0^{1/\Delta} \mathcal{I} dt$ within one Bloch cycle is indicated by the horizontal dashed lines. **b** Power spectral density of the imbalance $|\tilde{\mathcal{I}}(\nu)|^2$. Each spectrum is normalized to the respective dominant frequency and calculated with a discrete Fourier transform of the analytic time traces. The dashed lines show the Bloch oscillation amplitude in units of the lattice constant A/d .

$A = 6.7d$ many higher harmonics are present in the frequency spectrum, we recover a single-frequency oscillation for large tilts $\Delta/J > 5$.

The dimensionless Bloch oscillation amplitude A/d can be understood as a measure for the width of a Wannier-Stark state (Sec. 4.1.1) and should in that way also capture the number of Wannier-Stark states, overlapping with the initial Wannier state. Thus, we expect that the number of higher harmonics of the tilt Δ , contributing to the dynamics according to Eq. (4.3), is related to the dimensionless Bloch oscillation amplitude A/d . In Fig. 4.2b we compare the maximal number of higher harmonics in the frequency spectrum to A/d , which is indicated as a dashed line. For all tilts the Bloch oscillation amplitude approximates the number of higher harmonics reasonably well, when rounded to an integer, discarding only few higher-order harmonics in all cases. Note, the logarithmic scale in Fig. 4.2b, which emphasizes an exponential suppression of these higher-order components.

4.1.3. Collapse and revival of Bloch oscillations in a harmonic trap

While the preceding discussion applies to an ideal system, our experiment inevitably adds imperfections such as an external harmonic confinement due to the inhomogeneous spatial profile of the laser beams (see Sec. 2.3). Thus, at this point we study Bloch oscillations in the presence of a harmonic confinement with energy scale α that we include in the Wannier-Stark Hamiltonian in a similar manner as it was introduced in Eq. (1.7) for a free particle on a lattice in Sec. 1.1.2:

$$\hat{H}_{\text{WS}}^\alpha = -J \sum_{i=-L/2}^{L/2} \left(\hat{c}_i^\dagger \hat{c}_{i+1} + \hat{c}_{i+1}^\dagger \hat{c}_i \right) + \Delta \sum_{i=-L/2}^{L/2} i \hat{n}_i + \alpha \sum_{i=-L/2}^{L/2} i^2 \hat{n}_i. \quad (4.6)$$

In the presence of a tilt the dynamics are localized. Thus, boundary effects, such as a reduced expansion speed of a delocalized cloud of atoms at large enough evolution times (see Fig. 1.2) are absent. However, the harmonic confinement can also modify localized dynamics, since it can be understood as a quadratic correction term to the linear potential, which results in an inhomogeneous site-dependent tilt $\Delta_\alpha(i) = \Delta + 2\alpha i$ within the system. For our setup (see Sec. 6.1.2), we work in a parameter regime, where the local curvature is negligible compared to the tilt ($\alpha \ll \Delta$). Hence, the localized dynamics of each atom can be well described without harmonic confinement. In contrast, our observable, the imbalance, probes the dynamics globally, i.e. the dynamics are averaged over all atoms within the one-dimensional system. In the local density approximation the observed Bloch oscillation in such a system with harmonic confinement can be understood as a sum of Bloch oscillations with frequencies ranging between $\Delta - 2\alpha L/2$ and $\Delta + 2\alpha L/2$ with a step of 2α and a system size of L sites. Note, the scaling with system size, which enhances the effect of α for global probes. In order to understand the result of such a sum, we consider for instance a sum of sinusoidal oscillations

$$\sum_{i=-L/2}^{L/2} \cos(2\pi(\Delta + 2\alpha i)t) = \cos(2\pi\Delta t) \frac{\sin(2\pi(L+1)\alpha t)}{\sin(2\pi\alpha t)}. \quad (4.7)$$

This is an oscillation at frequency Δ together with an amplitude modulation with a beat note envelope at a frequency $(L+1)\alpha \approx L\alpha$ and nodes at $1/(2L\alpha)$. At large enough tilt, the Bessel-type Bloch oscillations are similar to sinusoidal oscillations and expected to behave in a qualitatively similar manner. Therefore, we anticipate a collapse at time $T_c \approx 1/(2L\alpha)$. In Fig. 4.3, we show a numerical simulation of Bloch oscillations in the presence of a harmonic confinement up to long evolution times. Indeed, we observe an envelope of the Bloch oscillations, which results in an initial damping with a time scale set by T_c (left inset in Fig. 4.3). The initial collapse is followed by a set of small revivals,

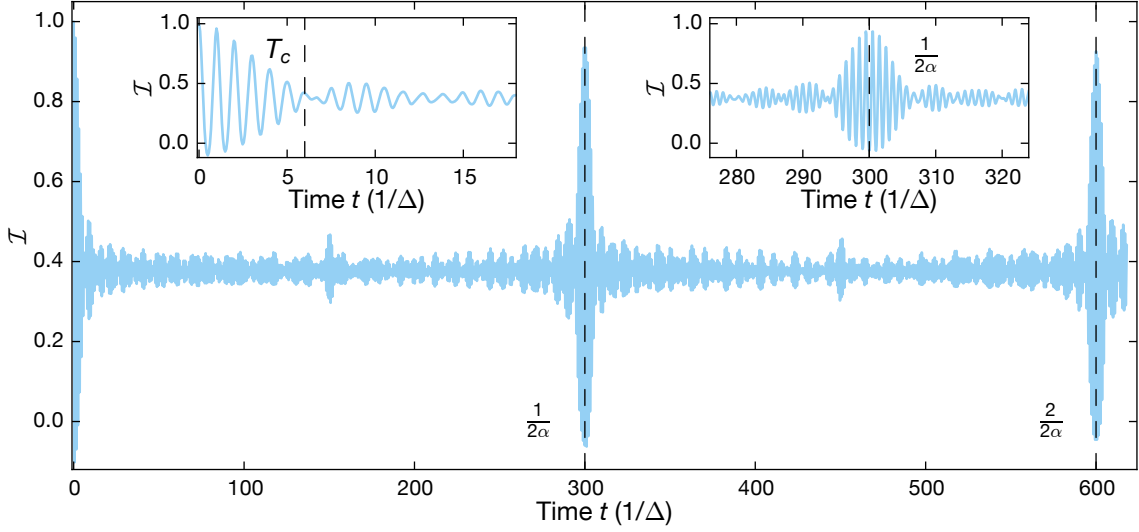


Figure 4.3.: Bloch oscillations in the presence of harmonic confinement. Numerical simulation of the imbalance in a system with size $L = 50$ for $J/\Delta = 1/3$ and $\alpha/\Delta = 1/600$. The carrier oscillation frequency is set by Δ as indicated in the two insets, which also show the beat note envelope with characteristic collapse time $T_c = 6/\Delta$, depicted by the dashed line in the left inset. The main plot shows super-revivals with $\mathcal{I}(t_\alpha) \simeq \mathcal{I}(t = 0)$ at $t_\alpha = n/(2\alpha)$, $n \in \mathbb{N}$, indicated by the dashed lines.

confirming the intuition of the beat note envelope, albeit the nodes are not located precisely at integer multiples of T_c . Surprisingly, the imbalance exhibits a super-revival back to the initial imbalance equal to one for late times (right inset in Fig. 4.3). These super-revivals correspond to maxima in Eq. (4.7) at times $t_\alpha = n/(2\alpha)$, $n \in \mathbb{N}$, where both the numerator and the denominator are equal to zero such that the limit needs to be inferred with l'Hôpital's rule. Indeed, the first two super-revivals shown in Fig. 4.3 are in agreement with this prediction. Physically, the super-revival corresponds to a rephasing of the Bloch oscillations, occurring at slightly different frequencies $\Delta_\alpha(i)$ according to the site i of the lattice. At times t_α , the time-evolving dynamical phases agree with each other on all sites of the lattice and are equal to the initial phase, when the dynamics were started, resulting in an imbalance equal to one.

4.1.4. Wannier-Stark localization: Imbalance of a Wannier-Stark state

In Fig. 4.3 we find that the imbalance time trace not only exhibits coherent dynamics, but also seemingly oscillates around a non-zero mean imbalance, similar to Fig. 4.2a. This becomes particularly obvious in between the super-revivals, where the oscillation

4. Theoretical background

amplitude is small. A non-zero mean imbalance is expected for large tilt, since in this regime, the particle is localized in the vicinity of its initial site. A physical interpretation of the mean imbalance can be obtained, when discussing the effect of noise on the coherent dynamics of the imbalance. While the imbalance maintains coherent oscillations even in the presence of harmonic confinement, this is an unrealistic scenario in any experiment, where any kind of noise eventually dephases the coherent dynamics. Therefore, a constant steady-state imbalance is expected to emerge that is potentially related to the mean imbalance $\bar{\mathcal{I}}$. Understanding the dephasing dynamics is very challenging, for it requires a good understanding of the origin of the noise and how it couples to the system.

In contrast, a rather simple and convenient approach is to consider the long-time limit of the dynamics in the density-matrix formalism. Here, detailed knowledge of the noise processes is not necessary since the noise-induced dephasing is captured empirically by setting all off-diagonal density matrix elements in the eigenbasis of the Hamiltonian to zero. This is equivalent to artificially destroying all coherences in the system and such a density matrix is called a diagonal ensemble. It can be understood as a time average of the density matrix of the initial state, since the dynamical phase factors on the off-diagonal density matrix elements average to zero. We illustrate this technique by calculating the steady-state imbalance of a wave packet initiated in the Wannier state $|i\rangle$, which evolves under the Hamiltonian \hat{H}_{WS} described in Eq. (4.1). The diagonal density matrix $\hat{\rho}$ of the initial state is described in terms of the Wannier-Stark states $|\beta_i\rangle$ of Hamiltonian \hat{H}_{WS}

$$\hat{\rho}^{\text{diag}} = \sum_{j \in \mathbb{Z}} |\beta_j\rangle\langle\beta_j| |\langle\beta_j|i\rangle|^2. \quad (4.8)$$

The imbalance operator $\hat{\mathcal{I}}$ is defined in terms of the Wannier basis states $|l\rangle$

$$\hat{\mathcal{I}} = \sum_{l \in \mathbb{Z}} |l\rangle\langle l| (-1)^l. \quad (4.9)$$

We evaluate the steady-state imbalance \mathcal{I}^∞ , which is the expectation value of the imbalance operator $\hat{\mathcal{I}}$ with respect to the diagonal density matrix $\hat{\rho}^{\text{diag}}$:

$$\begin{aligned}
 \mathcal{I}^\infty &= \text{tr} \left(\hat{\rho}^{\text{diag}} \hat{\mathcal{I}} \right) = \text{tr} \left(\sum_{j,l \in \mathbb{Z}} |\beta_j\rangle \langle \beta_j| |\langle \beta_j | i \rangle|^2 |l\rangle \langle l| (-1)^l \right) = \\
 &= \sum_{j,l \in \mathbb{Z}} |\langle \beta_j | l \rangle|^2 |\langle \beta_j | i \rangle|^2 (-1)^l = \sum_{j,l \in \mathbb{Z}} \mathcal{J}_{j-l}^2 \left(\frac{2J}{\Delta} \right) \mathcal{J}_{j-i}^2 \left(\frac{2J}{\Delta} \right) (-1)^l = \\
 &= (-1)^i \sum_{j \in \mathbb{Z}} \mathcal{J}_j^2 \left(\frac{2J}{\Delta} \right) (-1)^j \sum_{l \in \mathbb{Z}} \mathcal{J}_l^2 \left(\frac{2J}{\Delta} \right) (-1)^l = \\
 &= (-1)^i \mathcal{J}_0^2 \left(\frac{4J}{\Delta} \right) = \bar{\mathcal{I}}.
 \end{aligned} \tag{4.10}$$

The sign of the steady-state imbalance encodes, whether the initial state occupies an even or odd site and in the limit of large tilt $\Delta/J \rightarrow \infty$, the steady-state imbalance approaches one ($\mathcal{J}_0(0) = 1$). The last identity emphasizes that the diagonal ensemble ansatz is equivalent to calculating the time-averaged mean imbalance $\bar{\mathcal{I}}$. A convenient interpretation of the steady-state imbalance is found by comparing it to the imbalance $\mathcal{I}_{|\beta_i\rangle}$ of a Wannier-Stark state $|\beta_i\rangle$, i.e. an eigenstate of the Hamiltonian. Note, that all Wannier-Stark states are of the same functional form and can only be distinguished by their respective center of mass. The eigenstate imbalance $\mathcal{I}_{|\beta_i\rangle}$ yields

$$\mathcal{I}_{|\beta_i\rangle} = \sum_{l \in \mathbb{Z}} |\langle l | \beta_i \rangle|^2 (-1)^l = \sum_{l \in \mathbb{Z}} \mathcal{J}_{l-i}^2 \left(\frac{2J}{\Delta} \right) (-1)^l = (-1)^i \mathcal{J}_0 \left(\frac{4J}{\Delta} \right). \tag{4.11}$$

Hence, the steady-state imbalance can be interpreted in terms of the eigenstate imbalance

$$\mathcal{I}^\infty = (-1)^i \mathcal{I}_{|\beta_i\rangle}^2. \tag{4.12}$$

It is proportional to the squared imbalance of an eigenstate of the Hamiltonian \hat{H}_{WS} , underlining the capability of the steady-state imbalance as probe for localization throughout the spectrum. The steady-state imbalance is illustrated in Fig. 4.4. For large Δ/J the eigenstates are localized on a single lattice site and the steady-state imbalance monotonously approaches one with increasing Δ/J . As indicated by the probability distribution of the Wannier-Stark state in the inset of Fig. 4.4, already for $\Delta/J = 5$, the eigenstates are very well localized on a single lattice site only. For small Δ/J the eigenstates are spread out over more than one lattice site and the probability density on even and odd sites sensitively and non-monotonously depends on Δ/J , which is reflected in strong oscillations of the steady-state imbalance with decreasing Δ/J . In Sec. 4.1.1, we find that the width of a Wannier-Stark eigenstate can be approximated by the Bloch oscillation amplitude A and this approximation is well-justified for all parameter regimes considered in the

4. Theoretical background

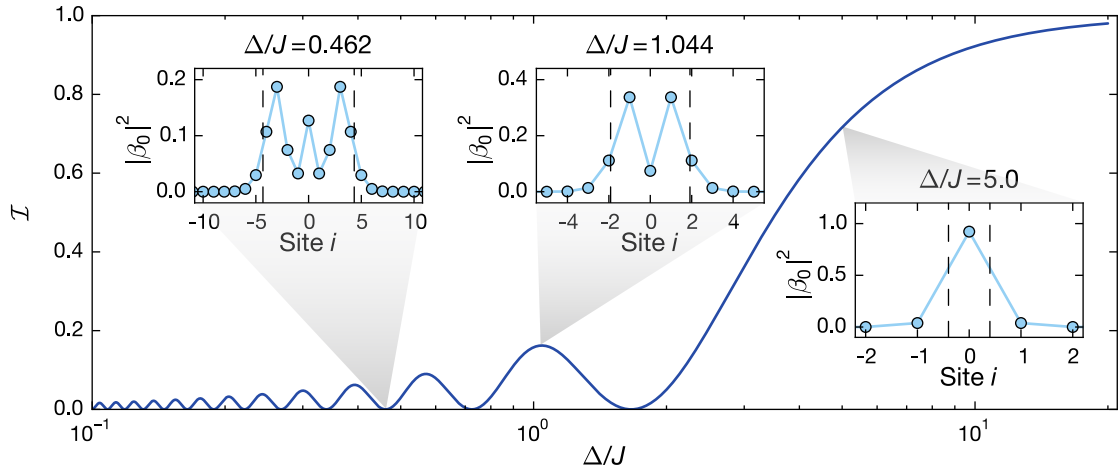


Figure 4.4.: Steady-state imbalance versus tilt. Imbalance \mathcal{I}^∞ of a particle initialized on an even site after all coherent dynamics are dephased according to Eq. (4.10) as a function of the tilt Δ in units of the tunneling rate J . The insets show the probability density $|\beta_0|^2 \equiv |\langle i|\beta_0\rangle|^2$ of finding the Wannier-Stark state $|\beta_0\rangle$ on lattice site i (i.e. Wannier state $|i\rangle$) for different tilts. The vertical dashed lines depict half the Bloch oscillation amplitude in units of the lattice spacing $A/(2d)$.

three insets in Fig. 4.4 as indicated by the dashed lines. While the eigenstates can also have a negative imbalance due to a majority of the probability density on odd sites, the steady-state imbalance cannot be negative. Note, that $\mathcal{I} = 0$ does not necessarily imply delocalized eigenstates, but can also be caused by fine tuned localized eigenstates, which have equal probability density on even and odd lattice sites as indicated by the inset for $\Delta/J = 0.462$. This tilt corresponds to the third root of the zeroth-order Bessel function $\mathcal{J}_0(4J/\Delta) = 0$ and results in an imbalance equal to zero according to Eq. (4.10). In contrast, the corresponding probability distribution of the eigenstate is still localized.

4.1.5. Role of the gauge: tilted lattice versus driven homogeneous lattice

The Hamiltonian \hat{H}_{WS} in Eq. (4.1) does not commute with spatial translations because of the tilted field. Additionally, the tilted field causes the energy to scale super-extensively with system size and results in an unbounded growth of the energy, which complicates a physical interpretation of the thermodynamic limit. An alternative approach to studying the problem of a particle in a tilted lattice can be pursued by using a time-dependent vector potential in the Hamiltonian instead of a linear potential. The equivalence of both approaches is best understood by reconsidering Maxwell's equations of a particle with charge q and mass m in an electromagnetic field. The Hamiltonian, describing the system in the continuum limit, is equal to

$$H(\vec{x}, \vec{p}) = \frac{(\vec{p} - q\vec{A}(\vec{x}, t))^2}{2m} + V(\vec{x}). \quad (4.13)$$

Here, we introduce the vector potential $\vec{A}(\vec{x}, t)$ and the scalar potential $V(\vec{x})$, which can be used to obtain the magnetic field \vec{B} and the electric field \vec{E} :

$$\vec{E}(\vec{x}, t) = -\partial_t \vec{A}(\vec{x}, t) - \vec{\nabla} V(\vec{x}) \quad (4.14)$$

$$\vec{B}(\vec{x}, t) = \vec{\nabla} \times \vec{A}(\vec{x}, t). \quad (4.15)$$

According to Eq. (4.14) a constant electric field E_0 along the x direction can be added to the Hamiltonian in two different ways. On the one hand, we can define a linear potential $V_{\text{field}}(x) = -E_0 x$. On the other hand, we can define a time-dependent vector potential $\vec{A}_{\text{field}}(t) = -E_0 t \hat{e}_x$, which does not depend on x and where \hat{e}_x is the unit vector along the x direction. The second approach results in a different Hamiltonian \hat{H}_A , which is translationally invariant and time-dependent. In our setup, the vector potential is $\vec{A}_{\text{tilt}}(t) = \Delta t / d \hat{e}_x \equiv A_0(t) \hat{e}_x$. It enters the Hamiltonian via the so-called Peierls substitution with a complex hopping amplitude [201, 202]

$$\hat{H}_A(t) = -J \sum_{i=-L/2}^{L/2} \left(e^{-i\theta(t)} \hat{c}_i^\dagger \hat{c}_{i+1} + e^{i\theta(t)} \hat{c}_{i+1}^\dagger \hat{c}_i \right). \quad (4.16)$$

The phase $\theta(t)$ can be calculated by using the vector potential $A_0(t)$ according to

$$\theta(t) = \int_0^d A_0(t) / \hbar dx = \Delta t / \hbar. \quad (4.17)$$

Thus the Hamiltonian $\hat{H}_A(t)$ is periodic in time and the frequency is set by Δ . Note, that due to the gauge covariance of the Schrödinger equation, the dynamics described by both Hamiltonians \hat{H}_A and \hat{H}_{WS} are related by the following unitary transformation $\hat{T}(t)$:

$$\hat{T}(t) \equiv e^{i \sum_i \Delta i \hat{n}_i t / \hbar}. \quad (4.18)$$

Using this transformation, the Schrödinger equation of a state $|\psi\rangle$ according to H_{WS} can be expressed in the new frame with state $|\psi_A\rangle = \hat{T}(t) |\psi\rangle$ according to

$$\begin{aligned}
 i\hbar \frac{d}{dt} \hat{T}^\dagger(t) |\psi_A\rangle &= \hat{H}_{WS} \hat{T}^\dagger(t) |\psi_A\rangle \\
 i\hbar \left(\hat{T}(t) \frac{d}{dt} \hat{T}^\dagger(t) + \frac{d}{dt} \right) |\psi_A\rangle &= \hat{T}(t) \hat{H}_{WS} \hat{T}^\dagger(t) |\psi_A\rangle \\
 i\hbar \frac{d}{dt} |\psi_A\rangle &= \hat{H}_A(t) |\psi_A\rangle ,
 \end{aligned} \tag{4.19}$$

where $\hat{H}_A(t) = \hat{T}(t) \hat{H}_{WS} \hat{T}^\dagger(t) - i\hbar \hat{T}(t) \partial_t \hat{T}^\dagger(t)$ is equivalent to Eq. (4.16). This transformation can be understood as interaction picture, since both the state $|\psi_A\rangle$ and the Hamiltonian \hat{H}_A are time-dependent. It can be applied in the same way to interacting Hamiltonians, for instance \hat{H}_{tFHM} in Eq. (4.20), since density operators \hat{n}_i are invariant under the unitary transformation $\hat{n}_{i,l}(t) = \hat{T}(t) \hat{n}_i \hat{T}^\dagger(t) = \hat{n}_i$. This is also convenient for the imbalance, which is a local density observable and hence is the same for both Hamiltonians. \hat{H}_A explicitly commutes with lattice translations, is well-defined in the thermodynamic limit and avoids the superextensive scaling contribution of the potential energy to the total energy of the system. It can be used to argue, why the imbalance is a reasonable probe for ergodicity-breaking even in interacting many-body systems with tilted field and super-extensive spectrum (Sec. 4.2.3).

4.2. Many-body dynamics in tilted Fermi-Hubbard chains

4.2.1. The tilted one-dimensional Fermi-Hubbard model

After analyzing the dynamics of a single particle in a tilted lattice, described by the Hamiltonian \hat{H}_{WS} in Eq. (4.1), we want to study more general dynamics of many interacting particles in a tilted lattice. A straightforward generalization of the single particle dynamics in the presence of interactions can be achieved by adding onsite interactions to \hat{H}_{WS} . This results in the tilted one-dimensional Fermi-Hubbard model with the Hamiltonian \hat{H}_{tFHM}

$$\hat{H}_{\text{tFHM}} = -J \sum_{i,\sigma=\uparrow,\downarrow} \left(\hat{c}_{i,\sigma}^\dagger \hat{c}_{i+1,\sigma} + \hat{c}_{i+1,\sigma}^\dagger \hat{c}_{i,\sigma} \right) + \Delta \sum_{i,\sigma=\uparrow,\downarrow} i \hat{n}_{i,\sigma} + U \sum_i \hat{n}_{i,\uparrow} \hat{n}_{i,\downarrow}, \tag{4.20}$$

where U is the onsite interaction strength and where we omitted the summation boundaries for simplicity, but imply $i \in [-L/2, L/2]$, analogous to the Wannier-Stark Hamiltonian in Eq. (4.1). The onsite interaction term results in a coupling between the single-particle states and thus the many-body wavefunction of N particles does not factorize into

N single-particle wavefunctions anymore. The resulting dynamics is more complex and depends on the parameter regime set by J , Δ and U .

A first insight into the role of interactions is obtained by transforming \hat{H}_{tFHM} from the Wannier basis into the Wannier-Stark basis. The transformation between the two basis sets is defined in Eq. (4.2) and the Hamiltonian \hat{H}_{tFHM} in the Wannier-Stark basis reads:

$$\hat{H}_{\text{tFHM}} = \Delta \sum_{j,\sigma} j \hat{\beta}_{j,\sigma}^\dagger \hat{\beta}_{j,\sigma} + \sum_{m,l,q,p} U_{m,l,q,p} \hat{\beta}_{m,\uparrow}^\dagger \hat{\beta}_{l,\uparrow} \hat{\beta}_{q,\downarrow}^\dagger \hat{\beta}_{p,\downarrow}, \quad (4.21)$$

where the matrix elements U_{mlqp} of the transformed interaction term are given by

$$U_{m,l,q,p} = \frac{U e^{i\frac{\pi}{2}(m-l+p-q)}}{2\pi} \int_{-\pi}^{\pi} d\tau e^{i(q+p-m-l)\tau} J_{m-l}[4\lambda \sin(\tau)] J_{q-p}[4\lambda \sin(\tau)], \quad (4.22)$$

with $\lambda = J/\Delta$. A detailed derivation of the matrix elements U_{mlqp} can be found in Appendix A. In the Wannier-Stark basis, we can infer some important effects, which are caused by a finite on-site interaction strength U .

First, the discrete spectrum of the non-interacting Hamiltonian \hat{H}_{WS} , constituting of a highly-degenerate Wannier-Stark ladder with level spacing Δ , is absent in \hat{H}_{tFHM} . In the non-interacting limit the remaining term $\hat{H}_{WS} = \sum_{j,\sigma} j \hat{\beta}_{j,\sigma}^\dagger \hat{\beta}_{j,\sigma}$ in Eq. (4.21) can be understood as center-of-mass operator in the Wannier-Stark basis. Clearly, many different configurations of N -particle Wannier-Stark states within the lattice share the same center-of-mass and in that way contribute to the degeneracy of the energy levels. Finite interactions lift these degeneracies, since they couple different Wannier-Stark states in Eq. (4.21). For $J \simeq \Delta \simeq U$, this leads to a dense energy spectrum [203] and has profound consequences on the Bloch oscillations, which exhibit a strong interaction-induced damping [194, 203, 204].

Second, there are two different kinds of matrix elements $U_{m,l,q,p}$ in Eq. (4.22): diagonal terms, where $m = l$ and $q = p$ and off-diagonal terms, where either $m \neq l$ or $q \neq p$ or both. The diagonal terms are analogous to on-site interactions in the Wannier basis ($m = q$), nearest-neighbor interactions ($m = q + 1$) and in general range- n terms ($m = q + n$). The off-diagonal terms consist of correlated hoppings of opposite spins, connecting the Wannier-Stark states $\hat{\beta}_{m,\uparrow}^\dagger \hat{\beta}_{l,\uparrow}$ for spin- \uparrow and the Wannier-Stark states $\hat{\beta}_{p,\downarrow}^\dagger \hat{\beta}_{q,\downarrow}$ for spin- \downarrow with a range $n' = m - l$ and a range $n'' = q - p$ hopping, respectively. The maximum achievable range n' and n'' for the off-diagonal terms is fixed by λ . From Sec. 4.1.1 we know that the Bessel function $\mathcal{J}_l(x)$ becomes small for $l \gtrsim x$. Thus, we expect large matrix elements only if $m - l \lesssim 4\lambda$ and $p - q \lesssim 4\lambda$ due to the Bessel functions in the integral in Eq. (4.22). This implies that we expect non-local dynamics in the limit of small tilt ($\lambda \rightarrow \infty$),

4. Theoretical background

which is not surprising, since the basis transform from Wannier states to Wannier-Stark states is non-local as well in the limit $\lambda \rightarrow \infty$. In contrast, in the limit of large tilt ($\lambda \rightarrow 0$), a Wannier-Stark state can be well approximated with a single Wannier state, because the two basis sets become identical in that limit [Eq. (4.2)]. As depicted in the inset of Fig. 4.4 even for moderate tilt $\Delta/J = 5$ we find $\hat{\beta}_j^\dagger \approx 0.96\hat{c}_j^\dagger + 0.20\hat{c}_{j+1}^\dagger - 0.20\hat{c}_{j-1}^\dagger$.

Thus, in the limit of large tilt, where Wannier states and Wannier-Stark states approximately coincide, we can take advantage of Eq. (4.21) to identify the leading order processes describing the dynamics. Expanding the Bessel functions up to λ^2 in the limit $\lambda \rightarrow 0$

$$\mathcal{J}_0(\lambda) = 1 - 4\lambda^2 \sin^2(\tau), \quad \mathcal{J}_1(\lambda) = 2\lambda \sin(\tau), \quad \mathcal{J}_2(\lambda) = 2\lambda^2 \sin^2(\tau), \quad (4.23)$$

we find only correlated-hopping processes up to range two, as higher-order Bessel functions are zero up to second order in λ . We first study the diagonal terms $U_{n,n,m,m}$

$$U \left(1 - \frac{4J^2}{\Delta^2} \right) \sum_n \hat{\beta}_{n,\uparrow}^\dagger \hat{\beta}_{n,\uparrow} \hat{\beta}_{n,\downarrow}^\dagger \hat{\beta}_{n,\downarrow} + \frac{2UJ^2}{\Delta^2} \sum_{n,\sigma} \hat{\beta}_{n+1,\sigma}^\dagger \hat{\beta}_{n+1,\sigma} \hat{\beta}_{n,\bar{\sigma}}^\dagger \hat{\beta}_{n,\bar{\sigma}}, \quad (4.24)$$

where we define $\bar{\sigma} = \{\downarrow, \uparrow\}$, indicating the respective opposite spin of $\sigma = \{\uparrow, \downarrow\}$. We find a renormalized on-site interaction term with $U_{n,n,n,n} = U(1 - \frac{4J^2}{\Delta^2})$ and additionally a nearest-neighbor interaction term with $U_{n,n,n+1,n+1} = \frac{2UJ^2}{\Delta^2}$. Interaction terms with longer range are zero, due to the phase factor in the integral of Eq. (4.22), which averages the integral to zero for larger ranges. The off-diagonal terms $U_{m,l,q,p}$ consist of many different correlated hoppings

$$\frac{UJ}{\Delta} \sum_{n,\sigma} \hat{\beta}_{n,\sigma}^\dagger \hat{\beta}_{n,\sigma} \left(\hat{\beta}_{n,\bar{\sigma}}^\dagger \hat{\beta}_{n+1,\bar{\sigma}} + \hat{\beta}_{n+1,\bar{\sigma}}^\dagger \hat{\beta}_{n,\bar{\sigma}} - \hat{\beta}_{n,\bar{\sigma}}^\dagger \hat{\beta}_{n-1,\bar{\sigma}} - \hat{\beta}_{n-1,\bar{\sigma}}^\dagger \hat{\beta}_{n,\bar{\sigma}} \right) \quad (4.25)$$

$$\frac{UJ^2}{2\Delta^2} \sum_{n,\sigma} \hat{\beta}_{n,\sigma}^\dagger \hat{\beta}_{n,\sigma} \left(\hat{\beta}_{n,\bar{\sigma}}^\dagger \hat{\beta}_{n+2,\bar{\sigma}} + \hat{\beta}_{n+2,\bar{\sigma}}^\dagger \hat{\beta}_{n,\bar{\sigma}} + \hat{\beta}_{n,\bar{\sigma}}^\dagger \hat{\beta}_{n-2,\bar{\sigma}} + \hat{\beta}_{n-2,\bar{\sigma}}^\dagger \hat{\beta}_{n,\bar{\sigma}} \right), \quad (4.26)$$

where we find one term proportional to λ and many more terms proportional to λ^2 , which we omit here for simplicity. Similarly to the diagonal terms, the phase factor of the integral in Eq. (4.22) ensures non-zero hopping rates only between Wannier-Stark states next to each other ($l \approx p$) and in that way keeps the hoppings "local". Out of many correlated hoppings up to λ^2 , only two terms conserve the center-of-mass, defined by the first term in Eq. (4.21)

$$\hat{T}_{XY}^{WS} = \frac{2UJ^2}{\Delta^2} \sum_{n,\sigma} \hat{\beta}_{n+1,\sigma}^\dagger \hat{\beta}_{n,\sigma} \hat{\beta}_{n,\bar{\sigma}}^\dagger \hat{\beta}_{n+1,\bar{\sigma}} \quad (4.27)$$

$$\hat{T}_3^{WS} = -\frac{UJ^2}{\Delta^2} \sum_{n,\sigma} \left(\hat{\beta}_{n+2,\sigma}^\dagger \hat{\beta}_{n+1,\sigma} \hat{\beta}_{n,\bar{\sigma}}^\dagger \hat{\beta}_{n+1,\bar{\sigma}} + \hat{\beta}_{n+1,\sigma}^\dagger \hat{\beta}_{n+2,\sigma} \hat{\beta}_{n+1,\bar{\sigma}}^\dagger \hat{\beta}_{n,\bar{\sigma}} \right). \quad (4.28)$$

\hat{T}_{XY}^{WS} only acts on the spin-sector, exchanging the spins of two neighboring Wannier-Stark states. \hat{T}_3^{WS} moves two Wannier-Stark states with opposite spin within a distance of two sites onto the same site. In the limit $\Delta \gg U$, where the center-of-mass is perturbatively conserved according to Eq. (4.21), we expect these two terms to dominate all other correlated hoppings as we shall see in Sec. 4.2.2.

To summarize this part, adding interactions to the single-particle Hamiltonian \hat{H}_{WS} leads to pronounced modifications of the dynamics. New energy levels emerge on top of the non-interacting Wannier-Stark ladder, which are expected to result in strong interaction-induced damping of the coherent Bloch oscillations especially when $U \simeq \Delta \simeq J$. We study this effect experimentally in Sec. 6.2.1. Furthermore, correlated hopping terms increase the mobility. While these terms diminish at large Δ/J , it seems unclear whether Wannier-Stark localization can survive in the presence of interactions at late times. This motivates the experimental studies in Sec. 6.2.2. In the limit of $\Delta \gg U$, we find that the dynamics might be dominated by only a single correlated hopping \hat{T}_3^{WS} , when neglecting spin-dynamics. Thus, this regime is the most promising candidate for the persistence of localization in the presence of interactions and we study it in more detail in the next Sec. 4.2.2.

While the derivation of the correlated hoppings in the Wannier-Stark basis is rather technical, we end this section with an intuitive two-particle picture in the Wannier basis, which was recently studied numerically as well [104]. In the regime $\Delta \gg U, J$ we can use second order perturbation theory in the hopping J . Starting with two particles with opposite spins on the same lattice site, the interaction energy is renormalized at second order in J . Each particle can hop to the left and back or to the right and back. Thus we find $U_{\text{eff}} = 2J^2/(U - \Delta) + 2J^2/(U + \Delta) = 4J^2U/(U^2 - \Delta^2)$. In the limit $\Delta \gg U$, this expression reduces to $U_{\text{eff}} = -4J^2U/\Delta^2$ in agreement with the renormalized onsite interaction strength in Eq. (4.24). Next, we start with two particles in opposite spins on neighboring sites. To second order in J the particles are coupled, since both of them can hop onto each other and back to the original state. This results in an effective hopping rate $J_{\text{eff}} = J^2/(-U - \Delta) + J^2/(-U + \Delta) = -2J^2U/(U^2 - \Delta^2)$, which in the limit $\Delta \gg U$ is equal to $J_{\text{eff}} = 2J^2U/\Delta^2$ in agreement with \hat{T}_{XY}^{WS} in Eq. (4.27) and proportional to \hat{T}_3^{WS} in Eq. (4.28). Finally, we start with two particles with an empty site in between. For this state and any other state with even larger distance between the particles, the effective hopping rate is zero to second order in J , since the particles cannot interact and the perturbative

corrections cancel. At higher orders in J , however, we acquire a finite effective hopping rate as long as the order is sufficiently high to result in a virtual interaction between the two particles. This illustrates, that interactions lead to correlated hoppings, which increase the mobility of particles compared to the non-interacting Wannier-Stark localized limit.

4.2.2. Analytic limits: The Schrieffer-Wolff transformation

Here we study two limiting cases of the Hamiltonian in Eq. (4.20) in the Wannier basis: The large-tilt limit $\Delta \gg |U|, J$ and the resonant regime $U = 2\Delta$ with $\Delta, |U| \gg J$. We derive an effective Hamiltonian by using a Schrieffer-Wolff transformation [205], which is a generic procedure to carry out degenerate perturbation theory. It was first used to derive the Kondo Hamiltonian from the Anderson Hamiltonian [206] and since then was applied to many other problems in condensed matter physics [205], such as studying the strongly interacting limit of the Fermi-Hubbard model [207]. Moreover, the first orders in the perturbative Schrieffer-Wolff transformation approach for static Hamiltonians, coincide with those in the high-frequency expansion in the interaction picture (Sec. 4.1.5) [208, 209]. The Schrieffer-Wolff transformation connects the original Hamiltonian \hat{H} to an effective Hamiltonian \hat{H}_{eff} with a unitary transformation, defined by the anti-hermitian Schrieffer-Wolff generator \hat{S}

$$\hat{H}_{\text{eff}} = e^{\mu\hat{S}}\hat{H}e^{-\mu\hat{S}} = \hat{H} + \mu[\hat{S}, \hat{H}] + \frac{\mu^2}{2}[\hat{S}, [\hat{S}, \hat{H}]] + \mathcal{O}(\mu^3) \quad (4.29)$$

where $\mu \ll 1$ is a small, dimensionless parameter. If the Hamiltonian \hat{H} exhibits an approximate conservation law, described by an operator \hat{L} , which is weakly perturbed by other terms in \hat{H} scaling with μ , i.e. $[\hat{H}, \hat{L}] = \mathcal{O}(\mu)$, \hat{S} can be chosen to enforce the conservation law in \hat{H}_{eff} up to a certain higher order in μ . Therefore, we have the exact relation $[\hat{H}_{\text{eff}}, \hat{L}] = 0$ for the effective Hamiltonian.

We outline this method for the limit of large tilt $\Delta \gg U, J$ in Eq. (4.20), i.e., we define $\mu = \lambda = J/\Delta$ similar to the previous section. In this limit, the leading order contribution of the Hamiltonian \hat{H}_{tFHM} is the dipole moment operator $\hat{D} = \Delta \sum_{i,\sigma=\uparrow,\downarrow} i\hat{n}_{i,\sigma}$, which measures the center of mass in the Wannier basis. \hat{D} is diagonal in the Wannier basis and largely degenerate, since many configurations of particles in the lattice can lead to the same dipole moment. Thus we can define a symmetry sector \mathcal{S} according to the dipole moment $\langle \hat{D} \rangle$ of the initial state. The dipole moment conservation of the Hamiltonian \hat{H}_{tFHM} is weakly broken by the hopping operator $\hat{T} = \sum_{i,\sigma=\uparrow,\downarrow} (\hat{c}_{i,\sigma}^\dagger \hat{c}_{i+1,\sigma} + \text{h.c.})$, coupling symmetry sectors with different dipole moments to first order in λ . We therefore have $[\hat{H}_{\text{tFHM}}, \hat{D}] = \mathcal{O}(\lambda)$. Performing a Schrieffer-Wolff transformation according to Eq. (4.29),

we construct the generator \hat{S}^{dip} , such that we get an effective Hamiltonian $\hat{H}_{\text{eff}}^{\text{dip}}$ with an exact conservation law $[\hat{H}_{\text{eff}}^{\text{dip}}, \hat{D}] = 0$. The coupling between different symmetry sectors is pushed to higher orders in λ , which are neglected in the effective Hamiltonian $H_{\text{eff}}^{\text{dip}}$.

Effective Hamiltonian in the dipole-conserving regime For a spin-chain, the derivation of the effective Hamiltonian in the dipole-conserving limit is outlined in Ref. [88]. For the Hamiltonian \hat{H}_{FHM} , the effective Hamiltonian up to $\mathcal{O}(\lambda^4)$ was derived as outlined in our recent publication [210] and we find:

$$\hat{H}_{\text{eff}}^{\text{dip}} = J^{(3)}\hat{T}_3 + 2J^{(3)}\hat{T}_{XY} + U\left(1 - \frac{4J^2}{\Delta^2}\right) \sum_i \hat{n}_{i,\uparrow}\hat{n}_{i,\downarrow} + 2J^{(3)} \sum_{i,\sigma} \hat{n}_{i,\sigma}\hat{n}_{i+1,\bar{\sigma}}, \quad (4.30)$$

where we neglect the dipole operator \hat{D} , which is by construction a constant of motion. $\bar{\sigma} = \{\downarrow, \uparrow\}$ indicates the respective opposite spin of $\sigma = \{\uparrow, \downarrow\}$, $J^{(3)} = \frac{J^2 U}{\Delta^2}$ and

$$\hat{T}_3 = \sum_{i,\sigma} \hat{c}_{i,\sigma}\hat{c}_{i+1,\sigma}^\dagger\hat{c}_{i+1,\bar{\sigma}}^\dagger\hat{c}_{i+2,\bar{\sigma}} + \text{h.c.}, \quad \hat{T}_{XY} = \sum_{i,\sigma} \hat{c}_{i,\sigma}^\dagger\hat{c}_{i+1,\bar{\sigma}}\hat{c}_{i+1,\sigma}^\dagger\hat{c}_{i,\sigma}. \quad (4.31)$$

Note, the similarity of the terms in $\hat{H}_{\text{eff}}^{\text{dip}}$ compared to the Hamiltonian in the Wannier-Stark basis in the limit of large tilt. We recover the onsite interactions and the nearest-neighbor interactions of Eq. (4.24) even with the same prefactors. Additionally, \hat{T}_3^{WS} in Eq. (4.28) corresponds to $J^{(3)}\hat{T}_3$ and the respective hopping rates differ only by a minus sign due to a different operator ordering. Similarly, we recover the spin-exchange term \hat{T}_{XY}^{WS} in Eq. (4.27), which is equivalent to $2J^{(3)}\hat{T}_{XY}$. As expected in the dipole conserving limit, correlated hoppings, which do not conserve the center of mass, are absent in $\hat{H}_{\text{eff}}^{\text{dip}}$, while they in general occur away from the limit $\Delta \gg U$ as exemplary shown in Eq. (4.25) and in Eq. (4.26). In the construction of $\hat{H}_{\text{eff}}^{\text{dip}}$ correlated hoppings, which violate center-of-mass conservation, are canceled by the first non-trivial term in the expansion of the Schrieffer-Wolff generator \hat{S}^{dip} , similar to Eq. (4.35)

$$\hat{S}^{\text{dip}} = \frac{J}{\Delta} \sum_{i,\sigma} (\hat{c}_{i,\sigma}^\dagger\hat{c}_{i+1,\sigma} - \hat{c}_{i+1,\sigma}^\dagger\hat{c}_{i,\sigma}) + \frac{JU}{\Delta^2} \sum_{i,\sigma} (\hat{n}_{i+1,\bar{\sigma}} - \hat{n}_{i,\bar{\sigma}}) (\hat{c}_{i,\sigma}^\dagger\hat{c}_{i+1,\sigma} - \hat{c}_{i+1,\sigma}^\dagger\hat{c}_{i,\sigma}), \quad (4.32)$$

which indeed consist of correlated hoppings without center of mass conservation.

4. Theoretical background

Effective Hamiltonian in the resonant regime $|U| \simeq 2\Delta$ In general, tilted lattices enable a resonant exchange between potential energy and interaction energy when $|U| = n\Delta$, $n \in \mathbb{Z}$ [211]. Since our experiments are performed with a charge-density wave (Sec. 5.2) with one atom on every second site, the resonance $|U| = 2\Delta$ can be studied well. This motivates a theoretical analysis of this resonance in the limit $U, \Delta \gg J$, where $\hat{H}_0 = \Delta \sum_{i,\sigma} i \hat{n}_{i,\sigma} + 2\Delta \sum_i \hat{n}_{i,\uparrow} \hat{n}_{i,\downarrow}$ is approximately conserved. \hat{H}_0 can either independently conserve the dipole moment and the number of doublons or the sum of the two. Similarly to the dipole-conserving regime the conservation of \hat{H}_0 is perturbed by the hopping term and we have $[\hat{H}_{\text{tFHM}}, \hat{H}_0] = \mathcal{O}(\lambda)$. We apply a Schrieffer-Wolff transformation to find the effective Hamiltonian $\hat{H}_{\text{eff}}^{\text{res}}$ and we choose the SW generator \hat{S}^{res} to enforce the conservation law $[\hat{H}_0, H_{\text{eff}}^{\text{res}}] = 0$. Up to second order in λ we find:

$$\hat{H}_{\text{eff}}^{\text{res}} = \frac{8J^2}{3\Delta} \sum_i \hat{n}_{i,\uparrow} \hat{n}_{i,\downarrow} - \frac{4J^2}{3\Delta} \hat{T}_{XY} + \frac{4J^2}{3\Delta} \hat{H}_D + \frac{J^2}{\Delta} \hat{T}_1 - \frac{2J^2}{\Delta} \hat{T}_2 + \frac{2J^2}{3\Delta} \hat{T}_3^D, \quad (4.33)$$

where we discard \hat{H}_0 , since it is conserved and we define

$$\begin{aligned} \hat{T}_1 &= \sum_{i,\sigma} (1 - \hat{n}_{i+2,\bar{\sigma}}) (1 - 2\hat{n}_{i+1,\bar{\sigma}}) \hat{n}_{i,\bar{\sigma}} \hat{c}_{i,\sigma}^\dagger \hat{c}_{i+2,\sigma} + \text{h.c.}, \\ \hat{T}_2 &= \sum_{i,\sigma} (1 - \hat{n}_{i+2,\bar{\sigma}}) \hat{n}_{i,\sigma} \hat{c}_{i,\bar{\sigma}}^\dagger \hat{c}_{i+1,\bar{\sigma}} \hat{c}_{i+1,\sigma}^\dagger \hat{c}_{i+2,\sigma} + \text{h.c.}, \\ \hat{T}_3^D &= \sum_{i,\sigma} (\hat{n}_{i,\sigma} - \hat{n}_{i+2,\bar{\sigma}})^2 (1 - 2(\hat{n}_{i+2,\bar{\sigma}} - \hat{n}_{i,\sigma})) \hat{c}_{i,\bar{\sigma}} \hat{c}_{i+1,\bar{\sigma}}^\dagger \hat{c}_{i+1,\sigma}^\dagger \hat{c}_{i+2,\sigma} + \text{h.c.}, \\ \hat{H}_D &= -2 \sum_i \hat{n}_{i,\uparrow} \hat{n}_{i,\downarrow} (\hat{n}_{i+1} - \hat{n}_{i-1}) - \sum_{i,\sigma} \hat{n}_{i,\sigma} \hat{n}_{i+1,\bar{\sigma}}. \end{aligned} \quad (4.34)$$

The first term in the expansion of the SW generator $\hat{S}^{\text{res}} = \sum \lambda^n \hat{S}_n^{\text{res}}$ takes the form

$$\hat{S}_0^{\text{res}} = \sum_{i,\sigma} \left(1 - 2\hat{n}_{i,\bar{\sigma}} - \frac{2}{3}\hat{n}_{i+1,\bar{\sigma}} + \frac{8}{3}\hat{n}_{i,\bar{\sigma}}\hat{n}_{i+1,\bar{\sigma}} \right) \hat{c}_{i+1,\sigma}^\dagger \hat{c}_{i,\sigma} - \text{h.c.} \quad (4.35)$$

Similar to the Hamiltonian $\hat{H}_{\text{eff}}^{\text{dip}}$ [Eq. (4.30)], $\hat{H}_{\text{eff}}^{\text{res}}$ involves a ‘‘dressed’’ \hat{T}_3^D term conserving both the dipole moment and the number of doublons independently, giving rise to doublon-assisted dipole conserving processes. Furthermore, the onsite interaction strength is renormalized ($U + 8J^2/(3\Delta^2)$), which we also observe in the dipole conserving limit. This causes a slight shift of the resonance and motivates the description $U \simeq 2\Delta$ for the resonant regime.

4.2.3. Nonergodicity due to Hilbert-space fragmentation

Sec. 4.2.1 shows that interactions in \hat{H}_{tFHM} lead to additional long-range correlated hoppings. Thus it is questionable, whether Wannier-Stark localization prevails at finite interaction strength. However, in Sec. 4.2.2 we find that in the limit of small tunneling J , approximate conservation laws emerge in the Hamiltonian \hat{H}_{tFHM} , which can be exploited to derive the effective Hamiltonians $\hat{H}_{\text{eff}}^{\text{dip}}$ [Eq. (4.30)] and $\hat{H}_{\text{eff}}^{\text{res}}$ [Eq. (4.33)], where only few short-range correlated hoppings are present. If we were to look for persisting Wannier-Stark localization when adding interactions, these Hamiltonians are the most promising candidates. Localization can survive at finite interaction strengths in the presence of disorder, giving rise to many-body-localization [18–20]. Such non-ergodic behavior was shown to result in a finite steady-state imbalance, when initializing the dynamics with a charge-density wave [63]. However, non-ergodic dynamics are scarce, since, usually, interacting many-body systems are expected to thermalize and obey the eigenstate-thermalization hypothesis (ETH), which assumes that each individual eigenstate behaves locally like a thermal ensemble and is believed to hold for generic ergodic systems [1–3].

Recently, a dipole-conserving spin-one Hamiltonian was studied, consisting of a similar term as \hat{T}_3 in $\hat{H}_{\text{eff}}^{\text{dip}}$ and indeed it was found that the spin-autocorrelation did not relax to the thermal prediction [85]. Such non-ergodic behavior was as well found in the dipole-conserving limit of the XXZ spin-1/2 chain with a linear potential [86, 88] and attributed to Hilbert-space fragmentation [85–88]. As expected from these previous studies, we confirm that Hilbert-space fragmentation is also present in dipole-conserving effective Hamiltonian $\hat{H}_{\text{eff}}^{\text{dip}}$ [210] and we additionally find this phenomenon in the effective Hamiltonian $\hat{H}_{\text{eff}}^{\text{res}}$, which has not been studied previously in the context of Hilbert-space fragmentation.

We illustrate this novel phenomenon with $\hat{H}_{\text{eff}}^{\text{res}}$, while similar arguments can be made for $\hat{H}_{\text{eff}}^{\text{dip}}$. Fig. 4.5a depicts the structure of the Hilbert space \mathcal{H} , which separates in different symmetry sectors \mathcal{S} due to the conservation law, described by the operator $\hat{H}_0 = \Delta \sum_{i,\sigma} i \hat{n}_{i,\sigma} + 2\Delta \sum_i \hat{n}_{i,\uparrow} \hat{n}_{i,\downarrow}$, which commutes with the effective Hamiltonian $[\hat{H}_0, H_{\text{eff}}^{\text{res}}] = 0$ (Sec. 4.2.2). Thus, the effective Hamiltonian incorporates a block diagonal structure in the occupation number basis of Wannier states and the dynamics is restricted to the symmetry sector, which hosts the initial product state. Notice that this conservation law is on top of the more general particle number conservation for each spin-state, which is independent of the parameter regime of \hat{H}_{tFHM} always valid.

Generically, after fixing this new global quantum number of the conservation law, the corresponding symmetry sector \mathcal{S} is fully connected by the action of the effective Hamiltonian and we would expect the initial state to thermalize within the respective subspace \mathcal{S} at late times, when it reaches considerable overlap with all other many-body states. In contrast, we realize that this is not the case for the effective Hamiltonian in Eq. (4.33). Here, the

4. Theoretical background

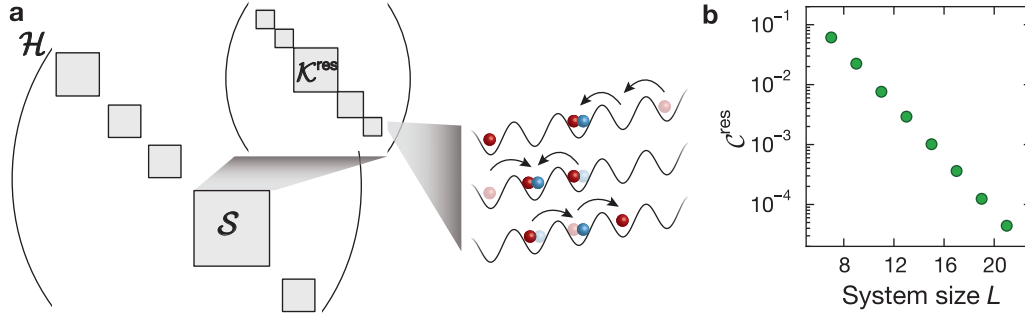


Figure 4.5.: Hilbert-space fragmentation. **a** Fragmentation of the emergent symmetry sectors \mathcal{S} of the Hilbert space \mathcal{H} of an effective Hamiltonian $\hat{H}_{\text{eff}}^{\text{res}}$, into dynamically disconnected fragments \mathcal{K} . The connectivity \mathcal{C}^{res} of each fragment \mathcal{K}^{res} is defined by the three correlated hopping operators $\hat{T}_1, \hat{T}_2, \hat{T}_3^D$ which are schematically depicted. **b** System size scaling of the connectivity \mathcal{C}^{res} for an initial Néel-ordered CDW state within the Hilbert space \mathcal{H} , restricted to zero magnetization and quarter filling.

symmetry sector decomposes into exponentially many disconnected fragments, so-called Krylov subspaces \mathcal{K}^{res} . The initial state can be connected only to other states within the Krylov space with the schematically shown correlated hoppings of $\hat{H}_{\text{eff}}^{\text{res}}$, illustrating the operators \hat{T}_1, \hat{T}_2 and \hat{T}_3^D . Thus the initial state remains trapped within such a fragment without exploring the whole symmetry sector.

The connectivity $\mathcal{C}^{\text{res}} = \dim(\mathcal{K}^{\text{res}})/\dim(\mathcal{H})$ is a measure for the relative size of the fragment \mathcal{K}^{res} within the Hilbert space \mathcal{H} . We use a Néel-ordered charge-density wave (CDW) initial state, where only every second lattice site is occupied and restrict the Hilbert space to quarter filling and zero magnetization due to particle number conservation. While in the experiment, we do not realize Néel-ordered CDW states, the connectivity of the experimentally realized initial state with random CDW spin-sector (Sec. 5.2) is the same as for the Néel-ordered CDW state due to the spin-exchange term in $\hat{H}_{\text{eff}}^{\text{res}}$ [Eq. (4.33)]. In Fig.4.5b, we show the system size scaling of the connectivity and find that it vanishes exponentially in the thermodynamic limit as expected in the regime of strong fragmentation [85–88]. The same scaling holds for the connectivity of the fragment within the symmetry sector \mathcal{S} . Note, that strong fragmentation is not a property of the CDW initial state, but we rather use this state here, since it corresponds to our initial state in the experiments in Sec. 5.2. In fact, Hilbert-space fragmentation predicts an initial-state dependence of the dynamics, where distinct thermalization properties are expected for different fragments [85, 86, 88].

The inability to explore the full symmetry sector due to Hilbert-space fragmentation shows non-ergodic dynamics. Such dynamics have been probed with the imbalance of an

initial charge-density wave in a system with disorder, which remained localized even in the presence of interactions [63]. In the clean translationally-invariant Fermi-Hubbard model the initial charge-density state (CDW) corresponds to an infinite temperature state and a finite imbalance value is a hallmark signature of localization. In the tilted model the spectrum is superextensive, complicating a meaningful definition of temperature. This problem can be overcome by transforming to the interaction picture with respect to the tilt potential. Such transformation is outlined for simplicity for the non-interacting Hamiltonian \hat{H}_{WS} in Sec. 4.1.5, but works similarly for the interacting Hamiltonian \hat{H}_{FHM} , since it leaves density operators invariant. In the interaction picture, we recover a homogeneous system, which allows us to establish the imbalance as a good probe for ergodicity breaking. Thus, we can probe non-ergodic dynamics due to Hilbert-space fragmentation with a finite imbalance of an initial CDW (See Sec. 4.3.1 and Sec. 4.3.2), as suggested in [86, 88, 104]. Remarkably, only few conservation laws are present when non-ergodic dynamics due to Hilbert-space fragmentation occurs. This is in stark contrast to an extensive set of local conservation laws, responsible for non-ergodic dynamics in MBL systems [18–20] and in integrable systems [6].

4.2.4. Symmetries in the tilted Fermi-Hubbard model

In Sec. 1.2.3, we discuss two important symmetries of the homogeneous one dimensional Fermi-Hubbard model: A dynamical symmetry between attractive and repulsive interactions and a mapping from hard-core fermions in the limit of large interaction strength to non-interacting spinless fermions. Here, we generalize these two symmetries to the tilted one-dimensional Fermi-Hubbard model.

The mapping between hard-core fermions and spinless fermions holds in the tilted Fermi-Hubbard model analogous to the derivation in Sec. 1.2.3. Only a spin-dependent tilt can break this symmetry, because in this case the effective Hamiltonian in Eq. (1.26) depends on the spin configuration. While we find a spin-dependent tilt in the experimental setup (Sec. 5.3), the tilt difference of the two spins is weak compared to the tunneling J and we usually have $(\Delta_{\downarrow} - \Delta_{\uparrow}) \lesssim 0.3J$.

The dynamical symmetry in the homogeneous Fermi-Hubbard model, as originally derived in [120], can be recovered in the presence of a tilt described by the Hamiltonian \hat{H}_{FHM} [Eq. (4.20)]. However, the assumptions need to be modified. Under a spatial inversion $\hat{\mathcal{P}}$, i.e., sending $i \rightarrow -i$ with respect to the center of a finite chain with length L , the tilted potential of the Hamiltonian changes sign. Using the π -boost \hat{B}_Q together with the inversion $\hat{\mathcal{P}}$

$$\hat{\mathcal{P}}\hat{B}_Q\hat{H}_{t\text{FHM}}(U,\Delta)\hat{B}_Q^\dagger\hat{\mathcal{P}}^\dagger = -\hat{H}_{t\text{FHM}}(-U,\Delta) \quad (4.36)$$

an equation similar to Eq. (S11) in [120] can be obtained. The experimental observable is the spin-resolved imbalance $\hat{\mathcal{I}}^\sigma = \sum_{i=-\frac{L}{2}}^{\frac{L}{2}} (-1)^i \hat{n}_{i,\sigma}$ (Sec. 5.1), which is invariant under inversion $\hat{\mathcal{I}}^\sigma \xrightarrow{\hat{\mathcal{P}}} \hat{\mathcal{I}}^\sigma$ and π -boost $\hat{\mathcal{I}}^\sigma \xrightarrow{\hat{B}_Q} \hat{\mathcal{I}}^\sigma$, but breaks time-reversal symmetry $\hat{\mathcal{T}}$. This symmetry is violated, because the spin degrees of freedom of the density operator $\hat{n}_{i,\sigma}$ are exchanged.

The Hamiltonian has an additional SU(2) spin symmetry and is invariant under spin-rotations around $\hat{S}^x = \sum_{\beta,\gamma=\uparrow,\downarrow} 1/2 \hat{c}_\beta^\dagger \sigma_{\beta\gamma}^x \hat{c}_\gamma$, where $\sigma_{\beta\gamma}^x$ are the matrix elements of the Pauli matrix. The local observable $\hat{n}_{i,\sigma}$ is invariant under the product of time reversal $\hat{\mathcal{T}}$ and π -rotations around x , and thus we obtain for the time-evolved imbalance operator $\hat{\mathcal{I}}_{(U,\Delta)}^\sigma$

$$\hat{\mathcal{P}}\hat{B}_Q e^{-i\pi\hat{S}^x} \hat{\mathcal{T}} \hat{\mathcal{I}}_{(U,\Delta)}^\sigma(t) \hat{\mathcal{T}}^{-1} e^{i\pi\hat{S}^x} \hat{B}_Q^\dagger \hat{\mathcal{P}}^\dagger = \hat{\mathcal{I}}_{(-U,\Delta)}^\sigma(t). \quad (4.37)$$

Next, we focus on the required symmetries of the initial state. For all experiments, we consider initial states that are an incoherent sum within the zero magnetization sector (thus $N_\uparrow = N_\downarrow$) with density matrix $\hat{\rho} = \frac{1}{\mathcal{N}} \sum_{\{\sigma\} | \sum_i \sigma_i = 0} |\psi_0(\{\sigma\})\rangle \langle \psi_0(\{\sigma\})|$, where each product state $|\psi_0(\{\sigma\})\rangle$, is given by a CDW of singlons. The sum runs over all possible permutations $\{\sigma\}$ of the spins within the zero magnetization sector. Under the combined action of time reversal and π -rotation around x , this state is left invariant up to a global phase. This is also the case for the π -boost \hat{B}_Q . Moreover under spatial inversion $\hat{\mathcal{P}}$ a configuration $\{\sigma_i\}$ is mapped onto another one $\{\sigma'_i\}$ appearing in the mixed state $\hat{\rho}$ with equal weight. Thus, the mixed state is also invariant under $\hat{\mathcal{P}}$. In conclusion, we find for our initial states

$$\mathcal{I}_{(U,\Delta)}^\sigma(t) = \mathcal{I}_{(-U,\Delta)}^\sigma(t). \quad (4.38)$$

Notice that this symmetry is broken in the presence of a spin-dependent tilt, because the spin-dependent tilt violates the SU(2) spin symmetry. However, similar to the discussion of the spin-dependent tilt in the mapping between hard-core fermions and spinless fermions, the spin-dependence in our system is weak and can be neglected.

4.3. Numerical results for different parameter regimes

4.3.1. Limitations of fragmentation in the dipole conserving regime

In Sec. 4.2.3 we find that the effective Hamiltonians $\hat{H}_{\text{eff}}^{\text{dip}}$ [Eq. (4.30)] and $\hat{H}_{\text{eff}}^{\text{res}}$ [Eq. (4.33)] exhibit Hilbert-space fragmentation, which results in non-ergodic dynamics and a finite steady-state imbalance even in the presence of interactions. Yet, experimentally we implement and probe the dynamics according to the Hamiltonian \hat{H}_{IFHM} in Eq. (4.20), and the effective descriptions of this Hamiltonian in the respective parameter regimes are always approximate, since they neglect higher-order terms. Thus, fragmentation in the Hamiltonian \hat{H}_{IFHM} might be a transient phenomenon, since higher-order terms will at late times always affect the dynamics. Indeed, it was found for the dipole conserving limit in spin-models that even dipole conserving higher-order terms couple different fragments and destroy Hilbert-space fragmentation, resulting in the system eventually thermalizing [85, 104].

Here, we show for the dipole-conserving regime described by $\hat{H}_{\text{eff}}^{\text{dip}}$ that estimating the transient time scales, which capture the dynamics caused due to fragmentation, requires a detailed analysis of both the diagonal and off-diagonal terms of the effective Hamiltonian. Diagonal terms only contain number operators $\hat{n}_{i,\sigma}$ and mainly constitute on-site interactions and nearest-neighbor interactions in the effective Hamiltonian. Off-diagonal terms mediate hoppings between different lattice sites, such as for example \hat{T}_3 , the dominant hopping occurring at a rate $J^{(3)} = \frac{J^2 U}{\Delta^2}$ in the dipole conserving limit ($\Delta/J \rightarrow \infty$, Eq. (4.30)). The so-called squeezing term \hat{T}_3 illustrates how diagonal and off-diagonal terms compete during the dynamics in the dipole conserving regime, since \hat{T}_3 requires the production of doublons. Creating a doublon is, however, penalized by the diagonal Fermi-Hubbard interaction with strength $\sim U$, which is much larger than the hopping rate $J^{(3)}$ of \hat{T}_3 in the dipole conserving limit. Therefore, an initial state consisting of a CDW of singlons without doublons remains frozen for exponentially long times $t \geq e^{c(\Delta/J)^2}$, where $c = \mathcal{O}(1)$. This is analogous to the stability of doublons in the repulsive Fermi-Hubbard model in the regime $U \gg J$ [168, 212]. It imposes further kinetic constraints not only due to the conservation law of the respective effective Hamiltonian, but additionally due to the conservation of the doublon number [87].

A similar argument can be made for the time scale on which higher-order off-diagonal terms, coupling different fragments, become effective and eventually destroy fragmentation, since by construction these terms are also dipole-conserving and might involve the generation of doublons. These terms add longer-range processes to the effective Hamiltonian and in general order- n terms generate longer range- n processes whose effective hopping rate scales as $J^{(n)} \sim J^{2k} U^{n-2k} / \Delta^{n-1}$ for some k . Any even order vanishes

4. Theoretical background

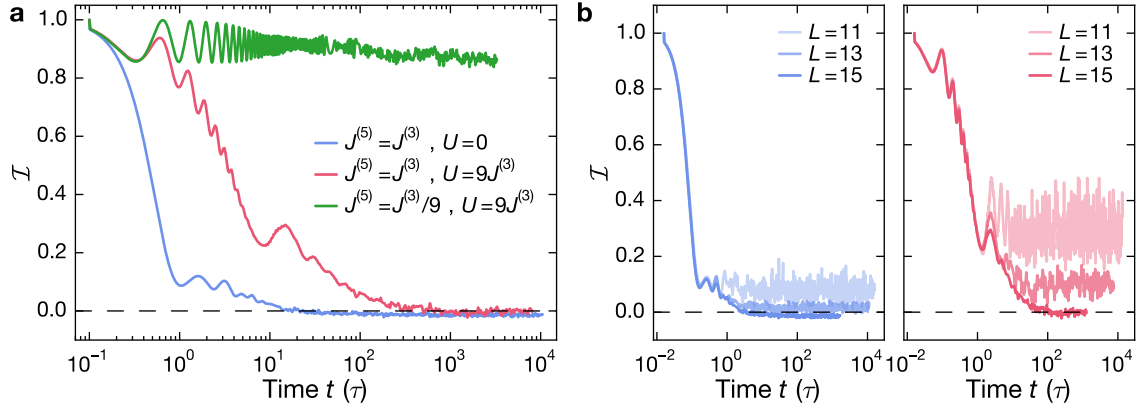


Figure 4.6.: Role of higher-order diagonal and off-diagonal terms. ED calculation of the imbalance for the Hamiltonian $\hat{H} = J^{(3)}(\hat{T}_3 + \hat{T}_{XY}) + J^{(5)}(\hat{T}_4 + \hat{T}_5) + U\hat{N}_{\text{doub}}$. **a** Imbalance for $J^{(5)} = J^{(3)}$, $U = 0$ (blue), $J^{(5)} = J^{(3)}$, $U = 9J^{(3)}$ (red), and $J^{(5)} = J^{(3)}/9$, $U = 9J^{(3)}$ (green) for system size $L = 15$. **b** Finite size scaling of the imbalance for $J^{(5)} = J^{(3)}$, $U = 0$ (left) and for $J^{(5)} = J^{(3)}$, $U = 9J^{(3)}$ (right). In both cases, we use $L = 11, 13, 15$ and increasing opacity corresponds to increasing system size. Numerical simulations were performed by Pablo Sala [210].

due to destructive interference: For every process started by a particle hopping to the left, there exists another process with a particle hopping to the right, thus contributing with opposite signs. The hopping rate of the next non-vanishing fifth-order scales as $J^{(5)} \sim J^4 U / \Delta^4$. We identify two terms at fifth order in the dipole conserving limit [210]: a 5-local term $\hat{T}_5 = \sum_{i,\sigma} (\hat{c}_{i,\sigma} \hat{c}_{i+2,\sigma}^\dagger \hat{c}_{i+2,\bar{\sigma}}^\dagger \hat{c}_{i+4,\bar{\sigma}} + \text{h.c.})$, with two opposite spins hopping to an intermediate site, requiring the creation of a doublon in the central site. A 4-local term $\hat{T}_4 = \sum_{i,\sigma} (\hat{c}_{i,\sigma} \hat{c}_{i+1,\sigma}^\dagger \hat{c}_{i+2,\bar{\sigma}}^\dagger \hat{c}_{i+3,\bar{\sigma}} + \text{h.c.})$ similar to the \hat{H}_4 Hamiltonian studied in [85], which populates nearby sites with opposite spin, thus interacting via the nearest-neighbor interaction appearing at third order in the effective Hamiltonian in the dipole conserving limit. In order to investigate the effects of additional higher order terms to the effective Hamiltonian $\hat{H}_{\text{eff}}^{\text{dip}}$ quantitatively, we construct the toy model Hamiltonian

$$\hat{H}_{\text{toy}} = J^{(3)}(\hat{T}_3 + \hat{T}_{XY}) + J^{(5)}(\hat{T}_4 + \hat{T}_5) + U\hat{N}_{\text{doub}}, \quad (4.39)$$

using $J^{(3)} = 1$ as unit of energy. This Hamiltonian contains the off-diagonal terms from Eq. (4.30), the fifth-order terms \hat{T}_4 and \hat{T}_5 with coupling strength $J^{(5)}$ as well as the diagonal energy penalty $U\hat{N}_{\text{doub}}$, where \hat{N}_{doub} measures the number of doublons. This toy model emulates an effective Hamiltonian, which is to lowest order (off-diagonal terms scaling with $J^{(3)}$) strongly fragmented, but where higher-order terms \hat{T}_4 and \hat{T}_5 perturb the fragmentation.

In Fig. 4.6a we show the time-evolution of the imbalance generated by \hat{H}_{toy} starting from a Néel-ordered CDW initial state for system size $L = 15$. We clearly observe an exponential decay of the imbalance for $J^{(3)}, J^{(5)} \sim \mathcal{O}(1)$ and $U = 0$ in agreement with the results in Refs. [85, 86]. However, the decay time scale increases strikingly, when adding on-site interactions such that $J^{(3)} = J^{(5)} = 1, U = 9$ corresponding to a ratio $U/J^{(3)} = 9$ in the perturbative expansion, which is consistent with $\Delta = 3J$ although the higher-order term is still unrealistically large ($J^{(5)} = J^{(3)}$). A more realistic regime is captured with $J^{(5)} = J^{(3)}/9$ and $U = 9$ due to the perturbative scalings. Here, the imbalance clearly remains finite on our time scales. Thus, the energy penalty given by the on-site interaction has a drastic effect on the decay of the imbalance caused by higher order terms, slowing down the dynamics tremendously. Fig. 4.6b and Fig. 4.6c show a finite-size scaling in the regimes $J^{(5)} = J^{(3)}$ with $U = 0$ and $J^{(3)} = J^{(5)}$ with $U = 9$, clearly indicating that large system sizes are necessary to capture the correct steady-state imbalance.

4.3.2. Limitations of fragmentation in the resonant regime $|U| \simeq 2\Delta$

Unlike the previous regime, at perfect resonance $U_{\text{res}} = 2\Delta \gg J$, neither the lowest-order dynamical processes generated by $\hat{H}_{\text{eff}}^{\text{res}}$ in Eq. (4.33) nor in general higher-order terms suffer from energy penalties, since doublons can be generated resonantly. Thus, at a time scale given by the fourth-order term $t \propto t_{th} = \hbar\Delta^3/J^4$, fragmentation phenomena are expected to break down, the imbalance decays and the system thermalizes. Note, that the third-order and in general any odd-order terms vanish due to the CDW initial state, requiring an even number of hoppings for a resonant exchange between tilt and interaction energy.

Here, we numerically study the resonant regime $|U| \simeq 2\Delta$ in the limit of large tilt $\Delta = 10J$, where according to the scaling of higher order terms, fragmentation should break down at $t \propto t_{th} = 1000\tau$ with $\tau = \hbar/J$. First, we focus on identifying the resonance between tilt and interaction strength in Fig. 4.7a using different system sizes $L = 9, 11, 13, 15$ to probe the time-averaged imbalance $\bar{\mathcal{I}}(T) \equiv \frac{1}{T} \int_0^T dt \mathcal{I}(t)$ of the exact Hamiltonian \hat{H}_{tFHM} [Eq. 4.20]. A sharp minimum of the imbalance occurs at $U = 19.85J$ (blue dashed line in Fig. 4.7a), which is very close to the perturbative prediction $U_{\text{res}} = 19.73J$ up to second order in J/Δ (black dashed line in Fig. 4.7a). Away from $|U| \simeq 2\Delta$ in the large U regime, the imbalance coincides with the analytical value in the non-interacting case (horizontal dashed line in Fig. 4.7a) and we conclude that the system is Wannier-Stark localized. Note, that the numerical results are consistent with the analytic prediction for the shifted resonance to second order even at 1000τ . While the imbalance at the minimum scales down with increasing system size the imbalance traces of the two largest system sizes $L = 13, 15$ agree well with each other.

4. Theoretical background

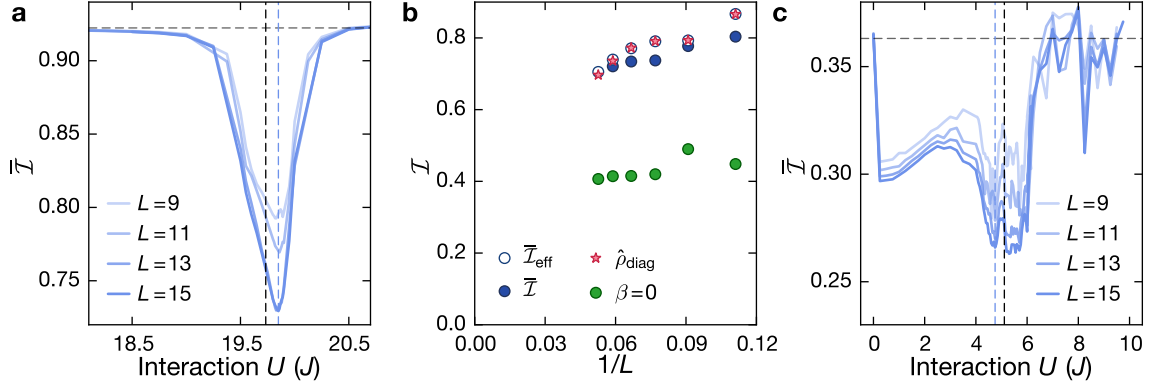


Figure 4.7.: Numerical study of the resonant regime $|U| \simeq 2\Delta$. **a** ED calculation of the time-averaged imbalance $\bar{\mathcal{I}} = 1/T \int_0^T \mathcal{I} dt$ at $\Delta = 10J$. Close to the minimum we use a grid with spacing $\delta U = 0.01J$ to locate the minimum at $U = 19.85J$ (blue dashed line). **b** Finite size scaling of the long-time value of the imbalance calculated with the effective Hamiltonian in Eq. (4.33) using a time-averaged imbalance with $T = 3000\tau$ ($\bar{\mathcal{I}}_{\text{eff}}$), a diagonal ensemble ansatz ($\hat{\rho}_{\text{diag}}$) and an infinite temperature prediction ($\beta = 0$). Additionally, the original Hamiltonian in Eq. (4.20) is used to compare to the time-averaged imbalance calculated with $T = 1000\tau$ ($\bar{\mathcal{I}}$). **c** Time-averaged imbalance for $\Delta = 3J$. Close to the minimum, we use a grid with spacing $\delta U = 0.05J$ and identify the lowest imbalance at $U = 4.75J$ (blue dashed line). In (a) and (c) the horizontal dashed line shows the analytical value $\bar{\mathcal{I}} = \mathcal{J}_0(4J/\Delta)^2$ in the non-interacting case. The vertical black dashed line indicates the resonant point, including the second order correction $U_{\text{res}} = 2\Delta - 8J^2/(3\Delta)$ of the effective Hamiltonian $\hat{H}_{\text{eff}}^{\text{res}}$. We use system sizes $L = 9, 11, 13, 15$ with increasing opacity and $T = 1000\tau$. All ED calculations were done with a Néel-ordered CDW initial state. Numerical simulations were performed by Pablo Sala [210].

After identifying the exact interaction strength $U = 19.85J$ at which the tilt resonance occurs at $\Delta = 10J$, we are in place to compare the dynamics of the exact Hamiltonian \hat{H}_{tFHM} on the tilt resonance, with the effective description using the Hamiltonian $\hat{H}_{\text{eff}}^{\text{res}}$ [Eq. (4.33)] up to second order in J/Δ . Note, that the shifted resonance is directly taken into account by the renormalized Fermi-Hubbard interaction in $\hat{H}_{\text{eff}}^{\text{res}}$. Benchmarking the dynamics with these two Hamiltonians in Fig. 4.7b reveals the effect of higher-order terms $\mathcal{O}(\lambda^4)$, which are neglected in $\hat{H}_{\text{eff}}^{\text{res}}$. The exact and the effective description of the time-averaged imbalance agree well up to long times $T \sim 10^3\tau$ compatible with the perturbative prediction $t_{\text{th}} = 1000\tau$. Consistent with a perturbative expansion in λ , which neglects higher order terms in the effective Hamiltonian, it yields a systematically larger imbalance compared to the exact Hamiltonian. Similar to the non-interacting case (Sec. 4.1.4), the diagonal ensemble ansatz with the effective Hamiltonian agrees well with the time averaged imbalance of the effective Hamiltonian showing no clear convergence in the thermodynamic limit.

Furthermore, we calculate the infinite temperature prediction for the imbalance assuming a thermalization within the fragment containing the Néel-ordered initial CDW state. The system size scaling of the infinite temperature prediction suggests a finite value, which could be interpreted as follows: Given an initial state that breaks even-odd sublattice symmetry, most dynamical processes in Eq.(4.33), except those generated by \hat{T}_3^D , do only transport particles in one of the sublattices. Thus, most states within the fragment have positive imbalance in agreement with the positive infinite temperature value. This explanation is in line with the observed ergodicity-breaking in dipole-conserving systems, where a finite value of the autocorrelation was observed even at infinite temperatures [85]. In the previous regime at $\Delta/J = 10$, the numerically accessible times were on the same order as the perturbative prediction for the time scale at which the effective Hamiltonian is affected by higher orders. Next, we reduce the tilt to $\Delta/J = 3$, investigating the imbalance in a regime, where the perturbative prediction yields $t_{th} = 27\tau$. Hence, the effect of higher order terms can be studied better on numerically accessible times. In Fig. 4.7c, we locate the minimum of the rather broad tilt resonance at $U = 4.75J$ (vertical blue dashed line), which is still in reasonable agreement with the prediction for the renormalized resonance according to \hat{H}_{eff}^{res} (vertical blue dashed line).

Having located the resonance at intermediate tilt $\Delta/J = 3$, we are in place to compare the dynamics on resonance $U \simeq 2\Delta$ to the strong tilt regime $\Delta/J = 10$. For completeness, we add the weak tilt regime $\Delta/J = 1$, where the tilt resonance is broader and less pronounced compared to $\Delta/J = 3$. Therefore, we also choose $U = 4.75J$ in this regime. In Fig. 4.8a we show numerical simulations of the imbalance \mathcal{I} calculated with \hat{H}_{tFHM} up to late times for different system sizes. In the large tilt regime, we find a stable imbalance for all system sizes, as we expect from the previous discussion in Fig. 4.7b. On numerically accessible times, the Hamiltonian on resonance is well captured by the effective Hamiltonian \hat{H}_{eff}^{res} , which exhibits Hilbert-space fragmentation and showcases a stable imbalance. In contrast, for the intermediate and the weak tilt regime the imbalance decays, but this decay is very slow in particular in the intermediate tilt regime. In this regime, we compare the imbalance, calculated with the exact Hamiltonian \hat{H}_{tFHM} to the imbalance evaluated with the effective Hamiltonian \hat{H}_{eff}^{res} [Eq.(4.33)], which maintains a steady-state (gray shaded trace in Fig. 4.8a). This comparison emphasizes, how slowly the imbalance of the exact Hamiltonian deviates from the effective description, although we expect higher order terms to be relevant at times on the order of $t = t_{th} = 27\tau$. Additionally, we find that the imbalance weakly scales down with system size. For small tilts, we clearly observe a decay of the imbalance to zero for large enough system sizes. Note, that while we used $L = 13, 15, 17$ for the intermediate and large tilt regime to minimize edge effects with an unoccupied odd site at the left and the right end of the system, we choose $L = 12, 14, 16$ for the weak tilt regime. In this regime, the initial CDW relaxes to a potentially thermal density distribution and such a distribution only has zero imbalance for an equal number

4. Theoretical background

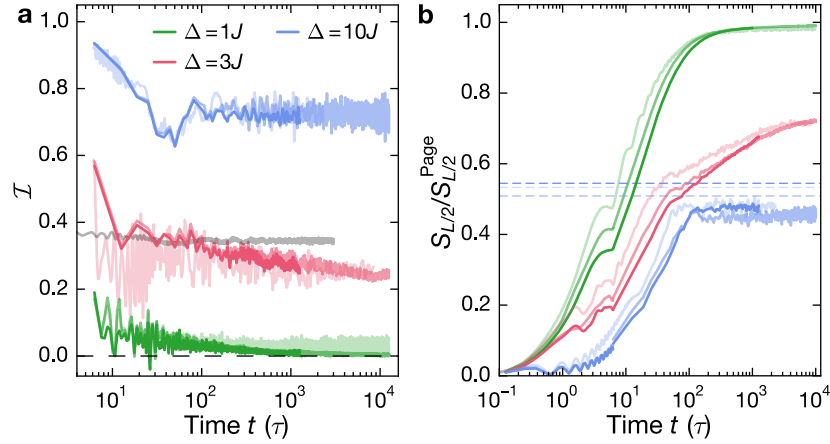


Figure 4.8.: Finite-size scaling analysis of imbalance and entanglement entropy. **a** Long-time behavior of the imbalance \bar{I} for system sizes $L = 13, 15, 17$ and $(\Delta = 10J, U = 19.85J)$ (blue), $(\Delta = 3J, U = 4.75J)$ (red) and system sizes $L = 12, 14, 16$ for $(\Delta = 1J, U = 4.75J)$ (green). The grey line corresponds to a simulation of the imbalance according to the effective Hamiltonian $\hat{H}_{\text{eff}}^{\text{res}}$ [Eq.(4.33)] for $L = 15$ and $\Delta = 3J$. Fluctuations in the data are reduced by using a running average with a time-window of 10τ . **b** Long-time behavior of the half-chain entanglement entropy $S_{L/2}$ normalized to the Page value $S_{L/2}^{\text{Page}}$ within the $(N_{\uparrow}, N_{\downarrow})$ symmetry sector for the same parameters as in (a) and system sizes $L = 13, 15, 17$. The dashed horizontal lines show the entanglement entropy of a random state within the fragment \mathcal{K}^{res} containing the Néel-ordered CDW initial state. Increasing opacity corresponds to increasing system size. All calculations use ED and were performed by Pablo Sala and Bharath Hebbe Madhusudhana [210].

of even and odd sites. Additionally, the breathing amplitude of the dynamics for $\Delta = 1J$ is four sites and boundary effects cannot be easily prevented by including an empty site at the edges. In Fig. 4.8b we show numerical simulations of the half-chain entanglement entropy $S_{L/2}$, normalized to the Page value $S_{L/2}^{\text{Page}}$ [213–215]. The Page value $S_{L/2}^{\text{Page}}$ is the half-chain entanglement entropy of a pure random state within the symmetry sector fixed by the particle numbers $N_{\uparrow}, N_{\downarrow}$. The half-chain entanglement entropy of an ergodic system at infinite temperature is in general expected to reach $S_{L/2} = S_{L/2}^{\text{Page}}$. In the weak tilt regime, the half-chain entanglement entropy converges towards the thermal Page value for large enough system sizes, which is consistent with a lack of memory of the initial state as observed with the imbalance. For an intermediate tilt, we observe a sub-thermal entanglement entropy, growing only very slowly at late times, which is consistent with the finite imbalance up to the latest times accessible in the simulations. For large tilt, the entanglement entropy reaches a plateau, which slightly depends on the system size. This saturation value of the entanglement entropy is slightly smaller than the entanglement entropy of a random state within the fragment \mathcal{K}^{res} (blue dashed lines for the different system sizes) in which the initial state is contained.

5. Setup and methods

5.1. Experimental sequence and observable

We prepare a degenerate Fermi gas of $50(5) \times 10^3$ ^{40}K atoms in a crossed beam dipole trap at the initial temperature $T/T_F = 0.15(1)$, where T_F is the Fermi temperature. The gas consists of an equal mixture of two spin components corresponding to the states $|\uparrow\rangle = |m_F = -7/2\rangle$ and $|\downarrow\rangle = |m_F = -9/2\rangle$ in the $F = 9/2$ ground-state hyperfine manifold. (For the non-interacting traces, we prepare a spin-polarized gas with all atoms in the state $|\downarrow\rangle$). Details on the preparation of a degenerate Fermi gas in our experiment can be found elsewhere [176].

Our sequence begins with loading the gas with a series of linear ramps into a three-dimensional (3D) optical lattice with wavelength $\lambda_l = 1064$ nm along the x direction and $\lambda_\perp = 738$ nm in the transverse directions (Fig. 5.1). We use repulsive interactions during the lattice loading with a scattering length of $a = 100a_0$ to suppress the generation of doublons (doubly-occupied sites). Next, we ramp up a short lattice with wavelength $\lambda_s = \lambda_l/2$ along the x direction, generating a charge-density-wave initial state (CDW) of singlons (singly-occupied sites), where $|\uparrow\rangle$ and $|\downarrow\rangle$ states are randomly distributed on even lattice sites and odd lattice sites are empty (Sec. 5.2). Finally, we complete the initial state preparation by applying a $100\ \mu\text{s}$ off-resonant light pulse to extinguish any residual doublons with light-assisted collisions, while negligibly harming atoms on singly-occupied sites due to vastly different loss rates (Sec. 2.2.2).

After cleaning the initial state from doublons, we freeze the initial state in the deep 3D lattice with a tilted superlattice along one of the axes to dephase remaining correlations between neighboring sites. The lattice depths during the freezing are $18 E_{rs}$ for the short lattice, $20 E_{rl}$ for the long lattice and $55 E_{r\perp}$ for the transverse lattices. The depths are given in the respective recoil energies, $E_{rj} = \hbar^2 k_j^2 / (2m)$, with $j \in \{l, s, \perp\}$, $k_j = 2\pi/\lambda_j$ the corresponding wave vector, m the mass of ^{40}K and $\hbar = h/(2\pi)$ the reduced Planck constant. The deep transverse lattices keep their lattice depths for the remaining sequence, decoupling the CDW initial state in each 1D tube aligned along x from neighboring tubes and in this way generating a 2D array of nearly independent 1D systems on experimentally relevant timescales. The residual coupling along the transverse directions is typically less

5. Setup and methods

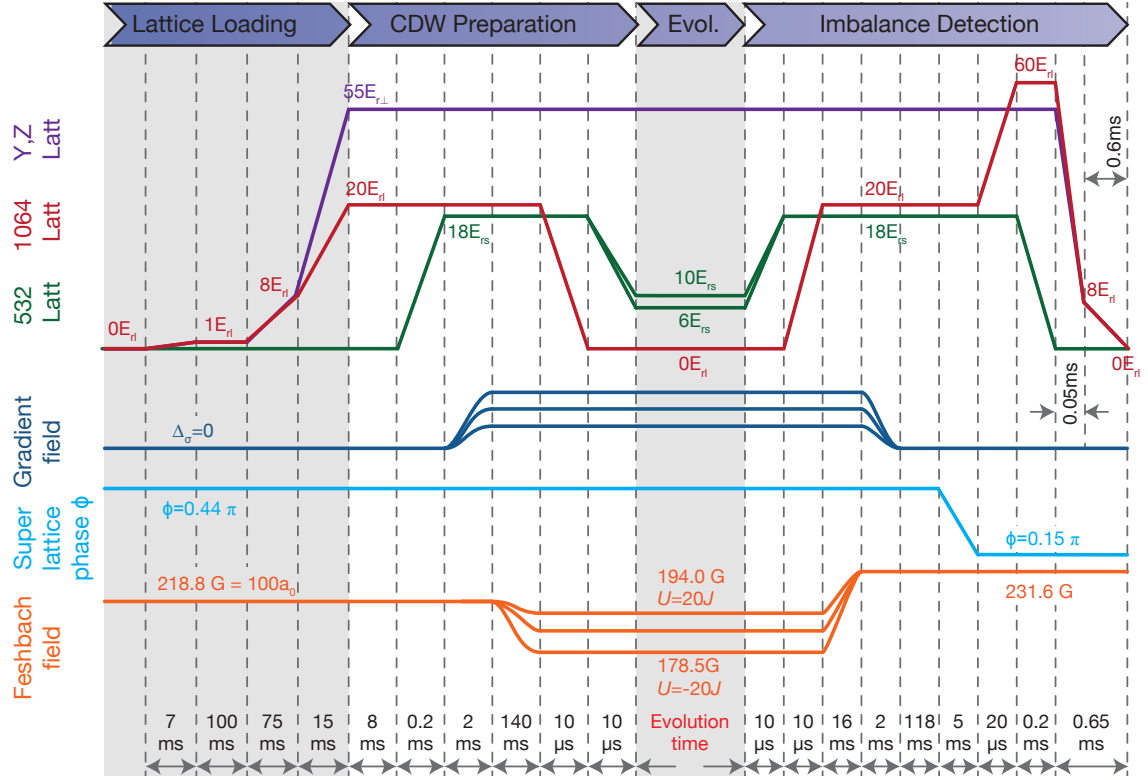


Figure 5.1: Timing protocol of the experimental sequence. Schematic sequence diagram showing the lattice depths, the superlattice phase, Feshbach field ramps and the gradient field ramps for loading, CDW preparation, time evolution and detection of the imbalance.

than 0.03 % of the coupling J along x . Using Gaussian fits to the atom cloud in the lattice, we characterize the 4σ width of the central tubes to $L_{\text{exp}} = 290(20)$ sites. Along the y direction and the z direction, our system consists of 150 sites and 22 sites, respectively.

Holding the atom cloud in the deep lattice additionally ensures that any residual dynamics are efficiently suppressed, while ramping up the magnetic field gradient and adjusting the interaction strength with a Feshbach resonance centered at 202.1 G. The magnetic field gradient is created with a single coil, the so-called gradient coil, which additionally contributes a strong homogeneous magnetic field up to 110 G. This field adds up to the homogeneous Feshbach field created by a separate pair of Helmholtz coils. Independent control of both the tilt and the interaction strength requires a tilt-dependent reduction of the Feshbach field and leads to extended waiting times in order to obtain stable currents through the coils, because of the necessary large dynamic range of the Feshbach field. We wait for 140 ms to reach the set Feshbach field for time evolution and another 136 ms to realize a stable Feshbach field for the final state read-out.

The magnetic field gradient induces a tilted potential, characterized by an energy dif-

ference $\Delta_{\uparrow,\downarrow}$ between neighboring sites, which weakly depends on the spin due to the different m_F quantum numbers; here $\Delta_{\uparrow} = 0.9\Delta_{\downarrow}$. After ramping both the magnetic field gradient and the Feshbach field to their respective set values, the dynamics are initiated by suddenly switching off the long lattice and quenching the short lattice to depths between $6 E_{rs}$ and $8 E_{rs}$. Simultaneously, the strength of the dipole trap is adjusted in order to compensate the anti-confining harmonic potential introduced by the lattice. After a variable evolution time t the on-site population is frozen by suddenly ramping up the longitudinal lattices to $18 E_{rs}$ and $20 E_{rl}$ respectively. Subsequently, we extract our observable, the spin-resolved imbalance [63, 140, 141]

$$\mathcal{I}^{\sigma} = (N_e^{\sigma} - N_o^{\sigma}) / (N_e^{\sigma} + N_o^{\sigma}), \quad (5.1)$$

by using a bandmapping technique (Sec. 5.2) in conjunction with Stern-Gerlach resolved absorption imaging. Here N_e^{σ} , (N_o^{σ}) denotes the total number of σ -atoms on even (odd) lattice sites.

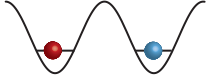
5.2. Initial state preparation & spin-resolved imbalance readout

Here, we explain the preparation of the initial states used in all experiments throughout this part and elaborate on details of the imbalance readout. We work with an equal mixture of both states ($N_{\uparrow} = N_{\downarrow}$) such that the total magnetization is zero. The CDW is prepared by taking advantage of the superlattice along the x direction. It is created after loading into the deep 3D optical lattice, by ramping up the short lattice $\lambda_s = 532$ nm in addition to the long lattice $\lambda_l = 1064$ nm at a superlattice phase of $\phi = 0.44\pi$ within $200 \mu\text{s}$. This creates strongly tilted double wells and the ramp time ensures that a singlon in the long lattice is adiabatically connected to the low-energy site of a double well (even site). In this way, we create double wells which host an atom on the even site, while the high energy site (odd site) is empty (Fig. 5.2a). Imperfections in loading the long lattice as well as extinguishing residual doublons results in a small hole fraction of 10% [169] on even sites.

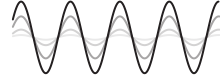
The initial state can be modeled as an incoherent mixture with an equal number of atoms in both spin states with density matrix $\hat{\rho} = \frac{1}{\mathcal{N}} \sum_{\{\sigma\} | \sum_i \sigma_i = 0} |\psi_0(\{\sigma\})\rangle \langle \psi_0(\{\sigma\})|$, where each product state $|\psi_0(\{\sigma\})\rangle$ is given by a CDW of singlons and where the sum runs over all \mathcal{N} possible permutations of spin configurations $\{\sigma\}$. The product state $|\psi_0(\{\sigma\})\rangle$ is defined as $|\psi_0(\{\sigma\})\rangle = \prod_{i=\text{even} \in \text{trap}} (\hat{c}_{i\uparrow}^{\dagger})^{n_{i\uparrow}} (\hat{c}_{i\downarrow}^{\dagger})^{n_{i\downarrow}} |0\rangle$, where $\hat{c}_{i\sigma}^{\dagger}$ is the fermionic creation operator, $n_{i\sigma} \in \{0, 1\}$, $\sigma \in \{\uparrow, \downarrow\}$, $n_i = n_{i\uparrow} + n_{i\downarrow} \leq 1$ and i is the lattice-site index along x and $|0\rangle$ denotes the vacuum state.

a Initial state preparation

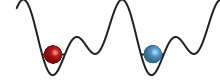
Load long lattice



Ramp up short lattice

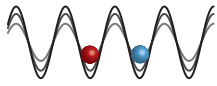


Project on even sites

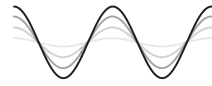


b Parity-projection

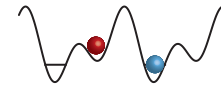
Freeze short lattice



Ramp up long lattice



Project on even/ odd sites

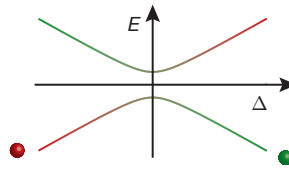


c State transfer

Couple the hyperfine states $m_F = -7/2$ and $m_F = -5/2$ using an RF-pulse



Sweep RF detuning δ

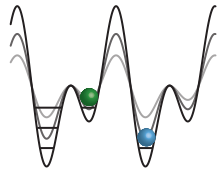


Transfer population from $m_F = -7/2$ to $m_F = -5/2$ with the RF pulse

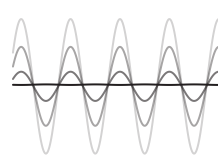


d Band transfer

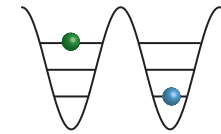
Adjust superlattice phase and ramp up long lattice



Remove short lattice

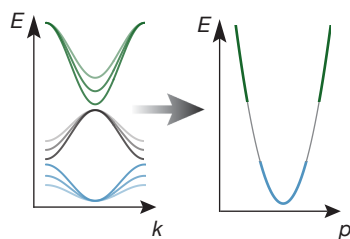


Atoms transferred to first and third band of the long lattice

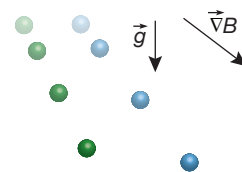


e Bandmapping and Stern-Gerlach resolved absorption imaging

Remove lattices adiabatically



Free expansion in magnetic field gradient



Absorption imaging

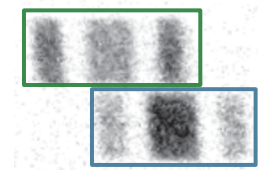


Figure 5.2.: Initial state preparation and imbalance readout in the superlattice. **a** CDW initial state preparation **b** freezing and parity-projection after time-evolution, starting the imbalance readout. **c** State transfer from $m_F = -7/2$ to $m_F = -5/2$ using a Landau-Zener sweep. **d** Band transfer: Atoms on even lattice sites are transferred to the first band in the long lattice, atoms on odd sites are transferred into the third band. **e** Bandmapping and absorption imaging after time-of-flight in a magnetic field gradient to separate the different m_F -components spatially. A typical absorption image of the spin-resolved imbalance is shown on the lower right. The bandmapping image for each spin is indicated by the respective rectangle.

We terminate the time evolution by ramping up the longitudinal lattices to $18 E_{rs}$ and $20 E_{rl}$, respectively, to freeze the onsite populations (Fig. 5.2b). Next, we apply a Landau-Zener sweep to convert atoms from $|\uparrow\rangle = |F = 9/2, m_F = -7/2\rangle$ to $|\rightarrow\rangle = |F = 9/2, m_F = -5/2\rangle$. This sweep is performed at a set magnetic field of 231.6 G, corresponding to the zero crossing of the Feshbach resonance between the two states $|\downarrow\rangle$ and $|\rightarrow\rangle$, centered around 224.2 G [216, 217]. We perform a linear frequency ramp with a duration of 10 ms centered at 51.87 MHz with a deviation of 1 MHz. The state transfer (Fig. 5.2c) increases the difference of the magnetic moments between the two states and is necessary to achieve a sufficient spatial separation of the two spin states during Stern-Gerlach resolved bandmapping. Removing interactions between these two states ensures the absence of interband oscillations after the transfer to the third band. Additionally, non-interacting bandmapping results in sharper edges of the absorption images and improves the accuracy of the imbalance measurement.

Finally, we apply a band transfer technique in the superlattice (Fig. 5.2d), which maps atoms on odd sites (high-energy site of each double well) into the third band of the long lattice, while atoms on even sites remain in the first band of the long lattice [140, 141]. Here, we require a different superlattice phase of $\phi = 0.15\pi$ to reach an optimal transfer efficiency to the third band. Afterwards we perform bandmapping and Stern-Gerlach resolved absorption imaging to evaluate the populations in the two different bands in a spin-resolved manner (Fig. 5.2e), such that we can investigate spin-dependent dynamics.

5.3. Creating a linear potential

The tilt is created by applying a magnetic field gradient. The energy E_{m_F} of each hyperfine state $|m_F\rangle$ in the $F = 9/2$ hyperfine ground-state manifold of ^{40}K in the presence of a magnetic field can be calculated analytically with the Breit-Rabi formula. Moreover, a magnetic field gradient results in a linear potential with the slope

$$\Delta_{m_F} = \frac{dE_{m_F}}{d|\mathbf{B}|} \partial_x \mathbf{B} \equiv \mu_{m_F} \partial_x \mathbf{B}. \quad (5.2)$$

Here, E_{m_F} is the hyperfine splitting energy of state $|m_F\rangle$ according to the Breit-Rabi formula, $|\mathbf{B}|$ is the magnitude of the magnetic field vector and we call μ_{m_F} the magnetic moment, causing a spin-dependence of the tilt Δ_{m_F} . In the Zeeman limit of weak field $B \rightarrow 0$, the ratio of different magnetic moments is equal to the ratio of the hyperfine quantum numbers of the corresponding states $\mu_{m_F}/\mu_{m'_F} = m_F/m'_F$, resulting in the maximum spin-dependence of the tilt $\Delta_{\uparrow}/\Delta_{\downarrow} = 7/9 = 78\%$ (Fig. 5.3b) for the two states used in the experiment. With increasing field the spin-dependence reduces, since the magnetic

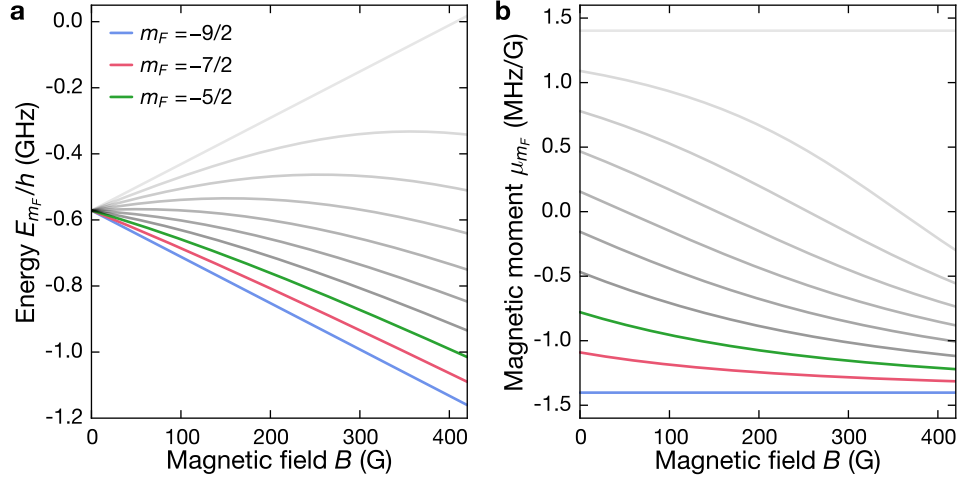


Figure 5.3.: Energy and magnetic moment for different hyperfine states of ^{40}K . The calculations are done using the Breit-Rabi formula for the ground state manifold $F = 9/2$ of ^{40}K . **a** Energies E_{m_F} and **b** magnetic moments μ_{m_F} of all hyperfine states $|m_F\rangle$ in a magnetic field. Green, red and blue lines correspond to $m_F = -5/2$, $m_F = -7/2$ and $m_F = -9/2$, respectively. These three states are used in the experiment. Gray lines represent the experimentally irrelevant states from $m_F = -3/2$ up to $m_F = 9/2$ with decreasing opacity.

moments are equal in the Paschen-Back limit of strong field $B \rightarrow \infty$. The magnetic fields used in this work are in between the two limits, yielding an intermediate spin-dependence of $\Delta_{\uparrow}/\Delta_{\downarrow} = 90.6\%$. In our setup, the magnetic field gradient is created with a single coil close to the atom cloud. The total magnetic field along the 1D tubes, generated by this coil, is given by $B(x) = B_0 + \partial_x B(x - x_0) + \partial_x^2(x - x_0)^2/2$ plus higher orders, which are negligible for our parameters. Here, x_0 is the center of the gradient coil, x is the relative distance of the atomic cloud. The gradient coil has a diameter of 25 mm, 20 windings and a mean distance to the atoms of 26.5 mm [176]. Currents up to 55 A are applied. We note, that the magnetic field generated by this configuration mainly possesses a large homogeneous contribution and a gradient part producing the linear potential. The weak field curvature part adds to the harmonic confinement of the lattice and dipole beams (Sec. 6.1.2).

5.4. Gradient-induced interaction averaging

The magnetic field gradient used for generating the tilt causes a local variation of the total magnetic field, which is used to set the interaction strength with a Feshbach resonance. Consequently, this variation of the magnetic field also induces a variation of the interaction strength over the length of a tube. From the typical center tube length of 290 lattice sites

and the shape of the Feshbach resonance we can calculate the impact of this averaging effect for a certain tilt and lattice configuration. The scattering length $a(B)$, set by the Feshbach resonance, is parameterized by

$$a(B) = a_{bg} \left(1 - \frac{w}{B - B_0} \right), \quad (5.3)$$

with background scattering length a_{bg} ($a_{bg} = 174a_0$ in our case), width w and center B_0 of the resonance. The onsite interaction U can be obtained from the scattering length by

$$U = \frac{4\pi\hbar^2 a(B)}{m} \int |w(\mathbf{r})|^4 dV \equiv \text{const} \times a(B), \quad (5.4)$$

where the integral is defined over the Wannier function $w(\mathbf{r})$ in three dimensions and m is the mass of ^{40}K . The tilt results in a linear variation of the magnetic field according to

$$B = B_c \pm dB = B_c \pm L_{\text{exp}} \Delta_{\downarrow} / (2\mu_{\downarrow}), \quad (5.5)$$

which is defined such that B_c is the magnetic field in the center of the lattice. Here, we explicitly calculate the variation for the state $|\downarrow\rangle$ with tilt Δ_{\downarrow} and magnetic moment μ_{\downarrow} . This finally leads to a variation of the interaction strength $U_{\text{var}} = U \pm dU$ according to

$$\pm dU = \text{const} \times a_{bg} \left(1 - \frac{w}{B_c - B_0 \pm L_{\text{exp}} \Delta_{\downarrow} / (2\mu_{\downarrow})} \right), \quad (5.6)$$

wherein the constant depends on the Wannier function integral and thus on the particular lattice configuration and the depths of the lattices. Fig. 5.4 shows dU as a function of the central interaction strength for the most extreme case of a 1D system with $8E_{rs}$ short lattice depth. For shallower lattices this effect diminishes. Due to the Gaussian density distribution of the cloud, assuming $L_{\text{exp}} = 290$ sites as tube length overestimates the averaging effect and gives a crude upper bound. The most pronounced effect of the interaction averaging is a finite interaction strength even when setting $U = 0$. For this reason, we revert to a spin-polarized measurement, when probing non-interacting physics. Note, that while the Stark model exhibits a dynamical U vs. $-U$ symmetry this averaging effect weakly breaks this symmetry.

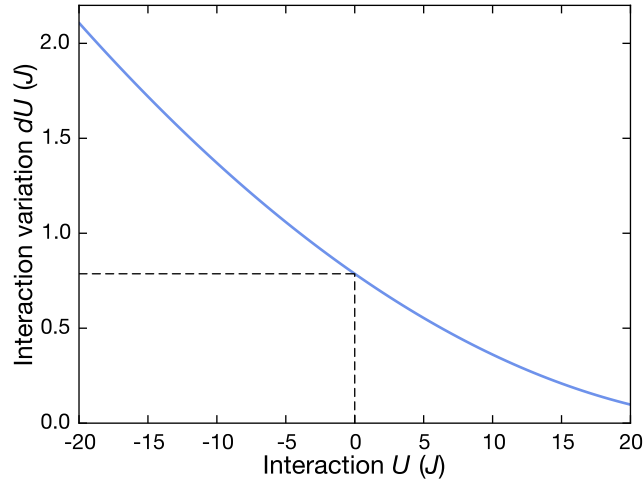


Figure 5.4.: Impact of interaction averaging. The figure shows the variation of the interaction strength across one tube with 290 lattice sites and a tilt of $\Delta = 1.8\text{kHz}$. Here we display the case of largest impact when the short lattice has a depth of $8E_{rs}$ and the perpendicular lattices have a depth of $55E_{r\perp}$. For shallower lattices such as the crossover regime the variation becomes weaker.

5.5. Calibration methods

In this section, we outline the calibration techniques to precisely determine the relevant parameters used throughout this part. In particular, we characterize the spin-dependent tilt Δ_σ , the tunneling rate J and the interaction strength U , which constitute all relevant parameters to describe the dynamics of our system according to the Hamiltonian in Eq. (6.1). Furthermore, an accurate determination of the superlattice phase ϕ ensures both a reliable CDW initial state preparation and a credible imbalance readout. Last, calibrating the imbalance to compensate for measurement imperfections guarantees a high fidelity for the comparison between experimental data and both numerical simulations and analytic results.

5.5.1. Spin-dependent tilt Δ_σ

The spin-dependent tilt is created with a gradient coil, which causes a magnetic field B_x that consists of a homogeneous field B_{x0} and a field gradient $\frac{dB_x}{dx}$ along the x direction. Additionally, the setup consists of one pair of coils in Helmholtz configuration to generate a homogeneous magnetic field B_z along the vertical z direction for controlling the interactions between the two spin states by a Feshbach resonance. Therefore, the total field B_0 , experienced by the ^{40}K atoms, is described by

$$\begin{aligned}
B_0(x) &= \sqrt{B_z^2 + B_x^2} = \sqrt{B_z^2 + \left(B_{x0} + x \frac{dB_x}{dx}\right)^2} \\
&\simeq B_z + \frac{B_{x0}^2}{2B_z} + \frac{B_{x0}}{B_z} \cdot x \frac{dB_x}{dx}.
\end{aligned} \tag{5.7}$$

In the last step we used that B_z is the strongest contribution such that the square root can be expanded up to first order and we neglect the term of the squared gradient. We note, that the strength of the gradient is reduced by the vertical field component and amplified by the homogeneous horizontal field. From this equation it follows that the calibration of tilt and interactions has to be an iterative process since these quantities strongly depend on each other. Firstly, we determine the required vertical magnetic field B_z in the presence of a current I_G in the gradient coil to generate a fixed total homogeneous magnetic field B_0 . For this sake we employ an RF sweep from $|F = 9/2, m_F = -9/2\rangle$ to $|F = 9/2, m_F = -7/2\rangle$ whose frequency is set to the value corresponding to B_0 . This yields

$$B_z(I_G) = B_0 - \frac{(aI_G)^2}{B_0} + bI_G, \tag{5.8}$$

with fit parameters a and b . From Eq. (5.7) it follows that $\Delta_\sigma \propto I_G^2$, where the proportionality constant depends on B_z . The current required to generate a certain tilt Δ_σ can be expressed with the relation

$$I_G = c\sqrt{\Delta_\sigma \cdot B_z}, \tag{5.9}$$

where c is some constant. We calibrate this fit parameter using single-particle Bloch oscillations and extract the oscillation frequency, set by the tilt Δ_σ , with the analytical model [Eq. (4.5)] using the first four oscillations to minimize effects of the damping. Finally, from Eq. (5.7) and Eq. (5.9) we see that it requires an iterative adaption of the current and the vertical field since they are strongly correlated. In the experiment we do two full iteration steps until the values have sufficiently converged.

In Fig. 5.5 we present a typical calibration measurement of the spin-dependent tilt with Bloch oscillations of a non-interacting spin mixture at $\Delta_\downarrow = 1.60(3)$ kHz and clearly see the different tilts directly in the oscillation frequency. Note, that the residual interactions, present in the spin-mixture due to interaction averaging, mainly affect the envelope of the oscillations due to interaction-induced damping. The frequency, in contrast, remains rather unaffected. Using the analytical expression according to Eq. (4.5) to fit the traces we extract a frequency difference of 170(2) Hz, which is in reasonable agreement with the calculated difference.

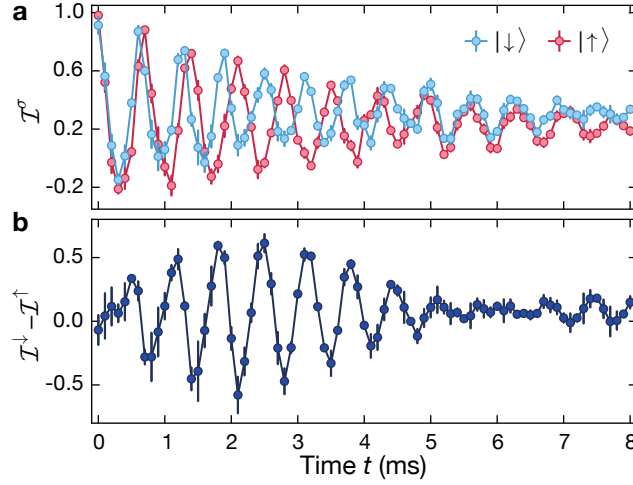


Figure 5.5.: Spin-resolved real-space Bloch oscillations. **a** Typical calibration measurement of the tilt Δ_σ for both spin-components using the spin-resolved imbalance \mathcal{I}^σ . Each data point consists of four independent measurements and error bars denote the SEM. We extract a spin-dependent tilt $\Delta_\downarrow/h = 1.60(1)$ kHz and we find a frequency difference of $(\Delta_\downarrow - \Delta_\uparrow)/h = 170(2)$ Hz, which is in reasonable agreement with the calculated difference. **b** Imbalance difference between $|\downarrow\rangle$ and $|\uparrow\rangle$. The resulting pattern exhibits a beat note, which is similar to the trigonometric identity $\cos(\omega_1 t) - \cos(\omega_2 t) = -2 \sin[(\omega_1 + \omega_2)t/2] \sin[(\omega_1 - \omega_2)t/2]$.

5.5.2. Tunneling rate J

All optical lattices are calibrated using Kapitza-Dirac scattering with a Bose-Einstein condensate of ^{87}Rb and the lattice depth calibration is then converted to ^{40}K . While this technique calibrates the tunneling J indirectly, as we need to calculate J from the calibrated lattice depth, we can also determine the tunneling J directly by using a fit of Eq. (4.5) to the short time dynamics ($U = 0J$, spin-polarized), as shown in Fig. 6.1. We only use times $t \leq 1.5$ ms such that the damping of the oscillations is negligible (the collapse time is $T_c = 8$ ms). For a set lattice depth of $8E_{rs}$ ($6E_{rs}$) the fit yields $J = h \cdot 0.54(1)$ kHz ($J = h \cdot 0.88(2)$ kHz) and agrees in both cases well with the calculated tunneling rate $J_{8E_{rs}} = h \cdot 0.543$ kHz and $J_{6E_{rs}} = h \cdot 0.896$ kHz, which assumes the calibrated lattice depths according to Kapitza-Dirac scattering.

An independent way to check the accuracy of determining J from the coherent short time dynamics can be pursued with the long time dynamics. According to Eq. (4.10), the stationary long time imbalance as a function of the tilt only requires the tunneling J as additional parameter. The solid line in Fig. 6.4 plots Eq. (4.10), where we use $J = h \cdot 0.54(1)$ kHz, obtained from the short time dynamics in Fig. 6.1b, for the only free parameter. The excellent agreement of analytic prediction and data at late times emphasizes the accuracy of calibrating J with the short time dynamics.

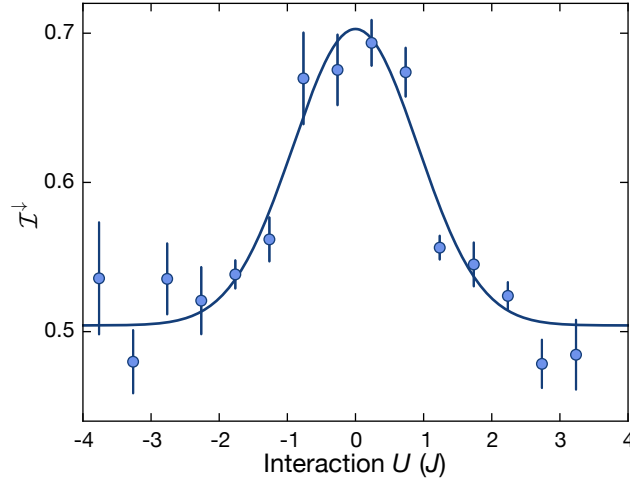


Figure 5.6.: Calibration of the zero-crossing of the Feshbach resonance. Imbalance of one spin-component \mathcal{I}^\downarrow versus interaction strength. We use a tilt $\Delta_\downarrow/h = 1.2$ kHz and measure the imbalance after $t = h/\Delta_\downarrow$. The tunneling rate is $J/h = 540$ Hz. Each data point consists of four independent measurements and error bars denote the SEM. The solid line is a Gaussian fit to capture the peak of the imbalance, corresponding to the zero-crossing of the Feshbach resonance.

5.5.3. Onsite interaction U

The non-interacting point of the Feshbach resonance between the states $|\uparrow\rangle$ and $|\downarrow\rangle$ and of the Feshbach resonance between the states $|\downarrow\rangle$ and $|\rightarrow\rangle$ is calibrated with Bloch oscillations. We hereby take advantage of the interaction-induced damping (Sec. 6.2.1) and the approximate dynamical symmetry between repulsive and attractive interactions (Sec. 4.2.4). Using a couple of different tilts Δ_\downarrow , we measure the imbalance at time $t = T_\downarrow = h/\Delta_\downarrow$ for each tilt, while scanning the Feshbach field. In Fig. 5.6 we show a typical calibration measurement for one tilt, where the zero-crossing of the Feshbach resonance is well detectable as the interaction strength with the largest imbalance. A finite interaction strength U causes a strong damping, which decreases the imbalance. Performing this measurement with different tilts ensures that the non-interacting point is the same for all tilts. This confirms that compensating the homogeneous magnetic field contribution of the gradient coil by adjusting the homogeneous Feshbach field is properly calibrated (Sec. 5.5.1).

Since the magnetic field $B_0 = 202.1$ G at the center of the Feshbach resonance is well known [218], the zero crossing is set by the width w_{202} plus the magnetic field of the center B_0 . We use the calibration of the zero crossing to determine a precise value for the width of the Feshbach resonance: $w_{202} = 7.1(1)$ G, in agreement with the literature [120]. The same measurement was performed for the Feshbach resonance between $|\downarrow\rangle$ and $|\rightarrow\rangle$ centered at $B = 224.2$ G [216], where we extract a width $w_{224} = 7.4(1)$ G, confirming the value of a different experiment [217]. The characterization of the Feshbach resonance together with

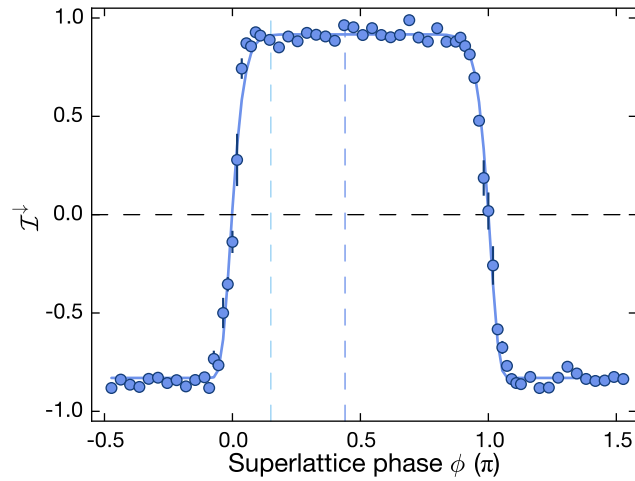


Figure 5.7.: Calibration of the superlattice phase. Imbalance of a spin-polarized gas versus the superlattice phase. We can clearly identify the zero-crossing of the imbalance corresponding to the symmetric configuration of each double well and a superlattice phase of integer multiples of π . The data points on the slopes with $\phi \in [-0.2\pi, 0.2\pi]$ and with $\phi \in [0.8\pi, 1.2\pi]$ are averaged twice and error bars denote the SEM, all other data points are not averaged. The solid line corresponds to a 16th order Gaussian to fit the zero-crossings of the imbalance. The high order Gaussian is chosen to reflect the close to rectangular shape of the imbalance trace. The vertical blue dashed lines correspond to the superlattice phase for the CDW preparation (dark blue) and for the imbalance readout (light blue).

the calibration of the lattice depth for both the orthogonal lattices and the short lattice along x yields a precise calibration for the onsite interaction U .

5.5.4. Superlattice phase

The superlattice phase is the relative phase between the short lattice and the long lattice [219]. It controls the energy offset between the two sites of a double well and is important in this work for the initial state preparation, the imbalance readout and the efficient freezing of the CDW initial state before the dynamics are initiated (Sec. 5.2). The superlattice phase is 2π -periodic and we define the symmetric configuration, where even and odd sites have the same energy, to occur at a superlattice phase $\phi = k \cdot \pi$, where $k \in \mathbb{Z}$. In our superlattice setup the 1064 nm laser of the long lattice serves as a master oscillator and its frequency is locked to a Fabry-Pérot cavity. The absolute short term stability of the master oscillator is 65 kHz over 100 ms and is characterized through the residual locking error [63]. The short lattice laser at 532 nm is offset locked relative to the second harmonic of the long lattice laser and the offset lock frequency sets the relative phase of the superlattice potential. Details of the superlattice lock can be found in [63].

The superlattice phase is calibrated according to the following measurement. We prepare a spin-polarized band-insulating cloud in a combination of the long lattice (depth is $20E_{rl}$) and the perpendicular lattices. Each well is then split non-adiabatically into a double well by adding the short lattice (depth is $18E_{rs}$) at a set superlattice phase. Then, the superlattice phase is adjusted to the reference phase, which we use to measure the imbalance. The superlattice phase ramp needs to be fast compared to the tunneling in the deep double wells to prevent any dynamics during the ramp. Subsequently, the imbalance is readout using the established sequence. A typical calibration measurement is shown in Fig. 5.7. We can clearly identify the zero crossing of the imbalance signal. The superlattice phase difference between two zero crossings corresponds to $\delta\phi = \pi$ and can be used to calibrate the set values in the sequence.

5.5.5. Imbalance

Measuring a perfect imbalance equal to one can be compromised by many artifacts such as an imperfect initial state preparation and a finite transfer efficiency of the population on odd sites into the third band. In order to calibrate these imperfections, we take two different sets of images. The first set measures the highest possible initial imbalance (around 0.92(2)) with no evolution time. The second set measures the imbalance after 25 ms evolution time without tilt, which is supposed to yield zero. We then calculate a matrix that maps the measured imbalances for these two sets to 1 (first set) and 0 (second set). In particular, we have to determine a 2×2 -matrix A^σ , for each state $\sigma = \uparrow, \downarrow$, which satisfies

$$\begin{pmatrix} n_{e,1}^\sigma & n_{e,2}^\sigma \\ n_{o,1}^\sigma & n_{o,2}^\sigma \end{pmatrix} A^\sigma = \begin{pmatrix} 1 & 0.5 \\ 0 & 0.5 \end{pmatrix}. \quad (5.10)$$

Here, $n_{e,i}^\sigma$ ($n_{o,i}^\sigma$) denote the relative atom number on even (odd) sites for the respective spin state and $i = 1, 2$ refers to the imbalance in the respective set (first or second set). This matrix is then used to rescale the measured imbalance for each spin component.

6. Experimental results

In this part, we present experimental results for the out-of-equilibrium dynamics in the tilted 1D Fermi-Hubbard model. In our system the tilt is generated with a magnetic field gradient, resulting in a weakly spin-dependent tilt $\Delta_\uparrow = 0.9\Delta_\downarrow$ due to the different m_F quantum numbers (Sec. 5.3). Therefore, we include this spin-dependent tilt in the Hamiltonian \hat{H}_{stFHM} , describing our dynamics

$$\hat{H}_{\text{stFHM}} = -J \sum_{i,\sigma=\uparrow,\downarrow} \left(\hat{c}_{i,\sigma}^\dagger \hat{c}_{i+1,\sigma} + \hat{c}_{i+1,\sigma}^\dagger \hat{c}_{i,\sigma} \right) + \sum_{i,\sigma=\uparrow,\downarrow} \Delta_\sigma i \hat{n}_{i,\sigma} + U \sum_i \hat{n}_{i,\uparrow} \hat{n}_{i,\downarrow}, \quad (6.1)$$

where the spin-dependent tilt is included in contrast to \hat{H}_{tFHM} in Eq. (4.20). While the previous theoretical discussion was done without spin-dependent tilt for simplicity, the results still apply without loss of generality in non-interacting limit, where each spin-component evolves independently and is probed with the spin-resolved imbalance (Sec. 5.1). This is not true in the presence of interaction, which couple both spin-components. Note, however, that the tilt dependence is weak compared to J , $\Delta_\downarrow - \Delta_\uparrow \lesssim 0.3J$ for the largest tilts used in the experiments. Furthermore, both the dynamical symmetry between repulsive and attractive interaction and the mapping from hard-core fermions to spin-less fermions are strictly valid only without spin-dependent tilt (Sec. 4.2.4). Clearly, we observe both symmetries for our system (Fig. 6.8b), in agreement with a weak effect of the spin-dependent on the dynamics.

6.1. Single-particle dynamics

6.1.1. Observation of real-space Bloch oscillations

In a tilted lattice initially localized atoms undergo Bloch oscillations, i.e. a periodic motion in real- and momentum-space, with a characteristic period set by the tilt. Bloch oscillations of site-localized atoms are known to exhibit breathing dynamics in real-space within one Bloch cycle. These dynamics result in a coherent spreading of the atom across multiple lattice sites before returning to the initial lattice site (Sec. 4.1.1). The extent of

6. Experimental results

this spreading is set by the spin-dependent Bloch oscillation amplitude $A_\sigma = 4Jd/\Delta_\sigma$ for each spin component $\sigma = \{\uparrow, \downarrow\}$ and we used the tunneling J and the lattice constant d . With the spin-resolved imbalance \mathcal{I}^σ , we probe these coherent breathing dynamics in a parity-projected manner (Sec. 4.1.2). Additionally, we can benchmark our results with analytic calculations according to Eq. (4.5). This enables us to use Bloch oscillations to precisely calibrate the parameters that characterize our system: the tunneling rate J and the spin-dependent tilt $\Delta_\downarrow, \Delta_\uparrow$.

In Fig. 6.1a we show the measured coherent short time dynamics of a spin-polarized Fermi gas for a weak tilt $\Delta_\downarrow = 1.2J$. As expected, we observe an oscillation with a main frequency set by the tilt. Apart from that, additional dynamics within one Bloch cycle clearly occur. In the weak tilt regime, we reach a Bloch oscillation amplitude $A_\downarrow \approx 3d$, suggesting that breathing dynamics across multiple lattice sites are at play within one Bloch cycle. The effect of these breathing dynamics on the coherent short time dynamics can be best understood, when contrasting the dynamics at weak tilt $\Delta_\downarrow = 1.2J$ with the dynamics at strong tilt $\Delta_\downarrow = 3J$, where the Bloch oscillation amplitude decreases significantly ($A_\downarrow \approx 1d$). In Fig. 6.1b, we observe clean sinusoidal oscillations with frequency Δ_\downarrow without additional oscillations within one Bloch cycle, suggesting that the breathing dynamics in this regime are negligible, as anticipated for a Bloch oscillation amplitude $A_\downarrow \approx 1d$.

To analyze the dominant frequencies in the coherent dynamics, we take a Fourier transform of the imbalance time traces and compute the power spectral density for both the regime of weak tilt (Fig. 6.1c) and the regime of strong tilt (Fig. 6.1d). For weak tilt, we find four distinct peaks in the spectrum, the Bloch frequency and an admixture of three higher harmonics with the largest spectral weight in the second harmonic. The appearance of higher harmonics is caused by contributions of multiple Wannier-Stark states to the dynamics. The Wannier-Stark states are the eigenstates of the Hamiltonian, generating the dynamics and can be understood as dressed Wannier states: They share the center of mass with the Wannier states and are localized for any tilt. Within their localization length, however, they can extend over a number of lattice sites, which is approximately determined by the Bloch oscillation amplitude (Sec. 4.1.2).

Preparing site-localized particles in a Wannier state, we can understand the dynamics in the tilted lattice from a projection of this initial Wannier state onto the Wannier-Stark eigenstates of the Hamiltonian generating the time-evolution in the tilted lattice. In the weak tilt regime, the Bloch oscillation amplitude $A_\downarrow \approx 3d$ ensures an overlap with multiple Wannier-Stark states centered on neighboring lattice sites. Since the energy difference between neighboring sites is set by Δ_\downarrow , we expect frequency components at integer multiples of Δ_\downarrow , with an upper bound determined by the Bloch oscillation amplitude A_\downarrow (Sec. 4.1.2). This is in good agreement with the data, shown in Fig. 6.1c. Investigating the regime of large tilt with a Bloch oscillation amplitude $A_\downarrow \approx 1d$ in Fig. 6.1d,

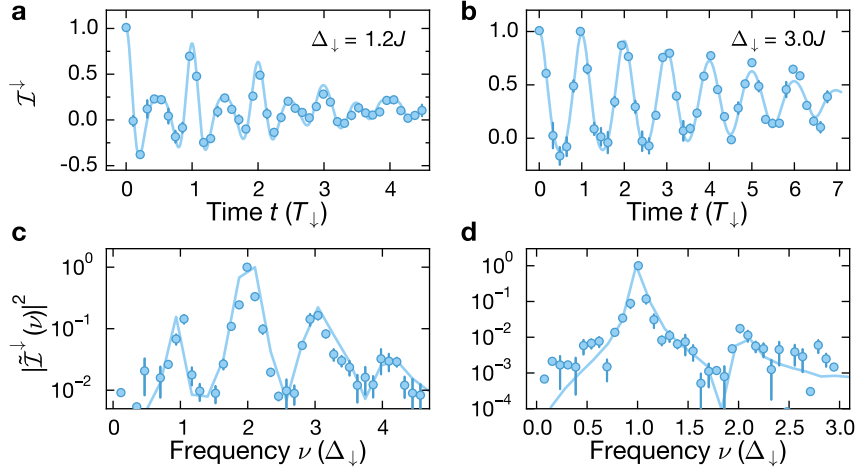


Figure 6.1.: Real-space Bloch oscillations. Upper panels: Imbalance at short times for a spin-polarized gas in state $|\downarrow\rangle$ for **a** $\Delta_{\downarrow} = 1.2J$ and $J = 0.88(2)$ kHz and for **b** $\Delta_{\downarrow} = 3J$ and $J = 0.54(2)$ kHz. $T_{\downarrow} = 1/\Delta_{\downarrow}$. Each data point is averaged four times and the error bars denote the SEM. The solid line is a numerical simulation using exact diagonalization and including the harmonic confinement to capture the dephasing (Sec. 4.1.3). Lower panels: Power spectral density $|\tilde{\mathcal{I}}^{\downarrow}(\nu)|^2$ as obtained from the Fourier transform \mathcal{F} of the time-dependent imbalance $\tilde{\mathcal{I}}^{\downarrow} = \mathcal{F}(\mathcal{I}^{\downarrow})$ in the upper panels, normalized to the peak power spectral density. **c** Power spectral density of the time trace in (a). **d** Power spectral density of the time trace in (b). We use time traces up to 8 ms, corresponding to a frequency resolution of 125 Hz in Fourier space. The solid line is the Fourier transform of the simulation in the upper panels normalized to the peak power spectral density.

we clearly observe that the number of higher harmonics decreases and as expected we are left with a strong first harmonic together with a very weak second harmonic. This establishes the power spectral density as efficient probe for both the Wannier-Stark energy levels and the number of eigenstates contributing to the dynamics.

6.1.2. Collapse time of real-space Bloch oscillations in a harmonic trap

The parity-projected Bloch oscillations in Fig. 6.1 display a clear envelope of the oscillation amplitude, which cannot be explained by the analytic result for the imbalance dynamics in Eq. (4.5). Before understanding the mechanism, which causes the envelope in the coherent short time oscillations, it is instructive to reconcile the experimental requirements for observing the oscillations in Fig. 6.1. Namely, the atoms (the total atom number is $N = 50 \cdot 10^3$) need to exhibit phase coherent dynamics and therefore, any kind of noise or spatial inhomogeneity within the atom cloud, causing a variation of the tunneling J or the tilt Δ_{\downarrow} needs to be absent on the timescale at which we probe the dynamics.

6. Experimental results

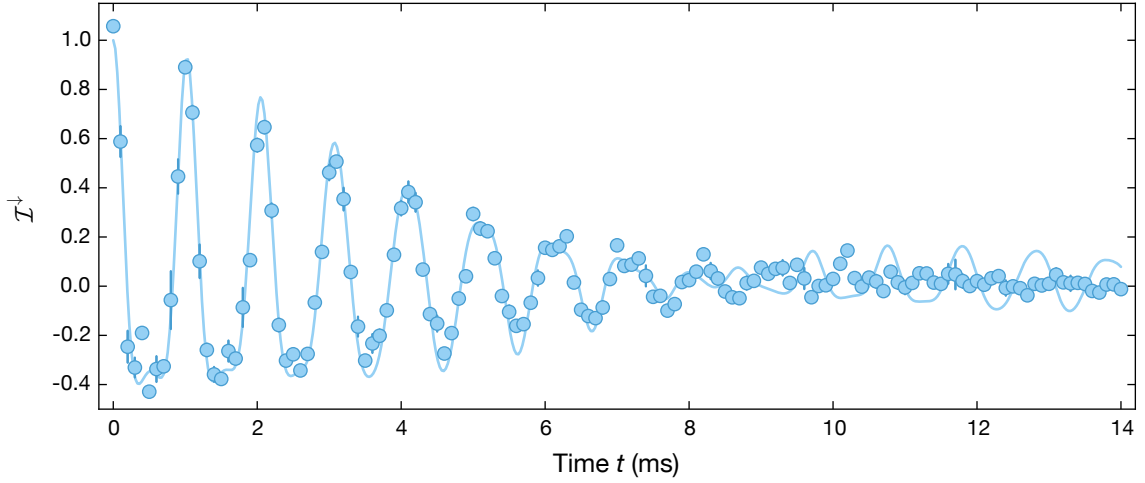


Figure 6.2.: Calibration of harmonic confinement. Imbalance \mathcal{I}^\downarrow for a spin-polarized gas with tilt $\Delta_\downarrow = 1.8J$ and $J = 540$ Hz. Each data point is averaged twice and error bars denote the SEM. The solid line is a fit to the data using a numerical calculation, which includes the harmonic confinement. The resulting collapse time T_c is 8 ms.

The residual harmonic trap, present in our setup, introduces a spatial inhomogeneity within the cloud of atoms, leading to a variation of the tilt and therefore to an averaging over many oscillation frequencies within each measurement. Note, that the harmonic confinement does not destroy the coherent dynamics, but rather leads to a periodic collapse and revival of the Bloch oscillations (Fig. 4.3). The shape of the envelope can be used to determine an upper bound for the trap frequency ω and the local curvature α , when extracting the collapse time $T_c = 1/(2L_{\text{exp}}\alpha)$ (Sec. 4.1.3). The harmonic confinement can be captured with numerical simulations for a non-interacting system in a lattice of size $L_{\text{exp}} = 290(20)d$ (4σ width of our cloud in the lattice) to determine the value of α , as a fit parameter. Corresponding to an experimentally measured imbalance time trace $\mathcal{I}^\downarrow(t_j) : j = 1, 2, \dots, n$, where n is the number of data points in time, we compute, the trace $\mathcal{I}_{\text{num}}^\downarrow(t_j; J, \Delta, \alpha)$ and then minimize $\sum_j |\mathcal{I}^\downarrow(t_j; J, \Delta, \alpha) - \mathcal{I}_{\text{num}}^\downarrow(t_j)|^2$ over alpha to determine the fit value. The harmonic confinement is extracted in Fig. 6.2. We find a collapse time of $T_c = 8$ ms, corresponding to $\alpha = 0.216$ Hz and $\omega/2\pi = \sqrt{\frac{2\alpha\hbar}{md^2}} = 39$ Hz.

Note, that due to the local nature of the dynamics in the Stark Hamiltonian, α is the important energy scale for the dynamics, characterizing the amount of curvature, which is experienced by every single atom. In our system, the tilt is on the order of $\Delta_{\uparrow,\downarrow} \approx 1000$ Hz and therefore the curvature is very weak ($\alpha/\Delta_{\uparrow,\downarrow} \approx 10^{-4}$). The reason why α is still observable in the short time dynamics is due to the averaging over the whole cloud, which enhances its effect on the collapse time by a factor $2L \approx 600$.

In Fig. 6.2 we clearly see that the numerical simulations show a small revival after the

collapse time, which is not well captured by the measured dynamics. The reason is that on top of the harmonic confinement, dephasing mechanism such as residual onsite disorder and lattice noise eventually destroy the coherence across the whole cloud and thus revivals are absent in the measurements. All these artifacts can in principle affect the envelope of the Bloch oscillations in addition to the harmonic confinement and the measured collapse time T_c is only an upper bound for the harmonic confinement. Despite putative additional artifacts, we find good agreement between numerical simulations using $\omega/2\pi = 39$ Hz and our experimental data.

6.1.3. Steady-state imbalance: probing incoherent dynamics

On time scales much larger than the collapse time T_c , all coherent dynamics are dephased. We probe the dynamics at late times in the regime of large tilt $\Delta_\downarrow = 3.3J$ and long evolution times up to approximately $t = 700\tau = 27T_c$, where $\tau = \hbar/J$ is the tunneling time. In Fig. 6.3 we study how the coherent short time dynamics, captured by real-space Bloch oscillations, evolves into a non-zero steady-state imbalance at times larger than the collapse time $t > T_c \approx 30\tau$. The steady-state imbalance is remarkably robust and persists without any sign of a decay up to the latest times probed in the experiment. The numerical simulations, including the harmonic confinement, agree well with both the coherent short time dynamics and the incoherent long time dynamics, apart from additional small revivals, which are not reproduced by the experiment. A possible approach to capture the incoherent long time dynamics analytically can be pursued by using a diagonal ensemble ansatz. This approach describes the dynamics with the density matrix formalism and the decoherences in the long time limit are artificially imposed by setting all off-diagonal elements of the density matrix to zero (Sec. 4.1.4). This density matrix is then used to calculate the steady-state imbalance and the result in Eq. (4.10) agrees very well with the observed dynamics (dashed line in Fig. 6.3). A first insight in what the diagonal ensemble ansatz means can be obtained by noting that this approach is equivalent to calculating the steady-state imbalance as time-average of the coherent short-time dynamics according to Eq. (4.5). Moreover, the diagonal ensemble ansatz offers an interesting interpretation of the steady-state value of the imbalance: It is a proxy for the number of lattice sites on which the Wannier-Stark states are localized and can be related to the Bloch oscillation amplitude (Sec. 4.1.4).

While the diagonal ensemble ansatz offers a convenient way to capture the observed decoherence without any knowledge about its microscopic details, it neglects the harmonic confinement. The numerical simulation, in contrast, can account for the harmonic confinement, but the decoherence can only be included based on a priori assumptions about the details of the noise, which are not well known. The fact that both the numerical

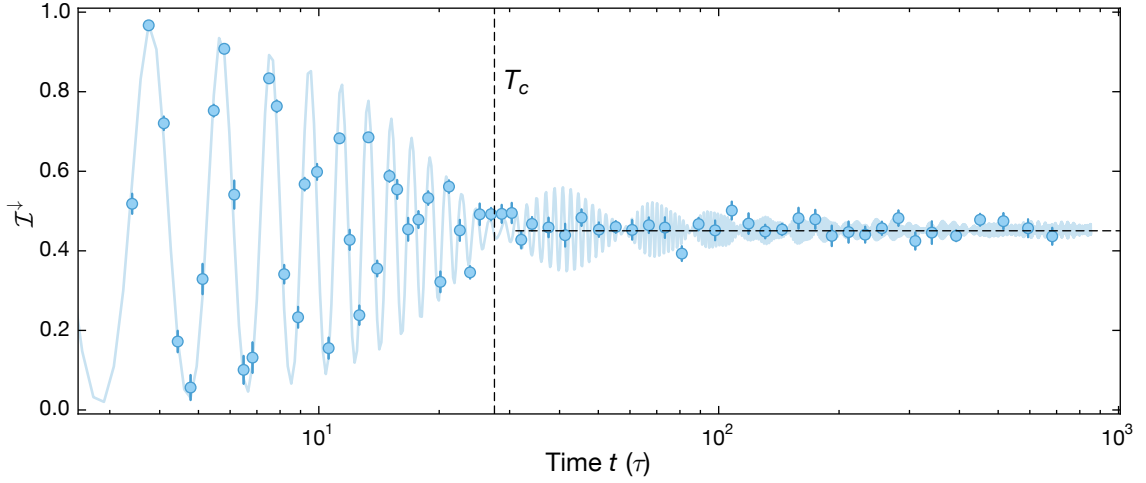


Figure 6.3.: Long-time dynamics of a spin-polarized Fermi gas in a tilted lattice. Imbalance \mathcal{I}^\downarrow of a spin-polarized Fermi gas as a function of time t in units of the tunneling time $\tau = \hbar/J$ for $\Delta_\downarrow = 3.3J$ and $J = 540$ Hz. Each data point is averaged over twelve measurements and the error bars denote the SEM. The solid line is a numerical simulation including a harmonic confinement of $\omega/(2\pi) = 39$ Hz, corresponding to a collapse time $T_c = 27\tau$. The dashed line is the analytic prediction for the steady-state imbalance according to Eq. (4.10).

simulations and the diagonal ensemble ansatz agree excellently with the experimental data is strong evidence that both the harmonic confinement and the additional dephasing mechanisms present in the experiment are negligible when discussing the steady-state imbalance for our parameter regime and on our time scales. Note, that the time scale is crucial here, since we do expect a complete revival of the Bloch oscillations resulting in an imbalance $\mathcal{I}^\downarrow = 1$ on a time scale set by $t \propto \hbar/\alpha$ (Sec. 4.1.3). This time scale would reveal a large deviation between the experimental data and the numerical simulations.

6.1.4. Observation of Wannier-Stark localization

The previous section shows that the steady-state imbalance can be well captured with a diagonal ensemble ansatz. Here we study the steady-state imbalance as a function of the tilt Δ_σ for both spin-components $\sigma = \{\uparrow, \downarrow\}$ using a spin-resolved imbalance measurement of a balanced spin-mixture. We use a Feshbach resonance to switch-off interactions between the two spin components. Any residual interactions due to tilt induced interaction averaging (Sec. 5.4) are negligible for the following discussion of the steady-state imbalance. Focusing on the state $|\downarrow\rangle$ in Fig. 6.4a, the imbalance \mathcal{I}^\downarrow shows a small peak at $\Delta_\downarrow \approx 1J$, which is followed by a local minimum consistent with zero imbalance at approximately $\Delta_\downarrow \approx 1.5J$. For larger tilts $\Delta_\downarrow \geq 1.5J$ the imbalance increases monotonously. The overall non-monotonous behavior of the imbalance is in agreement

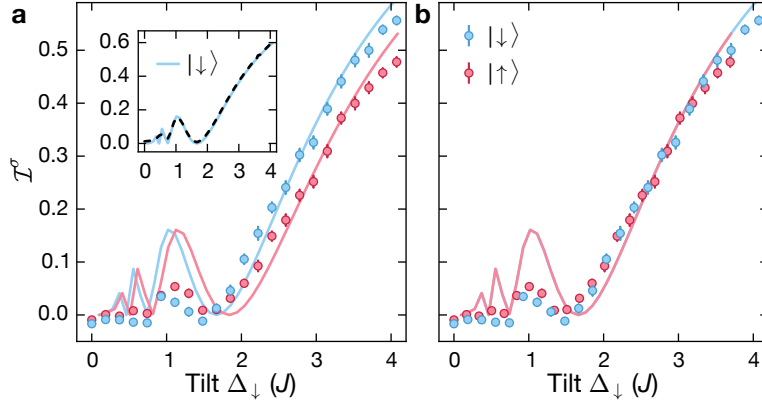


Figure 6.4.: Spin-resolved steady-state imbalance as a function of the tilt. **a** Spin-resolved steady-state imbalance versus the tilt for a non-interacting spin mixture with states $|\uparrow\rangle$, $|\downarrow\rangle$, respectively, at $J = 0.54(1)$ kHz. The data is obtained by averaging ten time steps equally spaced between 170τ and 200τ , where $\tau = \hbar/J$ is the tunneling time. Each time step is averaged three times, the error bars are SEM. Solid lines are analytic calculations according to Eq. (4.10). Inset: The dashed line is an exact diagonalization calculation with the same parameters as used in the experiment, including the harmonic confinement according to a collapse time $T_c = 8$ ms. The solid blue line shows the same data as in the main panel. **b** Same data as in (a) but the x-axis of the imbalance trace \mathcal{I}^\uparrow is rescaled according to $\Delta_\uparrow = 0.9\Delta_\downarrow$.

with a numerical calculation of the steady-state imbalance for the same parameters as used in the experiment, including the harmonic confinement (dashed line in inset of Fig. 6.4a). Overall, the harmonic confinement has a negligible effect on the steady-state imbalance for the range of tilts Δ_\downarrow probed in this experiment. The inset of Fig. 6.4a clearly shows, that the numerical simulations including the harmonic confinement are in excellent agreement with the analytic prediction for the steady-state imbalance [Eq. (4.10)], which is derived without harmonic confinement (Fig. 4.4).

The overall non-monotonous behavior of the steady-state imbalance is understood in terms of the localized eigenfunctions (Wannier-Stark states) of the Wannier-Stark Hamiltonian, which share the same functional form and can only be distinguished by the respective lattice site, hosting their center of mass (Eq. (4.4)). Using a diagonal ensemble calculation, which was shown to capture the imbalance dynamics well at long times in the previous section, the steady-state imbalance can be interpreted as the squared imbalance of a Wannier-Stark state [Eq. (4.10)]. This establishes the steady-state imbalance as a direct probe for localization in the spectrum of the Wannier-Stark Hamiltonian. For large tilt, the Wannier-Stark states are localized within a single lattice site, resulting in a steady-state imbalance approaching one monotonously. For small tilt, the Wannier-Stark states spread out over more than one lattice site and the precise weight on even and odd sites is strongly dependent on the tilt, resulting in the oscillatory behavior of the steady-state imbalance.

An imbalance equal to zero does therefore not necessarily indicate delocalization but rather corresponds to a special point, where the weight of the localized Wannier-Stark states is equally distributed on even and odd lattice sites.

Since the state-dependent Bloch oscillation amplitude $A_\sigma = 4Jd/\Delta_\sigma$ is the only parameter entering in the equation for the steady-state imbalance, we expect the steady-state imbalance \mathcal{I}^\uparrow of the state $|\uparrow\rangle$ to deviate from \mathcal{I}^\downarrow . This is in agreement with the data shown in Fig. 6.4a. For large tilts, we find $\mathcal{I}^\downarrow > \mathcal{I}^\uparrow$, which is consistent with the weaker localized Wannier-Stark states in the case of $|\uparrow\rangle$ compared to $|\downarrow\rangle$. (Remember that we have $\Delta_\uparrow = 0.9\Delta_\downarrow$). For weak tilts, our data is even consistent with a different local maximum around $\Delta_\sigma \approx J$ of the respective spin-dependent imbalances, resulting in an inversion of the imbalance $\mathcal{I}^\downarrow < \mathcal{I}^\uparrow$ for $J \lesssim \Delta_\sigma \lesssim 1.5J$ in agreement with the analytic result. The effect of the spin-dependent tilt becomes most obvious when rescaling the tilt for the state $|\uparrow\rangle$ according to $\Delta_\downarrow \rightarrow 0.9\Delta_\downarrow$, which accounts for the weaker tilt experience by the state $|\uparrow\rangle$. In Fig. 6.4b, we find that including this rescaling, both imbalance traces nearly perfectly collapse onto each other.

6.2. Many-body dynamics in the presence of interactions

6.2.1. Interacting-induced dephasing of Bloch oscillations

Bloch oscillations, in general, were found to persist for finite interactions, showing a rich variety of new dynamics depending on the parameter regime. For instance, in an experiment with a Bose-Einstein condensate in a lattice, momentum space Bloch oscillations were found to dephase, when the tilt and the interaction strength were comparable to the tunneling [194]. In contrast, in the limit of large interaction strength and tilt, an amplitude modulation set by the interaction strength was found on top of the carrier frequency set by the tilt [194, 220]. In a different experiment, the breathing dynamics of Bloch oscillations in real-space were investigated and it was found that doublons, stable compound particles for large enough interactions, show a faster oscillation than singlons because they experience twice the tilt due to their two-particle nature [102]. The sensitivity of Bloch oscillations on the interaction strength has additionally already been used to calibrate the zero crossing of Feshbach resonances, using Bloch oscillations in momentum space [217].

Here, we measure the spin-resolved imbalance to systematically study interaction effects in the dynamics of real-space Bloch oscillations in a parity-projected manner. We use a balanced spin-mixture to create a CDW of singlons as initial state and scan a large range of interaction strengths. The interaction effects are displayed by both spin-components in

the same manner, which allows us to focus on the analysis of one spin-component for the sake of simplicity. Furthermore, the coherent dynamics in the non-interacting limit are well understood and benchmarked with analytic solutions (Sec. 6.1.1) and numerical simulations to include the dephasing, induced by the harmonic confinement (Sec. 6.1.2). This enables us to precisely quantify additional effects arising in the presence of interactions.

In Fig. 6.5a we present a first set of measurements to study the coherent short-time dynamics at weak tilt $\Delta_{\downarrow} = 1.2J$. We find that the interacting spin-mixture ($U = 3J$) exhibits the same dominant frequency components as the non-interacting Bloch oscillations. Yet, the dephasing is strongly enhanced, which can be seen more directly by calculating the power spectral density (PSD) of the imbalance $|\tilde{\mathcal{I}}^{\sigma}(\nu)|^2$ (inset of Fig. 6.5a). The PSD is obtained from the Fourier transform \mathcal{F} of the time-dependent imbalance $\tilde{\mathcal{I}}^{\sigma} = \mathcal{F}(\mathcal{I}^{\sigma})$ in the main panel and normalized to the peak power spectral density. We use time traces up to 8 ms, corresponding to a frequency resolution of 125 Hz in Fourier space. In both cases, non-interacting and interacting, we find three distinct peaks in the spectrum, the Bloch frequency Δ_{\downarrow} and an admixture of two higher harmonics with the largest spectral weight in the second harmonic at $\nu_1 = 2\Delta_{\downarrow}/h$. For $U = 3J$ its weight is decreased by 70% compared to the non-interacting case.

In the non-interacting limit, the observed frequency components can be understood as a result of the energy levels of the Hamiltonian, forming the so-called Wannier-Stark ladder. We anticipate frequency components at integer multiples of Δ_{σ} , with an upper bound determined by the Bloch oscillation amplitude A_{σ}/d_s , which is a proxy for the number of Wannier-Stark states coupled to the initial state (Sec. 4.1.2). In the non-interacting case each energy level is highly degenerate. Finite interactions result in a coupling between different Wannier-Stark states and therefore lift the large degeneracy in the non-interacting case, causing a plethora of new energy levels to emerge (Sec. 4.2.1). These new energy levels alter the spectrum drastically and a qualitative understanding of the spectrum can only be obtained in certain limits of the parameters Δ , J and U . In the regime of weak tilt, where $\Delta_{\downarrow} \simeq J < U$, the spectrum is essentially dense: besides the main frequency and higher harmonics, which are set by the tilt Δ_{\downarrow} , many additional frequency components are involved in the dynamics [203]. These frequencies give rise to the interaction induced damping, which we observe in the measurements displayed in Fig. 6.5a.

In the limit of large tilt and interaction strength $U, \Delta_{\downarrow} \gg J$, the Hamiltonian becomes perturbatively diagonal in the Wannier basis and we expect few well defined frequencies to arise in the dynamics [203]. In turn, fewer frequencies in the spectrum should also reduce the interaction-induced damping. However, the CDW initial state limits the range of tilts for which we expect to observe interaction effects experimentally, since the Bloch oscillation amplitude needs to be at least on the order of the lattice constant. Otherwise, the overlap between neighboring particles becomes negligibly small. As a compromise,

6. Experimental results

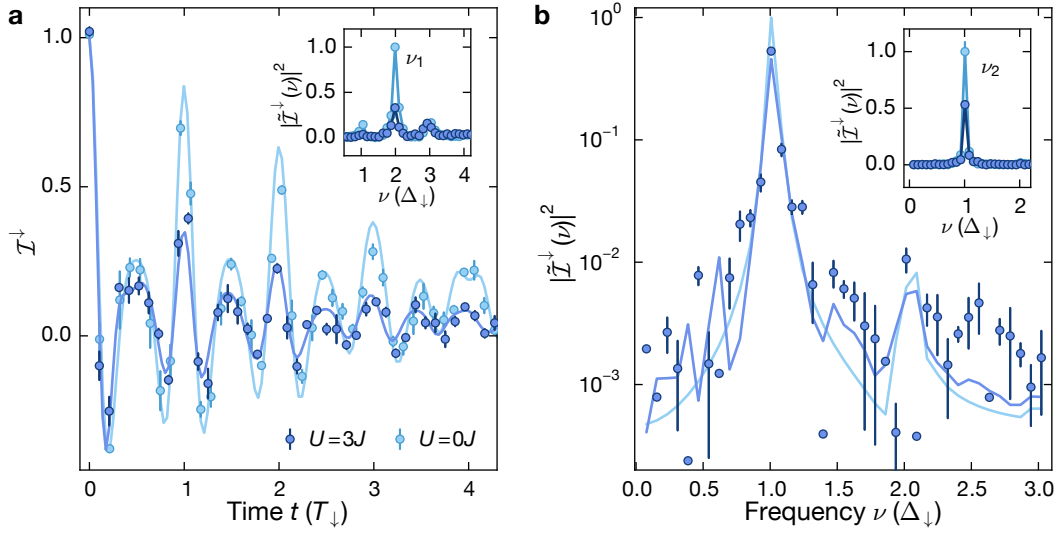


Figure 6.5: Real-space Bloch oscillations for interacting particles. **a** Time trace of the imbalance \mathcal{I}^\downarrow for $U = 0J$ (spin-polarized gas, light blue) and $U = 3J$ (spin-resolved measurement, dark blue) with $J/h = 0.88(2)$ kHz and $\Delta_\downarrow = 1.22(1)J$. Inset: Power spectral density (PSD) $|\tilde{\mathcal{I}}(\nu)|^2$ of the time traces shown in the main panel, normalized to the maximum of the non-interacting spectrum; $\nu_1 = 2\Delta_\downarrow/h$ indicates the dominant frequency component. **b** PSD $|\tilde{\mathcal{I}}(\nu)|^2$ for $U = 3J$ (spin-resolved measurement, dark blue), normalized to the maximum of the non-interacting spectrum; $J/h = 0.54(1)$ kHz and $\Delta_\downarrow = 2.96(3)J$. The data was obtained from time-traces as in (a). The Inset: PSD as in the main panel and for $U = 0J$ (spin-polarized gas, light blue). $\nu_2 = \Delta_\downarrow/h$ indicates the dominant frequency. Each data point in (a), (b) consists of four independent measurements and the error bars denote the SEM. Solid lines in all panels are numerical simulations using TEBD, which were done by Bharath Hebbe Madhusudhana [210].

we choose $\Delta_\downarrow = 3.0J$ to analyze the PSD of the coherent short-time dynamics in the regime of intermediate tilt, as depicted in Fig. 6.5b. While the largest spectral weight of the PSD is now contained in the Bloch frequency $\nu_2 = \Delta_\downarrow/h$, the reduction is still about 50% compared to the non-interacting case, indicating the sensitivity of the spectral weight as a measure of the interaction-induced dephasing.

Moreover, the onsite interactions lift the degeneracy of the energy levels in the Wannier-Stark spectrum, which results in additional frequency components in the PSD. For our parameters (Fig. 6.5b) they occur around $\approx \nu_2 \pm 0.5\Delta_\downarrow/h$ in the time-evolving block decimation (TEBD) simulations [221–223], consistent with our data. These additional frequency components can be understood in the limit $\Delta_\downarrow, U \gg J$ with second-order perturbation theory in the tunneling J from a two particle picture, yielding $J_{\text{eff}} \propto J^2 U / (U^2 - \Delta^2)$ (Sec. 4.2.1). Indeed, such side peaks are observed numerically at $\Delta \pm J_{\text{eff}}$ [224]. An experimental study of these side peaks is limited by the frequency resolution of the main peak at $\nu = \Delta_\downarrow$. The collapse time of $T_c = 8$ ms due to the harmonic confinement limits the

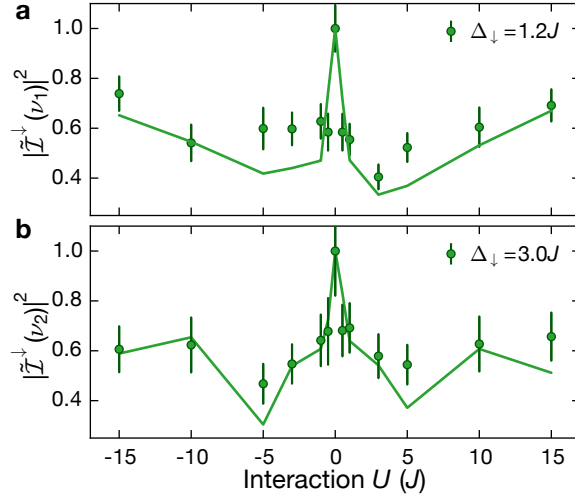


Figure 6.6.: Interaction scan of the peak power spectral density. We define the peak power spectral density $|\tilde{\mathcal{I}}(\nu_j)|^2$, which is evaluated by summing the PSD in a window of ± 3 data points around the dominant frequency ν_j , $j = \{1, 2\}$ at **a** $\Delta_{\downarrow} = 1.22(1)J$ and **b** $\Delta_{\downarrow} = 2.96(3)J$. The PSD is obtained from traces as shown in Fig. 6.5a. Solid lines in both panels are numerical simulations using TEBD, which were performed by Bharath Hebhe Madhusudhana [210].

obtainable frequency resolution to 125 Hz. Thus, for $|U - \Delta| \gg J$, the side peaks cannot be distinguished from the main peak, which is why we choose a regime close to the limitation of the perturbative result, which diverges at $U = \Delta$, where we expect the largest frequency difference between main peak and side peak. Note, that additional frequency components can in principle also result as an artifact of the Fourier transformation, due to the finite observation time. Here, the collapse of the coherent oscillations due to the harmonic confinement serves as a natural window function, suppressing these artifacts. Indeed, the PSD in the non-interacting limit, which is numerically obtained for the same parameters used in the experimental traces, shows a smooth behavior without any additional peaks. We conclude that artificial frequencies induced by the Fourier transform are negligible.

The sensitivity of the coherent short-time dynamics on the interaction strength is further highlighted by the strong interaction-dependence of the peak power spectral density (PPSD) $|\tilde{\mathcal{I}}(\nu_j)|^2$ of the respective dominant frequency components ν_j , $j = \{1, 2\}$, which is displayed in Fig. 6.6 for the regime of weak and intermediate tilt, respectively. We find a sharp decrease of the PPSD by about 40% already for small interaction strength $U = \pm 0.5J$ for $\Delta_{\sigma} = 1.2J$. After reaching a global minimum at intermediate interaction strength $2J \lesssim U \lesssim 5J$, which weakly depends on the tilt, the PPSD slowly recovers to the non-interacting value in the limit of large interactions, which is not yet reached for our parameter regime. The numerical simulation are overall in good agreement with the data. Additionally, the simulations support the experimentally observed trend, that the

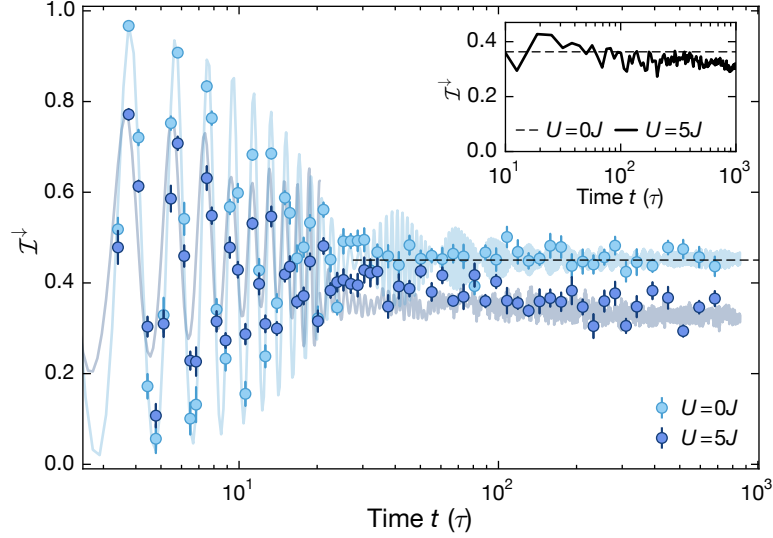


Figure 6.7.: Steady-state imbalance in the presence of interactions. Imbalance time traces at $\Delta_{\downarrow} = 3.30(3)J$ and $J/h = 0.54(1)$ kHz for $U = 0J$ (spin-polarized, light blue) and $U = 5J$ (spin-resolved measurement, dark blue). The dashed line shows the analytic prediction for the steady-state imbalance \mathcal{I}^{\downarrow} [Eq. (4.10)]. The shaded trace is an ED calculation for $L = 16$ using the same parameters as in the experiment. Each data point is averaged over twelve measurements and the error bars denote the SEM. Inset: ED calculation for $L = 16$ in a clean system with $\Delta_{\downarrow} = \Delta_{\uparrow} = 3J$, $\omega_h = 0$ and $U = 5J$ using a Néel-ordered initial CDW. The dashed lines show the analytic prediction for the non-interacting steady-state imbalance [Eq. (4.10)]. Numerical simulations were carried out by Bharath Hebbe Madhusudhana [210].

non-interacting limit is reached faster for smaller values of the tilt, where U/Δ_{\downarrow} is larger and therefore closer to the non-interacting limit at $U/\Delta_{\downarrow} \rightarrow \infty$.

6.2.2. Non-ergodic dynamics over a wide range of parameters

In the presence of interactions, correlated two-particle hoppings can arise. These hoppings can be readily inferred both from a perturbative two particle picture and from the structure of the Hamiltonian in the Wannier-Stark basis (Sec. 4.2.1). Therefore, the mobility of particles can be dramatically increased when interactions are present and it is a priori not clear, whether localized dynamics prevail at finite interaction strengths and whether a finite steady-state imbalance can be reached at late times, similar to the Wannier-Stark localization observed in the non-interacting regime in Sec. 6.1.3.

Analogous to the coherent short-time dynamics, the steady-state imbalance at late times can be captured analytically in the non-interacting limit and excellent agreement between analytic calculations and the experimental data verifies that the steady-state imbalance can

be understood in terms of Wannier-Stark localization (Sec. 6.1.4). The well understood non-interacting limit facilitates benchmarking additional effects in the presence of interactions, which we study in Fig. 6.7 up to long times $t \approx 700\tau$ for intermediate tilt $\Delta_{\downarrow} = 3.3J$ and interaction strength $U = 5J$. While the imbalance of the interacting trace is clearly lower than the imbalance of the Wannier-Stark localized trace in the non-interacting limit, we find a remarkable robustness of the imbalance on our time scales even in the presence of interactions. This suggests that additional correlated hoppings mediated by interactions (Sec. 4.2.1) are ineffective in reducing the imbalance to zero in the long-time dynamics, albeit interactions play a prominent role when dephasing the coherent Bloch oscillations at short times (Sec. 6.2.1). The steady state imbalance agrees well with numerical simulations of our system.

While experimental imperfection could in principle result in ineffective correlated hoppings, the numerical simulation in the inset clearly shows that this finite steady-state imbalance is not due to experimental imperfections, but present even for a clean system without harmonic confinement and without spin-dependent tilt. A Néel-ordered initial CDW is used to maximize interaction effects due to the absence of Pauli blocking as opposed to spin-polarized regions for the numerical simulations in the inset, in contrast to the random-spin initial state realized in the experiment and used for the numerical simulations in the main panel.

Since our CDW initial state can be understood as an infinite temperature state (Sec. 4.2.3), a finite steady-state imbalance at late times indicates non-ergodic behavior, irrespective of experimental imperfections. Moreover, this non-ergodic behavior survives over a wide range of parameters, which we study in Fig. 6.8. As a function of the tilt it qualitatively follows the behavior of the non-interacting system, but shows consistently lower steady-state values for intermediate interactions $U = 5J$ (Fig. 6.8a). Note, that the vanishing imbalance, as observed for $\Delta_{\downarrow} \approx 1.5J$ (dashed line in Fig. 6.8a), does not indicate delocalization. It results from localized Wannier-Stark orbitals with equal weight on even and odd sites, explained in more detail in Sec. 4.1.4.

For intermediate values of the tilt $\Delta/J \simeq 3$ we find a clear interaction dependence of the stationary value (Fig. 6.8b), which is similar for both spins and which is well reproduced by numerical simulations. The imbalance exhibits two important symmetries as a function of the interaction strength U . First, the behavior is found to be symmetric around $U = 0$, which we attribute to a dynamical symmetry, present in the limit of weak spin-dependence $[(\Delta_{\downarrow} - \Delta_{\uparrow}) \ll J]$ between attractive and repulsive interactions (see Sec. 4.2.4), similar to the homogeneous Fermi-Hubbard model (Sec. 1.2.3). Second, for large interactions and weak spin-dependence $(\Delta_{\downarrow} - \Delta_{\uparrow}) \ll J$, we expect the system to recover the non-interacting limit due to an exact mapping from hard-core fermions to spinless fermions, when doublons are absent in the initial state. This mapping is originally known from the homogeneous

6. Experimental results

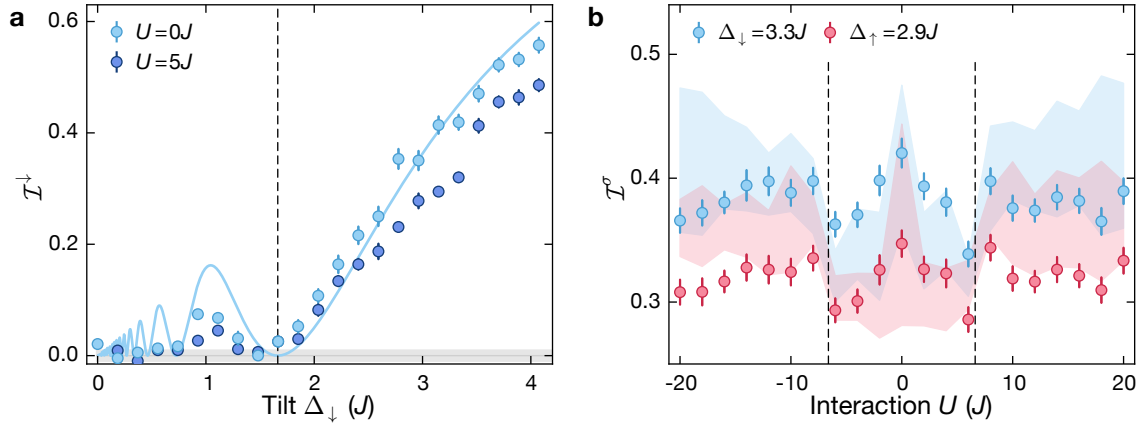


Figure 6.8: Finite steady-state imbalance over a large range of parameters. **a** Imbalance versus Δ_\downarrow measured at $U = 0J$ (spin-polarized, light blue) and $U = 5J$ (spin-resolved measurement, dark blue). Each data point is averaged over ten equally spaced times in a time window between 70τ and 100τ ($U = 0J$) and 340τ and 370τ ($U = 5J$). The solid line shows the analytic prediction for \mathcal{I}^\downarrow in the non-interacting case [Eq. (4.10)] and the dashed line indicates the first root of the Bessel function at $\Delta_\downarrow \approx 1.5J$. Imbalance values above the grey shaded area can significantly be distinguished from zero within our detection resolution. **b** Spin-resolved imbalance versus interaction strength at $\Delta_\downarrow = 3.30(3)J$. Each point is averaged over ten time steps equally spaced between 170τ and 200τ . The dashed line indicates the naive prediction for the tilt resonance at $|U| = 2\Delta_\downarrow$. The shaded trace is an ED simulation, which is averaged over the same time steps as in the experimental data and where the width indicates the 1σ standard deviation. Numerical simulations were done by Bharath Hebbe Madhusudhana [210].

Fermi-Hubbard model (Sec. 1.2.3), but it holds for our initial state even in the presence of a tilt as outlined in Sec. 4.2.4. Thus, at large interaction strength we expect a robust steady-state imbalance similar to Wannier-Stark localization in the non-interacting limit.

The steady state imbalance at intermediate tilt displays a global minimum for intermediate interactions, which we identify with resonant processes, where two singlons separated by two lattice sites form a doublon $|U| = 2\Delta$ (dashed line in Fig. 6.8b). Such tilt resonances, where long-range hoppings can take place were investigated with bosons [211] in the limit $J \rightarrow 0$. Here, we find that the minimum of the imbalance seems slightly shifted compared to the prediction for the resonance. Furthermore, it seems surprising that a finite steady-state imbalance can be maintained when long-range hoppings are present, which might rather hint towards delocalizing dynamics, that should cause a decay of the imbalance to zero. However, we find such a putative decay is absent in our data, which can be inferred from the time trace in Fig. 6.7 taken in the regime of the tilt resonance. The tilt resonance is investigated in more detail in Sec. 6.2.4. For now, we conclude that even in this regime, a robust steady-state imbalance is present, indicating non-ergodic dynamics on our experimentally accessible time scales.

In the presence of weak interactions it was recently predicted that localization survives in the limit of small but finite additional disorder or harmonic confinement, signalled by a finite steady-state imbalance [98, 99]. This localization phenomenon was termed Stark-many-body localization (Stark-MBL) in analogy to MBL in disordered systems without a linear potential (Sec. 4.2.1). Here, we indeed find that after a small decay at intermediate times a plateau of the imbalance develops, which persists for long evolution times up to 700τ (Fig. 6.7). However, interpreting the observed dynamics in terms of Stark-MBL remains challenging. First, the observed finite steady-state imbalance persists over a wide range of parameters, in particular far from the weakly interacting regime, which has not yet been studied in the context of Stark-MBL. Second, the harmonic confinement in our system is carefully calibrated in Sec. 6.1.2 and has a very weak curvature $\alpha = 0.216 \text{ Hz} < 10^{-3} \Delta_{\downarrow}$, much smaller than the typical tilt Δ_{\downarrow} . Consequently, the non-interacting steady-state imbalance in Fig. 6.7 can be excellently captured with an analytic diagonal ensemble ansatz, completely neglecting the harmonic confinement. The experimental data even reproduces the non-monotonic behavior of the steady-state imbalance in Fig. 6.8a at weak tilt, a regime that is very sensitive to the properties of the localized Wannier-Stark orbitals of the clean system. Third, numerical simulations in a clean system without spin-dependent tilt and without harmonic confinement in the inset of Fig. 6.7 find a robust steady-state imbalance in the presence of interactions. Therefore, it is conceivable that the Stark-MBL phenomenology is irrelevant on our time scales. Yet, at even later times effects of the small residual curvature might play a role.

While Stark-MBL relies on residual disorder or weak additional harmonic confinement, it was recently predicted for spin-models, that non-ergodic dynamics can even arise in a clean system without imperfections [85, 86, 88, 98, 104]. For the tilted Fermi-Hubbard model \hat{H}_{tFHM} [Eq. (4.20)] we find effective Hamiltonians in two different limits, $\hat{H}_{\text{eff}}^{\text{dip}}$ [Eq. (4.30)] in the dipole conserving limit of large tilt $\Delta \gg J, |U|$ and $\hat{H}_{\text{eff}}^{\text{res}}$ [Eq. (4.33)] on the tilt resonance $|U| = 2\Delta, U, \Delta \gg J$, which are derived perturbatively in powers of $\lambda = J/\Delta$. Both Hamiltonians exhibit Hilbert-space fragmentation (Sec. 4.2.3): The Hilbert space shatters into many disconnected sectors, so-called Krylov subspaces and the number of states within these subspaces normalized to the total Hilbert space decreases exponentially with system size. Thus, the dynamics remain trapped in the sector hosting the initial state, giving rise to non-ergodic behavior, signalled by a finite steady-state imbalance [86, 88, 104].

Since Hilbert-space fragmentation is obtained only for the effective Hamiltonians $H_{\text{eff}}^{\text{dip}}$, $H_{\text{eff}}^{\text{res}}$ to lowest order in λ , higher-order processes $\mathcal{O}(\lambda^4)$, relevant for $\Delta \simeq 3J$, couple different fragments and are expected to melt the CDW within the experimentally studied timescales [85]. In the case of $H_{\text{eff}}^{\text{dip}}$, these higher-order processes as well as the dominant off-diagonal contribution, however, require the production of doublons, which is penalized

by the on-site interaction U . We numerically show that this leads to a significant slowdown of the dynamics (Sec. 4.3.1), which could explain the robustness of the steady-state value observed in the experiment in Fig. 6.8b for weak interaction strength $U < \Delta$. Thus, for large values of the tilt, the doublon number is effectively conserved as well, which is suggested in Ref. [98].

Increasing the interaction strength in Fig. 6.8b away from the weak interaction regime we find the global imbalance minimum, attributed the tilt resonance. Notice that the observed shift of the resonance is consistent with the renormalized interaction strength occurring in the effective Hamiltonian $H_{\text{eff}}^{\text{res}}$ (Sec. 6.2.4). Furthermore, the time trace in Fig. 6.7 at $\Delta_{\downarrow} = 3.3J$ and $U = 5J$ precisely captures the regime of the tilt resonance, where the imbalance is minimal. The resonant formation of doublons is by construction not prohibited in the effective Hamiltonian $H_{\text{eff}}^{\text{res}}$ on the tilt resonance, as opposed to $H_{\text{eff}}^{\text{dip}}$. Therefore, we anticipate faster dynamics, which is indeed supported by the data in Fig. 6.7, showing initial faster dynamics before a lower steady-state imbalance is reached in the resonant regime. However, similar to the dipole conserving regime, for finite λ higher-order hopping processes $\mathcal{O}(\lambda^4)$ enable additional dynamics. These processes are expected to eventually melt the CDW completely, although the required timescales are very large (Sec. 4.3.2), in agreement with the robust steady-state imbalance values even for a rather tilt ($\Delta \simeq 3J$) up to evolution times of 700τ (Fig. 6.7).

6.2.3. Long-time dynamics in the limit of weak tilt

The dynamics in the tilted 1D Fermi-Hubbard model can be understood in terms of correlated hoppings, when interactions are present (Sec. 4.2.1). These hoppings increase the mobility of particles and were found to decrease the imbalance in particular in the limit of weak tilt (Sec. 4.3.2). In Fig. 6.9a we study the steady-state imbalance at late times $t \sim 200\tau$ at weak tilt $\Delta_{\downarrow} = 1.1J$ for various interaction strengths. We find that a finite value is maintained and largely independent of the interactions. Note, that a detailed study of the interaction induced relaxation dynamics of the imbalance in this regime is limited by the dynamic range of the imbalance, which is small even in the non-interacting limit in this regime. Despite these complications, the finite steady-state imbalance, well above our detection limit (grey shaded area in Fig. 6.9a), indicates that the putative thermalization of the system does not occur on our experimentally accessible time scales even in the limit of weak tilt.

The persistence of non-ergodicity down to very small values of the tilt is surprising, especially when reconciling with the strong interaction-induced damping of the coherent short-time dynamics in this regime, studied in Fig. 6.5a. Naively, one may expect that for large Bloch-oscillation amplitudes the interactions between particles cause a dephasing of

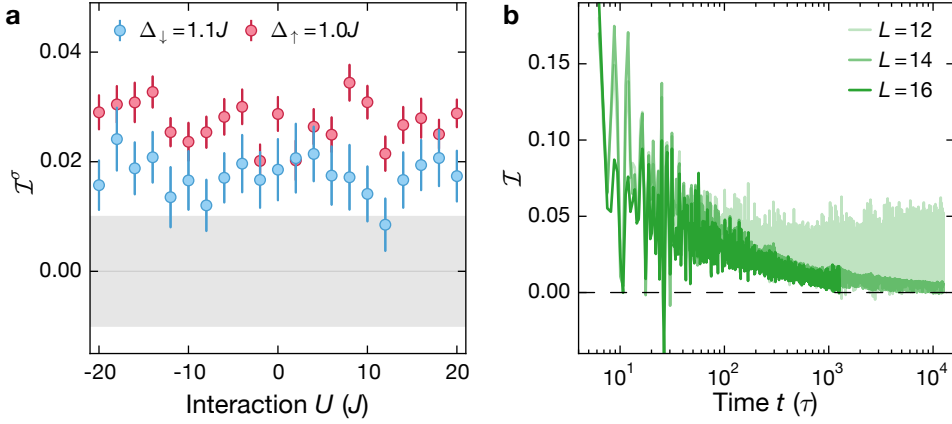


Figure 6.9.: Steady-state imbalance in the limit of weak tilt. **a** Spin-resolved imbalance versus interaction strength at $\Delta_\downarrow = 1.10(1)J$. Each point is averaged over ten time steps equally spaced between 170τ and 200τ . Imbalance values above the grey shaded area in (b),(c) can significantly be distinguished from zero within our detection resolution. **b** Long-time behavior of imbalance \mathcal{I} for system sizes $L = 12, 14, 16$ for $\Delta = 1J$ and $U = 4.75J$. We use a Néel-ordered singlon CDW in a clean system without harmonic confinement and spin-dependent tilt. Fluctuations in the data are reduced by using a running average with a time-window of 10τ . Numerical simulations were performed by Bharath Hebbe Madhusudhana [210].

the coherent dynamics that give rise to Wannier-Stark localization in the non-interacting limit and hence result in ergodic behavior. In a numerical analysis of this regime for a Néel-ordered singlon CDW we find that the imbalance decays to zero for evolution times on the order of $10^4 \tau$, which further agrees with the finite imbalance measured at $\sim 200 \tau$. The observed inversion of the spin-resolved imbalance $\mathcal{I}^\downarrow < \mathcal{I}^\uparrow$ (although $\Delta_\downarrow > \Delta_\uparrow$) is explained by the non-monotonic dependence of the stationary imbalance on the tilt for $\Delta_\sigma < 2J$ as shown in Fig. 6.8b. Thus, the numerical results support our expectation that thermalization occurs in the limit of weak tilt. However, even at weak tilt the relaxation dynamics are very slow, which is why we experimentally observe a finite steady state imbalance.

Note, that while we use a Néel-ordered singlon CDW initial state for the numerical analysis to maximize interaction effects, we can only access initial states with a random spin configuration in the experiments. In these initial states, spin-polarized regions are expected to statistically occur and locally result in non-interacting dynamics, which would exhibit Wannier-Stark localization and impede the relaxation dynamics driven by interactions. To first order, these spin-polarized regions need to be larger than the Bloch oscillation amplitude, i.e. the range over which particles can interact with each other (see the correlated hoppings in Sec. 4.2.1), to ensure non-interacting dynamics. Thus we expect that spin-polarized islands become more relevant with increasing Δ_\downarrow/J , when the

Bloch oscillation amplitude becomes small. Comparing a spin-scrambled singlon CDW initial state in the main panel of Fig. 6.7 at tilt $\Delta_{\downarrow} = 3.3J$ with the Néel-ordered singlon CDW initial state in the inset we witness little difference in the relaxation dynamics. Thus spin-polarized islands seem to not play an important role on our time scales.

6.2.4. Long-time dynamics at the tilt resonance

Characteristic for this regime at $U \simeq 2\Delta$ is a resonant generation of doublons, when starting from a singlon CDW initial state. A singlon can hop two lattice sites and convert the released potential energy into interaction energy by forming a doublon. The process is depicted as regime ① in Fig. 6.11b. While we already identified the global minimum of the imbalance in Fig. 6.8b with such a resonance, the imbalance minimum seems to occur at a slightly different interaction strength than the prediction $U = 2\Delta$ (see dashed line in Fig. 6.8b). Here, we precisely determine the resonant interaction strength U_{res} at the minimum of the imbalance in Fig. 6.10a for different tilts Δ_{\downarrow} by using a Gaussian fit to the imbalance \mathcal{I}^{\downarrow} . As expected from the limit of weak tilt (see Fig. 6.9a), where no interaction dependence of the imbalance was observable within the experimental uncertainty, the imbalance minimum becomes more pronounced with increasing tilt and the interaction strength U_{res} is well captured by the Gaussian fit.

In Fig. 6.10b we show the extracted resonant interaction strength U_{res} as a function of the tilt Δ_{\downarrow} and add the numerical simulations for the steady-state imbalance as a two-dimensional color plot. Clearly, the extracted data for the global imbalance minimum agrees well with the imbalance minimum predicted by the numerical simulations. As expected, both the data and the simulations are inconsistent with the naive expectation $U_{\text{res}} = 2\Delta_{\downarrow}$ (dashed line in Fig. 6.10b). The shifted resonance is an artifact of the initial state and the second-order tunneling process involved in the tilt resonance. To second order in the tunneling J , the interaction energy of a doublon in between two holes is corrected according to $2J^2/(U - \Delta) + 2J^2/(U + \Delta) = 4J^2U/(U^2 - \Delta^2)$, where we omitted the spin-dependent tilt for convenience. For $U = 2\Delta$, the tilt resonance is renormalized according to $U = 2\Delta \rightarrow U + 8J^2/(3\Delta^2) = 2\Delta$. This results in $U_{\text{res}} = 2\Delta_{\downarrow} - 8J^2/(3\Delta_{\downarrow}^2)$ (solid line in Fig. 6.10b), which is in excellent agreement with the data.

However, this imbalance reduction cannot solely be explained by the second-order resonant tunneling, because such process cannot change the imbalance: the dynamics has to exclusively take place on sites, with the same parity as used for the preparation of the initial singlon CDW state. A better microscopic understanding of the dynamics in this regime can be obtained from the strongly fragmented effective Hamiltonian $\hat{H}_{\text{eff}}^{\text{res}}$ [Eq. (4.33)] up to second order in $\lambda = J/\Delta$ (the third order vanishes). Higher-order hopping processes $\mathcal{O}(\lambda^4)$ enable additional dynamics in our regime of intermediate tilt and are expected

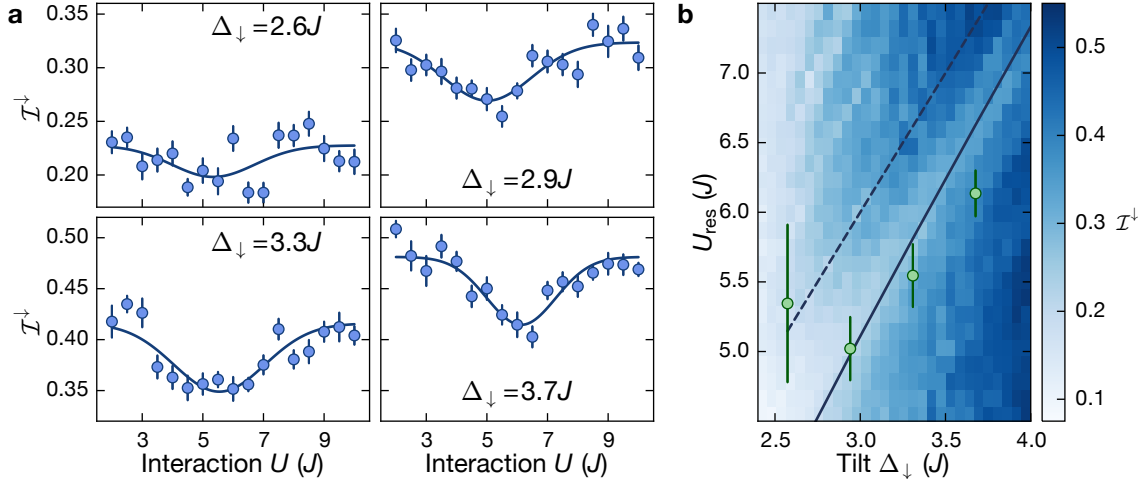


Figure 6.10.: Renormalized onsite interaction in the resonant regime. **a** Interaction scan of the imbalance \mathcal{I}^\downarrow for different tilts Δ_\downarrow . Each data point is averaged three times over ten equally spaced times in a window between 170τ and 200τ . Error bars denote the SEM. The solid line is a Gaussian fit $\mathcal{I}^\downarrow(U) = Ae^{-(U-U_{\text{res}})^2/(2\sigma^2)} + C$ with width σ and offset C , extracting the interaction energy U_{res} , where the imbalance is minimal. The fit yields $U_{\text{res}} = 5.3(6)J$ ($\Delta_\downarrow = 2.6J$), $U_{\text{res}} = 5.0(2)J$ ($\Delta_\downarrow = 2.9J$), $U_{\text{res}} = 5.5(2)J$ ($\Delta_\downarrow = 3.3J$) and $U_{\text{res}} = 6.1(2)J$ ($\Delta_\downarrow = 3.7J$). **b** Resonances extracted from interaction scans for $U > 0$ in (a) for different tilt values. The color plot is obtained using an ED calculation for the same parameters as in the experiment, but without harmonic confinement, for $L = 13$ sites. The dashed line corresponds to the resonance $U_{\text{res}} = 2\Delta_\downarrow$ and the solid line takes into account the second order correction $U_{\text{res}} = 2\Delta_\downarrow - 8J^2/(3\Delta_\downarrow)$. Numerical simulations were carried out by Bharath Hebba Madhusudhana [210].

to eventually melt the CDW completely, although we find in Fig.6.7 that the time scales for these additional processes are larger than experimentally relevant times. Thus the Hamiltonian $\hat{H}_{\text{eff}}^{\text{res}}$ can give good insights in the dominating hoppings processes. These processes are shown in Fig. 6.12c for our initial state, highlighting the importance of doublon-assisted tunneling processes for the reduction of the steady-state imbalance. Furthermore, $\hat{H}_{\text{eff}}^{\text{res}}$ predicts a renormalization of the onsite interaction (Sec. 4.2.2) in agreement with our data and the perturbative result.

6.2.5. Interpretation: Constrained dynamics in the presence of a tilt

In the regime of intermediate tilt, studied in Sec. 6.2.2 and in Sec. 6.2.4 we find evidence that expected higher order contributions $\mathcal{O}(\lambda^4)$ to the effective Hamiltonians $\hat{H}_{\text{eff}}^{\text{res}}$ and $\hat{H}_{\text{eff}}^{\text{dip}}$ might be ineffective on our time scales. This is supported by a numerical analysis in Sec. 4.3.1 for the dipole conserving regime, where higher orders as well as the effective Hamiltonian require the production of doublons, which is penalized by the onsite inter-

6. Experimental results

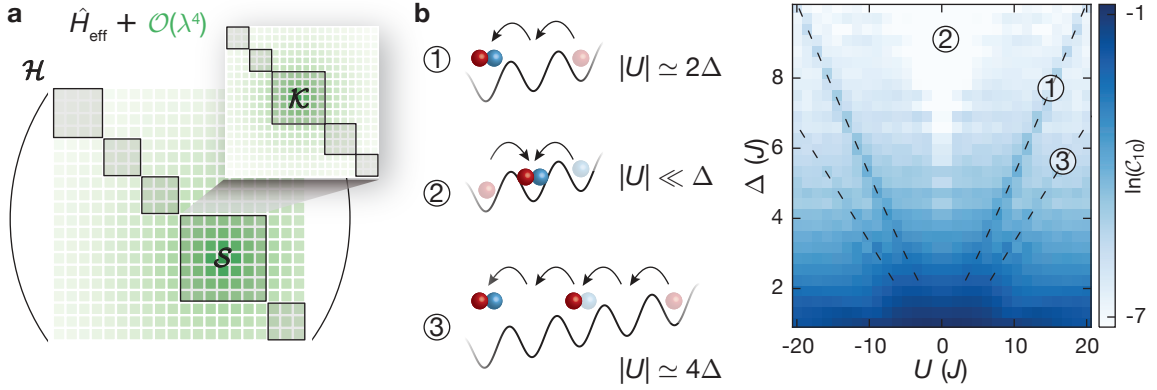


Figure 6.11.: Illustration of the structure of the Hilbert space. **a** Fragmentation of the emergent symmetry sectors \mathcal{S} of the Hilbert space \mathcal{H} of an effective Hamiltonian \hat{H}_{eff} , derived perturbatively in the parameter λ (black), into dynamically disconnected fragments \mathcal{K} . Higher-order terms $\mathcal{O}(\lambda^4)$ (green) soften the block-diagonal structure. **b** Right: Finite-time connectivity \mathcal{C}_ϵ (for a cut-off $\epsilon = 10\%$) as a measure of the fragment size defined as the fraction of states that participate in the dynamics up to an evolution time $T_{\mathcal{N}} = 1000\tau$. The calculation was performed for a Néel-ordered singlon CDW initial state, using exact diagonalization (ED) with system size $L = 13$ and $\Delta_{\uparrow} = \Delta_{\downarrow} \equiv \Delta$. The notation Δ is used, whenever the spin-dependency is neglected for simplicity. We find strongly-fragmented effective Hamiltonians in regime ① and ②, derived perturbatively in the parameter $\lambda = J/\Delta$. Numerical simulations were done by Bharath Hebbe Madhusudhana [210]. Left: dominant resonant tunneling processes for different regimes.

action. In a numerical analysis of the resonant regime in Sec. 4.3.2, where the resonant production of doublons is allowed, we find very slow dynamics even at intermediate tilt $\Delta = 3J$, in agreement with a steady-state imbalance on experimentally accessible time scales. This suggests that the relevant conservation laws of the strongly fragmented Hamiltonians in the limit of large tilt might still be approximately fulfilled on our time scales for the intermediate tilt used in the experiments. The strict block diagonal structure is softened at intermediate tilt and the evolution is no longer completely constrained to a certain fragment, as illustrated in Fig. 6.11a. In such a scenario, one may expect the system to become ergodic, however, several possible effects could still cause the imbalance to retain a finite value up to exponentially-long times. For instance, new renormalized conservation laws may emerge or a prethermal steady-state may develop [225–228].

Motivated by the experimentally observed non-ergodic behavior, we numerically study the dynamically relevant states for our system. If the structure of the strongly-fragmented Hamiltonian and its Krylov subspaces partially survives in our regime, we might be able to identify similar properties in the dynamically relevant set of states. Thus we characterize the dynamics by numerically constructing a dynamical fragment \mathcal{N}_ϵ (see Appendix B), which contains the dominant set of states, that participate in the time evolution up to a time $T_{\mathcal{N}}$ (as defined by a cut-off ϵ) starting from a Néel-ordered singlon CDW. This

allows us to define a finite-time connectivity $\mathcal{C}_\epsilon = \dim(\mathcal{N}_\epsilon) / \dim(\mathcal{H})$, which constitutes a measure for the size of the dynamical fragment \mathcal{N}_ϵ within the Hilbert space restricted to quarter filling and zero magnetization. Such a numerical construction is applicable in the whole parameter regime probed in this work, in contrast to effective Hamiltonians, which can only be derived explicitly in certain limits.

Fig. 6.11b depicts the finite time connectivity as a function of interaction strength and tilt. For simplicity, we study a clean system ($\omega_h = 0$, $\Delta_\uparrow = \Delta_\downarrow \equiv \Delta$) with a Néel-ordered CDW initial state. In the vicinity of the non-interacting limit the finite time connectivity exhibits a minimum, which becomes broader when increasing the tilt towards the dipole conserving regime ②. Here, the connectivity is drastically reduced even at intermediate interaction strength $U \simeq 3J$. Furthermore, we find two pronounced stripes indicating a larger connectivity compared to the dipole conserving regime at $|U| = 2\Delta - 8J^2 / (3\Delta^2)$ (dashed lines in Fig. 6.11b) which indicate the tilt resonance in regime ①. Moreover, a higher order tilt resonance is weakly visible in regime ③. We now focus on the regime $U \approx 2\Delta$, where the set of relevant states is largest due to the resonance between the interaction energy and the tilt energy.

In Fig. 6.12a, we show the density of states in the Hilbert space \mathcal{H} and compare it to the density of states in different numerical fragments. Centered around the energy of the initial state, the density of states acquires a finite width within the numerical fragments, that is approximately set by the many-body bandwidth $\pm 2JN$ of a typical homogeneous system without tilt (dashed line in Fig. 6.12a). In stark contrast to thermal systems, the low finite-time connectivity indicates that only a small fraction of states is relevant for the dynamics. Moreover, this fraction vanishes exponentially in the thermodynamic limit for finite evolution times up to 1000τ (Fig. 6.12b).

Since the perturbative Hamiltonian $\hat{H}_{\text{eff}}^{\text{res}}$ is only valid in the limit of large tilts, the intersection between the numerically constructed fragment and the analytical fragment \mathcal{K}^{res} is small for our experimental parameters $\Delta = 3J$ and $U = 5J$ (Fig. 6.12c). The analytical fragment is constructed by evaluating the connectivity of a Néel-ordered CDW initial state with the effective Hamiltonian $\hat{H}_{\text{eff}}^{\text{res}}$, as explained in Sec. 4.2.3. We expect, that the intersection between both fragments increases when reaching the large tilt limit until both sets coincide for $\lambda \rightarrow 0$. Indeed the normalized intersection saturates to one, although only for $\Delta/J \gg 20$. For this comparison the cut-off value $\epsilon(\mathcal{K}^{\text{res}})$ is chosen such that $\dim(\mathcal{N}_{\epsilon(\mathcal{K}^{\text{res}})}) = \dim(\mathcal{K}^{\text{res}})$, since generally, \mathcal{N}_ϵ contains a much larger number of states. Despite the large value of λ realized in the experiment, we find strong evidence that the slow dynamics is explained by the strongly-fragmented perturbative Hamiltonian, as highlighted by the resonance feature that is visible in the normalized intersection shown in the inset of Fig. 6.12c. The peak in the intersection between the numerical fragment and

6. Experimental results

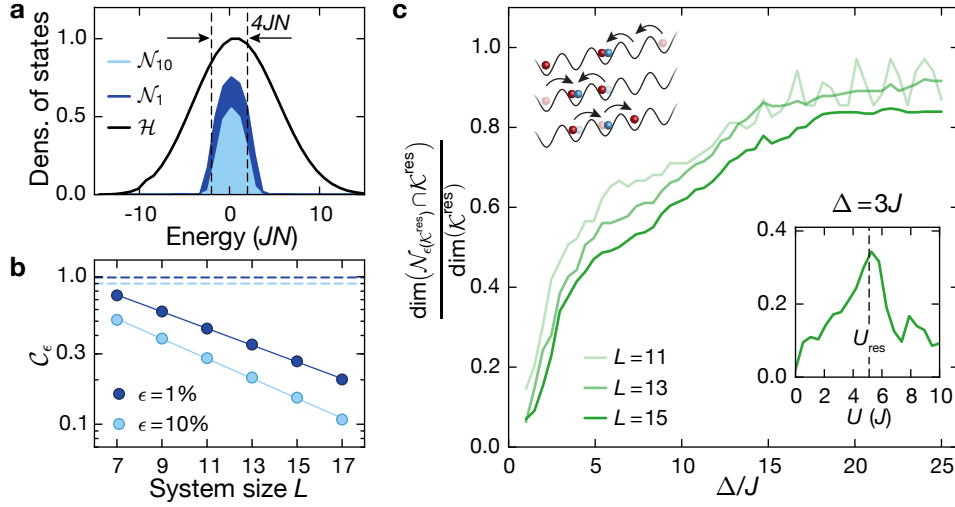


Figure 6.12.: Theoretical analysis of the relevant many-body states for $\omega_h = 0$, $\Delta_\uparrow = \Delta_\downarrow \equiv \Delta$ and a Néel-ordered initial state. **a** Density of states in the full Hilbert space \mathcal{H} restricted to quarter filling and zero magnetization for the numerical fragments \mathcal{N}_1 ($\epsilon = 1\%$), \mathcal{N}_{10} ($\epsilon = 10\%$), $U = 5J$, $\Delta = 3J$ and $T_{\mathcal{N}} = 1000\tau$, normalized to the maximum in \mathcal{H} ; $L = 15$. **b** Scaling of the finite-time connectivity \mathcal{C}_ϵ with system size for a time window $T_{\mathcal{N}} = 1000\tau$, $U = 5J$ and $\Delta = 3J$. Solid lines are exponential fits to the data. Dashed lines are the prediction for the finite-time connectivity of a thermal state, showing a constant scaling at $1 - \epsilon$. **c** Normalized intersection for $U = U_{\text{res}}$ between the Krylov subspace \mathcal{K}^{res} and the numerical fragment $\mathcal{N}_{\epsilon(\mathcal{K}^{\text{res}})}$, where $\dim(\mathcal{N}_{\epsilon(\mathcal{K}^{\text{res}})}) = \dim(\mathcal{K}^{\text{res}})$. The schematic shows the most important processes, connecting the states within the Krylov subspace \mathcal{K}^{res} . Inset: Normalized intersection as in the main plot for $\Delta = 3J$. The dashed line illustrates the resonance condition found in regime ①. Numerical simulations were done by Bharath Hebbe Madhusudhana [210].

the analytical fragment coincides well with the imbalance minimum at the tilt resonance, characterized in Fig. 6.10a, which is located at U_{res} (dashed line in the inset of Fig. 6.12c)

6.3. Conclusion and outlook

In conclusion, we have demonstrated both experimentally and numerically that non-ergodic behavior is present in the tilted 1D Fermi-Hubbard model over a wide range of parameters. This manifests itself through a finite steady-state imbalance up to approximately 700τ . We have found numerical evidence that this non-ergodic behavior is explained by an emergent Hilbert-space fragmentation, which occurs in our model in the dipole conserving regime and in the resonant regime $U \simeq 2\Delta$ in the limit $J/\Delta \rightarrow 0$. The analysis of the steady-state imbalance at late times is complemented with a thorough investigation of the coherent short time dynamics of the imbalance. We observe

real-space Bloch oscillations, which exhibit a strong interaction-induced damping already at weak interaction strength $U \simeq J$. This remarkably strong interaction effect together with the excellent agreement of the experimental results with analytic calculations in the non-interacting limit enabled us to precisely benchmark all important parameters of our system with the short-time dynamics. In this way, we ensure an overall excellent agreement with numerical simulations both in the short-time dynamics and in the non-ergodic long-time dynamics.

Future experiments could systematically investigate the initial-state dependence of the dynamics by preparing initial states within different fragments of the Hilbert-space. This could reveal distinct thermalization properties of the fragments, which is a characteristic feature of Hilbert-space fragmentation [85, 86, 88]. Conceptually it would be also interesting to reconcile the phenomenon of Stark MBL and Hilbert-space fragmentation, by studying the impact of weak disorder or residual harmonic confinement on the long-time dynamics. At late times the dynamics are expected to be dominated by a competition between weak disorder or residual harmonic confinement causing Stark-MBL and the higher-order perturbative processes that drive thermalization in the clean limit [104]. Moreover, periodic modulation could be used as an additional ingredient to realize other strongly-fragmented models, scarred models and time crystals [229–231]. Drive-induced localization could be investigated as well by implementing an oscillating linear potential [232, 233]. Furthermore, an extension to 2D could serve as a benchmark for the robustness of Hilbert-space fragmentation in the presence of multipolar conservation laws [86, 234]. This could be contrasted to recent studies in 2D in the hydrodynamic regime, where a tilt was only applied along one axis [146]. Investigating the stability of Hilbert-space fragmentation in the presence of a photon bath [192] could serve as additional benchmark and can be compared to the stability of a many-body localized system in the presence of such bath [65]. Additionally, it will be interesting to further explore the connection between lattice gauge theories and the phenomenon of Hilbert-space fragmentation [87, 108, 110, 235–237], which could be addressed experimentally in a similar model [238].

Part III.

Appendix

A. Fermi-Hubbard interaction in the Wannier-Stark basis

Here we want to give a derivation for the onsite interaction term in the one-dimensional Fermi-Hubbard model, when using the Wannier-Stark basis. This expression is important for the discussion in Sec. 4.2.1. The onsite interaction in the usual Wannier basis is

$$U \sum_{j \in \mathbb{Z}} \hat{n}_{j,\uparrow} \hat{n}_{j,\downarrow} = U \sum_{j \in \mathbb{Z}} \hat{c}_{j,\uparrow}^\dagger \hat{c}_{j,\uparrow} \hat{c}_{j,\downarrow}^\dagger \hat{c}_{j,\downarrow}, \quad (\text{A.1})$$

where $\hat{c}_{j,\sigma}^\dagger$ ($\hat{c}_{j,\sigma}$) is the fermionic creation (annihilation) operator in Wannier state $|j\rangle$ with spin $\sigma = \{\uparrow, \downarrow\}$ and U tunes the onsite interaction strength. We define the creation (annihilation) operator $\hat{\beta}_{l,\sigma}^\dagger$ ($\hat{\beta}_{l,\sigma}$) of a Wannier-Stark state $|l\rangle$ with spin σ in terms of the Wannier basis

$$\hat{c}_{j,\sigma}^\dagger = \sum_{l \in \mathbb{Z}} \mathcal{J}_{l-j}(\gamma) \hat{\beta}_{l,\sigma}^\dagger, \quad \hat{c}_{j,\sigma} = \sum_{l \in \mathbb{Z}} \mathcal{J}_{l-j}(\gamma) \hat{\beta}_{l,\sigma}, \quad (\text{A.2})$$

where $\gamma = 2J/\Delta$ and $\mathcal{J}_i(\gamma)$ is the i^{th} -order Bessel function of the first kind. Next, we express the onsite interaction term with the Wannier-Stark operators

$$U \sum_{j \in \mathbb{Z}} \sum_{l,m,p,q \in \mathbb{Z}} \mathcal{J}_{m-j}(\gamma) \mathcal{J}_{l-j}(\gamma) \mathcal{J}_{q-j}(\gamma) \mathcal{J}_{p-j}(\gamma) \hat{\beta}_{m,\uparrow}^\dagger \hat{\beta}_{l,\uparrow} \hat{\beta}_{q,\downarrow}^\dagger \hat{\beta}_{p,\downarrow}. \quad (\text{A.3})$$

In the subsequent sections, we derive a simplified version of Eq. (A.3) and calculate the leading order term in the limit of large tilt Δ .

A.1. Identities of Bessel functions

A couple of Bessel function identities are important for the subsequent calculations in the next sections. First, we require Neumann's formula to simply a product of two Bessel functions:

$$\mathcal{J}_p(x)\mathcal{J}_q(x) = \frac{2}{\pi} \int_0^{\pi/2} d\theta \cos[(p-q)\theta] \mathcal{J}_{p+q}[(2x \cos(\theta))]. \quad (\text{A.4})$$

Second, we require the representation of Bessel function in terms of an integral:

$$\mathcal{J}_n(x) = \frac{1}{2\pi} \int_{-\pi}^{\pi} d\tau e^{ix \sin(\tau) - in\tau}. \quad (\text{A.5})$$

Third, the Jacobi-Anger expansion for Bessel functions is very useful to convert complex exponential into Bessel functions:

$$e^{iz \cos(\psi)} = \sum_{n \in \mathbb{Z}} i^n \mathcal{J}_n(z) e^{in\psi}. \quad (\text{A.6})$$

Fourth, we conclude with important Bessel function identities concerning their parity:

$$\mathcal{J}_n(-x) = (-1)^n \mathcal{J}_n(x), \quad \mathcal{J}_{-n}(x) = (-1)^n \mathcal{J}_n(x). \quad (\text{A.7})$$

A derivation of all identities can be found in "A treatise on the theory of Bessel functions" by Watson [239].

A.2. Onsite interactions in the Wannier-Stark basis

We start the derivation with the onsite interaction term, expressed with the Wannier-Stark operators

$$U \sum_{j \in \mathbb{Z}} \sum_{l, m, p, q \in \mathbb{Z}} \mathcal{J}_{m-j}(\gamma) \mathcal{J}_{l-j}(\gamma) \mathcal{J}_{q-j}(\gamma) \mathcal{J}_{p-j}(\gamma) \hat{\beta}_{m,\uparrow}^\dagger \hat{\beta}_{l,\uparrow} \hat{\beta}_{q,\downarrow}^\dagger \hat{\beta}_{p,\downarrow}. \quad (\text{A.8})$$

First, we use Neumann's formula in Eq. (A.4) to simply this expression, by reducing the product of four Bessel functions into a product of two Bessel functions:

$$\begin{aligned}
 U \sum_{j \in \mathbb{Z}} \sum_{l, m, p, q \in \mathbb{Z}} \left(\frac{2}{\pi} \right)^2 \int_0^{\pi/2} \int_0^{\pi/2} d\theta d\phi \cos[(m-l)\theta] \mathcal{J}_{m+l-2j}[2\gamma \cos(\theta)] \\
 \times \cos[(q-p)\phi] \mathcal{J}_{q+p-2j}[2\gamma \cos(\phi)] \hat{\beta}_{m,\uparrow}^\dagger \hat{\beta}_{l,\uparrow} \hat{\beta}_{q,\downarrow}^\dagger \hat{\beta}_{p,\downarrow}.
 \end{aligned} \tag{A.9}$$

The sum over j in Eq. (A.9) only affects the product of the two remaining Bessel functions. Therefore, we first focus on this sum and take advantage of the integral representation of the Bessel function in Eq. (A.5) and the Jacobi-Anger expansion in Eq. (A.6). With these two identities, the sum over j in Eq. (A.9) can be expressed as

$$\begin{aligned}
 & \sum_{j \in \mathbb{Z}} \mathcal{J}_{m+l-2j}[2\gamma \cos(\theta)] \mathcal{J}_{q+p-2j}[2\gamma \cos(\phi)] \\
 &= \sum_{j \in \mathbb{Z}} \left(\frac{1}{2\pi} \right)^2 \int_{-\pi}^{\pi} d\tau \int_{-\pi}^{\pi} d\tau' e^{i2\gamma \cos(\theta) \sin(\tau) - i(m+l-2j)\tau} e^{i2\gamma \cos(\phi) \sin(\tau') - i(q+p-2j)\tau'} \\
 &= \sum_{j \in \mathbb{Z}} \left(\frac{1}{2\pi} \right)^2 \iint d\tau d\tau' \sum_{n, n' \in \mathbb{Z}} i^{n+n'} J_n[2\gamma \sin(\tau)] J_{n'}[2\gamma \sin(\tau')] e^{in\theta} e^{in'\phi} \\
 & \times e^{-i(m+l-2j)\tau} e^{-i(q+p-2j)\tau'} \\
 &= \left(\frac{1}{2\pi} \right)^2 \iint d\tau d\tau' \sum_{n, n' \in \mathbb{Z}} i^{n+n'} J_n[2\gamma \sin(\tau)] J_{n'}[2\gamma \sin(\tau')] e^{in\theta} e^{in'\phi} \\
 & \times e^{-i(m+l)\tau} e^{-i(q+p)\tau'} \sum_{j \in \mathbb{Z}} e^{i2j(\tau+\tau')} \\
 &= \left(\frac{1}{2\pi} \right)^2 \iint d\tau d\tau' \sum_{n, n' \in \mathbb{Z}} i^{n+n'} J_n[2\gamma \sin(\tau)] J_{n'}[2\gamma \sin(\tau')] e^{in\theta} e^{in'\phi} \\
 & \times e^{-i(m+l)\tau} e^{-i(q+p)\tau'} \sum_{j \in \mathbb{Z}} e^{i2j(\tau+\tau')} \\
 &= \left(\frac{1}{2\pi} \right)^2 \iint d\tau d\tau' \sum_{n, n' \in \mathbb{Z}} i^{n+n'} J_n[2\gamma \sin(\tau)] J_{n'}[2\gamma \sin(\tau')] e^{in\theta} e^{in'\phi} \\
 & \times e^{-i(m+l)\tau} e^{-i(q+p)\tau'} 2\pi \delta[(\tau + \tau')] \\
 &= \frac{1}{2\pi} \int d\tau \sum_{n, n' \in \mathbb{Z}} i^{n+n'} J_n[2\gamma \sin(\tau)] J_{n'}[2\gamma \sin(-\tau)] e^{in\theta} e^{in'\phi} e^{i(q+p-m-l)\tau}.
 \end{aligned} \tag{A.10}$$

Next, we insert Eq. (A.10) into Eq. (A.9) to integrate with respect to $d\phi$ and $d\theta$.

$$\begin{aligned}
U \sum_{l,m,p,q \in \mathbb{Z}} \left(\frac{2}{\pi} \right)^2 \int_0^{\pi/2} \int_0^{\pi/2} d\theta d\phi \cos[(m-l)\theta] \cos[(q-p)\phi] \\
\times \frac{1}{2\pi} \int d\tau \sum_{n,n' \in \mathbb{Z}} i^{n+n'} J_n[2\gamma \sin(\tau)] J_{n'}[2\gamma \sin(-\tau)] e^{in\theta} e^{in'\phi} e^{i(q+p-m-l)\tau} \quad (\text{A.11}) \\
\times \hat{\beta}_{m,\uparrow}^\dagger \hat{\beta}_{l,\uparrow} \hat{\beta}_{q,\downarrow}^\dagger \hat{\beta}_{p,\downarrow}.
\end{aligned}$$

Thus, we need to solve the following product of two integrals

$$\begin{aligned}
& \int_0^{\pi/2} d\theta \cos[(m-l)\theta] e^{in\theta} \int_0^{\pi/2} d\phi \cos[(q-p)\phi] e^{in'\phi} \\
&= \frac{1}{4} \int_0^{\pi/2} d\theta \left(e^{i(n-m+l)\theta} + e^{i(n+m-l)\theta} \right) \int_0^{\pi/2} d\phi \left(e^{i(n'-q+p)\phi} + e^{i(n'+q-p)\phi} \right) \quad (\text{A.12}) \\
&= \frac{\pi^2}{16} \left(\delta_{n,m-l} + \delta_{n,l-m} \right) \left(\delta_{n',q-p} + \delta_{n',p-q} \right) \\
&= \frac{\pi^2}{16} \left(\delta_{n,m-l} \delta_{n',q-p} + \delta_{n,m-l} \delta_{n',p-q} + \delta_{n,l-m} \delta_{n',q-p} + \delta_{n,l-m} \delta_{n',p-q} \right).
\end{aligned}$$

Inserting this result into Eq. (A.11) yields

$$\begin{aligned}
U \sum_{l,m,p,q \in \mathbb{Z}} \left(\frac{2}{\pi} \right)^2 \frac{1}{2\pi} \int d\tau \sum_{n,n' \in \mathbb{Z}} i^{n+n'} J_n[2\gamma \sin(\tau)] J_{n'}[2\gamma \sin(-\tau)] e^{i(q+p-m-l)\tau} \\
\times \frac{\pi^2}{16} \left(\delta_{n,m-l} \delta_{n',q-p} + \delta_{n,m-l} \delta_{n',p-q} + \delta_{n,l-m} \delta_{n',q-p} + \delta_{n,l-m} \delta_{n',p-q} \right) \\
\times \hat{\beta}_{m,\uparrow}^\dagger \hat{\beta}_{l,\uparrow} \hat{\beta}_{q,\downarrow}^\dagger \hat{\beta}_{p,\downarrow} \\
= U \sum_{l,m,p,q \in \mathbb{Z}} \frac{1}{8\pi} \int d\tau e^{i(q+p-m-l)\tau} \left(i^{m-l+q-p} J_{m-l}[2\gamma \sin(\tau)] J_{q-p}[2\gamma \sin(-\tau)] \quad (\text{A.13}) \right. \\
+ i^{m-l+p-q} J_{m-l}[2\gamma \sin(\tau)] J_{p-q}[2\gamma \sin(-\tau)] \\
+ i^{l-m+q-p} J_{l-m}[2\gamma \sin(\tau)] J_{q-p}[2\gamma \sin(-\tau)] \\
+ i^{l-m+p-q} J_{l-m}[2\gamma \sin(\tau)] J_{p-q}[2\gamma \sin(-\tau)] \left. \right) \\
\times \hat{\beta}_{m,\uparrow}^\dagger \hat{\beta}_{l,\uparrow} \hat{\beta}_{q,\downarrow}^\dagger \hat{\beta}_{p,\downarrow}
\end{aligned}$$

Finally, we use the identities for the parity of Bessel functions [Eq. (A.7)] to further simplify the sums in Eq. (A.13)

$$\begin{aligned}
& i^{m-l+q-p} J_{m-l}[2\gamma \sin(\tau)] J_{q-p}[2\gamma \sin(-\tau)] + i^{m-l+p-q} J_{m-l}[2\gamma \sin(\tau)] J_{p-q}[2\gamma \sin(-\tau)] \\
& + i^{l-m+q-p} J_{l-m}[2\gamma \sin(\tau)] J_{q-p}[2\gamma \sin(-\tau)] + i^{l-m+p-q} J_{l-m}[2\gamma \sin(\tau)] J_{p-q}[2\gamma \sin(-\tau)] \\
& = 4i^{m-l+q-p} J_{m-l}[2\gamma \sin(\tau)] J_{q-p}[2\gamma \sin(-\tau)] \\
& = 4i^{m-l+p-q} J_{m-l}[2\gamma \sin(\tau)] J_{q-p}[2\gamma \sin(\tau)].
\end{aligned} \tag{A.14}$$

Thus, the onsite interaction term in the Wannier-Stark basis can be expressed as

$$\begin{aligned}
\frac{U}{2\pi} \sum_{l,m,p,q \in \mathbb{Z}} i^{m-l+p-q} \int_{-\pi}^{\pi} d\tau e^{i(q+p-m-l)\tau} J_{m-l}[2\gamma \sin(\tau)] J_{q-p}[2\gamma \sin(\tau)] \\
\times \hat{\beta}_{m,\uparrow}^{\dagger} \hat{\beta}_{l,\uparrow} \hat{\beta}_{q,\downarrow}^{\dagger} \hat{\beta}_{p,\downarrow}.
\end{aligned} \tag{A.15}$$

We check that his expression is hermitian. Furthermore, in the limit $J/\Delta \rightarrow 0$ the transformation between the Wannier-Stark basis and the Wannier basis in Eq. (A.2) is equivalent to the identity. Therefore, we should recover an onsite interaction strength U for the onsite interactions in both the Wannier-Stark basis and the Wannier basis. In the Wannier-Stark basis, the matrix element for the "onsite" interaction strength $\hat{\beta}_{m,\uparrow}^{\dagger} \hat{\beta}_{m,\uparrow} \hat{\beta}_{m,\downarrow}^{\dagger} \hat{\beta}_{m,\downarrow}$ can be used to calculated the limit

$$\lim_{J/\Delta \rightarrow 0} \frac{U}{2\pi} \int_{-\pi}^{\pi} d\tau \mathcal{J}_0 \left[\frac{4J}{\Delta} \sin(\tau) \right] \mathcal{J}_0 \left[\frac{4J}{\Delta} \sin(\tau) \right] = \frac{U}{2\pi} \int_{-\pi}^{\pi} d\tau \mathcal{J}_0^2(0) = U. \tag{A.16}$$

This is in agreement with our expectations in the limit of large tilt and an important sanity check for the result in Eq. (A.15).

B. Numerical analysis of the dynamically relevant states

B.1. Construction of the numerical fragment

This section outlines how the dynamically most relevant states are identified in the occupation number basis and the set of these states defines the numerical fragment. We define the numerical fragment \mathcal{N}_ϵ as the span of a subset \mathcal{B}_ϵ of the number basis \mathcal{B} of the Hilbert space \mathcal{H} , where \mathcal{H} is restricted to quarter filling and zero magnetization due to the CDW initial state, prepared in the experiments (Sec. 5.2). We define the set \mathcal{B}_ϵ via its complement, $\mathcal{B}_\epsilon = \mathcal{B} \setminus \mathcal{B}_\epsilon^c$, where \mathcal{B}_ϵ^c would be ideally defined as the largest subset of \mathcal{B} satisfying $\max_{t < T_N} \sum_{n^c \in \mathcal{B}_\epsilon^c} |\langle n^c | \psi(t) \rangle|^2 < \epsilon$. Here T_N defines a time window for the evolution of the initial state $|\psi(t=0)\rangle$. Equivalently, a definition of the subset \mathcal{B}_ϵ as the smallest one, satisfying $\min_{t < T_N} \sum_{n \in \mathcal{B}_\epsilon} |\langle n | \psi(t) \rangle|^2 \geq 1 - \epsilon$ might also work. We use the complement, because it is easier to implement numerically.

This inequality condition for the complement would ensure that the residual overlap of $|\psi(t)\rangle$ outside of \mathcal{N}_ϵ at any time $t \leq T_N$ is bounded by ϵ . Constructing this \mathcal{B}_ϵ^c , however, involves a search in the powerset of \mathcal{B} , which is exponential in the dimension of \mathcal{H} . This is intractable even for relatively small system sizes such as $L = 7$. It follows from the inequality $\max_{t < T_N} \sum_{n^c} |\langle n^c | \psi(t) \rangle|^2 \leq \sum_{n^c} \max_{t < T_N} |\langle n^c | \psi(t) \rangle|^2$ that keeping the latter sum smaller than ϵ will ensure that the former sum is also bounded by ϵ . Moreover, the latter sum is computationally easier to handle. Hence, we use it to define the fragment.

Since we construct the numerical fragment \mathcal{N}_ϵ using a subset \mathcal{B}_ϵ^c , which is defined such that $\sum_{n^c} \max_{t < T_N} |\langle n^c | \psi(t) \rangle|^2 < \epsilon$, it is important to understand the gap in the related inequality $\max_{t < T_N} \sum_{n^c} |\langle n^c | \psi(t) \rangle|^2 \leq \sum_{n^c} \max_{t < T_N} |\langle n^c | \psi(t) \rangle|^2$. This gap only loosely depends on the sum $\sum_{n \in \mathcal{B}} \max_{t < T_N} |\langle n | \psi(t) \rangle|^2$, which is in general, not normalized. Although this sum can be as large as the dimension of \mathcal{H} , in the examples that we study, it remains small, i.e., < 10 for $L < 20$, and grows logarithmically in the dimension of \mathcal{H} .

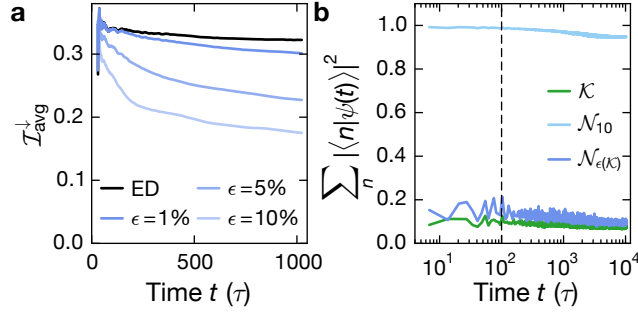


Figure B.1: Numerical fragment \mathcal{N}_ϵ . Both figures use $U = 5J$ and $\Delta_\downarrow = \Delta_\uparrow = 3J$. **a** Imbalance time traces calculated with different sets of states \mathcal{N}_ϵ and ED for $U = 5J$ and $\Delta = 3J$. $I_{\text{avg}}^\downarrow$ is calculated using a cumulative sum to reduce fluctuations; $L = 11$. **b** Contribution of the set of states $|n\rangle$ in the numerical fragments $\mathcal{N}_{\epsilon(\mathcal{K}^{\text{res}})}$ and \mathcal{N}_{10} and the fragment \mathcal{K}^{res} to the time-evolved initial state $|\psi(t)\rangle$. $T_{\mathcal{N}} = 100\tau$ (dashed line). Numerical simulation were performed by Bharath Hebhe Madhusudhana [210].

B.2. Numerical fragment \mathcal{N}_ϵ versus fragment \mathcal{K}^{res}

In Fig. B.1a, we investigate how well the imbalance can be captured, when using only the states within the numerical fragment. These states correspond to a small fraction compared to the states within the full Hilbert space and this fraction was found to vanish in the thermodynamic limit (Fig. 6.12b). We show imbalance time traces, calculated with a cumulative sum to reduce fluctuations and compare traces with different cut-off values ϵ to the exact numerical result, which we obtained with ED. We find that for $U = 5J$ and $\Delta = 3J$, already with a cut-off $\epsilon = 1\%$ we can reproduce the exact result well, larger cut-off values result in a deviation, which becomes more pronounced at later times.

In Fig. B.1b we show the overlap of the states $|n\rangle$ in different numerical fragments and in the Krylov subspace \mathcal{K}^{res} defined by the effective Hamiltonian $\hat{H}_{\text{eff}}^{\text{res}}$ [Eq. (4.33)] with the time evolved initial state $|\psi(t)\rangle$ is analyzed by calculating $\sum_n |\langle n|\psi(t)\rangle|^2$. While the overlap in our parameter regime is poorly captured by the states in the Krylov subspace \mathcal{K}^{res} (as expected because these states best describe the time evolution only in the limit $|U| = 2\Delta \gg J$), we can find the proper states by choosing a small enough ϵ . For \mathcal{N}_1 we get $\sum_n |\langle n|\psi(t)\rangle|^2 \approx 1$, which shows a very weak decay even up to $t = 10^4\tau$. Note that it is crucial to choose enough states for the numerical fragment. If we choose the same number of states as used in the Krylov subspace \mathcal{K}^{res} for the numerical fragment $\mathcal{N}_{\epsilon(\mathcal{K}^{\text{res}})}$, we cannot capture the time evolved initial state $|\psi(t)\rangle$ well.

Bibliography

- [1] J. M. Deutsch. “Quantum statistical mechanics in a closed system”. *Phys. Rev. A* 43.4 (1991), pp. 2046–2049 (cit. on pp. 1, 73).
- [2] M. Srednicki. “Chaos and quantum thermalization”. *Phys. Rev. E* 50.2 (1994), pp. 888–901 (cit. on pp. 1, 73).
- [3] M. Rigol, V. Dunjko, and M. Olshanii. “Thermalization and its mechanism for generic isolated quantum systems”. *Nature* 452.7189 (2008), pp. 854–858 (cit. on pp. 1, 73).
- [4] N. S. Krylov. *Works on the Foundation of Statistical Physics*. Princeton University Press, 1980 (cit. on p. 1).
- [5] G. Gallavotti. *Statistical Mechanics: A Short Treatise*. Springer, 1999 (cit. on p. 1).
- [6] P. Calabrese, F. H. L. Essler, and M. Fagotti. “Quantum Quench in the Transverse-Field Ising Chain”. *Phys. Rev. Lett.* 106.22 (2011), p. 227203 (cit. on pp. 1, 53, 75).
- [7] H. Bethe. “Zur Theorie der Metalle”. *Zeitschrift der Physik* 71 (3 1931), pp. 205–226 (cit. on pp. 1, 21).
- [8] B. Sutherland. *Beautiful Models*. WORLD SCIENTIFIC, 2004 (cit. on pp. 1, 2, 21).
- [9] F. Essler, H. Frahm, F. Göhmann, A. Klümper, and V. E. Korepin. “The one-dimensional Hubbard model”. *Cambridge University Press* (2005) (cit. on pp. 1, 7, 21).
- [10] E. H. Lieb and F. Y. Wu. “Absence of Mott Transition in an Exact Solution of the Short-Range, One-Band Model in One Dimension”. *Phys. Rev. Lett.* 20 (25 1968), p. 1445 (cit. on pp. 1, 2).
- [11] P. W. Anderson. “Absence of Diffusion in Certain Random Lattices”. *Phys. Rev.* 109 (5 1958), pp. 1492–1505 (cit. on p. 1).
- [12] E. Altman. “Many-body localization and quantum thermalization”. *Nat. Phys.* 14.10 (2018), pp. 979–983 (cit. on pp. 1, 2).
- [13] J. Z. Imbrie, V. Ros, and A. Scardicchio. “Local integrals of motion in many-body localized systems”. *Ann. Phys.* 529.7 (2017), p. 1600278 (cit. on p. 1).

- [14] M. Serbyn, Z. Papić, and D. A. Abanin. “Local Conservation Laws and the Structure of the Many-Body Localized States”. *Phys. Rev. Lett.* 111.12 (2013), p. 127201 (cit. on p. 1).
- [15] D. A. Huse, R. Nandkishore, and V. Oganesyan. “Phenomenology of fully many-body-localized systems”. *Phys. Rev. B* 90.17 (2014), p. 174202 (cit. on p. 1).
- [16] B. Bauer and C. Nayak. “Area laws in a many-body localized state and its implications for topological order”. *J. Stat. Mech. Theor. Exp.* 2013.09 (2013), P09005 (cit. on p. 1).
- [17] D. A. Huse, R. Nandkishore, V. Oganesyan, A. Pal, and S. L. Sondhi. “Localization-protected quantum order”. *Phys. Rev. B* 88.1 (2013), p. 014206 (cit. on p. 1).
- [18] R. Nandkishore and D. A. Huse. “Many-Body Localization and Thermalization in Quantum Statistical Mechanics”. *Annu. Rev. Condens. Matter Phys.* 6.1 (2015), pp. 15–38 (cit. on pp. 1, 53, 73, 75).
- [19] E. Altman and R. Vosk. “Universal Dynamics and Renormalization in Many-Body-Localized Systems”. *Annu. Rev. Condens. Matter Phys.* 6.1 (2015), pp. 383–409 (cit. on pp. 1, 53, 73, 75).
- [20] D. A. Abanin, E. Altman, I. Bloch, and M. Serbyn. “Colloquium : Many-body localization, thermalization, and entanglement”. *Rev. Mod. Phys.* 91.2 (2019), p. 021001 (cit. on pp. 1, 53, 73, 75).
- [21] J. H. Bardarson, F. Pollmann, and J. E. Moore. “Unbounded Growth of Entanglement in Models of Many-Body Localization”. *Phys. Rev. Lett.* 109 (1 2012), p. 017202 (cit. on p. 1).
- [22] R. Kosloff. “Quantum Thermodynamics: A Dynamical Viewpoint”. *Entropy* 15.6 (2013), pp. 2100–2128 (cit. on p. 1).
- [23] J. Eisert, M. Friesdorf, and C. Gogolin. “Quantum many-body systems out of equilibrium”. *Nat. Phys.* 11.2 (2015), pp. 124–130 (cit. on p. 2).
- [24] A. Polkovnikov, K. Sengupta, A. Silva, and M. Vengalattore. “Colloquium: Nonequilibrium dynamics of closed interacting quantum systems”. *Rev. Mod. Phys.* 83.3 (2011), pp. 863–883 (cit. on p. 2).
- [25] J. Z. Imbrie. “On Many-Body Localization for Quantum Spin Chains”. *J. Stat. Phys.* 163.5 (2016), pp. 998–1048 (cit. on p. 2).
- [26] I. Bloch, J. Dalibard, and W. Zwerger. “Many-body physics with ultracold gases”. *Rev. Mod. Phys.* 80.3 (2008), pp. 885–964 (cit. on p. 2).
- [27] T. Langen, R. Geiger, and J. Schmiedmayer. “Ultracold Atoms Out of Equilibrium”. *Annu. Rev. Condens. Matter Phys.* 6.1 (2015), pp. 201–217 (cit. on p. 2).

-
- [28] R. Blatt and C. F. Roos. “Quantum simulations with trapped ions”. *Nat. Phys.* 8.4 (2012), pp. 277–284 (cit. on p. 2).
- [29] M. Kjaergaard, M. E. Schwartz, J. Braumüller, P. Krantz, J. I.-J. Wang, S. Gustavsson, and W. D. Oliver. “Superconducting Qubits: Current State of Play”. *Annu. Rev. Condens. Matter Phys.* 11.1 (2020), pp. 369–395 (cit. on p. 2).
- [30] A. Browaeys and T. Lahaye. “Many-body physics with individually controlled Rydberg atoms”. *Nat. Phys.* 16.2 (2020), pp. 132–142 (cit. on p. 2).
- [31] T. Kinoshita, T. Wenger, and D. S. Weiss. “A quantum Newton’s cradle”. *Nature* 440 (2006), p. 900 (cit. on p. 2).
- [32] S. Hofferberth, I. Lesanovsky, B. Fisher, T. Schumm, and J. Schmiedmayer. “Non-equilibrium coherence dynamics in one-dimensional Bose gases”. *Nature* 449 (2007), p. 324 (cit. on p. 2).
- [33] M. Rigol. “Breakdown of Thermalization in Finite One-Dimensional Systems”. *Phys. Rev. Lett.* 103.10 (2009), p. 100403 (cit. on p. 2).
- [34] B. Paredes, A. Widera, V. Murg, O. Mandel, S. Fölling, I. Cirac, G. V. Shlyapnikov, T. W. Hänsch, and I. Bloch. “Tonks–Girardeau gas of ultracold atoms in an optical lattice”. *Nature* 429.6989 (2004), pp. 277–281 (cit. on p. 2).
- [35] J. M. Wilson, N. Malvania, Y. Le, Y. Zhang, M. Rigol, and D. S. Weiss. “Observation of dynamical fermionization”. *Science* 367.6485 (2020), pp. 1461–1464 (cit. on p. 2).
- [36] M. A. Cazalilla, R. Citro, T. Giamarchi, E. Orignac, and M. Rigol. “One dimensional bosons: From condensed matter systems to ultracold gases”. *Rev. Mod. Phys.* 83 (4 2011), p. 1405 (cit. on pp. 2, 7).
- [37] J. Berges, S. Borsányi, and C. Wetterich. “Prethermalization”. *Phys. Rev. Lett.* 93.14 (2004), p. 142002 (cit. on p. 2).
- [38] L. Vidmar and M. Rigol. “Generalized Gibbs ensemble in integrable lattice models”. *J. Stat. Mech. Theor. Exp.* 2016.6 (2016), p. 064007 (cit. on pp. 2, 7).
- [39] M. Gring, M. Kuhnert, T. Langen, T. Kitagawa, B. Rauer, M. Schreitl, I. Mazets, D. A. Smith, E. Demler, and J. Schmiedmayer. “Relaxation and Prethermalization in an Isolated Quantum System”. *Science* 337.6100 (2012), pp. 1318–1322 (cit. on p. 2).
- [40] C.-M. Schmied, A. N. Mikheev, and T. Gasenzer. “Non-thermal fixed points: Universal dynamics far from equilibrium”. *Int. J. Mod. Phys. A* 34.29 (2019), p. 1941006 (cit. on p. 2).
- [41] S. Erne, R. Bücker, T. Gasenzer, J. Berges, and J. Schmiedmayer. “Universal dynamics in an isolated one-dimensional Bose gas far from equilibrium”. *Nature* 563.7730 (2018), pp. 225–229 (cit. on p. 2).

- [42] M. Prüfer, P. Kunkel, H. Strobel, S. Lannig, D. Linnemann, C.-M. Schmied, J. Berges, T. Gasenzer, and M. K. Oberthaler. “Observation of universal dynamics in a spinor Bose gas far from equilibrium”. *Nature* 563.7730 (2018), pp. 217–220 (cit. on p. 2).
- [43] X. Zotos, F. Naef, and P. Prelovšek. “Transport and conservation laws”. *Phys. Rev. B* 55 (1997), p. 11029 (cit. on pp. 2, 7).
- [44] F. Heidrich-Meisner, A. Honecker, and W. Brenig. “Transport in quasi one-dimensional spin-1/2 systems”. *Eur. Phys. J. Special Topics* 151 (2007), p. 135 (cit. on pp. 2, 7).
- [45] R. Vasseur and J. Moore. “Nonequilibrium quantum dynamics and transport: from integrability to many-body localization”. *J. Stat. Mech. Theor. Exp.* 2016.6 (2016), p. 064010 (cit. on pp. 2, 7).
- [46] C. Karrasch, T. Prosen, and F. Heidrich-Meisner. “Proposal for measuring the finite-temperature Drude weight of integrable systems”. *Phys. Rev. B* 95 (6 2017), p. 060406 (cit. on pp. 2, 7).
- [47] H. Ott, E. de Mirandes, F. Ferlino, G. Roati, G. Modugno, and M. Inguscio. “Collisionally Induced Transport in Periodic Potentials”. *Phys. Rev. Lett.* 92 (2004), p. 160601 (cit. on p. 2).
- [48] N. Strohmaier, Y. Takasu, K. Günter, R. Jördens, M. Köhl, H. Moritz, and T. Esslinger. “Interaction-Controlled Transport of an Ultracold Fermi Gas”. *Phys. Rev. Lett.* 99 (2007), p. 220601 (cit. on p. 2).
- [49] U. Schneider, L. Hackermüller, J. P. Ronzheimer, S. Will, S. Braun, T. Best, I. Bloch, E. Demler, S. Mandt, D. Rasch, and A. Rosch. “Fermionic transport and out-of-equilibrium dynamics in a homogeneous Hubbard model with ultracold atoms”. *Nat. Phys.* 8 (2012), p. 213 (cit. on pp. 2, 7, 20, 25).
- [50] J. P. Ronzheimer, M. Schreiber, S. Braun, S. S. Hodgman, S. Langer, I. P. McCulloch, F. Heidrich-Meisner, I. Bloch, and U. Schneider. “Expansion Dynamics of Interacting Bosons in Homogeneous Lattices in One and Two Dimensions”. *Phys. Rev. Lett.* 110 (20 2013), p. 205301 (cit. on pp. 2, 4, 7, 13, 20, 25, 38, 50, 51).
- [51] L. Xia, J. Carrasquilla, A. Reinhard, J. M. Wilson, M. Rigol, and D. S. Weiss. “Quantum distillation and confinement of vacancies in a doublon sea”. *Nat. Phys.* 11 (4 2015), pp. 316–320 (cit. on pp. 2, 7, 41).
- [52] L. Vidmar, J. P. Ronzheimer, M. Schreiber, S. Braun, S. S. Hodgman, S. Langer, F. Heidrich-Meisner, I. Bloch, and U. Schneider. “Dynamical Quasicondensation of Hard-Core Bosons at Finite Momenta”. *Phys. Rev. Lett.* 115 (17 2015), p. 175301 (cit. on p. 2).
- [53] W. Xu, W. McGehee, W. Morong, and B. DeMarco. “Bad Metal in a Fermi Lattice Gas”. *arXiv:1606.06669* (2016) (cit. on p. 2).

-
- [54] R. Anderson, F. Wang, P. Xu, V. Venu, S. Trotzky, F. Chevy, and J. H. Thywissen. “Conductivity Spectrum of Ultracold Atoms in an Optical Lattice”. *Phys. Rev. Lett.* 122 (15 2019), p. 153602 (cit. on p. 2).
- [55] P. T. Brown, D. Mitra, E. Guardado-Sanchez, R. Nourafkan, A. Reymbaut, C.-D. Hébert, S. Bergeron, A.-M. S. Tremblay, J. Kokalj, D. A. Huse, P. Schauß, and W. S. Bakr. “Bad metallic transport in a cold atom Fermi-Hubbard system”. *Science* 363.6425 (2019), pp. 379–382 (cit. on pp. 2, 4).
- [56] S. Hild, T. Fukuhara, P. Schauß, J. Zeiher, M. Knap, E. Demler, I. Bloch, and C. Gross. “Far-from-Equilibrium Spin Transport in Heisenberg Quantum Magnets”. *Phys. Rev. Lett.* 113.14 (2014), p. 147205 (cit. on p. 2).
- [57] N. Jepsen, J. Amato-Grill, I. Dimitrova, W. W. Ho, E. Demler, and W. Ketterle. “Spin transport in a tunable Heisenberg model realized with ultracold atoms”. *arXiv:2005.09549* (2020) (cit. on p. 2).
- [58] M. A. Nichols, L. W. Cheuk, M. Okan, T. R. Hartke, E. Mendez, T. Senthil, E. Khatami, H. Zhang, and M. W. Zwierlein. “Spin transport in a Mott insulator of ultracold fermions”. *Science* 363.6425 (2019), pp. 383–387 (cit. on p. 2).
- [59] J.-P. Brantut, J. Meineke, D. Stadler, S. Krinner, and T. Esslinger. “Conduction of Ultracold Fermions Through a Mesoscopic Channel”. *Science* 337.6098 (2012), pp. 1069–1071 (cit. on p. 2).
- [60] G. Valtolina, A. Burchianti, A. Amico, E. Neri, K. Khani, J. A. Seman, A. Trombettoni, A. Smerzi, M. Zaccanti, M. Inguscio, and G. Roati. “Josephson effect in fermionic superfluids across the BEC-BCS crossover”. *Science* 350.6267 (2015), pp. 1505–1508 (cit. on p. 2).
- [61] M. Lebrat, P. Grišins, D. Husmann, S. Häusler, L. Corman, T. Giamarchi, J.-P. Brantut, and T. Esslinger. “Band and Correlated Insulators of Cold Fermions in a Mesoscopic Lattice”. *Phys. Rev. X* 8 (1 2018), p. 011053 (cit. on p. 2).
- [62] D. M. Basko, I. L. Aleiner, and B. L. Altshuler. “Metal–insulator transition in a weakly interacting many-electron system with localized single-particle states”. *Ann. Phys.* 321.5 (2006), pp. 1126–1205 (cit. on p. 2).
- [63] M. Schreiber, S. S. Hodgman, P. Bordia, H. P. Lüschen, M. H. Fischer, R. Vosk, E. Altman, U. Schneider, and I. Bloch. “Observation of many-body localization of interacting fermions in a quasirandom optical lattice”. *Science* 349.6250 (2015), p. 842 (cit. on pp. 2, 4, 24, 73, 75, 85, 94).
- [64] P. Bordia, H. P. Lüschen, S. S. Hodgman, M. Schreiber, I. Bloch, and U. Schneider. “Coupling Identical one-dimensional Many-Body Localized Systems”. *Phys. Rev. Lett.* 116.14 (2016), p. 140401 (cit. on p. 3).

- [65] H. P. Lüschen, P. Bordia, S. S. Hodgman, M. Schreiber, S. Sarkar, A. J. Daley, M. H. Fischer, E. Altman, I. Bloch, and U. Schneider. “Signatures of Many-Body Localization in a Controlled Open Quantum System”. *Phys. Rev. X* 7 (1 2017), p. 011034 (cit. on pp. 3, 119).
- [66] A. Rubio-Abadal, J.-y. Choi, J. Zeiher, S. Hollerith, J. Rui, I. Bloch, and C. Gross. “Many-Body Delocalization in the Presence of a Quantum Bath”. *Phys. Rev. X* 9.4 (2019), p. 041014 (cit. on pp. 3, 4).
- [67] J.-y. Choi, S. Hild, J. Zeiher, P. Schauß, A. Rubio-Abadal, T. Yefsah, V. Khemani, D. A. Huse, I. Bloch, and C. Gross. “Exploring the many-body localization transition in two dimensions”. *Science* 352.6293 (2016), pp. 1547–1552 (cit. on p. 3).
- [68] T. Kohlert, S. Scherg, X. Li, H. P. Lüschen, S. Das Sarma, I. Bloch, and M. Aidelsburger. “Observation of Many-Body Localization in a One-Dimensional System with a Single-Particle Mobility Edge”. *Phys. Rev. Lett.* 122.17 (2019), p. 170403 (cit. on pp. 3, 4).
- [69] M. Rispoli, A. Lukin, R. Schittko, S. Kim, M. E. Tai, J. Léonard, and M. Greiner. “Quantum critical behaviour at the many-body localization transition”. *Nature* 573.7774 (2019), pp. 385–389 (cit. on p. 3).
- [70] H. P. Lüschen, P. Bordia, S. Scherg, F. Alet, E. Altman, U. Schneider, and I. Bloch. “Observation of Slow Dynamics near the Many-Body Localization Transition in One-Dimensional Quasiperiodic Systems”. *Phys. Rev. Lett.* 119.26 (2017), p. 260401 (cit. on pp. 3, 4).
- [71] A. Lukin, M. Rispoli, R. Schittko, M. E. Tai, A. M. Kaufman, S. Choi, V. Khemani, J. Léonard, and M. Greiner. “Probing entanglement in a many-body-localized system”. *Science* 364.6437 (2019), pp. 256–260 (cit. on p. 3).
- [72] J. Smith, A. Lee, P. Richerme, B. Neyenhuis, P. W. Hess, P. Hauke, M. Heyl, D. A. Huse, and C. Monroe. “Many-body localization in a quantum simulator with programmable random disorder”. *Nat. Phys.* 12.10 (2016), pp. 907–911 (cit. on pp. 3, 4).
- [73] P. Roushan et al. “Spectroscopic signatures of localization with interacting photons in superconducting qubits”. *Science* 358.6367 (2017), pp. 1175–1179 (cit. on p. 3).
- [74] Q. Guo, C. Cheng, Z.-H. Sun, Z. Song, H. Li, Z. Wang, W. Ren, H. Dong, D. Zheng, Y.-R. Zhang, R. Mondaini, H. Fan, and H. Wang. “Observation of energy-resolved many-body localization”. *Nat. Phys.* (2020), pp. 1–6 (cit. on pp. 3, 4).
- [75] K. Xu, J.-J. Chen, Y. Zeng, Y.-R. Zhang, C. Song, W. Liu, Q. Guo, P. Zhang, D. Xu, H. Deng, K. Huang, H. Wang, X. Zhu, D. Zheng, and H. Fan. “Emulating Many-Body Localization with a Superconducting Quantum Processor”. *Phys. Rev. Lett.* 120.5 (2018), p. 050507 (cit. on pp. 3, 4).

-
- [76] K. X. Wei, C. Ramanathan, and P. Cappellaro. “Exploring Localization in Nuclear Spin Chains”. *Phys. Rev. Lett.* 120.7 (2018), p. 070501 (cit. on p. 3).
- [77] H. Bernien, S. Schwartz, A. Keesling, H. Levine, A. Omran, H. Pichler, S. Choi, A. S. Zibrov, M. Endres, M. Greiner, V. Vuletić, and M. D. Lukin. “Probing many-body dynamics on a 51-atom quantum simulator”. *Nature* 551.7682 (2017), pp. 579–584 (cit. on p. 3).
- [78] C. J. Turner, A. A. Michailidis, D. A. Abanin, M. Serbyn, and Z. Papić. “Weak ergodicity breaking from quantum many-body scars”. *Nat. Phys.* 14.7 (2018), pp. 745–749 (cit. on p. 3).
- [79] C. J. Turner, A. A. Michailidis, D. A. Abanin, M. Serbyn, and Z. Papić. “Quantum scarred eigenstates in a Rydberg atom chain: Entanglement, breakdown of thermalization, and stability to perturbations”. *Phys. Rev. B* 98.15 (2018), p. 155134 (cit. on p. 3).
- [80] N. Shiraishi and T. Mori. “Systematic Construction of Counterexamples to the Eigenstate Thermalization Hypothesis”. *Phys. Rev. Lett.* 119.3 (2017), p. 030601 (cit. on p. 3).
- [81] R. Mondaini, K. Mallayya, L. F. Santos, and M. Rigol. “Comment on “Systematic Construction of Counterexamples to the Eigenstate Thermalization Hypothesis””. *Phys. Rev. Lett.* 121.3 (2018), p. 038901 (cit. on p. 3).
- [82] S. Moudgalya, S. Rachel, B. A. Bernevig, and N. Regnault. “Exact excited states of nonintegrable models”. *Phys. Rev. B* 98.23 (2018), p. 235155 (cit. on p. 3).
- [83] T. Iadecola and M. Schecter. “Quantum many-body scar states with emergent kinetic constraints and finite-entanglement revivals”. *Phys. Rev. B* 101.2 (2020), p. 024306 (cit. on p. 3).
- [84] S. Chattopadhyay, H. Pichler, M. D. Lukin, and W. W. Ho. “Quantum many-body scars from virtual entangled pairs”. *Phys. Rev. B* 101.17 (2020), p. 174308 (cit. on p. 3).
- [85] P. Sala, T. Rakovszky, R. Verresen, M. Knap, and F. Pollmann. “Ergodicity Breaking Arising from Hilbert Space Fragmentation in Dipole-Conserving Hamiltonians”. *Phys. Rev. X* 10.1 (2020), p. 011047 (cit. on pp. 3, 4, 53, 73, 74, 77–79, 81, 111, 119).
- [86] V. Khemani, M. Hermele, and R. Nandkishore. “Localization from Hilbert space shattering: From theory to physical realizations”. *Phys. Rev. B* 101.17 (2020), p. 174204 (cit. on pp. 3, 53, 73–75, 79, 111, 119).
- [87] T. Rakovszky, P. Sala, R. Verresen, M. Knap, and F. Pollmann. “Statistical localization: From strong fragmentation to strong edge modes”. *Phys. Rev. B* 101 (12 2020), p. 125126 (cit. on pp. 3, 53, 73, 74, 77, 119).

- [88] S. Moudgalya, A. Prem, R. Nandkishore, N. Regnault, and B. A. Bernevig. “Thermalization and its absence within Krylov subspaces of a constrained Hamiltonian”. *arXiv:1910.14048* (2019) (cit. on pp. 3, 53, 71, 73–75, 111, 119).
- [89] R. M. Nandkishore and M. Hermele. “Fractons”. *Annu. Rev. Condens. Matter Phys.* 10.1 (2019), pp. 295–313 (cit. on p. 3).
- [90] M. Pretko, X. Chen, and Y. You. “Fracton phases of matter”. *Int. J. Mod. Phys. A* 35.06 (2020), p. 2030003 (cit. on p. 3).
- [91] S. Pai, M. Pretko, and R. M. Nandkishore. “Localization in Fractonic Random Circuits”. *Phys. Rev. X* 9.2 (2019), p. 021003 (cit. on p. 3).
- [92] J. P. Garrahan. “Aspects of non-equilibrium in classical and quantum systems: Slow relaxation and glasses, dynamical large deviations, quantum non-ergodicity, and open quantum dynamics”. *Physica A* 504 (2018), pp. 130–154 (cit. on p. 3).
- [93] N. Pancotti, G. Giudice, J. I. Cirac, J. P. Garrahan, and M. C. Bañuls. “Quantum East Model: Localization, Nonthermal Eigenstates, and Slow Dynamics”. *Phys. Rev. X* 10 (2 2020), p. 021051 (cit. on p. 3).
- [94] M. Nakamura, Z.-Y. Wang, and E. J. Bergholtz. “Exactly Solvable Fermion Chain Describing a $\nu = 1/3$ Fractional Quantum Hall State”. *Phys. Rev. Lett.* 109.1 (2012), p. 016401 (cit. on p. 3).
- [95] Z.-Y. Wang, S. Takayoshi, and M. Nakamura. “Spin-chain description of fractional quantum Hall states in the Jain series”. *Phys. Rev. B* 86.15 (2012), p. 155104 (cit. on p. 3).
- [96] E. J. Bergholtz, M. Nakamura, and J. Suorsa. “Effective spin chains for fractional quantum Hall states”. *Physica E. NanoPHYS* 09 43.3 (2011), pp. 755–760 (cit. on p. 3).
- [97] E. H. Rezayi and F. D. M. Haldane. “Laughlin state on stretched and squeezed cylinders and edge excitations in the quantum Hall effect”. *Phys. Rev. B* 50.23 (1994), pp. 17199–17207 (cit. on p. 3).
- [98] E. v. Nieuwenburg, Y. Baum, and G. Refael. “From Bloch oscillations to many-body localization in clean interacting systems”. *PNAS* 116.19 (2019), pp. 9269–9274 (cit. on pp. 3, 53, 111, 112).
- [99] M. Schulz, C. A. Hooley, R. Moessner, and F. Pollmann. “Stark Many-Body Localization”. *Phys. Rev. Lett.* 122.4 (2019), p. 040606 (cit. on pp. 3, 53, 111).
- [100] R. Ma, M. E. Tai, P. M. Preiss, W. S. Bakr, J. Simon, and M. Greiner. “Photon-Assisted Tunneling in a Biased Strongly Correlated Bose Gas”. *Phys. Rev. Lett.* 107.9 (2011), p. 095301 (cit. on p. 3).

-
- [101] C. Sias, A. Zenesini, H. Lignier, S. Wimberger, D. Ciampini, O. Morsch, and E. Arimondo. “Resonantly Enhanced Tunneling of Bose-Einstein Condensates in Periodic Potentials”. *Phys. Rev. Lett.* 98.12 (2007), p. 120403 (cit. on p. 3).
- [102] P. M. Preiss, R. Ma, M. E. Tai, A. Lukin, M. Rispoli, P. Zupancic, Y. Lahini, R. Islam, and M. Greiner. “Strongly correlated quantum walks in optical lattices”. *Science* 347.6227 (2015), pp. 1229–1233 (cit. on pp. 3, 55, 104).
- [103] M. Ben Dahan, E. Peik, J. Reichel, Y. Castin, and C. Salomon. “Bloch Oscillations of Atoms in an Optical Potential”. *Phys. Rev. Lett.* 76 (24 1996), pp. 4508–4511 (cit. on pp. 3, 55).
- [104] S. R. Taylor, M. Schulz, F. Pollmann, and R. Moessner. “Experimental probes of Stark many-body localization”. *Phys. Rev. B* 102.5 (2020), p. 054206 (cit. on pp. 3, 53, 69, 75, 77, 111, 119).
- [105] M. Schiulaz, A. Silva, and M. Müller. “Dynamics in many-body localized quantum systems without disorder”. *Phys. Rev. B* 91.18 (2015), p. 184202 (cit. on p. 4).
- [106] N. Y. Yao, C. R. Laumann, J. I. Cirac, M. D. Lukin, and J. E. Moore. “Quasi-Many-Body Localization in Translation-Invariant Systems”. *Phys. Rev. Lett.* 117.24 (2016), p. 240601 (cit. on p. 4).
- [107] Z. Papić, E. M. Stoudenmire, and D. A. Abanin. “Many-body localization in disorder-free systems: The importance of finite-size constraints”. *Ann. Phys.* 362 (2015), pp. 714–725 (cit. on p. 4).
- [108] A. Smith, J. Knolle, D. L. Kovrizhin, and R. Moessner. “Disorder-Free Localization”. *Phys. Rev. Lett.* 118 (26 2017), p. 266601 (cit. on pp. 4, 119).
- [109] A. Smith, J. Knolle, R. Moessner, and D. L. Kovrizhin. “Absence of Ergodicity without Quenched Disorder: From Quantum Disentangled Liquids to Many-Body Localization”. *Phys. Rev. Lett.* 119.17 (2017), p. 176601 (cit. on p. 4).
- [110] M. Brenes, M. Dalmonte, M. Heyl, and A. Scardicchio. “Many-Body Localization Dynamics from Gauge Invariance”. *Phys. Rev. Lett.* 120.3 (2018), p. 030601 (cit. on pp. 4, 119).
- [111] N. Darkwah Oppong, G. Pasqualetti, O. Bettermann, P. Zechmann, M. Knap, I. Bloch, and S. Fölling. “Probing transport and slow relaxation in the mass-imbalanced Fermi-Hubbard model”. *arXiv:2011.12411* (2020) (cit. on p. 4).
- [112] D. Jaksch, C. Bruder, J. I. Cirac, C. W. Gardiner, and P. Zoller. “Cold Bosonic Atoms in Optical Lattices”. *Phys. Rev. Lett.* 81.15 (1998), pp. 3108–3111 (cit. on p. 4).
- [113] M. P. A. Fisher, P. B. Weichman, G. Grinstein, and D. S. Fisher. “Boson localization and the superfluid-insulator transition”. *Phys. Rev. B* 40.1 (1989), pp. 546–570 (cit. on p. 4).

- [114] M. Greiner, O. Mandel, T. Esslinger, T. W. Hänsch, and I. Bloch. “Quantum phase transition from a superfluid to a Mott insulator in a gas of ultracold atoms”. *Nature* 415.6867 (2002), pp. 39–44 (cit. on p. 4).
- [115] U. Schneider, L. Hackermüller, S. Will, T. Best, I. Bloch, T. A. Costi, R. W. Helmes, D. Rasch, and A. Rosch. “Metallic and Insulating Phases of Repulsively Interacting Fermions in a 3D Optical Lattice”. *Science* 322.5907 (2008), p. 1520 (cit. on pp. 4, 35, 36).
- [116] E. Cocchi, L. A. Miller, J. H. Drewes, M. Koschorreck, D. Pertot, F. Brennecke, and M. Köhl. “Equation of State of the Two-Dimensional Hubbard Model”. *Phys. Rev. Lett.* 116 (17 2016), p. 175301 (cit. on p. 4).
- [117] E. Cocchi, L. A. Miller, J. H. Drewes, C. F. Chan, D. Pertot, F. Brennecke, and M. Köhl. “Measuring Entropy and Short-Range Correlations in the Two-Dimensional Hubbard Model”. *Phys. Rev. X* 7.3 (2017), p. 031025 (cit. on p. 4).
- [118] D. Greif, L. Tarruell, T. Uehlinger, R. Jördens, and T. Esslinger. “Probing Nearest-Neighbor Correlations of Ultracold Fermions in an Optical Lattice”. *Phys. Rev. Lett.* 106.14 (2011), p. 145302 (cit. on p. 4).
- [119] M. Köhl, H. Moritz, T. Stöferle, K. Günter, and T. Esslinger. “Fermionic Atoms in a Three Dimensional Optical Lattice: Observing Fermi Surfaces, Dynamics, and Interactions”. *Phys. Rev. Lett.* 94.8 (2005), p. 080403 (cit. on p. 4).
- [120] U. Schneider, L. Hackermüller, J. P. Ronzheimer, S. Will, S. Braun, T. Best, I. Bloch, E. Demler, S. Mandt, D. Rasch, and A. Rosch. “Fermionic transport and out-of-equilibrium dynamics in a homogeneous Hubbard model with ultracold atoms”. *Nat. Phys.* 8.3 (2012), pp. 213–218 (cit. on pp. 4, 75, 76, 93).
- [121] J. Koepsell, S. Hirthe, D. Bourgund, P. Sompet, J. Vijayan, G. Salomon, C. Gross, and I. Bloch. “Robust Bilayer Charge Pumping for Spin- and Density-Resolved Quantum Gas Microscopy”. *Phys. Rev. Lett.* 125.1 (2020), p. 010403 (cit. on p. 4).
- [122] T. Hartke, B. Oreg, N. Jia, and M. Zwierlein. “Doublon-Hole Correlations and Fluctuation Thermometry in a Fermi-Hubbard Gas”. *Phys. Rev. Lett.* 125.11 (2020), p. 113601 (cit. on p. 4).
- [123] L. W. Cheuk, M. A. Nichols, M. Okan, T. Gersdorf, V. V. Ramasesh, W. S. Bakr, T. Lompe, and M. W. Zwierlein. “Quantum-Gas Microscope for Fermionic Atoms”. *Phys. Rev. Lett.* 114.19 (2015), p. 193001 (cit. on p. 4).
- [124] E. Haller, J. Hudson, A. Kelly, D. A. Cotta, B. Peaudecerf, G. D. Bruce, and S. Kuhr. “Single-atom imaging of fermions in a quantum-gas microscope”. *Nat. Phys.* 11.9 (2015), pp. 738–742 (cit. on p. 4).

-
- [125] M. F. Parsons, F. Huber, A. Mazurenko, C. S. Chiu, W. Setiawan, K. Wooley-Brown, S. Blatt, and M. Greiner. “Site-Resolved Imaging of Fermionic ${}^6\text{Li}$ in an Optical Lattice”. *Phys. Rev. Lett.* 114.21 (2015), p. 213002 (cit. on p. 4).
- [126] A. Omran, M. Boll, T. A. Hilker, K. Kleinlein, G. Salomon, I. Bloch, and C. Gross. “Microscopic Observation of Pauli Blocking in Degenerate Fermionic Lattice Gases”. *Phys. Rev. Lett.* 115.26 (2015), p. 263001 (cit. on p. 4).
- [127] G. J. A. Edge, R. Anderson, D. Jarvis, D. C. McKay, R. Day, S. Trotzky, and J. H. Thywissen. “Imaging and addressing of individual fermionic atoms in an optical lattice”. *Phys. Rev. A* 92.6 (2015), p. 063406 (cit. on p. 4).
- [128] M. Boll, T. A. Hilker, G. Salomon, A. Omran, J. Nespolo, L. Pollet, I. Bloch, and C. Gross. “Spin- and density-resolved microscopy of antiferromagnetic correlations in Fermi-Hubbard chains”. *Science* 353.6305 (2016), pp. 1257–1260 (cit. on p. 4).
- [129] J. Vijayan, P. Sompet, G. Salomon, J. Koepsell, S. Hirthe, A. Bohrdt, F. Grusdt, I. Bloch, and C. Gross. “Time-resolved observation of spin-charge deconfinement in fermionic Hubbard chains”. *Science* 367.6474 (2020), pp. 186–189 (cit. on p. 4).
- [130] G. Salomon, J. Koepsell, J. Vijayan, T. A. Hilker, J. Nespolo, L. Pollet, I. Bloch, and C. Gross. “Direct observation of incommensurate magnetism in Hubbard chains”. *Nature* 565.7737 (2019), pp. 56–60 (cit. on p. 4).
- [131] D. Greif, M. F. Parsons, A. Mazurenko, C. S. Chiu, S. Blatt, F. Huber, G. Ji, and M. Greiner. “Site-resolved imaging of a fermionic Mott insulator”. *Science* 351.6276 (2016), pp. 953–957 (cit. on p. 4).
- [132] J. Koepsell, J. Vijayan, P. Sompet, F. Grusdt, T. A. Hilker, E. Demler, G. Salomon, I. Bloch, and C. Gross. “Imaging magnetic polarons in the doped Fermi-Hubbard model”. *Nature* 572.7769 (2019), pp. 358–362 (cit. on p. 4).
- [133] P. T. Brown, D. Mitra, E. Guardado-Sanchez, R. Nourafkan, A. Reymbaut, C.-D. Hébert, S. Bergeron, A.-M. S. Tremblay, J. Kokalj, D. A. Huse, P. Schauß, and W. S. Bakr. “Bad metallic transport in a cold atom Fermi-Hubbard system”. *Science* 363.6425 (2019), pp. 379–382 (cit. on p. 4).
- [134] P. T. Brown, D. Mitra, E. Guardado-Sanchez, P. Schauß, S. S. Kondov, E. Khatami, T. Paiva, N. Trivedi, D. A. Huse, and W. S. Bakr. “Spin-imbalance in a 2D Fermi-Hubbard system”. *Science* 357.6358 (2017), pp. 1385–1388 (cit. on p. 4).
- [135] D. Mitra, P. T. Brown, E. Guardado-Sanchez, S. S. Kondov, T. Devakul, D. A. Huse, P. Schauß, and W. S. Bakr. “Quantum gas microscopy of an attractive Fermi-Hubbard system”. *Nat. Phys.* 14.2 (2018), pp. 173–177 (cit. on p. 4).
- [136] L. W. Cheuk, M. A. Nichols, K. R. Lawrence, M. Okan, H. Zhang, and M. W. Zwierlein. “Observation of 2D Fermionic Mott Insulators of ${}^{40}\text{K}$ with Single-Site Resolution”. *Phys. Rev. Lett.* 116.23 (2016), p. 235301 (cit. on p. 4).

- [137] I. Bloch, J. Dalibard, and S. Nascimbène. “Quantum simulations with ultracold quantum gases”. *Nat. Phys.* 8.4 (2012), pp. 267–276 (cit. on p. 4).
- [138] C. A. Regal, C. Ticknor, J. L. Bohn, and D. S. Jin. “Creation of ultracold molecules from a Fermi gas of atoms”. *Nature* 424.47 (2003) (cit. on pp. 4, 34).
- [139] C. Chin, R. Grimm, P. Julienne, and E. Tiesinga. “Feshbach resonances in ultracold gases”. *Rev. Mod. Phys.* 82.2 (2010), pp. 1225–1286 (cit. on p. 4).
- [140] S. Fölling, S. Trotzky, P. Cheinet, M. Feld, R. Saers, A. Widera, T. Müller, and I. Bloch. “Direct observation of second-order atom tunnelling”. *Nature* 448.1029 (2007) (cit. on pp. 4, 85, 87).
- [141] J. Sebby-Strabley, M. Anderlini, P. S. Jessen, and J. V. Porto. “Lattice of double wells for manipulating pairs of cold atoms”. *Phys. Rev. A* 73 (3 2006), p. 033605 (cit. on pp. 4, 85, 87).
- [142] S. Trotzky, Y.-A. Chen, A. Flesch, I. P. McCulloch, U. Schollwöck, J. Eisert, and I. Bloch. “Probing the relaxation towards equilibrium in an isolated strongly correlated one-dimensional Bose gas”. *Nat. Phys.* 8.325 (2012) (cit. on p. 4).
- [143] R. P. Feynman. “Simulating physics with computers”. *Int. J. Theor. Phys.* 21 (6 1982), pp. 467–488 (cit. on p. 4).
- [144] P. Bordia, H. Lüschen, S. Scherg, S. Gopalakrishnan, M. Knap, U. Schneider, and I. Bloch. “Probing Slow Relaxation and Many-Body Localization in Two-Dimensional Quasiperiodic Systems”. *Phys. Rev. X* 7.4 (2017), p. 041047 (cit. on p. 4).
- [145] E. Guardado-Sanchez, B. M. Spar, P. Schauss, R. Belyansky, J. T. Young, P. Bienias, A. V. Gorshkov, T. Iadecola, and W. S. Bakr. “Quench Dynamics of a Fermi Gas with Strong Long-Range Interactions”. *arXiv:2010.05871* (2020) (cit. on p. 4).
- [146] E. Guardado-Sanchez, A. Morningstar, B. M. Spar, P. T. Brown, D. A. Huse, and W. S. Bakr. “Subdiffusion and Heat Transport in a Tilted Two-Dimensional Fermi-Hubbard System”. *Phys. Rev. X* 10.1 (2020), p. 011042 (cit. on pp. 4, 119).
- [147] G. Baym and C. Pethick. “Landau Fermi-Liquid Theory”. *Wiley, New York* (1991) (cit. on p. 7).
- [148] T. Giamarchi. “Quantum Physics in One Dimension”. *Oxford university press* (2004) (cit. on p. 7).
- [149] A. Klümper. “Integrability of Quantum Spin Chains: Theory and Applications to the Spin-1/2 XXZ Chain”. *Lect. Notes Phys.* 645 (2004), p. 349 (cit. on p. 7).
- [150] M. Rigol, V. Dunjko, V. Yurovsky, and M. Olshanii. “Relaxation in a Completely Integrable Many-Body Quantum System: An Ab Initio Study of the Dynamics of the Highly Excited States of 1D Lattice Hard-Core Bosons”. *Phys. Rev. Lett.* 98 (2007), p. 050405 (cit. on p. 7).

-
- [151] B. Bertini, F. Heidrich-Meisner, C. Karrasch, T. Prosen, R. Steinigeweg, and M. Znidaric. "Finite-temperature transport in one-dimensional quantum lattice models". *arXiv:2003.03334* (2020) (cit. on p. 7).
- [152] H. J. Korsch and S. Mossmann. "An algebraic solution of driven single band tight binding dynamics". *Phys. Lett.* 317.1 (2003), pp. 54–63 (cit. on p. 16).
- [153] P. Révész. *Random Walk in Random and Non-Random Environments*. 3rd. WORLD SCIENTIFIC, 2013 (cit. on p. 17).
- [154] N. Chernov and D. Dolgopyat. "THE GALTON BOARD: LIMIT THEOREMS AND RECURRENCE". *J. Am. Math. Soc* 22.3 (2009), pp. 821–858 (cit. on p. 17).
- [155] S. E. Venegas-Andraca. "Quantum walks: a comprehensive review". *Quantum Inf. Process.* 11.5 (2012), pp. 1015–1106 (cit. on pp. 17, 18).
- [156] E. Farhi and S. Gutmann. "Quantum computation and decision trees". *Phys. Rev. A* 58.2 (1998), pp. 915–928 (cit. on p. 17).
- [157] Y. Aharonov, L. Davidovich, and N. Zagury. "Quantum random walks". *Phys. Rev. A* 48.2 (1993), pp. 1687–1690 (cit. on p. 17).
- [158] O. Mülken and A. Blumen. "Continuous-time quantum walks: Models for coherent transport on complex networks". *Phys. Rep.* 502.2 (2011), pp. 37–87 (cit. on p. 17).
- [159] A. M. Childs. "Universal Computation by Quantum Walk". *Phys. Rev. Lett.* 102.18 (2009), p. 180501 (cit. on p. 18).
- [160] N. B. Lovett, S. Cooper, M. Everitt, M. Trevers, and V. Kendon. "Universal quantum computation using the discrete-time quantum walk". *Phys. Rev. A* 81.4 (2010), p. 042330 (cit. on p. 18).
- [161] M. S. Underwood and D. L. Feder. "Universal quantum computation by discontinuous quantum walk". *Phys. Rev. A* 82.4 (2010), p. 042304 (cit. on p. 18).
- [162] L. Vidmar, S. Langer, I. P. McCulloch, U. Schneider, U. Schollwöck, and F. Heidrich-Meisner. "Sudden expansion of Mott insulators in one dimension". *Phys. Rev. B* 88 (23 2013), p. 235117 (cit. on pp. 19, 20, 30, 31, 48, 50).
- [163] S. Langer, M. J. A. Schuetz, I. P. McCulloch, U. Schollwöck, and F. Heidrich-Meisner. "Expansion velocity of a one-dimensional, two-component Fermi gas during the sudden expansion in the ballistic regime". *Phys. Rev. A* 85 (4 2012), p. 043618 (cit. on pp. 20, 30, 48).
- [164] Z. Mei, L. Vidmar, F. Heidrich-Meisner, and C. J. Bolech. "Unveiling hidden structure of many-body wave functions of integrable systems via sudden-expansion experiments". *Phys. Rev. A* 93 (2 2016), p. 021607 (cit. on pp. 23, 32, 48, 52).

- [165] C. J. Bolech, F. Heidrich-Meisner, S. Langer, I. P. McCulloch, G. Orso, and M. Rigol. “Long-Time Behavior of the Momentum Distribution During the Sudden Expansion of a Spin-Imbalanced Fermi Gas in One Dimension”. *Phys. Rev. Lett.* 109 (11 2012), p. 110602 (cit. on pp. 23, 32, 52).
- [166] M. A. Cazalilla, R. Citro, T. Giamarchi, E. Orignac, and M. Rigol. “One dimensional bosons: From condensed matter systems to ultracold gases”. *Rev. Mod. Phys.* 83 (4 2011), pp. 1405–1466 (cit. on pp. 24, 25).
- [167] U. Schneider. “Interacting fermionic atoms in optical lattices - A quantum simulator for condensed matter physics”. PhD thesis. Johannes Gutenberg-Universität Mainz, 2011 (cit. on pp. 25, 37, 47).
- [168] D. A. Abanin, W. De Roeck, and F. Huveneers. “Exponentially Slow Heating in Periodically Driven Many-Body Systems”. *Phys. Rev. Lett.* 115 (25 2015), p. 256803 (cit. on pp. 26, 39, 77).
- [169] S. Scherg, T. Kohlert, J. Herbrych, J. Stolpp, P. Bordia, U. Schneider, F. Heidrich-Meisner, I. Bloch, and M. Aidelsburger. “Nonequilibrium Mass Transport in the 1D Fermi-Hubbard Model”. *Phys. Rev. Lett.* 121 (13 2018), p. 130402 (cit. on pp. 27, 29, 31, 45, 51, 85).
- [170] F. Heidrich-Meisner, S. R. Manmana, M. Rigol, A. Muramatsu, A. E. Feiguin, and E. Dagotto. “Quantum distillation: Dynamical generation of low-entropy states of strongly correlated fermions in an optical lattice”. *Phys. Rev. A* 80 (4 2009), p. 041603 (cit. on pp. 29, 41, 43, 47, 52).
- [171] J. Herbrych, A. E. Feiguin, E. Dagotto, and F. Heidrich-Meisner. “Efficiency of fermionic quantum distillation”. *Phys. Rev. A* 96 (3 2017), p. 033617 (cit. on pp. 29, 41, 43, 45).
- [172] T. Enss and J. Sirker. “Light cone renormalization and quantum quenches in one-dimensional Hubbard models”. *New J. Phys.* 14 (2012), p. 023008 (cit. on p. 31).
- [173] A. Bauer, F. Dorfner, and F. Heidrich-Meisner. “Temporal decay of Néel order in the one-dimensional Fermi-Hubbard model”. *Phys. Rev. A* 91 (5 2015), p. 053628 (cit. on p. 31).
- [174] S. Sorg, L. Vidmar, L. Pollet, and F. Heidrich-Meisner. “Relaxation and thermalization in the one-dimensional Bose-Hubbard model: A case study for the interaction quantum quench from the atomic limit”. *Phys. Rev. A* 90 (3 2014), p. 033606 (cit. on pp. 31, 50).
- [175] C. Boschi, D. E., E. Ercolessi, L. Ferrari, P. Naldesi, F. Ortolani, and L. Taddia. “Bound states and expansion dynamics of interacting bosons on a one-dimensional lattice”. *Phys. Rev. A* 90 (4 2014), p. 043606 (cit. on p. 32).

-
- [176] T. Rom. “Bosonische und fermionische Quantengase in dreidimensionalen optischen Gittern”. PhD thesis. Ludwig-Maximilians-Universität München, 2009 (cit. on pp. 33, 83, 88).
- [177] M. T. DePue, C. McCormick, S. L. Winoto, S. Oliver, and D. S. Weiss. “Unity Occupation of Sites in a 3D Optical Lattice”. *Phys. Rev. Lett.* 82 (11 1999), pp. 2262–2265 (cit. on p. 37).
- [178] R. Rausch and M. Potthoff. “Filling-dependent doublon dynamics in the one-dimensional Hubbard model”. *Phys. Rev. B* 95 (4 2017), p. 045152 (cit. on p. 39).
- [179] A. Rosch, D. Rasch, B. Binz, and M. Vojta. “Metastable Superfluidity of Repulsive Fermionic Atoms in Optical Lattices”. *Phys. Rev. Lett.* 101 (26 2008), p. 265301 (cit. on p. 40).
- [180] K. Winkler, G. Thalhammer, F. Lang, R. Grimm, J. H. Denschlag, A. J. Daley, A. Kantian, H. P. Bahler, and P. Zoller. “Repulsively bound atom pairs in an optical lattice”. *Nature* 441 (2006), p. 853 (cit. on p. 40).
- [181] M. T. DePue, C. McCormick, S. L. Winoto, S. Oliver, and D. S. Weiss. “Unity Occupation of Sites in a 3D Optical Lattice”. *Phys. Rev. Lett.* 82 (11 1999), p. 2262 (cit. on p. 41).
- [182] D. Muth, D. Petrosyan, and M. Fleischhauer. “Dynamics and evaporation of defects in Mott-insulating clusters of boson pairs”. *Phys. Rev. A* 85 (2012), p. 013615 (cit. on pp. 41, 43).
- [183] C. Hofrichter. “Probing the SU(N) Fermi-Hubbard model with ytterbium atoms in an optical lattice”. PhD thesis. Johannes Gutenberg-Universität Mainz, 2016 (cit. on p. 42).
- [184] I. Bengtsson and K. Zyczkowski. “Geometry of Quantum States: An Introduction to Quantum Entanglement”. *Cambridge University Press* (2006) (cit. on p. 47).
- [185] J.-S. Bernier, C. Kollath, A. Georges, L. De Leo, F. Gerbier, C. Salomon, and M. Köhl. “Cooling fermionic atoms in optical lattices by shaping the confinement”. *Phys. Rev. A* 79 (6 2009), p. 061601 (cit. on p. 47).
- [186] T.-L. Ho and Q. Zhou. “Universal Cooling Scheme for Quantum Simulation”. *arXiv:0911.5506* (2009) (cit. on p. 47).
- [187] M. Lubasch, V. Murg, U. Schneider, J. I. Cirac, and M.-C. Bañuls. “Adiabatic Preparation of a Heisenberg Antiferromagnet Using an Optical Superlattice”. *Phys. Rev. Lett.* 107.16 (2011), p. 165301 (cit. on p. 47).
- [188] C. S. Chiu, G. Ji, A. Mazurenko, D. Greif, and M. Greiner. “Quantum state engineering of a Hubbard system with ultracold fermions”. *Phys. Rev. Lett.* 120 (24 2018), p. 243201 (cit. on p. 47).

- [189] J. Kajala, F. Massel, and P. Törmä. “Expansion Dynamics in the One-Dimensional Fermi-Hubbard Model”. *Phys. Rev. Lett.* 106 (2011), p. 206401 (cit. on p. 50).
- [190] J. Kajala, F. Massel, and P. Törmä. “Expansion dynamics of the Fulde-Ferrell-Larkin-Ovchinnikov state”. *Phys. Rev. A* 84 (4 2011), p. 041601 (cit. on p. 52).
- [191] H. Lu, L. O. Baksmaty, C. J. Bolech, and H. Pu. “Expansion of 1D Polarized Superfluids: The Fulde-Ferrell-Larkin-Ovchinnikov State Reveals Itself”. *Phys. Rev. Lett.* 108 (22 2012), p. 225302 (cit. on p. 52).
- [192] L.-N. Wu and A. Eckardt. “Bath-Induced Decay of Stark Many-Body Localization”. *Phys. Rev. Lett.* 123.3 (2019), p. 030602 (cit. on pp. 53, 119).
- [193] R. Yao and J. Zakrzewski. “Many-body localization of bosons in an optical lattice: Dynamics in disorder-free potentials”. *Phys. Rev. B* 102 (10 2020), p. 104203 (cit. on p. 53).
- [194] F. Meinert, M. J. Mark, E. Kirilov, K. Lauber, P. Weinmann, M. Gröbner, and H.-C. Nägerl. “Interaction-Induced Quantum Phase Revivals and Evidence for the Transition to the Quantum Chaotic Regime in 1D Atomic Bloch Oscillations”. *Phys. Rev. Lett.* 112.19 (2014), p. 193003 (cit. on pp. 55, 67, 104).
- [195] Z. A. Geiger, K. M. Fujiwara, K. Singh, R. Senaratne, S. V. Rajagopal, M. Lipatov, T. Shimasaki, R. Driben, V. V. Konotop, T. Meier, and D. M. Weld. “Observation and Uses of Position-Space Bloch Oscillations in an Ultracold Gas”. *Phys. Rev. Lett.* 120.21 (2018), p. 213201 (cit. on p. 55).
- [196] F. Meinert, M. Knap, E. Kirilov, K. Jag-Lauber, M. B. Zvonarev, E. Demler, and H.-C. Nägerl. “Bloch oscillations in the absence of a lattice”. *Science* 356.6341 (2017), pp. 945–948 (cit. on p. 55).
- [197] T. Li, L. Duca, M. Reitter, F. Grusdt, E. Demler, M. Endres, M. Schleier-Smith, I. Bloch, and U. Schneider. “Bloch state tomography using Wilson lines”. *Science* 352.6289 (2016), pp. 1094–1097 (cit. on p. 55).
- [198] M. Aidelsburger, M. Lohse, C. Schweizer, M. Atala, J. T. Barreiro, S. Nascimbène, N. R. Cooper, I. Bloch, and N. Goldman. “Measuring the Chern number of Hofstadter bands with ultracold bosonic atoms”. *Nat. Phys.* 11.2 (2015), pp. 162–166 (cit. on p. 55).
- [199] J. Feldmann, K. Leo, J. Shah, D. A. B. Miller, J. E. Cunningham, T. Meier, G. von Plessen, A. Schulze, P. Thomas, and S. Schmitt-Rink. “Optical investigation of Bloch oscillations in a semiconductor superlattice”. *Phys. Rev. B* 46.11 (1992), pp. 7252–7255 (cit. on p. 55).
- [200] T. Hartmann, F. Keck, H. J. Korsch, and S. Mossmann. “Dynamics of Bloch oscillations”. *New J. Phys.* 6 (2004), pp. 2–2 (cit. on pp. 56, 57).

-
- [201] R. Peierls. “Zur Theorie des Diamagnetismus von Leitungselektronen”. *Zeitschrift für Physik* 80.11 (1933), pp. 763–791 (cit. on p. 65).
- [202] M. Aidelsburger. “Artificial gauge fields with ultracold atoms in optical lattices”. PhD thesis. Ludwig-Maximilians-Universität München, 2015 (cit. on p. 65).
- [203] A. V. Ponomarev. “Dynamics of cold Fermi atoms in one-dimensional optical lattices”. PhD thesis. Univ. Freiburg, 2008 (cit. on pp. 67, 105).
- [204] A. Buchleitner and A. R. Kolovsky. “Interaction-Induced Decoherence of Atomic Bloch Oscillations”. *Phys. Rev. Lett.* 91.25 (2003), p. 253002 (cit. on p. 67).
- [205] S. Bravyi, D. P. DiVincenzo, and D. Loss. “Schrieffer–Wolff transformation for quantum many-body systems”. *Ann. Phys.* 326.10 (2011), pp. 2793–2826 (cit. on p. 70).
- [206] J. R. Schrieffer and P. A. Wolff. “Relation between the Anderson and Kondo Hamiltonians”. *Phys. Rev.* 149 (2 1966), pp. 491–492 (cit. on p. 70).
- [207] T. Barthel, C. Kasztelan, I. P. McCulloch, and U. Schollwöck. “Magnetism, coherent many-particle dynamics, and relaxation with ultracold bosons in optical superlattices”. *Phys. Rev. A* 79 (5 2009), p. 053627 (cit. on p. 70).
- [208] E. S. Mananga and T. Charpentier. “Introduction of the Floquet-Magnus expansion in solid-state nuclear magnetic resonance spectroscopy”. *J. Chem. Phys.* 135.4 (2011), p. 044109 (cit. on p. 70).
- [209] M. Bukov, L. D’Alessio, and A. Polkovnikov. “Universal high-frequency behavior of periodically driven systems: from dynamical stabilization to Floquet engineering”. *Adv. Phys.* 64.2 (2015), pp. 139–226 (cit. on p. 70).
- [210] S. Scherg, T. Kohlert, P. Sala, F. Pollmann, B. H. M., I. Bloch, and M. Aidelsburger. “Observing non-ergodicity due to kinetic constraints in tilted Fermi-Hubbard chains”. *arXiv:2010.12965* (2020) (cit. on pp. 71, 73, 78, 80, 82, 106–108, 110, 113, 115, 116, 118, 130).
- [211] F. Meinert, M. J. Mark, E. Kirilov, K. Lauber, P. Weinmann, M. Grobner, A. J. Daley, and H.-C. Nägerl. “Observation of many-body dynamics in long-range tunneling after a quantum quench”. *Science* 344.6189 (2014), pp. 1259–1262 (cit. on pp. 72, 110).
- [212] R. Sensarma, D. Pekker, E. Altman, E. Demler, N. Strohmaier, D. Greif, R. Jördens, L. Tarruell, H. Moritz, and T. Esslinger. “Lifetime of double occupancies in the Fermi-Hubbard model”. *Phys. Rev. B* 82 (22 2010), p. 224302 (cit. on p. 77).
- [213] D. N. Page. “Average entropy of a subsystem”. *Phys. Rev. Lett.* 71 (9 1993), pp. 1291–1294 (cit. on p. 82).

- [214] L. Vidmar and M. Rigol. “Entanglement Entropy of Eigenstates of Quantum Chaotic Hamiltonians”. *Phys. Rev. Lett.* 119.22 (2017) (cit. on p. 82).
- [215] G. De Tomasi and I. M. Khaymovich. “Multifractality Meets Entanglement: Relation for Nonergodic Extended States”. *Phys. Rev. Lett.* 124.20 (2020) (cit. on p. 82).
- [216] C. A. Regal and D. S. Jin. “Measurement of Positive and Negative Scattering Lengths in a Fermi Gas of Atoms”. *Phys. Rev. Lett.* 90 (23 2003), p. 230404 (cit. on pp. 87, 93).
- [217] R. Jördens. “Metallic and Mott-Insulating Phases in Fermionic Quantum Gases”. PhD thesis. Zürich: ETH Zurich, 2010 (cit. on pp. 87, 93, 104).
- [218] C. A. Regal, M. Greiner, and D. S. Jin. “Observation of Resonance Condensation of Fermionic Atom Pairs”. *Phys. Rev. Lett.* 92 (4 2004), p. 040403 (cit. on p. 93).
- [219] S. Fölling. “Probing strongly correlated states of ultracold atoms in optical lattices”. PhD thesis. Johannes Gutenberg-Universität Mainz, 2008 (cit. on p. 94).
- [220] M. Gustavsson, E. Haller, M. J. Mark, J. G. Danzl, G. Rojas-Kopeinig, and H.-C. Nägerl. “Control of Interaction-Induced Dephasing of Bloch Oscillations”. *Phys. Rev. Lett.* 100.8 (2008), p. 080404 (cit. on p. 104).
- [221] U. Schollwöck. “The density-matrix renormalization group in the age of matrix product states”. *Ann. Phys.* 326.1 (2011), p. 96 (cit. on p. 106).
- [222] J. Hauschild and F. Pollmann. “Efficient numerical simulations with Tensor Networks: Tensor Network Python (TeNPy)”. *SciPost Phys. Lect. Notes* (2018), p. 5 (cit. on p. 106).
- [223] G. Vidal. “Efficient Simulation of One-Dimensional Quantum Many-Body Systems”. *Phys. Rev. Lett.* 93 (4 2004), p. 040502 (cit. on p. 106).
- [224] B. Hebbe Madhusudhana, S. Scherg, T. Kohlert, I. Bloch, and M. Aidelsburger. “Benchmarking an approximate theory for localized 1D Fermi-Hubbard system on a quantum simulator”. *In preparation* () (cit. on p. 106).
- [225] J. Wurtz and A. Polkovnikov. “Emergent conservation laws and nonthermal states in the mixed-field Ising model”. *Phys. Rev. B* 101 (19 2020), p. 195138 (cit. on p. 116).
- [226] D. A. Abanin, W. De Roeck, W. W. Ho, and F. Huveneers. “Effective Hamiltonians, prethermalization, and slow energy absorption in periodically driven many-body systems”. *Phys. Rev. B* 95 (1 2017), p. 014112 (cit. on p. 116).
- [227] W. De Roeck and V. Verreet. “Very slow heating for weakly driven quantum many-body systems”. *arXiv:1911.01998* (2019) (cit. on p. 116).
- [228] D. V. Else, B. Bauer, and C. Nayak. “Prethermal Phases of Matter Protected by Time-Translation Symmetry”. *Phys. Rev. X* 7 (1 2017), p. 011026 (cit. on p. 116).

-
- [229] S. Pai and M. Pretko. “Dynamical Scar States in Driven Fracton Systems”. *Phys. Rev. Lett.* 123.13 (2019), p. 136401 (cit. on p. 119).
- [230] H. Zhao, J. Vovrosh, F. Mintert, and J. Knolle. “Quantum Many-Body Scars in Optical Lattices”. *Phys. Rev. Lett.* 124.16 (2020), p. 160604 (cit. on p. 119).
- [231] A. Kshetrimayum, J. Eisert, and D. M. Kennes. “Stark time crystals: Symmetry breaking in space and time”. *Phys. Rev. B* 102 (19 2020), p. 195116 (cit. on p. 119).
- [232] E. Bairey, G. Refael, and N. H. Lindner. “Driving induced many-body localization”. *Phys. Rev. B* 96 (2 2017), p. 020201 (cit. on p. 119).
- [233] D. S. Bhakuni, R. Nehra, and A. Sharma. “Drive-induced many-body localization and coherent destruction of Stark many-body localization”. *Phys. Rev. B* 102.2 (2020), p. 024201 (cit. on p. 119).
- [234] J. Feldmeier, P. Sala, G. de Tomasi, F. Pollmann, and M. Knap. “Anomalous Diffusion in Dipole- and Higher-Moment Conserving Systems”. *arXiv:2004.00635* (2020) (cit. on p. 119).
- [235] S. Pai and M. Pretko. “Fractons from confinement in one dimension”. *Phys. Rev. Research* 2.1 (2020), p. 013094 (cit. on p. 119).
- [236] R. Verdel, F. Liu, S. Whitsitt, A. V. Gorshkov, and M. Heyl. “Real-time dynamics of string breaking in quantum spin chains”. *Phys. Rev. B* 102.1 (2020), p. 014308 (cit. on p. 119).
- [237] Z.-C. Yang, F. Liu, A. V. Gorshkov, and T. Iadecola. “Hilbert-Space Fragmentation from Strict Confinement”. *Phys. Rev. Lett.* 124.20 (2020), p. 207602 (cit. on p. 119).
- [238] B. Yang, H. Sun, R. Ott, H.-Y. Wang, T. V. Zache, J. C. Halimeh, Z.-S. Yuan, P. Hauke, and J.-W. Pan. “Observation of gauge invariance in a 71-site Bose-Hubbard quantum simulator”. *arXiv:2003.08945* (2020) (cit. on p. 119).
- [239] G. N. Watson. “A Treatise on the Theory of Bessel Functions”. *Cambridge University Press* (1995) (cit. on p. 124).

Acknowledgement

After many years in the Bloch group, I want to say thank you to all the amazing people, who contributed in some way to this thesis. First of all, I say thank you to Immanuel Bloch, who gave me the chance to work in his group, travel to international conferences and learn from discussions with many different people in other labs. In particular, I want to thank him for his instructive and direct feedback during meetings. Moreover, he gave me the freedom to play in the lab and test my own ideas. Second, I want to thank Monika Aidelsburger for her supervision and her time for many discussions about experimental results and their interpretation. Furthermore, I am particularly happy, that experiments at Fermi1 will carry on under her supervision.

Moreover, I want to thank my colleagues in the Fermi1 team, who I had the pleasure to work with. It was a great time! In particular, I want to thank Thomas Kohlert for a great time in the lab, for patiently dealing with both my good and my bad habits and for teaching me many useful things, such as how to change and how to kill laser diodes. Special thanks go to Bharath Hebbe Madhusudhana as well, for his brilliant understanding of both physics and math. I learned so many things during the discussions we had and I am utterly thankful, that he joined our team as postdoc. Many thanks go to Hernik Lüschen, for teaching me many tricks on how to run the experiment, for many wonderful trips to the mountains and for a lot of climbing advice. Finally I say thank you to Pranjali Bordia for teaching me a lot about many-body localization in the beginning of my PhD and I thank Michael Schreiber for a lot of technical advice regarding the experiment and its subtleties.

Besides the team in the lab, I also had the chance to work with many brilliant theorists. A big thank you goes to Jan Stolpp, Jacek Herbrych, Fabian Heidrich-Meisner and Frank Pollmann. Especially, I want to thank Pablo Sala for his endeavor to patiently teach me all important details on Hilbert-space fragmentation.

A big thank you goes out to all my colleagues at other experiments in the Bloch group. In particular, I want to thank: Nelson Darkwah Oppong, for many espressos at Dinatale and the wonderful trip to DAMOP in Florida. Christian Schweizer, for sharing his wisdom on superlattices and in general for his brilliant and helpful advice, whenever it was necessary. Martin Reitter, for entertaining late nights out, stories on astronauts, and a flight around

Bibliography

Starnberger See. Toni Rubio Abadal, for many discussion on localization and a great time at the conference at ICFO in Barcelona. Sebastian Hild, Moritz Höfer, Johannes Zeiher and Christoph Braun, for many hiking and skiing trips and a lot of fun in the mountains.

Many thanks to everybody who proof-read parts of this thesis: Thomas Kohlert, Bharath Hebbe Madhusudhana, Henrik Lüschen, Anna-Sophia Mäder, Lukas Schepp, Christian Schweizer, Nelson Darkwah Oppong and Monika Aidelsburger.

I want to thank Ildiko Kecskesi, who always found a solution to any seemingly impossible problem regarding both administration and IT. Furthermore, I am very thankful for many discussions with Bodo Hecker on electronic circuits and their implementation in the lab.

Last but not least, I want to thank my family for their support, whenever it was necessary. I want to thank Florian Wolf and Dimitri Pimenov, who I met, when starting my physics degree at the university and who remained dear friends every since, contributing advice in difficults times during my PhD and many fun Schafkopf evenings.